

**LIGHT TRANSPORT IN TISSUE**

APPROVED BY  
SUPERVISORY COMMITTEE:

Supervisor: \_\_\_\_\_

Supervisor: \_\_\_\_\_

\_\_\_\_\_

\_\_\_\_\_

\_\_\_\_\_

Dedicated to  
My Grandfather  
Arthur Isaac Johnson

**LIGHT TRANSPORT IN TISSUE**

by

**SCOTT ALAN PRAHL, B.S.**

**DISSERTATION**

Presented to the Faculty of the Graduate School of  
The University of Texas at Austin  
in Partial Fulfillment  
of the Requirements  
for the Degree of

**DOCTOR OF PHILOSOPHY**

THE UNIVERSITY OF TEXAS AT AUSTIN

December 1988

## Acknowledgements

I would like to express my gratitude to Dr. Welch who provided funding, much needed perspective, and an introduction to the art of the absence of politics; to Dr. Valvano for the Macintosh II used for all parts of this dissertation, to Dr. Jacques for “rolling up his sleeves and getting his hands dirty;” to Dr. Pearce for stimulating (nay exhilarating) Friday afternoon research meetings and general harassing; to Dr. van Gemert who insisted that what I was doing was “not unimportant;” to Dr. Yoon for arguments about optical stuff and philosophy; and to almost doctor Cheong for always being too kind. Finally, I must thank Anne for loving me through the evolution of each chapter as we (the chapter and I) metamorphosed from a glimmer of an idea, into equations, graphs, figures and tables, into a few typeset pages, and finally into a monster. Without Anne I would not be finished yet, and may not have ever finished.

# LIGHT TRANSPORT IN TISSUE

Publication No. \_\_\_\_\_

**Scott Alan Prahl, Ph.D.**  
**The University of Texas at Austin, 1988**

**Supervisors: A. J. Welch**  
**J. W. Valvano**

Two numerical solutions for radiative transport in tissue are presented: the Monte Carlo and the adding-doubling methods. Both methods are appropriate for tissues with internal reflection at boundaries and anisotropic scattering patterns. The adding-doubling method yields accurate solutions in one-dimension. The slower Monte Carlo method is the only exact solution available for finite beam irradiance of tissue. Convolution formulas for calculation of fluence rates for circularly symmetric flat and Gaussian irradiances using the Monte Carlo impulse response are presented.

The delta-Eddington method is extended to include many boundary conditions appropriate for tissue optics. The delta-Eddington method is compared with exact methods. Delta-Eddington reflection and transmission are least accurate for thin tissues and mismatched boundary conditions. Fluence calculations obtained with the delta-Eddington approximation are inaccurate (>50% error) for tissues with both mismatched boundaries and high albedos.

A method and theory for the measurement of the phase function of tissue is presented. The method is shown to have a tendency to overestimate the

isotropic scattering component in tissues with mismatched boundaries. A graph is presented to correct the overestimate. The backscattered peak in goniophotometer measurements is shown to result from reflection of the forward peak and not from a backward peak in the phase function. Measurements on human dermis indicate that the phase function can be described by a modified Henyey-Greenstein phase function.

A practical method for measuring the optical properties of tissue as a function of wavelength is presented. Evaluation of the technique indicates that the method is accurate to 10% for all optical properties of tissue when sample thicknesses exceed one optical depth. This technique is applied to bloodless human dermis as a function of wavelength and to bloodless human aorta during moderate power ( $\sim 100 \text{ mW/mm}^2$ ) argon laser irradiation as a function of irradiation time.

# Table of Contents

<b>Acknowledgements</b>	<b>iv</b>
<b>Abstract</b>	<b>v</b>
<b>Chapter 1. Introduction and Background</b>	<b>1</b>
1.1 Motivation . . . . .	2
1.2 General assumptions . . . . .	3
1.3 Definitions and nomenclature . . . . .	4
1.3.1 Dimensional quantities . . . . .	4
1.3.2 Dimensionless quantities . . . . .	5
1.3.3 Phase functions . . . . .	6
1.3.4 The transport equation . . . . .	11
1.4 Goals . . . . .	12
<b>Chapter 2. Monte Carlo</b>	<b>15</b>
2.1 Methods . . . . .	16
2.1.1 Fixed stepsize method . . . . .	17
2.1.2 Variable stepsize method . . . . .	20
2.1.3 Variance reduction techniques . . . . .	22
2.2 Mechanics of photon propagation . . . . .	25
2.3 Phase function . . . . .	27
2.4 Photon absorption . . . . .	27
2.5 Internal reflection . . . . .	28
2.6 Convolution . . . . .	30
2.7 Verification . . . . .	35
2.8 Conclusions . . . . .	39

<b>Chapter 3. The Adding-Doubling Method</b>	<b>40</b>
3.1 Definition of reflection and transmission operators . . . . .	43
3.2 Derivation of the adding-doubling method . . . . .	46
3.3 The redistribution function . . . . .	48
3.4 Reflection and transmission of thin layers . . . . .	49
3.5 Boundary conditions . . . . .	51
3.6 Implementation . . . . .	53
3.7 Tabulated values . . . . .	54
3.8 Conclusions . . . . .	56
<b>Chapter 4. The Delta-Eddington Approximation</b>	<b>63</b>
4.1 Derivation of the diffusion equation . . . . .	63
4.2 Boundary conditions . . . . .	68
4.2.1 Index matching, no incident diffuse light . . . . .	69
4.2.2 Index matching, diffuse light incident . . . . .	72
4.2.3 Index mismatch, no incident diffuse light . . . . .	73
4.2.4 Index mismatch, diffuse light incident . . . . .	76
4.2.5 Glass slide — no incident diffuse light . . . . .	77
4.2.6 Glass slide — diffuse light incident . . . . .	78
4.2.7 Index matching, no incident diffuse light, both media scattering	79
4.2.8 Index mismatch, no incident diffuse light, both media scattering	79
4.3 Dimensionless form of the diffusion equation . . . . .	81
4.4 Solution of the one-dimensional diffusion equation . . . . .	84
4.4.1 Non-conservative scattering ( $a' < 1$ ), finite slab . . . . .	84
4.4.2 Non-conservative scattering ( $a' < 1$ ), semi-infinite slab . . . . .	85
4.4.3 Conservative scattering $a = 1$ , finite slab . . . . .	86
4.4.4 Conservative scattering ( $a = 1$ ), semi-infinite slab . . . . .	86
4.5 Reflection, transmission, and fluence rates in one-dimension . . . . .	87
4.6 Three-dimensional solution of the diffusion equation . . . . .	89
4.6.1 Formal solution of $\phi_a(\mathbf{r})$ in terms of Green's functions . . . . .	89
4.6.2 The Green's Function for an Infinite Slab . . . . .	92
4.6.3 Explicit Expressions for $\phi_a(\mathbf{r})$ . . . . .	93
4.6.4 Flux, Reflection, and Transmission in Three Dimensions . . . . .	95



4.7	Evaluation of the Delta-Eddington Approximation . . . . .	95
4.7.1	Comparison of total reflection and transmission . . . . .	95
4.7.2	Comparison of Fluence Rates . . . . .	96
4.8	Conclusions . . . . .	99
<b>Chapter 5. Goniophotometry</b>		<b>104</b>
5.1	Single scattering approximation . . . . .	105
5.2	Experimental apparatus . . . . .	107
5.3	Tissue preparation . . . . .	110
5.4	Data reduction . . . . .	112
5.4.1	Corrections for internal reflection and refraction . . . . .	113
5.4.2	Least squares fit . . . . .	116
5.5	Evaluation of the method . . . . .	121
5.6	Experimental results . . . . .	126
5.7	Conclusions . . . . .	130
<b>Chapter 6. Spectrophotometry</b>		<b>131</b>
6.1	Inverse method . . . . .	133
6.1.1	Evaluation of the inverse method . . . . .	140
6.1.2	Experimental measurements . . . . .	145
6.1.3	Conclusions . . . . .	156
<b>Chapter 7. Conclusions</b>		<b>157</b>
7.1	Discussion . . . . .	159
<b>Appendices</b>		<b>161</b>
<b>Appendix A1. Random Variables with Non-Uniform Density Functions</b>		<b>162</b>
A1.1	Analytic Method . . . . .	162
A1.2	Monte Carlo Method . . . . .	165
A1.3	Discrete form of the Analytic Method . . . . .	166

<b>Appendix A2. Internal Reflection</b>	<b>167</b>
A2.1 Basic Reflection Formulas . . . . .	167
A2.2 Fresnel Reflection in a Glass Slide . . . . .	170
A2.3 Reflection Moments $R_0$ , $R_1$ , and $R_2$ . . . . .	171
A2.4 Star's Approximation . . . . .	172
A2.5 Keijzer's Approximation . . . . .	174
A2.6 Walsh's Analytic Solution for $R_1$ . . . . .	175
A2.7 Egan Polynomial Approximation for $R_1$ . . . . .	175
A2.8 Polynomial Approximations to $R_0$ , $R_1$ , and $R_2$ . . . . .	181
A2.9 Approximations for the Boundary Coefficient $A$ . . . . .	181
A2.10 The Boundary Condition Parameter in the Presence of a Glass Slide .	185
<b>Appendix A3. Solid Angle Integrals and Dirac-Delta Functions</b>	<b>187</b>
A3.1 Integrals over entire spheres . . . . .	187
A3.2 Integrals over hemispheres . . . . .	190
A3.3 Delta functions . . . . .	194
A3.4 Examples of Delta Functions . . . . .	195
<b>Appendix A4. Numerical Details of the 3D Diffusion Solution</b>	<b>196</b>
A4.1 Eigenvalues . . . . .	196
A4.1.1 One eigenvalue less than $\pi/2\tau'$ . . . . .	197
A4.1.2 More than one eigenvalue less than $\pi/2\tau'$ . . . . .	199
A4.2 Summation of series . . . . .	199
<b>Bibliography</b>	<b>203</b>
<b>Vita</b>	<b>211</b>

# Chapter 1

## Introduction and Background

### Introduction

The goal of this dissertation is to answer the fundamental question “How is light distributed inside a tissue during laser irradiation?” Since the light distribution in a tissue is dependent on its optical properties, the fundamental problem naturally splits into two related questions: “What is the light distribution during irradiation in a tissue with known optical properties?” and “What are the optical properties of a tissue and how might they be measured?” Heretofore, these two questions have been addressed in ways which ignored or roughly approximated two important physical features: boundary conditions and anisotropic scattering. In this dissertation, boundary conditions and scattering functions characteristic of tissues are carefully implemented and included in all calculations.

In Chapters 2 and 3, accurate models for calculation of light distributions based on known optical properties are developed. In Chapter 4 a fast approximate method for these calculations is presented. In the last two chapters, two different techniques for measuring optical properties are outlined.

## 1.1 Motivation

The laser as a tool is becoming available to a growing number of physicians, but before the doctor can use this tool he must select a laser, a beam power, a spot size, and an irradiation time. Since small differences in any of these parameters can determine whether an application is efficacious or disastrous, some *a priori* knowledge about the effects of each parameter is needed. This information is usually provided by mathematical models.

Any model of a laser treatment—photochemical, thermal, or ablative—is based on the distribution of light in the tissue. For example, in thermal and ablative applications, the light distribution is directly proportional to the heat source used in the thermal model. In photochemical applications involving hematoporphyrin derivative, the release of singlet oxygen is proportional to the light distribution. Since photodynamic, thermal, and ablative models are only as good as the optical model they are based on, it is unfortunate that current biomedical light transport models are approximate (e.g., the diffusion approximation) or heuristic (Kubelka-Munk). The paint, paper, photographic, and plastic industries; meteorology; oceanography; astrophysics; analytic chemistry; and biology have all used exact optical models; however, these methods have heretofore not been utilized in biomedical applications.

Accurate models are needed because approximate models fail near tissue boundaries. In many applications, the distribution of light immediately beneath the point of irradiation is critical. In these regions the assumptions made in the approximate models are worst. For example, in the Kubelka-Munk approximation the distribution of light immediately subsurface is assumed isotropic. Since

light must undergo several scattering events before an isotropic profile is reached this approximation is poorest near the surface.

The optical properties of some tissues have been measured, but often in the context of the heuristic Kubelka-Munk model and consequently, these parameters should only be used with the Kubelka-Munk theory. Existing methods are impractical for measurement of optical properties as a function of wavelength. Current methods are ill-suited because they require diffuse light [64], many sample thicknesses [70], or goniophotometric measurements [13]. A practical method for measurement of optical properties as a function of wavelength is needed. The single scattering phase function (defined below) characterizing a tissue must also be measured. Recent attempts to measure the phase function [5, 13] have not generated quantitative expressions that may be used in more complete models.

## 1.2 General assumptions

This section outlines the fundamental assumptions made throughout this dissertation. First, the distribution of light is assumed static with time, and consequently, both optical properties which change and irradiance times shorter than about one nanosecond are excluded. Second, all media are assumed to have homogeneous optical properties. This restriction may be relaxed somewhat in the models presented, but all results in this dissertation are for strictly optically homogeneous media.

A third assumption is that the tissue geometry may be approximated by an infinite plane-parallel slab of finite thickness. Such a shape allows generalization to layered tissues or extension to an infinitely thick tissue. This assumption

requires that the beam width be smaller than the width of the tissue.

The tissue is assumed to have a uniform index of refraction. This ensures that light will travel in a straight line until it is scattered or absorbed. The boundaries are assumed smooth and to reflect specularly according to Fresnel's law. The last assumption is that the polarization of light may be ignored.

### 1.3 Definitions and nomenclature

In this section the nomenclature used in this dissertation is presented. In Section 1.3.1 variables with dimensions are introduced. The next section introduces the albedo and optical thickness. In Section 1.3.3 the phase function is discussed and relations between the Henyey-Greenstein phase function and the delta-Eddington phase function are given. In Section 1.3.4 the transport equation is introduced.

#### 1.3.1 Dimensional quantities

Tissue is assumed to be a random turbid medium, with variations in the optical properties small enough to prevent localized absorption. In other words, tissue is considered to have volumetric scattering and absorption properties rather than being composed of discrete scattering and absorption centers distributed in a non-scattering, non-absorbing medium. The advantage to the distributed scattering center approach is that for perfect spheres the phase function is known, however there is little similarity between perfect spheres and tissue. Volumetric absorption (or scattering) is obtained by multiplying an absorption (or scattering) cross section with the density of absorbers (or scatterers) [31]. This is how the absorption coefficients  $\mu_a$  and scattering coefficient  $\mu_s$  are defined. The scattering and absorption coefficient are typically measured in inverse millimeters

and the reciprocal of these coefficients is the average distance that light will travel before being scattered or absorbed, respectively.

The thickness of the slab is denoted by  $d$ . In addition to the thickness, light propagation through a slab is determined by three parameters: the absorption and scattering coefficients and the phase function. The phase function is the fraction of light scattered into the direction of the unit vector  $\hat{\mathbf{s}}'$  by light incident from the direction of the unit vector  $\hat{\mathbf{s}}$ . The phase function is discussed in detail below.

The radiance is  $L(\mathbf{r}, \hat{\mathbf{s}})$ ; the position is denoted by the vector  $\mathbf{r}$  and the radiance is specified by the direction of the unit vector  $\hat{\mathbf{s}}$ . The radiance has units of energy per area per solid angle (Watts  $\text{sr}^{-1} \text{cm}^2$ ). Sometimes this is called “specific intensity” or just “intensity.”

The fluence  $\phi(\mathbf{r})$  is the total radiance at a point  $\mathbf{r}$ . The fluence is obtained by integrating the radiance over all angles. The product of the fluence and the absorption coefficient equals the heat source: the amount of energy deposited in a unit volume of tissue.

### 1.3.2 Dimensionless quantities

When dimensionless units are used, light propagation is dependent upon three parameters: the albedo, the optical depth or thickness, and the phase function. The albedo  $a$  is a dimensionless parameter defined as the ratio of scattering to the sum of scattering and absorption. The albedo varies between zero and one: a value of zero indicates the absence of scattering and a value of one indicates that the tissue does not absorb light. The optical depth  $\tau$  is the product of the tissue thickness and the sum of the scattering and absorption coefficient. An

optical depth of one indicates that there is a probability of  $e^{-1} = 37\%$  that light will travel at least that distance without scattering or absorbing.

### 1.3.3 Phase functions

When light strikes a particle with an index of refraction different from its environment, the light is refracted. The angle at which the light is bent is a function of the size and shape of the particle as well as the wavelength of the incident light and the incidence angle of the light. In general, each particle will have a different scattering profile. This scattering profile is called the phase function. This name is misleading since the scattering profile has no connection with the phase of the incident light waves and would be more appropriately called a scattering function.

The phase function  $p(\hat{\mathbf{s}}, \hat{\mathbf{s}}')$  describes the amount of light scattered from the direction denoted by the unit vector  $\hat{\mathbf{s}}$  into the direction  $\hat{\mathbf{s}}'$ . There are a number of ways in which the phase function may be normalized, but the most natural is that used by the astrophysicists. They treat the phase function as a probability distribution; consequently, their normalization condition requires the integral of the phase function over all angles to equal unity

$$\int_{4\pi} p(\hat{\mathbf{s}}, \hat{\mathbf{s}}') d\omega = 1 \quad (1.1)$$

where  $d\omega$  is a differential solid angle in the  $\hat{\mathbf{s}}$  direction. This condition does not permit the phase function to describe absorption of light by the particle, the phase function is a description of only the distribution of scattering by the particle. Thus  $p(\hat{\mathbf{s}}, \hat{\mathbf{s}}') d\omega$  is the probability that a photon incident from the  $\hat{\mathbf{s}}$  direction will leave in the differential unit of solid angle in the  $\hat{\mathbf{s}}'$  direction.



The phase function will differ in general from particle to particle. For simplicity an average phase function which adequately describes the most important features of the scattering process is used. This average phase function is further constrained by assuming that the probability of scattering from one direction into another is a function only of the angle between the two directions, thus  $p(\hat{\mathbf{s}}, \hat{\mathbf{s}}') = p(\hat{\mathbf{s}} \cdot \hat{\mathbf{s}}') = p(\cos \theta)$ .

The simplest phase function is the isotropic phase function

$$p(\hat{\mathbf{s}} \cdot \hat{\mathbf{s}}') = \frac{1}{4\pi} \quad (1.2)$$

The factor of  $1/4\pi$  results from the normalization condition (1.1) and the fact that there are  $4\pi$  steradians in a complete circle. The phase function has units of  $\text{sr}^{-1}$ .

If the phase function is not isotropic, then a parameter called the average cosine of the phase function is used to describe the degree of anisotropy of the phase function. This parameter is often denoted by  $g$  and is defined as the integral over all angles of the phase function multiplied by the cosine of the angle

$$g = \int_{4\pi} p(\hat{\mathbf{s}} \cdot \hat{\mathbf{s}}') (\hat{\mathbf{s}} \cdot \hat{\mathbf{s}}') d\omega \quad (1.3)$$

The choice of a single scattering phase function is a compromise between realism and mathematical tractability. Jacques *et al.* have shown that a modified Henyey-Greenstein function describes single particle light scattering in human dermis quite well [32]. More recently Yoon *et al.* have found similar results for human aorta [69]. The modified Henyey-Greenstein function is

$$p_{\text{m-HG}}(\cos \theta) = \frac{1}{4\pi} \left[ \beta + (1 - \beta) \frac{1 - g_{\text{HG}}^2}{(1 + g_{\text{HG}}^2 - 2g_{\text{HG}} \cos \theta)^{3/2}} \right] \quad (1.4)$$

In this function, the first term  $\beta$  represents the amount of light scattered isotropically. The second term is the Henyey-Greenstein function. The function is normalized such that the integral of the phase function over all solid angles is unity. When  $\beta = 0$  this phase function reduces to the Henyey-Greenstein phase function.

A popular phase function is the Eddington phase function

$$p_{\text{Eddington}}(\cos \theta) = \frac{1}{4\pi} [1 + 3g' \cos \theta] \quad (1.5)$$

With this approximation the transport equation may be reduced into a diffusion equation [31, 55]. Such a solution provides a qualitative picture of radiative transport in media which is not highly forward scattering. Unfortunately, the anisotropy (the average cosine of the phase function) for tissue such as dermis [32], aorta [70] and bladder [9] have values of 0.8–0.9. This suggests that the Eddington approximation would not be very good for modeling light in such tissues.

Another possible phase function is the delta-Eddington approximation [34],

$$p_{\delta\text{-E}}(\cos \theta) = \frac{1}{4\pi} [2f\delta(1 - \cos \theta) + (1 - f)(1 + 3g' \cos \theta)] \quad (1.6)$$

where  $f$  is the fraction of light scattered into the forward peak and  $g'$  is an asymmetry factor. As  $f \rightarrow 1$  the phase function becomes exactly a delta function, and as  $f \rightarrow 0$  the phase function reduces to the Eddington approximation. This phase function also allows reduction of the transport equation to a diffusion equation. Consequently, it is desirable to approximate the *modified* Henyey-Greenstein function using the delta-Eddington phase function. Joseph *et al.* used the delta-Eddington phase function above to approximate the Henyey-Greenstein phase

function [34]. Only slight modification must be made to their derivation to arrive at an approximation for the modified Henyey-Greenstein function.

Recalling that the Dirac delta function may be expanded as a sum of Legendre polynomials [44] allows expansion of the delta-Eddington phase function

$$p_{\delta-E}(\cos \theta) = \frac{1}{4\pi} \left[ f \sum_{n=0}^{\infty} (2n+1) P_n(\cos \theta) + (1-f)(1+3g'P_1(\cos \theta)) \right] \quad (1.7)$$

collecting like terms

$$p_{\delta-E}(\cos \theta) = \frac{1}{4\pi} [1 + 3[f + g'(1-f)]P_1(\cos \theta) + 5fP_2(\cos \theta) + \dots] \quad (1.8)$$

The modified Henyey-Greenstein phase function may also be expanded as a sum of Legendre polynomials using the expansion from [60] for the Henyey-Greenstein function

$$p_{m-HG}(\cos \theta) = \frac{1}{4\pi} \left[ \beta P_0(\cos \theta) + (1-\beta) \sum_{n=0}^{\infty} (2n+1) g_{HG}^n P_n(\cos \theta) \right] \quad (1.9)$$

and collecting like terms

$$p_{m-HG}(\cos \theta) = \frac{1}{4\pi} [1 + 3(1-\beta)g_{HG}P_1(\cos \theta) + 5(1-\beta)g_{HG}^2P_2(\cos \theta) + \dots] \quad (1.10)$$

Now the first terms of each series are equated. The very first term ( $n = 0$ ) is  $1/4\pi$  for both series. This results from the normalization of the phase functions. The next term ( $n = 1$ ) corresponds to three times the average cosine of the phase function  $g$  [31]. Thus for the delta-Eddington approximation, the average cosine of the phase function is

$$g = f + (1-f)g' \quad (1.11)$$

and for the modified Henyey-Greenstein function the average cosine is

$$g = (1-\beta)g_{HG} \quad (1.12)$$

The average cosine of the phase function  $g$  is a measure of how much light is scattered in the forward direction. The anisotropy can be any value between  $-1$  and  $1$ . If  $g = -1$ , then scattering is completely in the backwards direction; if  $g = 1$ , then scattering is totally in the forwards direction; and if  $g = 0$ , then scattering is isotropic. If Equations (1.11) and (1.12) are equated then a relation between the parameters of the two phase functions is obtained

$$f + (1 - f)g' = (1 - \beta)g_{\text{HG}} \quad (1.13)$$

Proceeding in a similar manner, the second moments of the two phase functions may be equated

$$f = (1 - \beta)g_{\text{HG}}^2 \quad (1.14)$$

And using Equation (1.13) an expression for  $g'$  may be obtained

$$g' = \frac{g_{\text{HG}}(1 - g_{\text{HG}})}{\frac{1}{1 - \beta} - g_{\text{HG}}^2} \quad (1.15)$$

Notice that if  $g_{\text{HG}} \rightarrow 1$  then  $g' \rightarrow 0$  provided that  $\beta \neq 0$ , otherwise  $g' \rightarrow \frac{1}{2}$ .

For example, measurements of the phase function of dermis at 633 nm yields the modified Henyey-Greenstein parameters  $g_{\text{HG}} = 0.91$  and  $\beta = 0.10$ . Using Equations (1.14) and (1.15) the corresponding values for the delta-Eddington phase function may be found, i.e.,  $f = 0.75$  and  $g' = 0.29$ . This illustrates the way that the delta-Eddington approximation accommodates for strongly forward scattering phase functions by lumping a large portion of the scattering into the forward directed Dirac delta function and allowing the anisotropy to fall. Increased accuracy results since it is known that the diffusion approximation is poor for large values of anisotropy but is relatively good when the scattering is nearly isotropic.

For completeness, the following equations relate the modified Henyey-Greenstein parameters to the delta-Eddington parameters

$$g_{\text{HG}} = \frac{f + (1-f)g'}{1-\beta} \quad \text{and} \quad \beta = 1 - \frac{f}{g_{\text{HG}}^2} \quad (1.16)$$

These are useful as long as  $f$  is not zero. If  $f$  is zero then no solution is possible, because the equations relating the first and second moments are no longer independent.

### 1.3.4 The transport equation

The transport equation describes the behavior of light in a slab [8]

$$(\hat{\mathbf{s}} \cdot \nabla)L(\mathbf{r}, \hat{\mathbf{s}}) = -\mu_t L(\mathbf{r}, \hat{\mathbf{s}}) + \mu_s \int_{4\pi} p(\hat{\mathbf{s}}, \hat{\mathbf{s}}') L(\mathbf{r}, \hat{\mathbf{s}}) d\omega' \quad (1.17)$$

Here the integral is over all solid angles and  $d\omega'$  is the differential solid angle in the direction  $\hat{\mathbf{s}}'$ . Notice that the radiance is a function of five variables: three in the  $\mathbf{r}$  vector and two in the  $\hat{\mathbf{s}}$  unit vector. (Since  $\hat{\mathbf{s}}$  is a unit vector the magnitude is fixed and consequently one degree of freedom has been removed.) The left hand side of the transport equation describes the rate of change of the intensity at the point indicated by  $\mathbf{r}$  in the direction  $\hat{\mathbf{s}}$ . This rate of change is equal to the intensity lost due to absorption and scattering (the first term on the R.H.S.) plus the intensity gained through light scattering from all other directions into the direction  $\hat{\mathbf{s}}$  (the last term on the R.H.S.).

The assumptions implicit in the transport equation are those mentioned in the assumptions Section 1.2 above. The first of these is that the medium is assumed to be homogeneous. This means that any variation in the scattering and absorption of the medium must be on length scales much smaller than

the depth of the slab. Another more questionable assumption, from a tissue optics standpoint, is that each particle is sufficiently isolated that its scattering pattern is independent of all other particles. This is known as the far field approximation in geometrical optics, and is clearly violated for typical tissues because the scattering and absorbing particles are in contact with one another. A related assumption is that scattering by all particles may be described by a single function known as the phase function. This means that there exists an ensemble average scattering pattern for all the scattering centers in the medium. Yet another assumption is that the intensity distribution is assumed to be in a steady state, which is valid if the light is incident for longer than a few nanoseconds. Finally, it is assumed that there are no light sources in the medium.

## 1.4 Goals

The primary goal of this dissertation is to permit accurate estimates of the light distributions in tissue during laser irradiation. This goal has two separate but related tasks:

1. Develop an exact solution to calculate light fluences
2. Develop methods to measure the optical properties of a tissue.

The first task is dealt with in the chapters 2 and 3 according to the method of solution. These are

- Develop a Monte Carlo model for 3D problems
- Develop an adding-doubling model for 1D slab problems

The Monte Carlo method is the currently the only way to calculate fluence for finite width beams with index mismatching and anisotropic scattering. Chapter 3 discusses the adding-doubling method. This method is very accurate and much faster than the Monte-Carlo method. Unfortunately, the adding-doubling method is restricted to one dimension. Consequently, the Monte Carlo and the adding-doubling methods are complementary accurate techniques useful in different contexts.

Related to the first goal, but mainly useful for the second goal is the delta-Eddington approximation. This approximation is an improvement on the diffusion approximation. The delta-Eddington approximation is very fast and can be used in iterative procedures to determine the optical properties of tissues. Goals related to the delta-Eddington approximation are

- Develop a delta-Eddington model for fast, approximate solutions
- Determine accuracy of delta-Eddington approximation

Chapter 4 is devoted to these two subgoals. The Monte Carlo and adding-doubling methods are used to evaluate the delta-Eddington approximation.

The measurement of optical properties falls into two categories. The first one concerns the measurement of the phase function

- Give a method for measuring the phase function of tissue
- Determine accuracy of the method
- Make measurements on human dermis

The method for measuring the phase function is based on the single scattering approximation. The range of optical thicknesses over which this technique is applicable is evaluated using the adding-doubling method as “truth.” In Chapter 5 the method is outlined, the accuracy of the method is checked, and results for human dermal samples are reported.

In Chapter 6 a method for measuring the optical properties with a spectrophotometer is discussed.

- Present the inverse iterative method
- Determine errors in the inverse method
- Make measurements on human dermis

The iterative method is outlined in Chapter 6, as well as the limits of its applicability, and experimental results for human dermis.



# Chapter 2

## Monte Carlo

### Introduction

Monte Carlo refers to a technique first proposed by Metropolis and Ulam [42] to simulate physical processes using a stochastic model. In a radiative transport problem, the Monte Carlo method consists of recording photons histories as they are scattered and absorbed. Monte Carlo programs with great sophistication have been developed—an extreme example is the **MCNP** Monte Carlo code package at Los Alamos that has involved over 250 person years of development [14]. The Monte Carlo method has been used infrequently to model laser-tissue interactions, but these applications have so far neglected anisotropy and internal light reflection (e.g., [65]).

This chapter describes a simple Monte Carlo code specifically for use in modeling light transport in a tissue and includes the formulas necessary to implement the Monte Carlo method in computer code. It discusses the reflection of a photon from boundaries, shows how the phase function may be used to generate new scattering angles, discusses a few variance reduction schemes to improve efficiency, gives a method for estimating the uncertainty in any Monte Carlo calculation, and verifies the implementation by comparison against known solutions. The verified Monte Carlo model is used to evaluate the finite beam

size delta-Eddington approximation in Chapter 4.

The Monte Carlo method is attractive because it is easily implemented and sufficiently flexible that complex tissues may be modeled. Theoretically, Monte Carlo solutions can be obtained for any desired accuracy. However the accuracy is proportional to  $1/\sqrt{N}$  where  $N$  is the number of photons propagated. Thus relative errors less than a few tenths of a percent will require the propagation of substantial numbers of photons ( $\sim 10^6 - 10^9$ ) and require large amounts of computer time.

## 2.1 Methods

This section outlines two different Monte Carlo methods: the physics is the same for both methods, but one method uses fixed stepsizes and the other uses variable stepsizes for each propagation step. Both methods begin by launching a photon downwards into the tissue at the origin. If a collimated beam is normally incident on a slab, the photon is initially directed directly downwards into the tissue. If the incident light is diffuse, then the photon direction is chosen randomly from all possible directions in the downward hemisphere. For a finite beam size the origin of the beam is randomly chosen based either on the incident beam's profile or the fluence rate is found using a convolution technique similar to those in Section 2.5.

Once launched, the photon is moved a distance  $\Delta s$  where it may be scattered, absorbed, propagated undisturbed, internally reflected, or transmitted out of the tissue. The photon is repeatedly moved until it either escapes from or is absorbed by the tissue. If the photon escapes from the tissue, the reflection or transmission of the photon is recorded. If the photon is absorbed, the position

of the absorption is recorded. Once this has been done a new photon is launched at the origin. This process is repeated until the desired number of photons have been propagated. The recorded reflection, transmission, and absorption profiles will approach true values (for a tissue with the specified optical properties) as the number of photons propagated approaches infinity.

### 2.1.1 Fixed stepsize method

The simplest Monte Carlo method propagates each photon with small, fixed incremental stepsizes. A flowchart describing the process is shown in Figure 2.1. Three questions arise: “What should the stepsize  $\Delta s$  be?”, “What is the probability of the photon being scattered?” and, “What is the probability of the photon being absorbed?”

The fixed stepsize  $\Delta s$  chosen must be small relative to the average mean free path of a photon in the tissue. The mean free path is the reciprocal of the total attenuation coefficient.

$$\Delta s \ll \frac{1}{\mu_a + \mu_s} \quad (2.1)$$

If  $\Delta s$  is too small the photon will rarely interact with the tissue and the Monte Carlo method will be inefficient. It was found that a stepsize  $\Delta s$  of one-tenth of a mean free path yielded reasonable results.

The probability of absorption of a photon travelling a distance  $\Delta s$  is given by Beer’s Law

$$P\{\text{absorption}\} = 1 - e^{-\mu_a \Delta s} \quad (2.2)$$

Expanding the exponential in a Taylor series, and letting  $\mu_a \Delta s \rightarrow 0$ , shows that

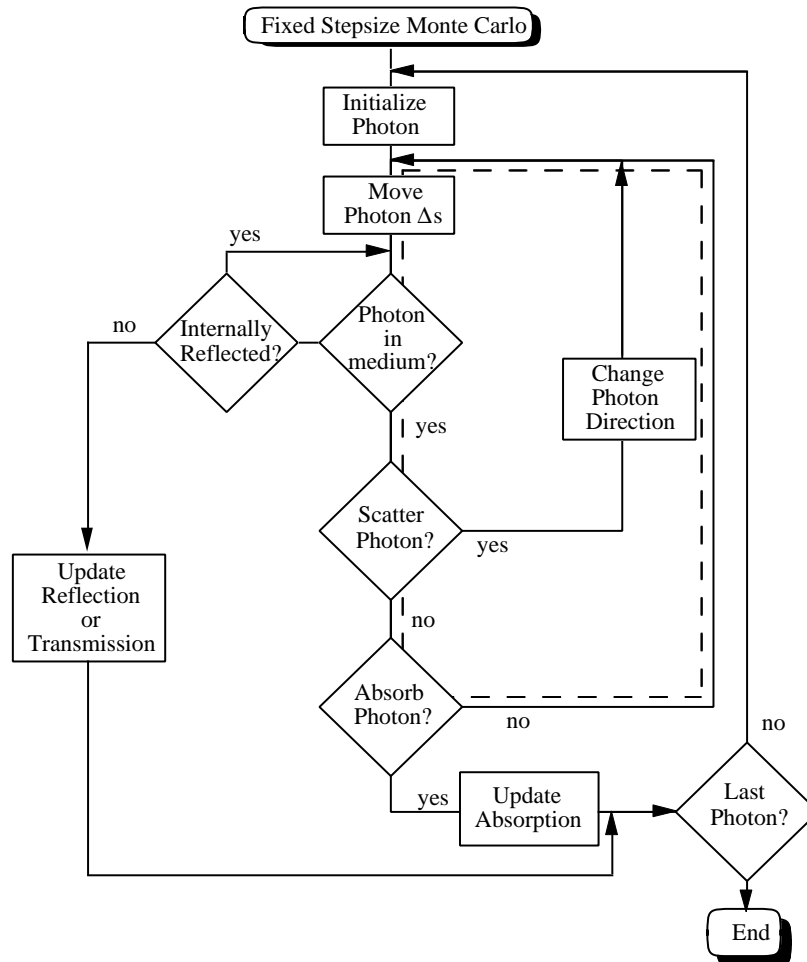


Figure 2.1: Flowchart of Monte Carlo with fixed propagation stepsize. The small stepsize  $\Delta s$  required causes most of the computation time is spent in the inner (dashed) loop. Since the statistics are only changed in the “Update Absorption” and “Update Reflection and Transmission” boxes this method is inefficient.

the probability of photon absorption is

$$P\{\text{absorption}\} \approx \mu_a \Delta s \quad (2.3)$$

Similarly, the probability that the photon will scatter in this distance is

$$P\{\text{scattering}\} = 1 - e^{-\mu_s \Delta s} \quad (2.4)$$

and for short pathlengths  $\Delta s$

$$P\{\text{scattering}\} \approx \mu_s \Delta s \quad (2.5)$$

Assuming three disjoint events (1) absorption, (2) scattering, and (3) no interaction between the tissue and the photon, the sum of the three events equals unity. This implicitly assumes that the photon cannot be scattered and absorbed in the same propagation step. To determine if a photon is scattered or absorbed, a random number  $\xi$  uniformly distributed between zero and one is generated and compared with the probability of absorption. If,

$$\xi < P\{\text{absorption}\} \quad (2.6)$$

then the photon is absorbed and a new photon is launched. If  $\xi$  is between

$$P\{\text{absorption}\} \leq \xi < P\{\text{absorption}\} + P\{\text{scattering}\} \quad (2.7)$$

then the photon is scattered and a new photon direction is chosen based on the phase function for the medium. If the photon is neither scattered nor absorbed then the photon has propagated the distance  $\Delta s$  without interaction.

One advantage of this method is that it is simple to implement. Moreover, since the stepsize is fixed, each step corresponds to a given length of time, and a

time history can be generated. The primary disadvantage is that this technique is slow: the photon must be moved an average of  $(\mu_a + \mu_s)/\Delta s$  times before it is either absorbed or scattered. The number of propagation steps required becomes prohibitive for highly scattering media, since the total distance travelled before absorption is large compared with the stepsize.

### 2.1.2 Variable stepsize method

The second Monte Carlo method varies the distance  $\Delta s$  that the photon is moved each propagation step. The stepsize  $\Delta s$  is chosen in such a way that it is the distance at which the photon is either scattered or absorbed. If distances in the tissue have been non-dimensionalized (Section 4.5) so that the mean free path is unity, then the probability density function for  $\Delta s$  is  $e^{-\Delta s}$ . Appendix A1 shows how a stepsize  $\Delta s$  with this probability density function may be generated as a function of a random number  $\xi$  uniformly distributed between zero and one

$$\Delta s = -\ln \xi \quad (2.8)$$

When  $\Delta s$  is chosen in this manner, the photon is forced either to scatter or be absorbed after each propagation step. Given that the photon is either absorbed or scattered, the probability that it is scattered is equal to the ratio of the scattering coefficient to the sum of the absorption and scattering coefficients (the albedo). If  $\xi$  is a random number uniformly distributed between zero and one, then the photon is scattered if

$$\xi < \frac{\mu_s}{\mu_a + \mu_s} = a. \quad (2.9)$$

Otherwise, the photon is absorbed. If a photon is scattered then a new photon direction is chosen based on the phase function, otherwise the photon is absorbed

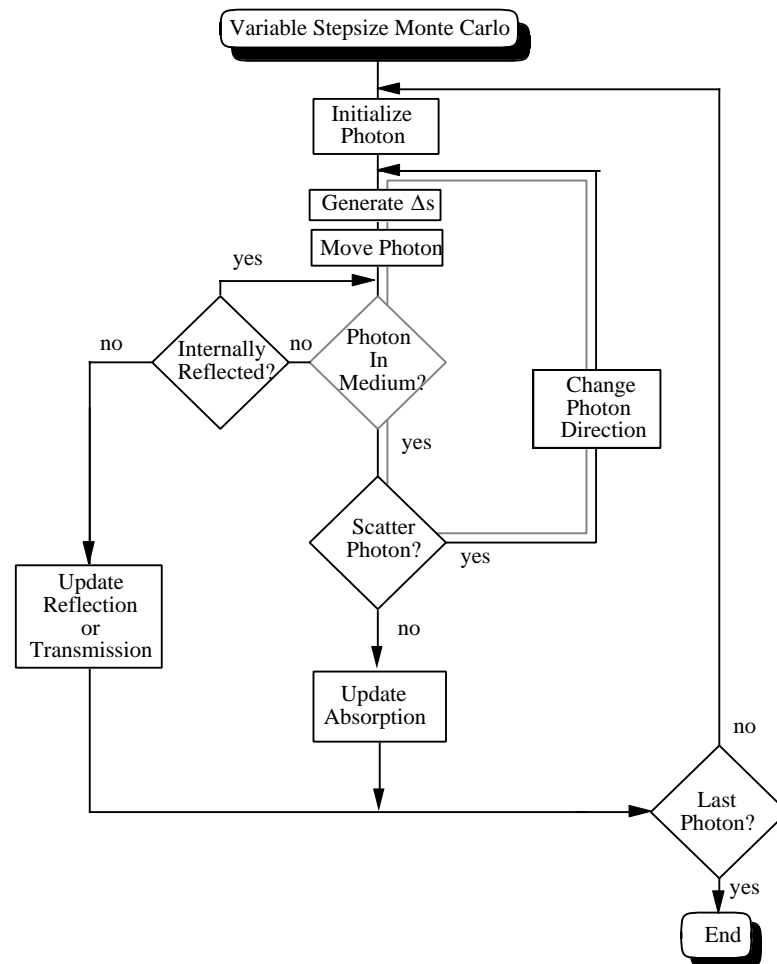


Figure 2.2: Flowchart for the variable stepsize Monte Carlo technique. Notice that each time through the inner (dashed) loop, the photon is either scattered or absorbed.

and a new photon is launched. This process is described in the flowchart in Figure 2.2.

### 2.1.3 Variance reduction techniques

Variance reduction techniques are used to reduce the number of photons necessary to achieve the desired accuracy for a Monte Carlo calculation. These techniques have a long history and the important ones were first implemented by Kahn [35, 36, 38, 37]. More recently, a summary of current variance reduction techniques is given by Hendricks and Booth [25]. A simple proof that the variance is smaller when implicit capture is used (described below) is given by Sobol' [57]. The flowchart in Figure 2.3 illustrates how variance reduction techniques fit into a Monte Carlo program.

The technique of implicit capture as described by Witt was used to reduce the variance in the Monte Carlo model [68]. This technique assigns a weight to each photon as it enters tissue. After each propagation step, the particle's weight is reduced by the probability of absorption. The usual method completely absorbs a photon according to the probability of absorption. Thus the implicit capture technique provides some absorption information at each photon step, rather than just at times when the photon is completely absorbed.

As an example, consider the use of the implicit capture technique with the variable stepsize method. In this case, the photon's weight is reduced by a factor of  $(1 - a)$  which represents the fraction of the photon absorbed at each propagation step. This ensures that photons are not killed after a significant amount of computation time has been spent to transport them long distances. This is the basis for the improvement or, as Hendricks and Booth put it, "All



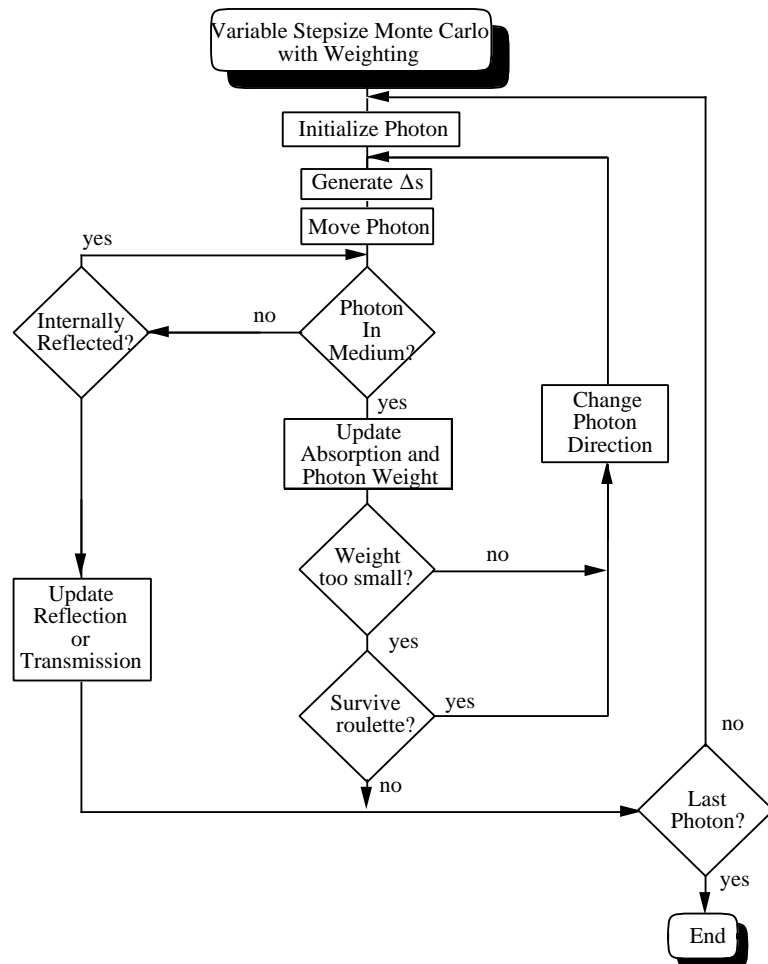


Figure 2.3: Monte Carlo with variable stepsize and the implicit capture technique for variance reduction. This is the flowchart for the Monte Carlo program verified below and used to calculate solutions used in Section 4.6.

variance reduction schemes work by putting a large number of particles of low weight in regions of interest and allowing only a small number of particles with high weight in unimportant regions of phase space.”

The implicit capture technique is equivalent to propagating many photons (a packet) along each path through the tissue. The size of the packet is described by a weight coefficient. After each photon step a fraction  $(1 - a)$  of the photons travelling along the path is absorbed, and the weight coefficient is reduced accordingly. The packet of photons is propagated until the weight coefficient drops below a specified tolerance.

How should the photon (packet) be terminated? The weight will never reach zero, and continuing to propagate a photon with a minuscule weight adds little information to the problem solution. Absorbing or discarding all the remaining weight, after the weight falls below a minimum, skews the absorption profile or violates energy conservation. A technique called roulette is used to terminate a photon once its weight drops below a specified minimum. The roulette technique gives such a photon (with weight  $w$ ) one chance in  $m$  of surviving with a weight  $mw$  or else its weight is reduced to zero. The photon is thereby killed in an unbiased fashion, without sacrificing energy conservation and without continuing propagation until its weight has reached zero.

The converse technique, called splitting, might be used to improve statistics in another situation. When a photon passes into the a more “interesting” region, a photon with weight  $w$  may be split into  $m$  different photons each with weight  $w/m$ . This conserves energy and improves the statistics in the region of greater interest. When a photon passes into a region of lesser interest, then, roulette is used to reduce the number of photons in that region.

## 2.2 Mechanics of photon propagation

A photon is uniquely described by five variables: three spatial coordinates for the position and two directional angles for the direction of travel. Initially, cylindrical coordinates were used for the photon's position and two angle variables relative to the line between the photon and the origin were used for its direction. Cylindrical coordinates were chosen for symmetry reasons. The primary disadvantage of this description was that the angle variables changed with each photon step, even when the photon continued travelling in the same direction. Another less critical problem was that this geometry has several special trigonometric cases, which complicates the mechanics of photon propagation.

Alternatively, Carter and Everett have described the photon's spatial position with Cartesian coordinates and the direction of travel with three direction cosines [6]. The required formulas for propagation are simpler, and the angle variables describing photon direction do not change unless the photon's direction changes. The direction cosines are specified by taking the cosine of the angle that the photon's direction makes with each axis. These are specified by  $\mu_x$ ,  $\mu_y$ , and  $\mu_z$  corresponding to each of the  $x$ -,  $y$ -, and  $z$ -axes respectively (Figure 2.4A). For a photon located at  $(x, y, z)$  travelling a distance  $\Delta s$  in the direction  $(\mu_x, \mu_y, \mu_z)$ , the new coordinates  $(x', y', z')$  are given by

$$\begin{aligned} x' &= x + \mu_x \Delta s \\ y' &= y + \mu_y \Delta s \\ z' &= z + \mu_z \Delta s \end{aligned} \tag{2.10}$$

If a photon is scattered at an angle  $(\theta, \phi)$  from the direction  $(\mu_x, \mu_y, \mu_z)$  in which

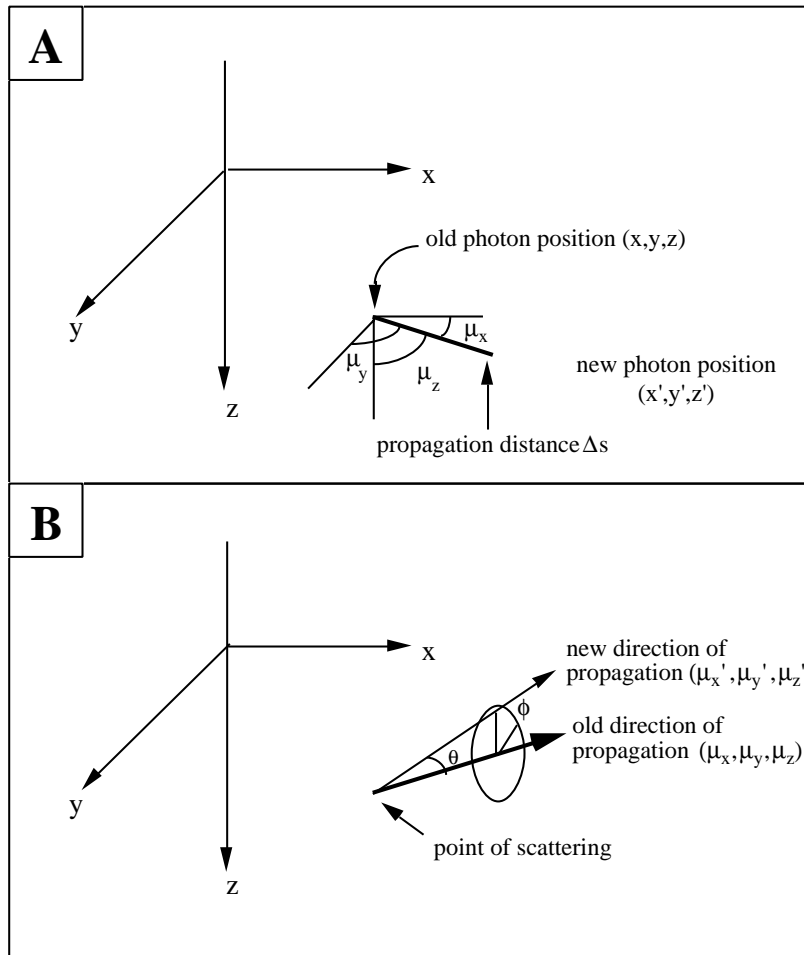


Figure 2.4: Monte Carlo coordinate system. Figure A shows the Cartesian coordinate system and how the photon's direction cosines are specified. Figure B shows how  $\theta$  and  $\phi$  are specified when a photon is scattered.

it is travelling (Figure 2.4B), then the new direction  $(\mu'_x, \mu'_y, \mu'_z)$  is specified by

$$\begin{aligned}\mu'_x &= \frac{\sin \theta}{\sqrt{1-\mu_z^2}}(\mu_x \mu_z \cos \phi - \mu_y \sin \phi) + \mu_x \cos \theta \\ \mu'_y &= \frac{\sin \theta}{\sqrt{1-\mu_z^2}}(\mu_y \mu_z \cos \phi + \mu_x \sin \phi) + \mu_y \cos \theta \\ \mu'_z &= -\sin \theta \cos \phi \sqrt{1-\mu_z^2} + \mu_z \cos \theta\end{aligned}\tag{2.11}$$

If the angle is too close to the normal (say  $|\mu_z| > 0.99999$ ), the following formulas should be used

$$\begin{aligned}\mu'_x &= \sin \theta \cos \phi \\ \mu'_y &= \sin \theta \sin \phi \\ \mu'_z &= \mu_z / |\mu_z| \cos \phi\end{aligned}\tag{2.12}$$

to obtain the new photon directions.

### 2.3 Phase function

Any phase function may be used with the Monte Carlo method. A normalized phase function describes the probability density function for the angle at which a photon is scattered. Anisotropic scattering is characterized by a non-uniform density function. Random scattering angles with non-uniform distributions may be generated using the techniques of Appendix A1. Generating functions for isotropic, Henyey-Greenstein, and modified Henyey-Greenstein phase functions are given in this appendix.

### 2.4 Photon absorption

An absorption event requires that the absorbed photon fraction be added to a matrix in which different elements correspond to different positions in the tissue.

For example, if a weighting technique is used with the variable stepsize method, the appropriate element of the absorption matrix is incremented by  $(1-a)w$ . The number of bins in the absorption matrix is determined by the spatial resolution desired. Increasing the number of entries increases the spatial resolution, but also increases the absorption uncertainty in each element (because fewer absorption events will take place in each element and the error is inversely proportional to the square root of the number of absorption events). The fluence rate is obtained by dividing the final value of each matrix element by (1) the equivalent spatial volume of the element, (2) the absorption coefficient, (3) the total number of photons propagated, and (4) the initial weight of each photon.

## 2.5 Internal reflection

The possibility of internal reflection occurs when the photon is propagated across an index of refraction discontinuity. Typically, reflection will only occur at the boundaries of the medium. The probability that a photon will be reflected is determined by the Fresnel reflection  $R(\theta_i)$

$$R(\theta_i) = \frac{1}{2} \left[ \frac{\sin^2(\theta_i - \theta_t)}{\sin^2(\theta_i + \theta_t)} + \frac{\tan^2(\theta_i - \theta_t)}{\tan^2(\theta_i + \theta_t)} \right] \quad (2.13)$$

where  $\theta_i = \cos^{-1} \mu_z$  is the angle of incidence on the boundary and the angle of transmission  $\theta_t$  is given by Snell's law

$$n_i \sin \theta_i = n_t \sin \theta_t \quad (2.14)$$

where  $n_i$  and  $n_t$  are the indices of refraction of the medium from which the photon is incident and transmitted, respectively. A random number  $\xi$  uniformly distributed between zero and one is used to decide whether the photon is reflected

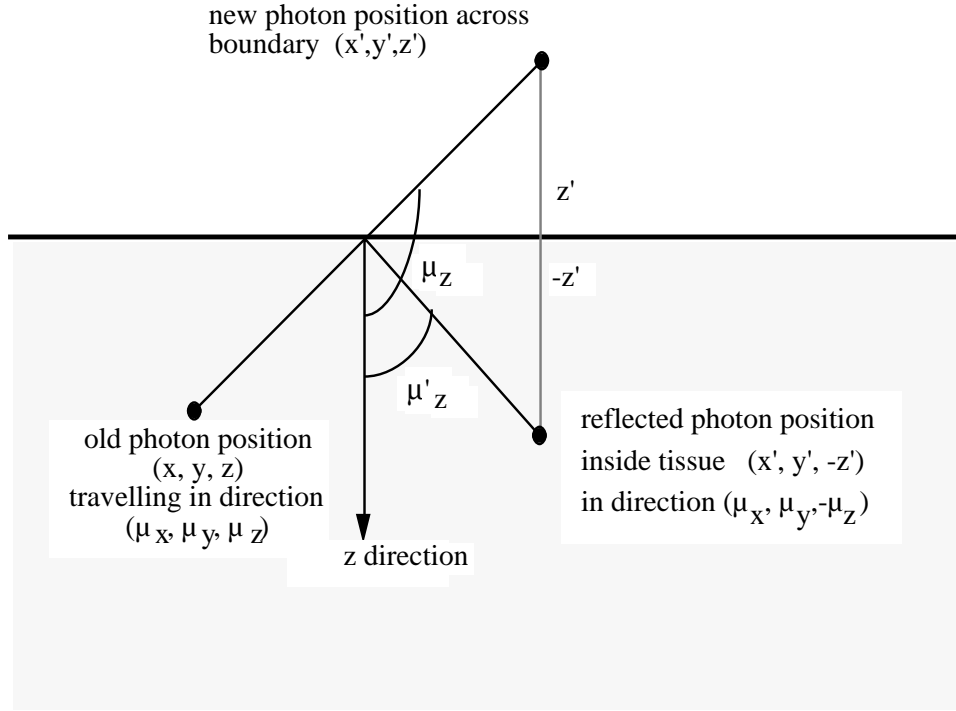


Figure 2.5: Geometry of photon reflection at an interface. In the slab geometry shown only the  $z$ -coordinate and  $\mu_z$  direction angle change.

or transmitted. If  $\xi < R(\theta_i)$  then the photon is reflected, otherwise the photon is transmitted. The details of how the photon is reflected depends upon the variance reduction technique used in the Monte Carlo method.

Once a photon leaves the tissue a new photon is initialized, except when photon weighting is used. If the photon is internally reflected, then the position and direction of the photon are adjusted accordingly. For a slab with thickness  $t$ , the exiting photon position is obtained by computing the position assuming transmission and changing only the  $z$  component of the photon coordinates

$$z' = \begin{cases} -z & \text{if } z < 0, \\ 2\tau - z & \text{if } z > \tau. \end{cases} \quad (2.15)$$

The change in photon direction is

$$\mu'_z = -\mu_z \quad (2.16)$$

and both  $\mu_x$  and  $\mu_y$  remain unchanged (Figure 2.5). When photon weighting is used then the photon may be both reflected and transmitted. If the old weight is  $w$ , then the new weight of the transmitted photon is  $w' = w(1 - R(\theta_i))$ . The reflected photon's position and direction are calculated as above and the new weight of the photon is given by  $w' = wR(\theta_i)$ .

When a glass slide placed on the surface of the tissue, creating a tissue-glass-air interface, the situation is slightly more complicated than for a tissue-air interface. When no weighting is used then reflection coefficients are calculated for each interface and the photon is propagated until it is reflected by or transmitted through the glass slide. For weighted photons, the photon should be split into two photons at each interface—one that is transmitted and one that is reflected. These photons in turn would be propagated and split as necessary until all photons are terminated. This has the advantage of creating many photons with small weights near the surface, which is a region of interest. The disadvantage is that this is awkward to implement. A simpler method is to no longer treat the photon as weighted, and let the whole weight of the photon either be reflected or transmitted at all interfaces.

## 2.6 Convolution

Potentially, the fluence rate for any irradiation profile may be obtained by launching photons distributed spatially with a probability density function equal to the irradiation profile. Since many photons must be launched *at a fixed point* before



the random fluctuation of the Monte Carlo process becomes small, launching photons from different places increases the total number of photons which must be launched before statistical errors become negligible. Fortunately, the fluence rate which results from photons launched at a single point corresponds to the Green's function  $G(x, y, z)$  for the medium. Since the irradiation source profile is not a function of depth, the convolution is independent of  $z$ .

The fluence rate for an arbitrary irradiation profile may be obtained by convolving the Green's function profile with the irradiation source function  $S(x, y)$

$$\Phi(x, y, z) = \int_{-\infty}^{\infty} \int_{-\infty}^{\infty} G(x', y', z') S(x - x', y - y') dx' dy' \quad (2.17)$$

In cylindrical coordinates, the convolution of a cylindrically symmetric irradiation source  $S(r)$  and Green's function  $G(r)$  will be cylindrically symmetric. This convolution may be written (referring to Figure 2.6)

$$\Phi(r) = \int_0^{\infty} S(r') \left[ \int_0^{2\pi} G(\sqrt{r'^2 + r^2 - 2rr' \cos \theta}) d\theta \right] r' dr' \quad (2.18)$$

or alternatively as,

$$\Phi(r) = \int_0^{\infty} G(r') \left[ \int_0^{2\pi} S(\sqrt{r'^2 + r^2 - 2rr' \cos \theta}) d\theta \right] r' dr' \quad (2.19)$$

Both integrals should give the same results, providing a convenient check on any convolution implementation. The advantage of Equation (2.19) is that the integral over the source needs to be done just once for a particular radius  $r$  and absorption distributions at all depths for the radius  $r$  can be calculated.

A Gaussian source function with a  $e^{-2}$  radius of  $R$  is given by

$$S(r) = S_0 e^{-2(r/R)^2} \quad (2.20)$$

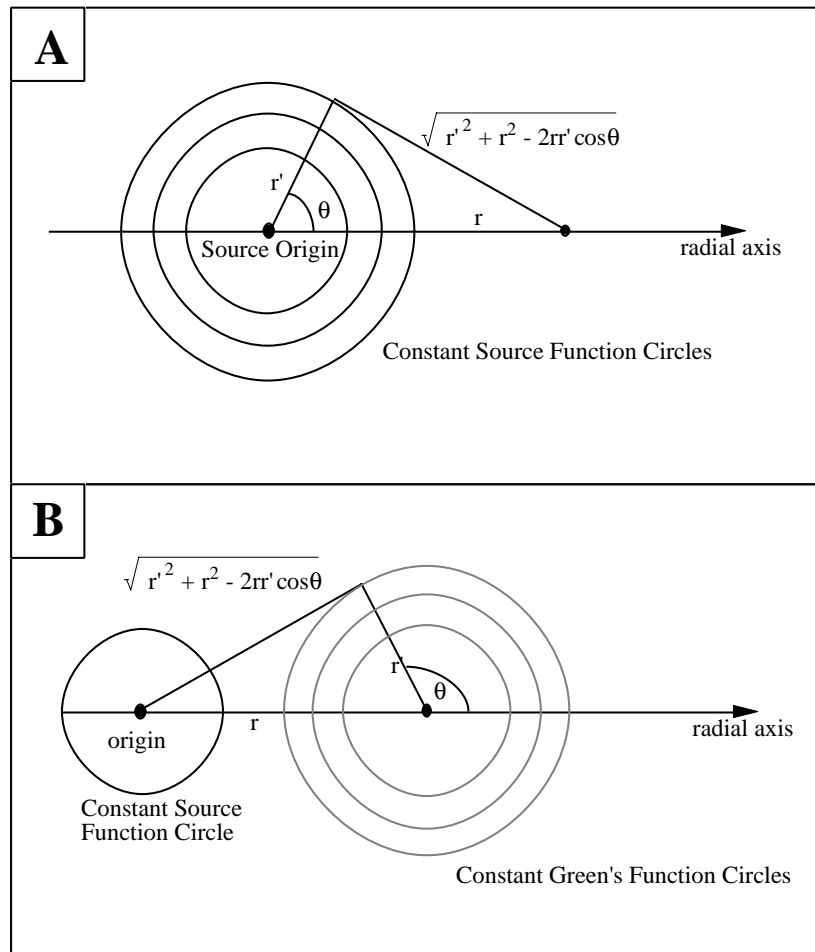


Figure 2.6: Illustration of the difference between convolution Equations (2.18) and (2.19). Figure A shows a circle of constant Green's function and Figure B shows the circle of constant source. Cylindrical symmetry in both the Green's function and the source has been assumed.

where  $S_0$  is related to the total power  $P$  of the beam by

$$S_0 = \frac{2P}{\pi R^2} \quad (2.21)$$

Substituting Equation (2.20) into Equation (2.19) yields

$$\Phi(r) = S_0 e^{-2(r/R)^2} \int_0^\infty G(r') e^{-2(r'/R)^2} \left[ \int_0^{2\pi} e^{4rr' \cos \theta / R^2} d\theta \right] r' dr' \quad (2.22)$$

The integral in brackets reduces to a zero order modified Bessel function, and the Equation for the fluence becomes

$$\Phi(r, z) = S_0 e^{-2(r'/R)^2} \int_0^\infty G(r', z) e^{-2(r'/R)^2} I_0(4rr'/R^2) 2\pi r' dr', \quad (2.23)$$

The source function for a flat beam with radius  $R$  is

$$S(r') = \begin{cases} S_0 & \text{if } r' \leq R, \\ 0 & \text{otherwise.} \end{cases} \quad (2.24)$$

where  $S_0$  equals the total power divided by the area of the beam. Substituting Equation (2.24) into Equation (2.19) yields

$$\Phi(r, z) = S_0 \int_0^\infty G(r', z) \Theta(r, r') 2\pi r' dr' \quad (2.25)$$

where the different cases for  $\Theta(r, r')$  are shown in Figure 2.7. Specifically,

$$\Theta(r, r') = \begin{cases} 1 & \text{if } 0 \leq r \leq R - r', \\ \frac{1}{\pi} \cos^{-1} \left[ \frac{r'^2 + r^2 - R^2}{2rr'} \right] & \text{if } |R - r'| \leq r \leq R + r', \\ 0 & \text{otherwise.} \end{cases} \quad (2.26)$$

These convolution equations are used to calculate the finite beam fluence rates used in Chapter 4 to evaluate the accuracy of the three-dimensional delta-Eddington fluence rate. Since the Monte Carlo method is used as the standard against which the delta-Eddington approximation is compared, the Monte Carlo method was tested extensively. The results of these tests are presented below.

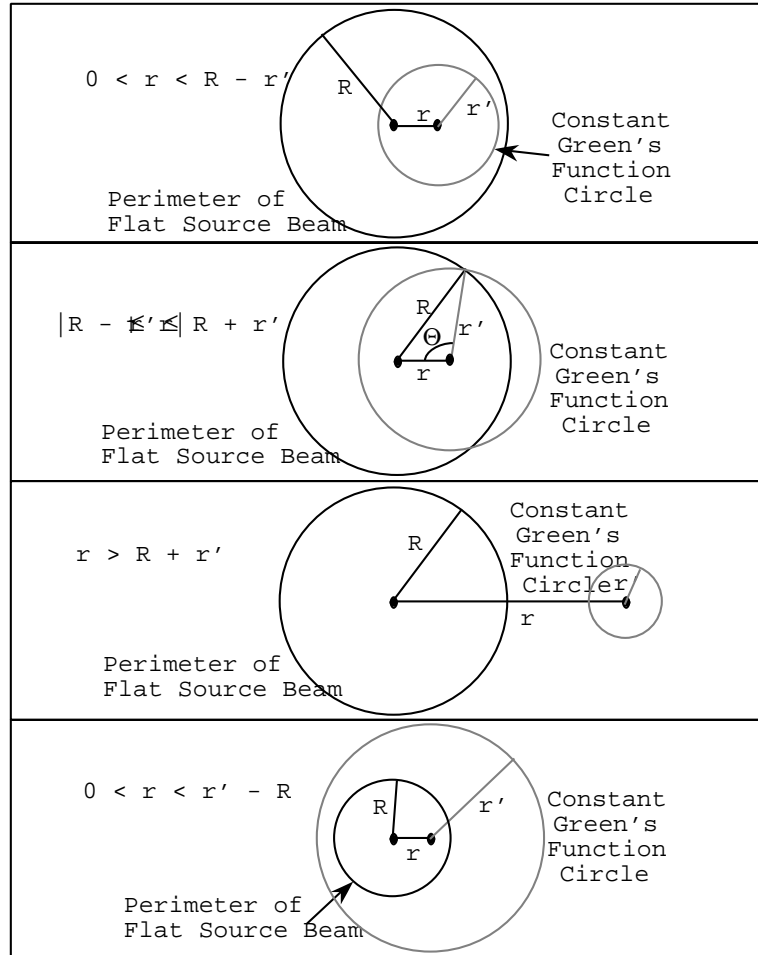


Figure 2.7: Illustration of different relations between the flat beam diameter  $R$ , the radius at which the fluence is desired  $r$  and the integration radius  $r'$  of a constant Green's function value. Integration of the source function around the gray circles yields  $2\pi S_0$  in the top case,  $2\Theta S_0$  in the next, and zero for the last two cases.

## 2.7 Verification

Both Monte Carlo methods were implemented. The variable stepsize method was much faster and the fixed stepsize method was abandoned. The variable stepsize Monte Carlo method was checked to ensure that the sum of the transmission, reflection, and absorption was unity. The method was verified by comparing the Monte Carlo reflection and transmission results with known values.

Three different comparisons with exact values for testing all aspects of the Monte Carlo implementation were used. The errors shown in all the figures are standard errors (i.e., the standard deviations of the mean). These values were obtained by splitting one large Monte Carlo run of say 50,000 photons into ten runs of 5,000 each. The results of these ten runs were averaged and the standard error was computed.

For an anisotropic phase function and a slab geometry of finite thickness with index matching, van de Hulst's tables served as a reference for reflection and transmission as a function of angle [1980b]. The phase function is for the Henyey-Greenstein phase function with an average cosine of 0.75. The slab was two optical depths thick, and index-matched with its environment. Light was uniformly incident normal to the slab. The average results from the Monte Carlo program with ten runs of 50,000 photons are plotted with standard errors, along with exact values from van de Hulst in Figures 2.8 and 2.9. The values for total reflection and total transmission are

Quantity	van de Hulst	Monte Carlo	std. dev.
Total Reflection	0.09739	0.0971	0.0003
Total Transmission	0.66096	0.6616	0.0005

Finding exact solutions for media which are not index matched is difficult, but Giovanelli provides data for a semi-infinite slab with isotropic scattering and

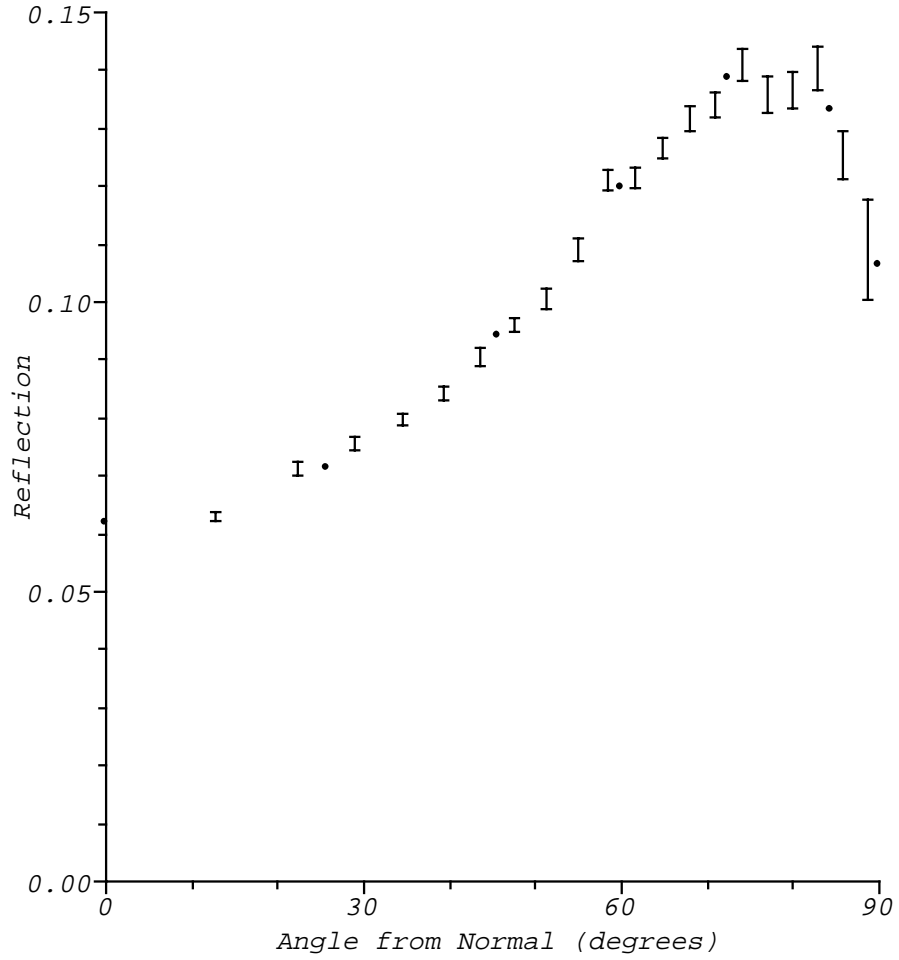


Figure 2.8: Comparison of exact reflection values (filled circles) with variable stepsize Monte Carlo simulation. Scattering is anisotropic ( $g=0.75$ ) and distributed according to the Henyey-Greenstein phase function. The index of refraction of the tissue equals that of its environment. The albedo is 0.9 and the thickness of the slab is two optical depths. Error bars indicate standard errors in the Monte Carlo simulation.

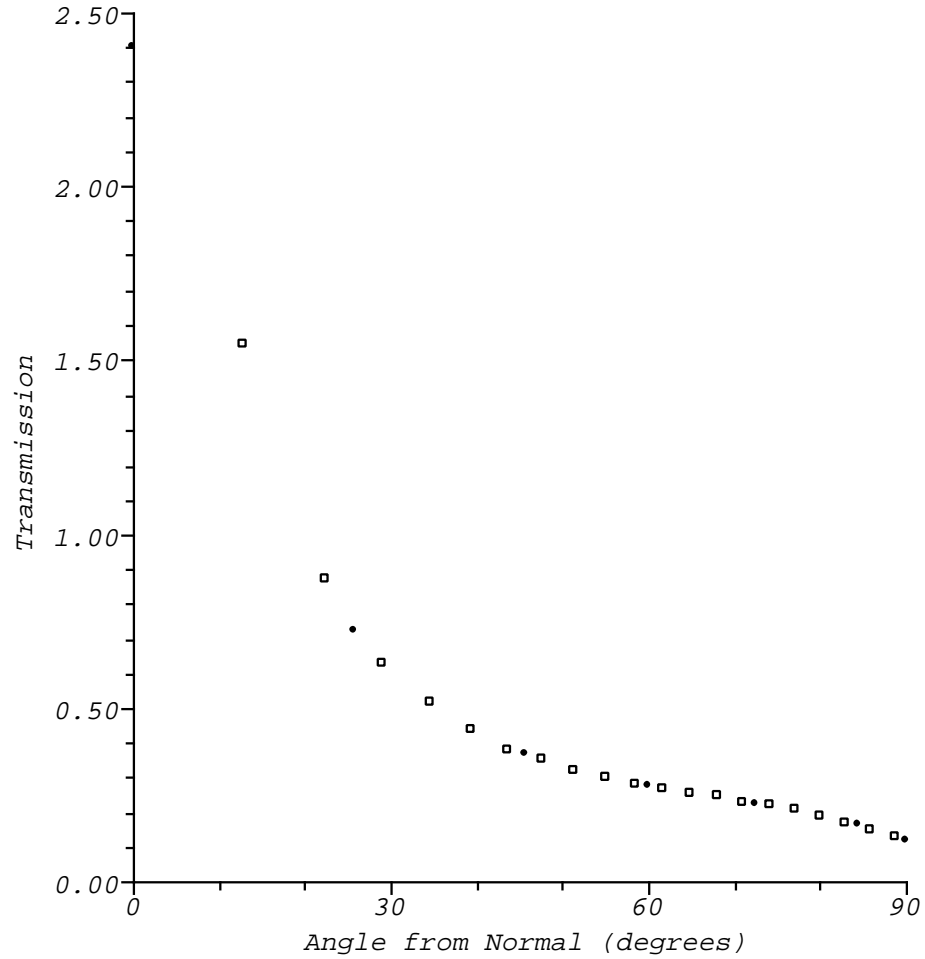


Figure 2.9: Comparison of exact transmission values (filled circles) with variable stepsize Monte Carlo simulation (empty squares). Scattering is anisotropic ( $g=0.75$ ) and distributed according to the Henyey-Greenstein phase function. The index of refraction of the tissue equals that of its environment. The albedo is 0.9 and the thickness of the slab is two optical depths. Standard errors are smaller than the empty squares.

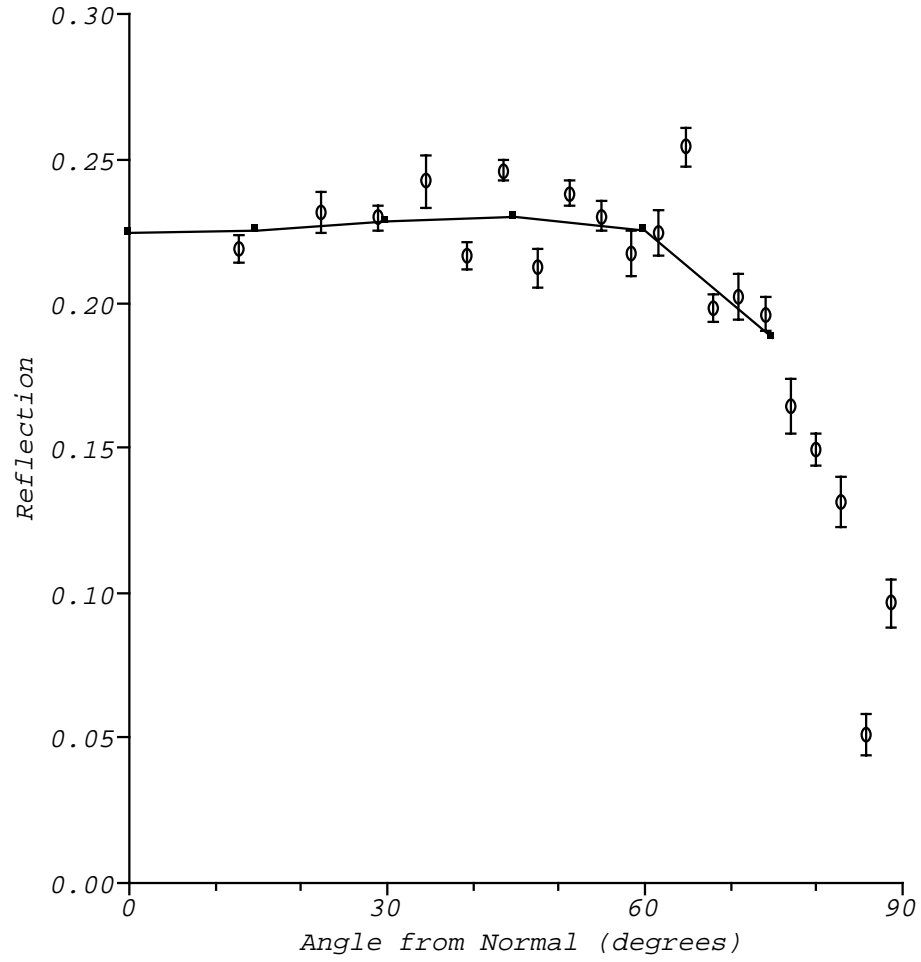


Figure 2.10: Comparison of exact reflection values (filled squares) with Monte Carlo simulation (empty circles). The tissue is semi-infinite with an index of refraction mismatch of 1.5 to 1.0 at the tissue-air interface. The albedo is 0.9 and scattering is isotropic. Error bars indicate standard errors.



an index of refraction mismatch of 1.5 to 1.0 [16]. The internal reflection assumes Fresnel Reflection. The average of ten Monte Carlo runs of 5,000 photons with the values from Giovanelli are plotted in Figure 2.10. The albedo is 0.9 and light is normally incident. The values for total reflection are shown below

	Giovanelli	Monte Carlo	std. dev.
Total Reflection	0.2600	0.26079	0.00079

## 2.8 Conclusions

The Monte Carlo model allows calculation of reflection, transmission, and fluence rates in tissue. Both mismatched boundary conditions and anisotropic scattering have been included, thereby increasing the realism of the model. A variable-stepsize weighted Monte Carlo model has been implemented and validated by comparison with published tables. This Monte Carlo model may be used to calculate fluence rates for finite beams by convolving the impulse response with either flat or Gaussian beam irradiation profiles. Analytic expressions that facilitate such calculations have been presented.

## Chapter 3

# The Adding-Doubling Method

### Introduction

Non-stochastic solutions of the radiative transport equation are used for simple geometries when accurate solutions are required. The most common techniques for solving the transport equation are successive scattering, Ambartsumian's method, the discrete ordinate method, Chandrasekhar's  $X$  and  $Y$  functions, and the adding-doubling method. Most of these methods are appropriate only for a slab geometry and the solutions obtained are one-dimensional. The adding-doubling method was chosen for calculating solutions because it permits (1) anisotropic scattering, (2) arbitrarily thick tissues, (3) Fresnel boundary conditions, (4) inhomogeneous layers, and (5) relatively fast computation. The short review below gives a brief description of all the methods and indicates advantages and disadvantages of each (extensive reviews are given by [27, 24, 29, 60]).

The successive scattering method (or Neumann series solution) starts by calculating the distribution of all light that has been scattered once: this is the first-order scattered light distribution. The first-order distribution is used to find the second-order light distribution. This process is repeated until the distribution of light scattered  $n$  times is negligible. The distributions for all orders are summed to determine the final distribution of light in the slab. This method is

easily adapted to inhomogeneous layers and anisotropic phase functions; unfortunately, it becomes prohibitively slow for optically thick tissues ( $\tau > 1$ ) [59, 29].

Ambartsumian's method (invariant embedding) uses the principle that when a layer is added to the top of a homogeneous slab with the same optical properties, the reflection and transmission will be equivalent to those obtained by adding the layer to the bottom instead. When the added layer is thin enough that single scattering is valid, then simple equations can be derived for the reflection and transmission of the combined layers [24]. Solutions for thick layers are built up by adding many thin layers. This method works well with inhomogeneous media, but solutions for optically thick samples require extensive computation [1, 8, 3].

Chandrasekhar analytically manipulates the invariant embedding equations to obtain integral equations defining the  $X$  and  $Y$  functions [8]. The  $X$  and  $Y$  functions depend on only one angle variable and must be solved numerically. These functions are very complicated for anisotropic phase functions [24], and flexible extensions to inhomogeneous media have not been made [27], making this method more limited in application than others described in this section.

The method of discrete ordinates divides the radiative transport equation into  $N$  discrete fluxes to obtain  $N$  equations in  $N$  unknowns. These equations are solved numerically [41]. This method is useful when the phase function can be expressed as the sum of a few Legendre polynomials. For these cases, the discrete ordinate method quickly yields results accurate to about one percent [24]. A major difficulty with this technique is that highly anisotropic phase functions require a large number of fluxes; when the number of fluxes exceeds

20–30, the system of equations that must be solved becomes numerically ill-conditioned [40, 29, 67].

The adding method requires that the reflection and transmission for two slabs be known. If the reflection and transmission (for all angles of incidence and exitance) of two slabs are known, then the transmission and reflection for a slab comprised of these two individual slabs can be determined. The doubling method refers to the special case in which both slabs are identical. When the added layer is very thin this method reduces to Ambartsumian’s method. The adding-doubling method has the advantage that (1) only numerical integrations over angle are required; (2) physical interpretation of results can be made at each step; (3) the method is equivalent for isotropic and anisotropic scattering; and (4) results are obtained for all angles of incidence used in the integration [29].

The doubling method was first used in radiative transfer by van de Hulst [59]. The doubling method has been extended to include the addition of two dissimilar layers (see review by [47].) Once the transmission and reflection for a thin slab are known, then the reflection and transmission for a slab of arbitrary thickness maybe found by repeatedly doubling the thickness of the thin slab until the desired thickness is reached. If the slab is sufficiently thin then single scattering approximations accurately estimate the reflection and transmission for the slab. These expressions are detailed in Section 3.1 below as well as criteria for evaluating “sufficiently thin.”

This chapter describes an implementation of the adding-doubling method for solving the radiative transport equations numerically. Any phase function may be chosen to characterize scattering in the medium and any tissue optical

thickness is possible. Tissue layers with different optical properties may be added together to find the reflection and transmission for inhomogeneous layered media. Light normally incident on a slab is azimuthally independent. Consequently, the adding-doubling method presented is assumed free of azimuthal dependence. Boundaries characterized by specular Fresnel reflection are discussed in Section 3.5.

Finally it should be emphasized that the adding-doubling method (like all the methods described) is one-dimensional, and confined to a slab geometry. Existing solutions for the three-dimensional problem of a searchlight (or laser) incident on a slab are restricted to particular choices of optical properties [8, 52, 10].

### 3.1 Definition of reflection and transmission operators

Denote the cosine of the angle that a right circular cone makes with the normal by  $\mu$  (Figure 3.1A). Furthermore let the incident radiance, which is a function of incident angle  $\mu$ , be denoted by  $L_{rmincident}^+(\mu)$  where the plus sign indicates the downward direction. The total radiance transmitted through the slab at a particular cosine angle  $\mu'$  is given by [60]

$$L_{transmitted}^+(\mu') = \int_0^1 T(\mu', \mu) L_{incident}^+(\mu) 2\mu d\mu \quad (3.1)$$

The total radiance reflected by the sample is

$$L_{reflected}^-(\mu') = \int_0^1 R(\mu', \mu) L_{incident}^+(\mu) 2\mu d\mu \quad (3.2)$$

The operators  $T(\mu, \mu_0)$  and  $R(\mu, \mu_0)$  may be written in matrix form

$$T^{ij} = T(\mu_i, \mu_j) \quad R^{ij} = R(\mu_i, \mu_j) \quad (3.3)$$

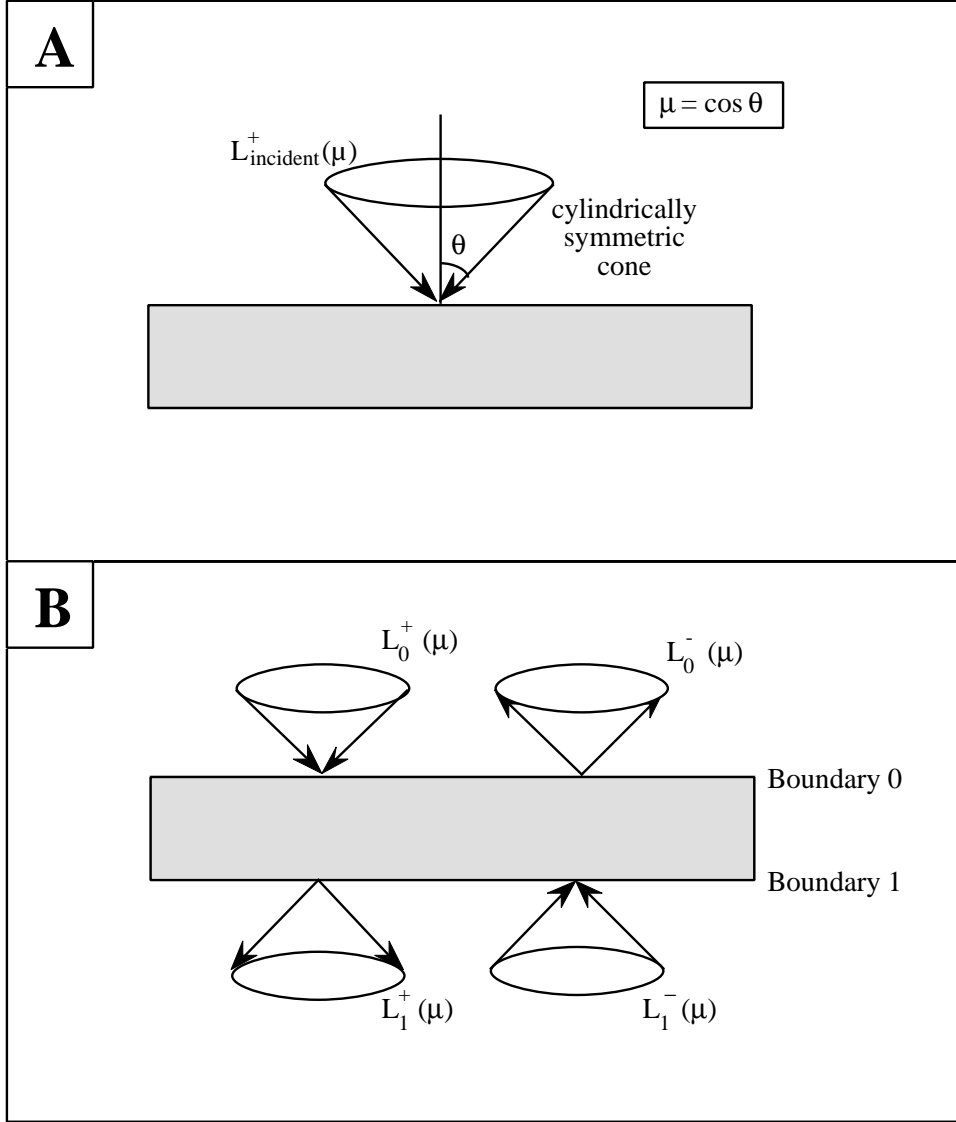


Figure 3.1: Geometric description of nomenclature. Figure A illustrates the incident radiance  $L_{\text{incident}}^+$  with the cosine of the angle of incidence equal to  $\mu_0$ . Figure B shows the nomenclature for the upward and downward radiances from each surface of the slab.

where the angles  $\mu_i$  and  $\mu_j$  are chosen according to the particular quadrature scheme desired. The superscripts  $ij$  indicate the entry  $ij$  in the matrices  $T$  and  $R$ . The radiances  $L^+(\mu)$  and  $L^-(\mu)$  correspondingly may be written as vectors

$$L^i = L(\mu_i) \quad (3.4)$$

The matrix star multiplication  $A \star B$  is defined to directly correspond to an integration similar to those in Equations (3.1) and (3.2)

$$A \star B = \int_0^1 A(\mu, \mu') B(\mu', \mu'') 2\mu d\mu \quad (3.5)$$

then

$$A \star B = \sum_j A^{ij} 2\mu_j w_j B^{jk} \quad (3.6)$$

where  $\mu_j$  is the  $j$ th quadrature angle and  $w_j$  is its corresponding weight. The identity matrix  $E$  is then

$$E^{ij} = \frac{1}{2\mu_i w_i} \delta_{ij} \quad (3.7)$$

where  $\delta_{ij}$  is the usual Kronecker delta. Grant and Hunt have shown that this algebra is a semi-group [21, 22] and have proven that all matrix manipulations in Section 3.2 are valid mathematically. It is sometimes useful to consider these matrix “star multiplications” as normal matrix multiplications which include a diagonal matrix  $c$

$$c_{ij} = 2\mu_i w_i \delta_{ij} \quad (3.8)$$

Thus a matrix star multiplication may be written

$$A \star B = A c B \quad (3.9)$$

where the multiplications on the R.H.S. of Equation (3.9) are usual matrix multiplications.

### 3.2 Derivation of the adding-doubling method

This derivation follows Plass *et al.* [47] with the terms representing internal sources omitted for clarity. Define  $T_{nm}$  and  $R_{nm}$  as the transmission and reflection operators for light incident on side  $n$  and exiting side  $\mu$ . Homogeneous tissues have no preferred direction and so the matrices are equal  $T_{nm} = T_{mn}$  and  $R_{nm} = R_{mn}$  (The matrices are also symmetric.) Let the vector  $L_0^+(\mu)$  denote the radiance incident from on side 0 of the slab 01, and  $L_1^-(\mu)$  denote the radiance incident on side 1. Similarly define  $L_0^-$  and  $L_1^+$  as the radiance exiting the slab from sides 0 and 1 respectively (Figure 3.1B). The downward radiance from side 1 is the sum of the transmitted incident radiance from side 0 and the reflected radiance from side 1,

$$L_1^+ = T_{01}L_0^+ + R_{10}L_1^- \quad (3.10)$$

The upward radiance from side 0 is the transmitted radiance from side 1 and the reflected radiance from side 0

$$L_1^- = R_{01}L_0^+ + T_{10}L_1^- \quad (3.11)$$

Analogous formulas apply to a layer 12

$$L_2^+ = T_{12}L_1^+ + R_{21}L_2^- \quad (3.12)$$

$$L_1^- = R_{12}L_1^+ + T_{21}L_2^- \quad (3.13)$$

Juxtaposition of layers 01 and 12 yields a combined layer 02. The equations relating the radiances exiting from the top and bottom of this slab are

$$L_2^+ = T_{02}L_0^+ + R_{20}L_2^- \quad (3.14)$$

$$L_0^- = R_{02}L_0^+ + T_{20}L_2^- \quad (3.15)$$



Presumably, the reflection and transmission operators for the 01 and 12 layers are known. The reflection and transmission operators for the 02 layer are needed in terms of those for the 01 and 12 layers. To do this Equation (3.10) is multiplied by  $R_{12}$  from the left and added to Equation (3.13). Since the terms containing  $L_1^+$  cancel

$$(E - R_{12}R_{10})L_1^- = R_{12}T_{01}L_0^+ + T_{21}L_2^- \quad (3.16)$$

Multiplying Equation (3.16) on the left by  $(E - R_{12}R_{10})^{-1}$  yields

$$L_1^- = (E - R_{12}R_{10})^{-1}(R_{12}T_{01}L_0^+ + T_{21}L_2^-) \quad (3.17)$$

This equation expresses the upward radiance at the interface between two layers. An equation for the downward mid-layer radiance can be obtained similarly using Equations (3.13) and (3.10)

$$L_1^+ = (E - R_{10}R_{12})^{-1}(T_{01}L_0^+ + R_{10}T_{21}L_2^-) \quad (3.18)$$

Substituting Equation (3.18) into Equation (3.12) yields

$$L_2^+ = \left[ T_{12}(E - R_{10}R_{12})^{-1}T_{01} \right] L_0^+ + \left[ T_{12}(E - R_{10}R_{12})^{-1}R_{10}T_{21} + R_{21} \right] L_2^- \quad (3.19)$$

Comparing this equation with Equation (3.14) indicates that

$$T_{02} = T_{12}(E - R_{10}R_{12})^{-1}T_{01} \quad (3.20)$$

$$R_{20} = T_{12}(E - R_{10}R_{12})^{-1}R_{10}T_{21} + R_{21} \quad (3.21)$$

Similarly Equation (3.11) can be substituted into Equation (3.13) to obtain

$$T_{20} = T_{10}(E - R_{12}R_{10})^{-1}T_{21} \quad (3.22)$$

$$R_{02} = T_{10}(E - R_{12}R_{10})^{-1}R_{12}T_{01} + R_{01} \quad (3.23)$$

Equations (3.20)–(3.23) define the reflection and transmission operators for a layer comprised of two individual layers in terms of reflection and transmission operators for each layer.

### 3.3 The redistribution function

The single scattering phase function  $p(\theta)$  for a tissue determines the amount of light scattered at an angle  $\theta$  from the direction of incidence. The redistribution function determines the fraction of light from a cone of angle  $u$  will be scattered into a cone of angle  $v$ . It is the transmission operator for a single scattering event. The redistribution function  $h(u, v)$  is calculated by averaging the phase function over all possible azimuthal angles for fixed angles  $u$  and  $v$ ,

$$h(u, v) = \frac{1}{2\pi} \int_0^{2\pi} p \left[ uv + \sqrt{1-u^2} \sqrt{1-v^2} \cos \phi \right] d\phi \quad (3.24)$$

If the cosine of the angle of incidence or exitance is unity ( $u = 1$  or  $v = 1$ ) then the redistribution function is equivalent to the phase function  $h(1, v) = p(v)$ . In the case of isotropic scattering the redistribution function is a constant

$$h(u, v) = \frac{1}{4\pi} \quad (3.25)$$

For Henyey-Greenstein scattering, the redistribution function may be expressed in terms of a complete elliptic integral of the second kind [62]

$$h(u, v) = \frac{2}{\pi} \frac{1-g^2}{\sqrt{\alpha+\gamma}(\alpha-\gamma)} E(k) \quad (3.26)$$

where  $g$  is the average cosine of the Henyey-Greenstein phase function and

$$\alpha = 1 + g^2 - 2guv \quad \gamma = 2g\sqrt{1-u^2}\sqrt{1-v^2} \quad k = \sqrt{\frac{2\gamma}{\alpha+\gamma}} \quad (3.27)$$

and  $E(k)$  is the complete elliptical integral tabulated by Jahnke and Emde [33]. This function may be calculated with numerical routines by Press *et al.* [49]. The redistribution function for the modified Henyey-Greenstein phase function follows directly from Equations (3.25) and (3.26)

$$h(u, v) = \beta + (1 - \beta) \frac{2}{\pi} \frac{1 - g^2}{\sqrt{\alpha + \gamma}(\alpha - \gamma)} E(k) \quad (3.28)$$

Other phase functions require numerical integration of Equation (3.24). If the phase function is highly anisotropic, then the integration over the azimuthal angle is particularly difficult and care must be taken to ensure that the integration is accurate. This is important because errors in the redistribution function enter directly into the reflection and transmission operators for thin layers. These errors will be doubled with each successive addition of layers and small errors will rapidly increase.

The normalization of the phase functions provides a check on the accuracy of the quadrature method [19, 18].

$$\frac{1}{2} \sum_{i=1}^n w_i [h(\mu_i, m\mu_j) + h(-\mu_i, \mu_j)] = 1 \quad (3.29)$$

where  $n$  is the number of quadrature angles used and the minus sign in the second term represents the “reflected” component of the scattered light. If relation (3.29) is not satisfied then the number of quadrature angles should be increased. This is not always practical and a number of phase function renormalization methods have been developed to remedy this problem (see review in [67]).

### 3.4 Reflection and transmission of thin layers

Starting the adding-doubling method requires knowledge of the reflection and transmission operators for a thin slab. Several methods exist for obtaining these

operators: diamond initialization [66], infinitesimal generator [20], and successive scattering [28]. The first two methods have been compared by Wiscombe who found that the more complicated diamond initialization technique was better about two-thirds of the time [67]. The successive scattering technique was the first method used for calculating the reflection and transmission operators of a thin slab [63]. With this method initial optical depths up to  $\tau \sim 1$  are possible although Hansen and Travis indicate that an optical thickness of  $\tau \sim 2^{-10}$  is optimal for this starting method [24]. The infinitesimal generator technique assumes that the tissue is sufficiently thin that single scattering accurately estimates the reflection and transmission for the slab. This is the method implemented for calculations in this chapter because of its simplicity.

Single scattering equations for the reflection and transmission functions are given by van de Hulst for isotropic scattering [60]. For azimuthally independent anisotropic scattering the redistribution function must be included. The single scattering reflection function for thin layers is

$$R(a, \tau, \mu, \mu_0) = \frac{a\pi h(\mu, -\mu_0)}{\mu + \mu_0} \left[ 1 - \exp\left(-\frac{\tau}{\mu} - \frac{\tau}{\mu_0}\right) \right] \quad (3.30)$$

The slight difference from van de Hulst results from differences in phase function normalization. At grazing angles ( $\mu_0 = \mu = 0$ ), the reflection has a singularity

$$R(a, \tau, 0, 0) = \infty \quad (3.31)$$

When the angle of incidence is not equal to the angle of transmission ( $\mu_0 \neq \mu$ ), then the transmission function is given by

$$T(a, \tau, \mu, \mu_0) = \frac{a\pi h(\mu, -\mu_0)}{\mu_0 - \mu} \left[ \exp\left(-\frac{\tau}{\mu_0}\right) - \exp\left(-\frac{\tau}{\mu}\right) \right] \quad (3.32)$$

When  $\mu_0 = \mu$  then the primary beam (with an incident cone of  $\mu$ ) must be included,

$$T(a, \tau, \mu, \mu) = \frac{a\pi h(\mu, \mu)}{\mu} \exp\left(-\frac{\tau}{\mu_0}\right) + \frac{1}{2\mu} \exp\left(-\frac{\tau}{\mu}\right) \quad (3.33)$$

The factor of  $2\mu$  in the unscattered beam results from the use of star multiplication. Finally, for grazing incidence ( $\mu = \mu_0 = 0$ ), the transmission is zero

$$T(a, \tau, 0, 0) = 0 \quad (3.34)$$

### 3.5 Boundary conditions

Boundary conditions are implemented in the adding-doubling method by creating a layer which mimics the reflection and transmission at a boundary. This layer is added to a slab to find the reflection and transmission for a slab including the boundary conditions. If  $r(\mu)$  is the Fresnel reflection for light incident from a medium with index of refraction  $n_0$  on a medium with index of refraction  $n_1$  then

$$R_{01}(\mu_i, \mu_j) = \frac{r(\mu_i)}{2\mu_i} \delta_{ij} \quad (3.35)$$

$$T_{01}(\mu_i, \mu_j) = \frac{1 - r(\mu_i)}{2\mu_i} \left(\frac{n_1}{n_0}\right)^2 \delta_{ij} \quad (3.36)$$

The square of the ratio of the indices of refraction is due to the  $n^2$ -Law of radiance (Appendix A2) which accounts for the difference in radiances across across an index of refraction mismatch. The factor of  $2\mu$  is included to compensate for star multiplication. If a glass slide is present then Equation (A2.21) should be used to calculate  $r(\mu_i)$  with  $n_i = n_{\text{tissue}}$ ,  $n_g = n_{\text{glass}}$  and  $n_t = n_{\text{outside}}$ . Both operators are diagonal because light is specularly reflected and the angle of incidence equals the

angle of reflection. The reflection and transmission operators for light travelling from medium 1 into medium 0 are

$$R_{10}(\mu_i, \mu_j) = R_{01}(\mu_i, \mu_j) \quad (3.37)$$

$$T_{10}(\mu_i, \mu_j) = T_{01}(\mu_i, \mu_j) \left(\frac{n_0}{n_1}\right)^4 \delta_{ij} \quad (3.38)$$

Since light is refracted at the boundary, care must be taken to ensure that the incident and reflected fluxes are identified with the proper angles. For example, if eleven Gaussian quadrature angles are used, all but three are totally internally reflected at an interface with  $n_1 = 1.5$  and  $n_2 = 1.0$ . This is caused by the uneven distribution of quadrature points over the integration interval—in the Gaussian quadrature scheme oblique angles are emphasized over angles near normal and, therefore, most of the quadrature angles undergo total internal reflection.

If equal boundary conditions exist on both sides of the slab then, by symmetry, the transmission and reflection operator for light travelling from the top to the bottom are equal to those for light propagating from the bottom to the top. Consequently only one set need be calculated. This leads to a faster method for calculating the reflection and transmission for a slab with equal boundary conditions on each side. Let the top boundary be layer 01, the medium layer 12, and the bottom layer 23. The boundary conditions on each side are equal:  $R_{01} = R_{32}$ ,  $R_{10} = R_{23}$ ,  $T_{01} = T_{32}$ , and  $T_{10} = T_{23}$ . For example the light reflected from layer 01 (travelling from boundary 0 to boundary 1) will equal the amount of light reflected from layer 32, since there is no physical difference between the two cases. The switch in the numbering arises from the fact that light passes from the medium to the outside at the top surface by going from 1 to 0, and

from 2 to 3 on the bottom surface. The reflection and transmission for the slab with boundary conditions are  $R_{30}$  and  $T_{03}$  respectively. These are given by

$$T_{02} = T_{12}(E - R_{10}R_{12})^{-1}T_{01} \quad (3.39)$$

$$R_{20} = T_{12}(E - R_{10}R_{12})^{-1}R_{10}T_{21} + R_{21} \quad (3.40)$$

and

$$T_{03} = T_{10}(E - R_{20}R_{10})^{-1}T_{02} \quad (3.41)$$

$$R_{30} = T_{10}(E - R_{20}R_{10})^{-1}R_{20}T_{01} + R_{01} \quad (3.42)$$

Further increases in efficiency may be made by exploiting the diagonal nature of the reflection and transmission operators for an interface, since most matrix/matrix multiplications above become vector/matrix multiplications.

### 3.6 Implementation

The equations given in Section 3.2 are entirely appropriate if the direct beam coincides with one of the quadrature angles. If this is not the case, then the equations for doubling become more complex. Equations with separate terms for primary and scattered light are given in Hansen and Travis [24] and van de Hulst [60].

Every matrix multiplication is an integration (Section 3.1). Quadrature methods improve the integration accuracy using a fixed number of points judiciously chosen. Gaussian quadrature gives very good answers, but unfortunately none of the quadrature points corresponds to normal incidence. Lobatto quadrature [43] includes normal incidence as a quadrature point, but it also includes a quadrature point at  $\mu = 0$ . This leads to singularities in the reflection matrix

(Equation (3.31)). Those using Lobatto quadrature have found it comparable in accuracy to Gaussian quadrature [47].

Since quadrature points seldom coincide with angles at which information is desired, interpolation to points of interest is required. Because the reflection and transmission operators are functions of  $\mu$  and  $\mu'$ , two-dimensional interpolation methods must be used. Bicubic spline interpolation [49] works well for small numbers of quadrature points, but is slow when many quadrature points are used. Polynomial interpolation [49] also works well for small numbers of quadrature points, but is useless for large numbers of points. Simple bilinear interpolation is fast for any number of quadrature points but is considerably less accurate than spline interpolation. Consequently, splines were used for one-dimensional interpolation and bilinear interpolation was used when two-dimensional interpolation was required.

### 3.7 Tabulated values

This section verifies the implementation of the doubling method and gives four digit reflection and transmission results for various albedos and optical thicknesses. The results from this chapter are summarized in Tables 3.1–3.6. The first four tables are calculations for slabs with matched boundary conditions. The last two tables give reflection and transmission values for a air-slide-tissue-slide-air sandwich.

Tables 3.1 and 3.2 give reflection and transmission for light normally incident on slabs of various optical depths and albedos. Isotropic scattering was assumed for these tables. Values for reflection and transmission for various optical depths  $\tau = 2^{-5}$  to  $\tau = 2^5$  and  $\tau = \infty$  are identical to those tabulated



	a=0.4	a=0.8	a=0.95	a=0.99
Giovanelli	.0858	.2072	.4155	.6541
Doubling	.0859	.2075	.4160	.6547

by van de Hulst [60]. When the medium is conservative ( $a = 1$ ), large optical depths ( $\tau \sim 2^{14}$ ) are required before the slab becomes effectively semi-infinite. The adding-doubling method is subject to anomalous absorption arising from quadrature errors when optical depths become this large. The diffusion approximation was used to calculate reflection and transmission for conservative scattering and optical depths larger than  $\tau = 2^{10}$ , because the diffusion approximation is more accurate in the diffusion region (large optical depths). This ensured that all entries in these tables were accurate to 0.01%.

Tables 3.3 and 3.4 give reflection and transmission for anisotropic scattering with a Henyey-Greenstein phase function. Many values in this table are also tabulated by van de Hulst ( $\tau = 2^0$  to  $\tau = 2^4$  and  $\tau = \infty$ ) [61]. The values in Tables 3.3 and 3.4 are identical to those of van de Hulst, thus verifying the implementation for anisotropic scattering.

Correct implementation of the boundary conditions is verified by comparison with Giovanelli [16] who calculated reflection from a semi-infinite slab bounded by glass slides. The indices of refraction were  $n_{\text{slab}} = 1.333$ ,  $n_{\text{glass}} = 1.532$ , and  $n_{\text{outside}} = 1.0$ . Giovanelli states that the fourth digit in his values is questionable.

Once both anisotropy and the boundary conditions were verified, Tables 3.5 and 3.6 were calculated. These tables give reflection and transmission for a air-glass-tissue-glass-air sandwich. These values have not been tabulated elsewhere, and will serve as “truth” for evaluation of the delta-Eddington ap-

proximation.

### 3.8 Conclusions

The adding-doubling method has been implemented with boundary conditions and scattering functions similar to those for tissue. The adding-doubling method is one-dimensional and with a modest number of quadrature angles ( $N = 16$ ) very accurate results may be obtained (0.01%). The adding-doubling method is not as flexible as the Monte Carlo method, but it is a valuable standard against which other one-dimensional methods may be compared. The tabulated values (Tables 3.1–3.6) of reflection and transmission presented in this chapter will be used to evaluate the accuracy of the one-dimensional delta-Eddington approximation in the Chapter 4.

$n$	$a = 1$	$a = .99$	$a = .95$	$a = .9$	$a = .8$	$a = .6$	$a = .4$	$a = .2$
-15	.0000	.0000	.0000	.0000	.0000	.0000	.0000	.0000
-14	.0000	.0000	.0000	.0000	.0000	.0000	.0000	.0000
-13	.0001	.0001	.0001	.0000	.0000	.0000	.0000	.0000
-12	.0001	.0001	.0001	.0001	.0001	.0001	.0000	.0000
-11	.0002	.0002	.0002	.0002	.0002	.0002	.0001	.0000
-10	.0005	.0005	.0005	.0004	.0004	.0003	.0002	.0001
-9	.0010	.0010	.0009	.0009	.0008	.0006	.0004	.0002
-8	.0019	.0019	.0019	.0018	.0016	.0012	.0008	.0004
-7	.0039	.0038	.0037	.0035	.0031	.0023	.0015	.0008
-6	.0077	.0077	.0074	.0069	.0061	.0046	.0030	.0015
-5	.0154	.0152	.0146	.0137	.0121	.0090	.0059	.0029
-4	.0303	.0300	.0286	.0269	.0236	.0173	.0112	.0055
-3	.0589	.0582	.0553	.0518	.0450	.0323	.0207	.0099
-2	.1117	.1101	.1039	.0965	.0824	.0573	.0356	.0167
-1	.2025	.1989	.1851	.1690	.1401	.0927	.0553	.0250
0	.3413	.3329	.3017	.2674	.2108	.1295	.0734	.0320
1	.5175	.4975	.4287	.3616	.2659	.1510	.0820	.0349
2	.6909	.6450	.5124	.4081	.2840	.1553	.0833	.0352
3	.8218	.7287	.5344	.4148	.2853	.1554	.0834	.0352
4	.9036	.7513	.5355	.4149	.2853	.1554	.0834	.0352
5	.9498	.7527	.5355	.4149	.2853	.1554	.0834	.0352
6	.9743	.7527	.5355	.4149	.2853	.1554	.0834	.0352
7	.9870	.7527	.5355	.4149	.2853	.1554	.0834	.0352
8	.9935	.7527	.5355	.4149	.2853	.1554	.0834	.0352
9	.9968	.7527	.5355	.4149	.2853	.1554	.0834	.0352
10	<i>.9984</i>	.7527	.5355	.4149	.2853	.1554	.0834	.0352
11	<i>.9992</i>	.7527	.5355	.4149	.2853	.1554	.0834	.0352
12	<i>.9996</i>	.7527	.5355	.4149	.2853	.1554	.0834	.0352
13	<i>.9998</i>	.7527	.5355	.4149	.2853	.1554	.0834	.0352
14	<i>.9999</i>	.7527	.5355	.4149	.2853	.1554	.0834	.0352

Table 3.1: Total reflection from a slab for normal incidence as a function of optical depth ( $\tau = 2^n$ ) and albedo ( $a$ ). Scattering is isotropic ( $g = 0$ ), the boundary conditions are matched, and all digits shown are significant. The diffusion method was used for the italicized entries, all others were obtained with the doubling method.

$n$	$a = 1$	$a = .99$	$a = .95$	$a = .9$	$a = .8$	$a = .6$	$a = .4$	$a = .2$
-15	1.0000	1.0000	1.0000	1.0000	1.0000	1.0000	1.0000	1.0000
-14	1.0000	1.0000	1.0000	1.0000	1.0000	1.0000	.9999	.9999
-13	.9999	.9999	.9999	.9999	.9999	.9999	.9999	.9999
-12	.9999	.9999	.9999	.9999	.9998	.9998	.9998	.9998
-11	.9998	.9998	.9997	.9997	.9997	.9997	.9996	.9996
-10	.9995	.9995	.9995	.9995	.9994	.9993	.9992	.9991
-9	.9990	.9990	.9990	.9989	.9988	.9986	.9984	.9982
-8	.9980	.9980	.9980	.9979	.9977	.9973	.9969	.9965
-7	.9961	.9961	.9959	.9957	.9953	.9945	.9937	.9930
-6	.9923	.9922	.9919	.9914	.9906	.9891	.9875	.9860
-5	.9846	.9844	.9838	.9830	.9814	.9782	.9751	.9721
-4	.9697	.9693	.9680	.9663	.9630	.9567	.9506	.9449
-3	.9411	.9403	.9375	.9340	.9272	.9146	.9030	.8924
-2	.8883	.8867	.8806	.8733	.8595	.8349	.8136	.7951
-1	.7975	.7941	.7808	.7654	.7378	.6928	.6577	.6296
0	.6587	.6510	.6226	.5916	.5414	.4714	.4251	.3923
1	.4825	.4657	.4093	.3565	.2860	.2111	.1730	.1502
2	.3091	.2755	.1869	.1285	.0751	.0394	.0272	.0215
3	.1782	.1221	.0408	.0160	.0047	.0012	.0006	.0004
4	.0964	.0296	.0020	.0002	.0000	.0000	.0000	.0000
5	.0502	.0019	.0000	.0000	.0000	.0000	.0000	.0000
6	.0257	.0000	.0000	.0000	.0000	.0000	.0000	.0000
7	.0130	.0000	.0000	.0000	.0000	.0000	.0000	.0000
8	.0065	.0000	.0000	.0000	.0000	.0000	.0000	.0000
9	.0032	.0000	.0000	.0000	.0000	.0000	.0000	.0000
10	<i>.0016</i>	.0000	.0000	.0000	.0000	.0000	.0000	.0000
11	<i>.0008</i>	.0000	.0000	.0000	.0000	.0000	.0000	.0000
12	<i>.0004</i>	.0000	.0000	.0000	.0000	.0000	.0000	.0000
13	<i>.0002</i>	.0000	.0000	.0000	.0000	.0000	.0000	.0000
14	<i>.0001</i>	.0000	.0000	.0000	.0000	.0000	.0000	.0000

Table 3.2: Total transmission by a slab for normal incidence as a function of optical depth ( $\tau = 2^n$ ) and albedo ( $a$ ). Scattering is isotropic ( $g = 0$ ), the boundary conditions are matched, and all digits shown are significant. The diffusion method was used for the italicized entries, all others were obtained with the doubling method.

$n$	$g = 0$			$g = .5$			$g = .875$		
	$a = .6$	$a = .9$	$a = .99$	$a = .6$	$a = .9$	$a = .99$	$a = .6$	$a = .9$	$a = .99$
-15	.0000	.0000	.0000	.0000	.0000	.0000	.0000	.0000	.0000
-14	.0000	.0000	.0000	.0000	.0000	.0000	.0000	.0000	.0000
-13	.0000	.0000	.0001	.0000	.0000	.0000	.0000	.0000	.0000
-12	.0001	.0001	.0001	.0000	.0000	.0000	.0000	.0000	.0000
-11	.0002	.0002	.0002	.0000	.0001	.0001	.0000	.0000	.0000
-10	.0003	.0004	.0005	.0001	.0002	.0002	.0000	.0000	.0000
-9	.0006	.0009	.0010	.0002	.0003	.0003	.0000	.0000	.0001
-8	.0012	.0018	.0019	.0004	.0006	.0007	.0001	.0001	.0001
-7	.0023	.0035	.0038	.0008	.0012	.0013	.0001	.0002	.0002
-6	.0046	.0069	.0077	.0016	.0024	.0026	.0003	.0004	.0005
-5	.0090	.0137	.0152	.0031	.0048	.0053	.0005	.0008	.0009
-4	.0173	.0269	.0300	.0060	.0096	.0107	.0010	.0016	.0018
-3	.0323	.0518	.0582	.0114	.0190	.0216	.0019	.0033	.0037
-2	.0573	.0965	.1101	.0208	.0375	.0438	.0035	.0064	.0076
-1	.0927	.1690	.1989	.0353	.0720	.0878	.0059	.0125	.0157
0	.1295	.2674	.3329	.0527	.1298	.1707	.0089	.0238	.0327
1	.1510	.3616	.4975	.0658	.2045	.3053	.0116	.0422	.0691
2	.1553	.4081	.6450	.0698	.2612	.4698	.0128	.0658	.1417
3	.1554	.4148	.7287	.0700	.2770	.6001	.0129	.0826	.2584
4	.1554	.4150	.7513	.0700	.2778	.6561	.0129	.0864	.3753
5	.1554	.4150	.7527	.0700	.2778	.6644	.0129	.0866	.4312
6	.1554	.4150	.7527	.0700	.2778	.6646	.0129	.0866	.4396
7	.1554	.4150	.7527	.0700	.2778	.6646	.0129	.0866	.4397
8	.1554	.4150	.7527	.0700	.2778	.6646	.0129	.0866	.4397
9	.1554	.4150	.7527	.0700	.2778	.6646	.0129	.0866	.4397

Table 3.3: Total reflection for normal incidence as a function of optical depth ( $\tau = 2^n$ ) and albedo ( $a$ ) for three different anisotropies ( $g = 0$ ,  $g = 0.5$  and  $g = 0.875$ ) using a Henyey-Greenstein phase function and matched boundary conditions. All digits shown are significant.

$n$	$g = 0$			$g = .5$			$g = .875$		
	$a = .6$	$a = .9$	$a = .99$	$a = .6$	$a = .9$	$a = .99$	$a = .6$	$a = .9$	$a = .99$
-15	1.0000	1.0000	1.0000	1.0000	1.0000	1.0000	1.0000	1.0000	1.0000
-14	1.0000	1.0000	1.0000	1.0000	1.0000	1.0000	1.0000	1.0000	1.0000
-13	.9999	.9999	.9999	.9999	1.0000	1.0000	.9999	1.0000	1.0000
-12	.9998	.9999	.9999	.9999	.9999	1.0000	.9999	1.0000	1.0000
-11	.9997	.9997	.9998	.9998	.9999	.9999	.9998	.9999	1.0000
-10	.9993	.9995	.9995	.9995	.9998	.9998	.9996	.9999	1.0000
-9	.9986	.9989	.9990	.9990	.9995	.9997	.9992	.9998	.9999
-8	.9973	.9979	.9980	.9980	.9990	.9993	.9984	.9995	.9998
-7	.9945	.9957	.9961	.9961	.9980	.9986	.9967	.9990	.9997
-6	.9891	.9914	.9922	.9921	.9960	.9972	.9935	.9980	.9994
-5	.9782	.9830	.9844	.9843	.9920	.9944	.9870	.9960	.9988
-4	.9567	.9663	.9693	.9685	.9839	.9886	.9741	.9921	.9975
-3	.9146	.9340	.9403	.9372	.9675	.9770	.9487	.9841	.9950
-2	.8349	.8733	.8867	.8758	.9341	.9533	.8993	.9679	.9898
-1	.6928	.7654	.7940	.7602	.8672	.9057	.8068	.9354	.9790
0	.4714	.5916	.6510	.5629	.7391	.8145	.6458	.8702	.9558
1	.2111	.3565	.4657	.2955	.5233	.6603	.4067	.7432	.9057
2	.0394	.1285	.2755	.0743	.2505	.4527	.1539	.5212	.8002
3	.0012	.0160	.1221	.0041	.0544	.2438	.0197	.2335	.6081
4	.0000	.0002	.0296	.0000	.0025	.0860	.0003	.0410	.3522
5	.0000	.0000	.0019	.0000	.0000	.0120	.0000	.0012	.1263
6	.0000	.0000	.0000	.0000	.0000	.0002	.0000	.0000	.0171
7	.0000	.0000	.0000	.0000	.0000	.0000	.0000	.0000	.0003
8	.0000	.0000	.0000	.0000	.0000	.0000	.0000	.0000	.0000
9	.0000	.0000	.0000	.0000	.0000	.0000	.0000	.0000	.0000

Table 3.4: Total transmission for normal incidence as a function of optical depth ( $\tau = 2^n$ ) and albedo ( $a$ ) for three different anisotropies ( $g = 0$ ,  $g = .5$  and  $g = 0.875$ ) using a Henyey-Greenstein phase function and matched boundary conditions. All digits shown are significant.

$n$	$g = 0$			$g = .5$			$g = .875$		
	$a = .6$	$a = .9$	$a = .99$	$a = .6$	$a = .9$	$a = .99$	$a = .6$	$a = .9$	$a = .99$
-20	.0789	.0789	.0789	.0789	.0789	.0789	.0789	.0789	.0789
-19	.0789	.0789	.0789	.0789	.0789	.0789	.0789	.0789	.0789
-18	.0789	.0789	.0790	.0789	.0789	.0789	.0789	.0789	.0789
-17	.0789	.0790	.0790	.0789	.0789	.0790	.0789	.0789	.0789
-16	.0789	.0790	.0790	.0789	.0790	.0790	.0789	.0789	.0789
-15	.0790	.0790	.0790	.0789	.0790	.0790	.0789	.0789	.0790
-14	.0790	.0790	.0790	.0789	.0790	.0790	.0789	.0789	.0790
-13	.0790	.0790	.0790	.0789	.0790	.0790	.0789	.0790	.0790
-12	.0790	.0790	.0790	.0790	.0790	.0790	.0789	.0790	.0790
-11	.0790	.0791	.0791	.0790	.0790	.0791	.0789	.0790	.0790
-10	.0790	.0792	.0793	.0790	.0791	.0792	.0789	.0790	.0790
-9	.0791	.0795	.0797	.0790	.0792	.0794	.0789	.0790	.0790
-8	.0792	.0800	.0805	.0790	.0795	.0799	.0788	.0790	.0791
-7	.0795	.0811	.0821	.0790	.0800	.0808	.0787	.0791	.0793
-6	.0801	.0833	.0852	.0791	.0811	.0826	.0786	.0792	.0797
-5	.0812	.0876	.0915	.0792	.0833	.0861	.0781	.0794	.0804
-4	.0832	.0959	.1036	.0794	.0875	.0932	.0774	.0799	.0820
-3	.0870	.1115	.1268	.0796	.0956	.1071	.0759	.0808	.0850
-2	.0931	.1391	.1693	.0799	.1102	.1333	.0730	.0825	.0910
-1	.1013	.1817	.2405	.0795	.1342	.1805	.0680	.0855	.1031
0	.1084	.2326	.3422	.0769	.1649	.2554	.0604	.0899	.1267
1	.1107	.2689	.4552	.0717	.1867	.3485	.0516	.0940	.1701
2	.1106	.2795	.5506	.0686	.1880	.4323	.0463	.0915	.2336
3	.1106	.2803	.6088	.0684	.1857	.4933	.0453	.0816	.2871
4	.1106	.2803	.6259	.0684	.1855	.5222	.0453	.0776	.3068
5	.1106	.2803	.6270	.0684	.1855	.5268	.0453	.0775	.3124
6	.1106	.2803	.6270	.0684	.1855	.5269	.0453	.0775	.3132
7	.1106	.2803	.6270	.0684	.1855	.5269	.0453	.0775	.3132
8	.1106	.2803	.6270	.0684	.1855	.5269	.0453	.0775	.3132

Table 3.5: Total reflection as a function of optical depth ( $\tau = 2^n$ ) and albedo ( $a$ ) for three different anisotropies ( $g = 0$ ,  $g = .5$ , and  $g = 0.875$ ) using a Henyey-Greenstein phase function. The slab ( $n_{\text{slab}} = 1.4$ ) is bounded by glass slides ( $n_{\text{glass}} = 1.5$ ) and air ( $n_{\text{air}} = 1.0$ ). All digits shown are significant.

$n$	$g = 0$			$g = .5$			$g = .875$		
	$a = .6$	$a = .9$	$a = .99$	$a = .6$	$a = .9$	$a = .99$	$a = .6$	$a = .9$	$a = .99$
-20	.9211	.9211	.9211	.9211	.9211	.9211	.9211	.9211	.9211
-19	.9211	.9211	.9211	.9211	.9211	.9211	.9211	.9211	.9211
-18	.9211	.9211	.9211	.9211	.9211	.9211	.9211	.9211	.9211
-17	.9211	.9211	.9211	.9211	.9211	.9211	.9211	.9211	.9211
-16	.9210	.9211	.9211	.9211	.9211	.9211	.9211	.9211	.9211
-15	.9210	.9210	.9210	.9210	.9210	.9211	.9210	.9211	.9211
-14	.9210	.9210	.9210	.9210	.9210	.9210	.9210	.9211	.9211
-13	.9210	.9210	.9210	.9210	.9210	.9210	.9210	.9210	.9211
-12	.9209	.9209	.9209	.9209	.9210	.9210	.9209	.9210	.9210
-11	.9207	.9208	.9208	.9208	.9209	.9209	.9208	.9210	.9210
-10	.9203	.9205	.9206	.9204	.9207	.9208	.9206	.9209	.9210
-9	.9195	.9200	.9202	.9198	.9203	.9205	.9202	.9207	.9209
-8	.9180	.9189	.9193	.9186	.9196	.9200	.9194	.9204	.9208
-7	.9150	.9166	.9176	.9162	.9180	.9190	.9177	.9197	.9205
-6	.9090	.9123	.9142	.9113	.9150	.9170	.9143	.9184	.9200
-5	.8971	.9036	.9075	.9017	.9091	.9129	.9077	.9158	.9189
-4	.8738	.8865	.8942	.8826	.8972	.9048	.8945	.9105	.9167
-3	.8289	.8535	.8688	.8456	.8738	.8890	.8686	.9001	.9124
-2	.7458	.7916	.8218	.7758	.8287	.8587	.8188	.8792	.9035
-1	.6032	.6829	.7414	.6521	.7448	.8030	.7269	.8378	.8856
0	.3940	.5131	.6208	.4587	.6017	.7100	.5710	.7574	.8491
1	.1673	.2970	.4697	.2251	.3966	.5793	.3486	.6115	.7766
2	.0297	.1029	.3049	.0530	.1784	.4241	.1261	.3888	.6488
3	.0009	.0126	.1453	.0028	.0377	.2503	.0153	.1548	.4734
4	.0000	.0002	.0360	.0000	.0017	.0925	.0002	.0255	.2800
5	.0000	.0000	.0023	.0000	.0000	.0130	.0000	.0007	.1031
6	.0000	.0000	.0000	.0000	.0000	.0003	.0000	.0000	.0141
7	.0000	.0000	.0000	.0000	.0000	.0000	.0000	.0000	.0003
8	.0000	.0000	.0000	.0000	.0000	.0000	.0000	.0000	.0000

Table 3.6: Total transmission as a function of optical depth ( $\tau = 2^n$ ) and albedo ( $a$ ) for three different anisotropies ( $g = 0.0$ ,  $g = 0.5$  and  $g = 0.875$ ) using a Henyey-Greenstein phase function. The slab ( $n_{\text{slab}} = 1.4$ ) is bounded by glass slides ( $n_{\text{glass}} = 1.5$ ) and air ( $n_{\text{air}} = 1$ ). All digits shown are significant.



## Chapter 4

# The Delta-Eddington Approximation

### Introduction

This chapter describes the delta-Eddington approximation to the radiative transport equation. In Section 4.1 the diffusion equation is derived from the transport equation; this derivation follows that of [30] with the exception that the Eddington phase function has been replaced by the delta-Eddington phase function of Joseph *et al.* [34]. New boundary conditions required for a number of different physical situations are derived in Section 4.1. The results of the previous sections are converted into dimensionless units in Section 4.2. The one-dimensional diffusion equation is solved analytically in Section 4.3, and in Section 4.4 the calculation of flux, reflection, and transmission is discussed. The three-dimensional cylindrically symmetric solution to the diffusion equation is presented in Section 4.5. In Section 4.6 the solutions obtained using the diffusion approximation are compared with exact solutions obtained with the adding-doubling method.

### 4.1 Derivation of the diffusion equation

The radiative transport equation is [8]

$$(\hat{\mathbf{s}} \cdot \nabla)L(\mathbf{r}, \hat{\mathbf{s}}) = -\mu_t L(\mathbf{r}, \hat{\mathbf{s}}) + \mu_s \int_{4\pi} P(\hat{\mathbf{s}}, \hat{\mathbf{s}}')L(\mathbf{r}, \hat{\mathbf{s}}') d\omega' \quad (4.1)$$

where  $L(\mathbf{r}, \hat{\mathbf{s}})$  is the radiance ( $\text{W cm}^{-2}\text{sr}^{-1}$ ) at position  $\mathbf{r}$  in the direction of the unit vector  $\hat{\mathbf{s}}$ . The differential solid angle  $d\omega'$  has the unit vector  $\hat{\mathbf{s}}'$  as an outward normal. The phase function  $p(\hat{\mathbf{s}}, \hat{\mathbf{s}}')$  represents the fraction of light scattered from the direction  $\hat{\mathbf{s}}'$  into the direction  $\hat{\mathbf{s}}$ . The phase function is normalized such that it is unity when integrated over all directions.

The scattering medium is an infinite slab with finite thickness and infinite breadth. The inward normal to the top of the slab is chosen as the positive  $z$ -direction. The top surface is illuminated with a monodirectional flux  $\pi F_0(r)$

$$L_{\text{inc}}(r, \hat{\mathbf{s}}) = \pi F_0(r) \delta((\hat{\mathbf{s}} \cdot \hat{\mathbf{z}}) - (\hat{\mathbf{s}}_0 \cdot \hat{\mathbf{z}})) = \pi F_0 \delta(\mu - \mu_0) \quad (4.2)$$

where  $\hat{\mathbf{z}}$  is a unit vector in the direction of the  $z$ -axis and  $\hat{\mathbf{s}}_0$  is a unit vector in the direction of the incident flux and  $\mu$  is the cosine of the angle  $\hat{\mathbf{s}}$  makes with the  $z$ -axis. The delta function  $\delta(\mu - \mu_0)$  is discussed in Appendix A3. Historically, the factor of  $\pi$  is included so that an isotropic diffuse source  $F_0(r)$  will result in a flux of  $\pi F_0(r)$  at a surface,

$$\int_{2\pi} F_0(r) (\hat{\mathbf{s}} \cdot \hat{\mathbf{z}}) d\omega = F_0(r) \int_0^1 \mu d\mu \int_0^{2\pi} d\phi = \pi F_0(r) \quad (4.3)$$

If the irradiance  $E_0(r)$  represents collimated light, then  $E_0(r) = \pi F_0(r)$ .

Notice that  $L_{\text{inc}}(\mathbf{r}, \hat{\mathbf{s}})$  includes contributions from a cone containing all vectors having  $\hat{\mathbf{s}} \cdot \hat{\mathbf{z}} = \mu_0$ , and not just one particular azimuthal angle. This simplifies the mathematics by eliminating any azimuthal dependence of radiance in the slab. The radiance  $L(\mathbf{r}, \hat{\mathbf{s}})$  is a function of only the position  $\mathbf{r}$  and the angle  $\cos^{-1}(\hat{\mathbf{s}} \cdot \hat{\mathbf{z}})$ .

The phase function is modelled as a delta-Eddington phase function

$$P_{\text{delta-E}}(\cos \theta) = \frac{1}{4\pi} \{2f\delta(1 - \cos \theta) + (1 - f)(1 + 3g' \cos \theta)\} \quad (4.4)$$

where  $\cos \theta = (\hat{\mathbf{s}} \cdot \hat{\mathbf{s}}')$  is the cosine of the angle between the incident and the scattered light. The first term accounts for strong scattering in the forward direction and the second term approximates a more diffuse type of scattering. The parameter  $f$  determines the fraction of light scattered into the forward peak (the delta function) and  $g'$  denotes the degree of asymmetry in the diffuse portion of the scattering. The factor of  $1/4\pi$  is included for normalization.

Substituting Equation (4.4) into (4.1) yields

$$(\hat{\mathbf{s}} \cdot \nabla)L(\mathbf{r}, \hat{\mathbf{s}}) = -\mu'_t L(\mathbf{r}, \hat{\mathbf{s}}) + \frac{\mu_s}{4\pi} \int_{4\pi} L(\mathbf{r}, \hat{\mathbf{s}}')[1 + 3g'(\hat{\mathbf{s}} \cdot \hat{\mathbf{s}}')] d\omega' \quad (4.5)$$

where the reduced scattering coefficient is  $\mu'_s = \mu_s(1 - f)$  and the transport coefficient is  $\mu'_t = \mu'_s + \mu_a$ . The transport  $\mu'_t$  and reduced scattering  $\mu'_s$  coefficients are less than the corresponding total attenuation  $\mu_t$  and scattering coefficients  $\mu_s$  respectively and represent *effective* total attenuation and scattering. The scattering coefficient is reduced because light scattered into the forward peak of Equation (4.4) is indistinguishable from unscattered light. The fraction of light *not* scattered into the forward peak is  $(1 - f)$ , and consequently, the scattering coefficient is reduced by a factor of  $(1 - f)$ . Thus the reduced scattering coefficient  $\mu'_s$  represents the amount of light scattered out of the collimated portion of the radiance and into the diffuse portion of the radiance.

The radiance is divided into collimated and diffuse components

$$L(\mathbf{r}, \hat{\mathbf{s}}) = L_{\text{coll}}(\mathbf{r}, \hat{\mathbf{s}}) + L_d(\mathbf{r}, \hat{\mathbf{s}}) \quad (4.6)$$

The collimated radiance includes both the light scattered into a direction parallel to the incident beam and any unscattered light. Because the collimated radiance includes light scattered forward, the beam is attenuated not by the usual total

attenuation coefficient  $\mu_t$  but by the transport coefficient  $\mu'_t$ . The collimated light is attenuated at a rate proportional to the transport coefficient.

$$(\hat{\mathbf{s}}_0 \cdot \nabla)L_{\text{coll}}(\mathbf{r}, \hat{\mathbf{s}}) = -\mu'_t L_{\text{coll}}(\mathbf{r}, \hat{\mathbf{s}}) \quad (4.7)$$

The amount of collimated light entering the slab is given by Equation (4.2), less the amount of light lost to specular reflection from the surface

$$L_{\text{coll}}(\mathbf{r}, \hat{\mathbf{s}}) = (1 - r_s)\pi F_0(r)\delta(\mu - \mu_0) \quad (4.8)$$

where  $r_s$  is the specular reflection coefficient given by the usual Fresnel reflection formula for specular reflection for an angle of incidence  $\cos \theta_0 = \hat{\mathbf{s}}_0 \cdot \hat{\mathbf{z}}$

$$r_s = \frac{1}{2} \left[ \frac{\sin^2(\theta_0 - \theta_t)}{\sin^2(\theta_0 + \theta_t)} + \frac{\tan^2(\theta_0 - \theta_t)}{\tan^2(\theta_0 + \theta_t)} \right] \quad (4.9)$$

The incident and transmitted angles  $\theta_0$  and  $\theta_t$  are related by Snell's law

$$n_{\text{tissue}} \sin \theta_t = n_{\text{air}} \sin \theta_0$$

where  $n_{\text{air}}$  and  $n_{\text{tissue}}$  are the indices of refraction of air and tissue. The solution of Equation (4.7) subject to the initial condition of Equation (4.8) is

$$L_{\text{coll}}(\mathbf{r}, \hat{\mathbf{s}}) = (1 - r_s)\pi F_0(r) \exp(-\mu'_t z / \mu_0) \delta(\mu - \mu_0) \quad (4.10)$$

where  $z/\mu_0$  is the distance incident light travels in tissue to reach a depth  $z$  in the slab. Substituting Equation (4.6) into (4.5) and simplifying using Equations (4.7) and (4.10) yields

$$\begin{aligned} (\hat{\mathbf{s}} \cdot \nabla)L_d(\mathbf{r}, \hat{\mathbf{s}}) &= -\mu'_t L_d(\mathbf{r}, \hat{\mathbf{s}}) + \frac{\mu'_s}{4\pi} \int_{4\pi} L_d(\mathbf{r}, \hat{\mathbf{s}}') [1 + 3g'(\hat{\mathbf{s}} \cdot \hat{\mathbf{s}}')] d\omega' \\ &+ \frac{\mu'_s}{4\pi} (1 - r_s)\pi F_0(r) \exp(-\mu'_t z / \mu_0) [1 + 3g'\mu_0\mu] \end{aligned} \quad (4.11)$$

where  $\hat{\mathbf{s}} \cdot \hat{\mathbf{s}}'$  has been rewritten in terms of the spherical angles determining  $\hat{\mathbf{s}}$  and  $\hat{\mathbf{s}}'$ . If  $\mu = \hat{\mathbf{s}} \cdot \hat{\mathbf{z}}$  and  $\mu' = \hat{\mathbf{s}}' \cdot \hat{\mathbf{z}}$  then

$$\hat{\mathbf{s}} \cdot \hat{\mathbf{s}}' = \mu\mu' - \sqrt{1 - \mu^2}\sqrt{1 - \mu'^2} \cos(\phi - \phi') \quad (4.12)$$

The Eddington or diffusion approximation characterizes the diffuse radiance as a sum of a diffuse radiant fluence  $\phi_d(\mathbf{r})$  and a diffuse radiant flux per unit area  $\mathbf{F}_d(\mathbf{r})$ . These are defined as the first two moments of the radiance  $L_d(\mathbf{r}, \hat{\mathbf{s}})$

$$\varphi_d(\mathbf{r}) = \int_{4\pi} L_d(\mathbf{r}, \hat{\mathbf{s}}') d\omega' \quad \text{and} \quad \mathbf{F}_d(\mathbf{r}) = \int_{4\pi} L_d(\mathbf{r}, \hat{\mathbf{s}}') \hat{\mathbf{s}} d\omega' \quad (4.13)$$

The diffuse radiance can then be expressed as

$$L_d(\mathbf{r}, \hat{\mathbf{s}}) = \frac{1}{4\pi} \varphi_d(\mathbf{r}) + \frac{3}{4\pi} \mathbf{F}_d(\mathbf{r}) \cdot \hat{\mathbf{s}} \quad (4.14)$$

The factors of  $1/4\pi$  and  $3/4\pi$  in Equation (4.14) result from normalization. Equation (4.14) represents the first two terms of the Taylor expansion for the diffuse radiance  $L_d(\mathbf{r}, \hat{\mathbf{s}})$ , where  $\phi_d(\mathbf{r})$  represents the isotropic and  $\mathbf{F}_d(\mathbf{r})$  the anisotropic contribution to the diffuse radiance.

Recalling the solid angle integration identities (see Appendix A3)

$$\int_{4\pi} \hat{\mathbf{s}} \cdot \mathbf{A} d\omega = 0 \quad \text{and} \quad \int_{4\pi} (\hat{\mathbf{s}} \cdot \mathbf{A})(\hat{\mathbf{s}} \cdot \mathbf{B}) d\omega = \frac{4\pi}{3} (\mathbf{A} \cdot \mathbf{B}) \quad (4.15)$$

and substituting Equation (4.14) into (4.11) and using (4.15) to simplify yields the following equation for the diffuse radiance

$$\begin{aligned} (\hat{\mathbf{s}} \cdot \nabla) \varphi_d(\mathbf{r}) + 3(\hat{\mathbf{s}} \cdot \nabla)(\mathbf{F}_d(\mathbf{r}) \cdot \hat{\mathbf{s}}) &= -\mu_a \varphi_d(\mathbf{r}) - 3(\mu'_t - g\mu'_s)(\mathbf{F}_d(\mathbf{r}) \cdot \hat{\mathbf{s}}) \\ &+ \mu'_s(1 - r_s)\pi F_0(r) \exp(-\mu'_t z/\mu_0)(1 + 3g'\mu\mu_0) \end{aligned} \quad (4.16)$$

Integration of Equation (4.17) over all directions and using relations (4.15) results in the following equation for the diffuse flux

$$\nabla \cdot \mathbf{F}_d(\mathbf{r}) = -\mu_a \varphi_d(\mathbf{r}) + \mu'_s(1 - r_s)\pi F_0(r) \exp(-\mu'_t z/\mu_0) \quad (4.17)$$

Here the L. H. S. represents the net change in the diffuse radiant flux. This equals the intensity lost through absorption of the diffuse radiant fluence plus that gained through scattering of collimated light into the diffuse portion of the radiance. Multiplying Equation (4.17) by  $\hat{\mathbf{s}}$  and integrating over all angles yields an energy flux equation for the diffuse radiance which states that the change in the diffuse fluence equals the diffuse flux lost to absorption plus that gained from collimated light.

$$\nabla \varphi_d(\mathbf{r}) = -3\mu'_{tr} \mathbf{F}_d(\mathbf{r}) + 3g'\mu'_s(1-r_s)\pi F_0(r) \exp(-\mu'_t z/\mu_0)\mu_0 \hat{\mathbf{z}} \quad (4.18)$$

where  $\mu'_{tr} = \mu_a + \mu'_s(1-g')$  is the reduced transport coefficient. The reduced transport coefficient incorporates forward scattered light from the second term of the delta-Eddington phase function into the collimated beam in much the same way that such light for the first term was incorporated into expressions for the reduced scattering coefficient. Taking the divergence of Equation (4.18) and solving for  $\nabla \cdot \mathbf{F}_d(\mathbf{r})$  yields

$$\nabla \cdot \mathbf{F}_d(\mathbf{r}) = -\frac{1}{3\mu'_{tr}} \nabla^2 \varphi_d(\mathbf{r}) - \frac{g'\mu'_s\mu'_t}{\mu'_{tr}}(1-r_s)\pi F_0(r) \exp(-\mu'_t z/\mu_0) \quad (4.19)$$

Equating Equation (4.17) and (4.19) leads to a Helmholtz equation

$$\nabla^2 \varphi_d(\mathbf{r}) - 3\mu'_{tr}\mu_a \varphi_d(\mathbf{r}) = -3\mu'_s(\mu'_{tr} + \mu'_t g')(1-r_s)\pi F_0(r) \exp(-\mu'_t z/\mu_0) \quad (4.20)$$

which is the well-known diffusion equation. The R. H. S. of this equation represents the collimated irradiation source.

## 4.2 Boundary conditions

The appropriate boundary conditions for light scattering at the interface between two media are introduced in this section. These boundary conditions for the

diffuse radiance  $L_d(\mathbf{r}, \hat{\mathbf{s}})$  at the slab boundaries must be specified before the diffusion equation may be solved. They are appropriate for use with the diffusion equation. The majority of this section treats the interface between a scattering medium (tissue) and a non-scattering medium (e.g., air, glass, water-glass-air).

The simplest situation has matched indices of refraction across the boundary and no incident diffuse light. This first case considered is uncomplicated by either reflected light—caused by index of refraction mismatching—or source terms arising from incident diffuse light. The next case (index matching, diffuse light incident) illustrates how a problem involving diffuse or Lambertian irradiance may be solved by including an extra term in the boundary conditions. Boundaries between two media with different indices of refraction are treated next, both with and without diffuse incidence. Finally, boundaries between two scattering media are considered. First with and then without index of refraction matching. These cases are particularly important when light scattering in multi-layered tissue is modelled.

#### 4.2.1 Index matching, no incident diffuse light

If no diffuse light is incident on the top surface of the slab, then the obvious boundary condition for diffuse light in the slab at a boundary is

$$L_d(\mathbf{r}, \hat{\mathbf{s}}) = 0 \quad \text{if} \quad \hat{\mathbf{s}} \cdot \hat{\mathbf{z}} > 0, \quad \text{at } z = 0 \quad (4.21)$$

where the vector  $\mathbf{r}$  has the usual cylindrical coordinates  $(r, z, \theta)$  and  $\hat{\mathbf{z}}$  is directed into the slab. Condition (4.21) requires that diffuse light from all inward directions be zero at the top surface. Recalling the diffuse radiance in the diffusion

approximation (Equation (4.14))

$$L_d(\mathbf{r}, \hat{\mathbf{s}}) = \frac{1}{4\pi}\varphi_d(\mathbf{r}) + \frac{3}{4\pi}\mathbf{F}_d(\mathbf{r}) \cdot \hat{\mathbf{s}}$$

It is evident that since both  $\phi_d(\mathbf{r})$  and  $\mathbf{F}_d(\mathbf{r})$  are independent of  $\hat{\mathbf{s}}$ , both must be identically zero to satisfy condition (4.21) and the boundary condition in Equation (4.21) cannot be used.

The usual choice for a boundary condition at a surface is the Marshak condition [7]. This condition requires that the diffuse radiant flux per unit area downwards at the surface equal zero.

$$\int_{2\pi \mu \geq 0} L_d(\mathbf{r}, \hat{\mathbf{s}})(\hat{\mathbf{s}} \cdot \hat{\mathbf{z}}) d\omega = 0 \quad \text{at} \quad z = 0 \quad (4.22)$$

The notation “ $2\pi \mu \geq 0$ ” under the integral sign indicates that the integration is done over the hemisphere in which  $\mu$  is positive. The positive  $z$ -direction is into the slab and the cosine angles  $\mu = \hat{\mathbf{s}} \cdot \hat{\mathbf{z}}$  are all positive for directions pointing forwards or into the slab. The extra  $(\hat{\mathbf{s}} \cdot \hat{\mathbf{z}})$  term is needed to project the radiance in the  $z$ -direction. Equation (4.22) may be rewritten using expansion (4.14) for the diffuse radiance

$$\int_{2\pi \mu \geq 0} L_d(\mathbf{r}, \hat{\mathbf{s}})(\hat{\mathbf{s}} \cdot \hat{\mathbf{z}}) d\omega = \frac{1}{4\pi} \int_{2\pi \mu \geq 0} \varphi_d(\mathbf{r})(\hat{\mathbf{s}} \cdot \hat{\mathbf{z}}) d\omega + \frac{3}{4\pi} \int_{2\pi \mu \geq 0} (\mathbf{F}_d(\mathbf{r}) \cdot \hat{\mathbf{z}})(\hat{\mathbf{s}} \cdot \hat{\mathbf{z}}) d\omega \quad (4.23)$$

Further simplification is obtained using the hemispherical Equations (A3.12) and (A3.16) from Appendix A3,

$$\int_{2\pi \mu \geq 0} L_d(\mathbf{r}, \hat{\mathbf{s}})(\hat{\mathbf{s}} \cdot \hat{\mathbf{z}}) d\omega = \frac{1}{4}\varphi_d(\mathbf{r}) + \frac{1}{2}(\mathbf{F}_d(\mathbf{r}) \cdot \hat{\mathbf{z}}) = 0 \quad (4.24)$$

Recalling the relation between  $\mathbf{F}_d(\mathbf{r})$  and  $\phi_d(\mathbf{r})$ , Equation (4.18)

$$\nabla \varphi_d(\mathbf{r}) = -3\mu'_{tr}\mathbf{F}_d(\mathbf{r}) + 3g'\mu'_s(1 - r_s)\pi F_0(r) \exp(-\mu'_t z/\mu_0)\mu_0\hat{\mathbf{z}}$$



and taking the vector dot product of Equation (4.18) with  $\hat{\mathbf{z}}$  yields upon rearrangement

$$\mathbf{F}_d(\mathbf{r}) \cdot \hat{\mathbf{z}} = -\frac{1}{3\mu'_{tr}} \frac{\partial \varphi_d(\mathbf{r})}{\partial z} + \frac{g' \mu'_s}{\mu'_{tr}} (1 - r_s) \pi F_0(r) \exp(-\mu'_t z / \mu_0) \mu_0 \quad (4.25)$$

Substituting Equation (4.25) into (4.24) and simplifying yields the boundary condition for diffuse light at the upper boundary

$$\varphi_d(\mathbf{r}) - h \frac{\partial \varphi_d(\mathbf{r})}{\partial z} = -Q(\mathbf{r}) \quad \text{at} \quad z = 0 \quad (4.26)$$

where ( $r_s = 0$  for matched indices of refraction)

$$h = \frac{2}{3\mu'_{tr}} \quad \text{and} \quad Q(\mathbf{r}) = 3hg' \mu'_s \pi F_0(r) \exp(-\mu'_t z / \mu_0) \mu_0 \quad (4.27)$$

The anisotropic surface factor  $Q(\mathbf{r})$  results from the difference in scattering into the forward and backward hemispheres at the boundary due to anisotropic scattering. This factor is zero when scattering is isotropic ( $g' = 0$ ).

The boundary condition for light at the bottom boundary (located at  $z = d$ ) is

$$\int_{2\pi} \int_{\mu \leq 0} L_d(\mathbf{r}, \hat{\mathbf{s}}) (-\hat{\mathbf{s}} \cdot \hat{\mathbf{z}}) d\omega = 0 \quad \text{at} \quad z = d \quad (4.28)$$

The inward normal to the slab at the bottom boundary is  $-\hat{\mathbf{z}}$ , and  $(-\hat{\mathbf{z}} \cdot \hat{\mathbf{s}})$  is a positive projection angle needed to project the diffuse radiance onto the  $-\hat{\mathbf{z}}$  axis. Since

$$\int_{2\pi} \int_{\mu \leq 0} L_d(\mathbf{r}, \hat{\mathbf{s}}) (-\hat{\mathbf{s}} \cdot \hat{\mathbf{z}}) d\omega = \frac{1}{4} \varphi_d(\mathbf{r}) - \frac{1}{2} (\mathbf{F}_d(\mathbf{r}) \cdot \hat{\mathbf{z}}) = 0 \quad (4.29)$$

the boundary condition (4.22) becomes

$$\varphi_d(\mathbf{r}) + h \frac{\partial \varphi_d(\mathbf{r})}{\partial z} = Q(\mathbf{r}) \quad \text{at} \quad z = d \quad (4.30)$$

with  $h$  and  $Q(r)$  defined in Equation (4.27) above. Equations (4.26) and (4.30) are the appropriate boundary conditions for tissue embedded in a non-scattering environment. Reflection had not been considered and so these boundary conditions implicitly require the scattering media to have the same index of refraction as the tissue. Equation (4.30) is also appropriate for tissue having a black backing, since in this case light is not internally reflected (i.e., all light reaching the black rear surface is absorbed.)

#### 4.2.2 Index matching, diffuse light incident

When the light incident on a slab is diffuse, either in addition to the collimated incidence or as the sole light source, it is included in the boundary conditions. The diffuse radiance  $L_{di}(\mathbf{r}, \hat{\mathbf{s}})$  is assumed isotropic (Lambertian) and might be generated experimentally with an integrating sphere. Since the net diffuse radiant flux downwards equals the net flux of the incident diffuse radiance.

$$\int_{2\pi} \int_{\mu \geq 0} L_d(\mathbf{r}, \hat{\mathbf{s}})(\hat{\mathbf{s}} \cdot \hat{\mathbf{z}}) d\omega = \int_{2\pi} \int_{\mu \geq 0} L_{di}(\mathbf{r}, \hat{\mathbf{s}})(\hat{\mathbf{s}} \cdot \hat{\mathbf{z}}) d\omega \quad \text{at} \quad z = 0 \quad (4.31)$$

Equation (4.31) may be simplified using Equation (4.24) and using the isotropy of the incident diffuse radiance  $L_{di}(\mathbf{r}, \hat{\mathbf{s}})$

$$\frac{1}{4}\varphi_d(\mathbf{r}) + \frac{1}{2}(\mathbf{F}_d(\mathbf{r}) \cdot \hat{\mathbf{z}}) = \pi L_{di}(\mathbf{r}, \hat{\mathbf{s}}) \quad (4.32)$$

Substituting the expression for  $\mathbf{F}_d(\mathbf{r}) \cdot \hat{\mathbf{z}}$  from Equation (4.25) and simplifying yields

$$\varphi_d(\mathbf{r}) - h \frac{\partial \varphi_d(\mathbf{r})}{\partial z} = -Q(\mathbf{r}) + 4\pi L_{di}(\mathbf{r}, \hat{\mathbf{s}}) \quad \text{at} \quad z = 0 \quad (4.33)$$

where

$$h = \frac{2}{3\mu'_{tr}} \quad \text{and} \quad Q(\mathbf{r}) = 3hg'\mu'_s\pi F_0(r) \exp(-\mu'_t z/\mu_0)\mu_0 \quad (4.34)$$

The anisotropic surface factor  $Q(\mathbf{r})$  accounts for the difference in scattering into the forward and backward hemispheres. The surface factor  $Q(\mathbf{r})$  is zero when scattering is isotropic ( $g' = 0$ ).

For completeness, when diffuse light is incident on the bottom surface of the slab then the appropriate boundary condition becomes

$$\varphi_d(\mathbf{r}) + h \frac{\partial \varphi_d(\mathbf{r})}{\partial z} = Q(\mathbf{r}) + 4\pi L_{di}(\mathbf{r}, \hat{\mathbf{s}}) \quad \text{at} \quad z = d \quad (4.35)$$

where  $h$  and  $Q(\mathbf{r})$  are defined in Equation (4.34). Both Equations (4.33) and (4.35) assume that the scattering medium is adjacent to non scattering media. Furthermore, the non-scattering media must have the same index of refraction as the scattering media. If either of these conditions is not satisfied then these are not physically appropriate. Consequently, these boundary conditions are not particularly useful for solving multi-layered problems since adjacent tissues may have different optical properties and will both probably scatter light.

### 4.2.3 Index mismatch, no incident diffuse light

If the indices of refraction are mismatched and no diffuse light is incident on the slab, then boundary condition (4.22) becomes

$$\int_{2\pi \mu \geq 0} L_d(\mathbf{r}, \hat{\mathbf{s}})(\hat{\mathbf{s}} \cdot \hat{\mathbf{z}}) d\omega = \int_{2\pi \mu \leq 0} r(-\hat{\mathbf{z}} \cdot \hat{\mathbf{s}}) L_d(\mathbf{r}, \hat{\mathbf{s}})(-\hat{\mathbf{s}} \cdot \hat{\mathbf{z}}) d\omega \quad \text{at} \quad z = 0 \quad (4.36)$$

where  $r(-\hat{\mathbf{z}} \cdot \hat{\mathbf{s}})$  is the reflection coefficient given by the Fresnel Equation (4.9). This equation states that the average downward radiance equals the reflected upward radiance. The Fresnel reflection is an even function of  $\mu$ , so  $r(\mu) = r(-\mu)$ . The R.H.S. of Equation (4.36) may be expanded using Equation (4.14)

$$\int_{2\pi \mu \leq 0} L_d(\mathbf{r}, \hat{\mathbf{s}})(-\hat{\mathbf{s}} \cdot \hat{\mathbf{z}}) r(\hat{\mathbf{z}} \cdot \hat{\mathbf{s}}) d\omega = \frac{1}{4\pi} \int_{2\pi \mu \leq 0} \varphi_d(\mathbf{r})(-\hat{\mathbf{s}} \cdot \hat{\mathbf{z}}) r(\hat{\mathbf{z}} \cdot \hat{\mathbf{s}}) d\omega$$

$$+ \frac{3}{4\pi} \int_{2\pi} \int_{\mu \leq 0} (\mathbf{F}_d(\mathbf{r}) \cdot \hat{\mathbf{z}})(-\hat{\mathbf{s}} \cdot \hat{\mathbf{z}})r(\hat{\mathbf{z}} \cdot \hat{\mathbf{s}}) d\omega \quad (4.37)$$

Since the first term on the R.H.S. of Equation (4.37) is independent of the azimuthal angle, it becomes

$$\frac{1}{4\pi} \int_{2\pi} \int_{\mu \leq 0} \varphi_d(\mathbf{r})(-\hat{\mathbf{s}} \cdot \hat{\mathbf{z}})r(\hat{\mathbf{z}} \cdot \hat{\mathbf{s}}) d\omega = -\frac{1}{2} \varphi_d(\mathbf{r}) \int_{-1}^0 r(\mu)(-\mu) d\mu \quad (4.38)$$

Decomposing the flux into tangential  $\hat{\mathbf{t}}$  and perpendicular  $\hat{\mathbf{z}}$  components

$$\mathbf{F}_d(\mathbf{r}) = F_{dt}(\mathbf{r})\hat{\mathbf{t}} + F_{dn}(\mathbf{r})\hat{\mathbf{z}} \quad (4.39)$$

allows simplification of the second term on the R.H.S. of Equation (4.37). The integral of the tangential component is zero due to the azimuthal independence

$$\int_{2\pi} \int_{\mu \leq 0} (\mathbf{F}_{dt}(\hat{\mathbf{t}} \cdot \hat{\mathbf{s}})(-\hat{\mathbf{s}} \cdot \hat{\mathbf{z}})r(\hat{\mathbf{z}} \cdot \hat{\mathbf{s}}) d\omega = -\int_0^{2\pi} \cos \phi d\phi \int_{-1}^0 r(\mu)\mu(1-\mu^2)^{1/2} d\mu \quad (4.40)$$

The integral of the normal component of the diffuse radiant flux is

$$\frac{3}{4\pi} \int_{2\pi} \int_{\mu \leq 0} \mathbf{F}_{dn}(-\hat{\mathbf{z}} \cdot \hat{\mathbf{s}})(-\hat{\mathbf{s}} \cdot \hat{\mathbf{z}})r(\hat{\mathbf{z}} \cdot \hat{\mathbf{s}}) d\omega = -\frac{3}{2} F_{dn} \int_{-1}^0 r(\mu)\mu^2 d\mu \quad (4.41)$$

Define the reflection coefficients  $R_1$  and  $R_2$  as

$$\begin{aligned} \frac{R_1}{2} &= \int_0^1 r(\mu)\mu d\mu = -\int_{-1}^0 r(\mu)\mu d\mu \\ \text{and} \quad \frac{R_2}{3} &= \int_0^1 r(\mu)\mu^2 d\mu = \int_{-1}^0 r(\mu)\mu^2 d\mu \end{aligned} \quad (4.42)$$

where the factors of 1/2 and 1/3 are included to ensure normalization. The symmetry of the reflection  $r(\mu) = r(-\mu)$  has been used to relate the integrals in (4.42). Tables for  $R_1$  and  $R_2$  may be found in Appendix A2 as a function of the index of refraction ratio between the two media.

Equation (4.41), definitions (4.42), and  $\mathbf{F}_{dn}(\mathbf{r}) = \mathbf{F}_d(\mathbf{r}) \cdot \hat{\mathbf{z}}$  allow Equation (4.37) to be written

$$\int_{2\pi} \int_{\mu \leq 0} L_d(\mathbf{r}, \hat{\mathbf{s}})r(\hat{\mathbf{s}} \cdot \hat{\mathbf{z}})(-\hat{\mathbf{s}} \cdot \hat{\mathbf{z}}) d\omega = \frac{R_1}{4} \varphi_d(\mathbf{r}) - \frac{R_2}{2} (\mathbf{F}_d(\mathbf{r}) \cdot \hat{\mathbf{z}}) \quad (4.43)$$

Equations (4.43) and (4.24) reduce the boundary condition (4.36) to

$$\frac{1}{4}\varphi_d(\mathbf{r}) + \frac{1}{2}(\mathbf{F}_d(\mathbf{r}) \cdot \hat{\mathbf{z}}) = \frac{R_1}{4}\varphi_d(\mathbf{r}) - \frac{R_2}{2}(\mathbf{F}_d(\mathbf{r}) \cdot \hat{\mathbf{z}}) \quad (4.44)$$

Substituting Equation (4.25) into (4.44) and simplifying yields the following mixed inhomogeneous boundary condition for the diffuse radiance

$$\varphi_d(\mathbf{r}) - A_{\text{top}}h\frac{\partial\varphi_d(\mathbf{r})}{\partial z} = -A_{\text{top}}Q(\mathbf{r}) \quad \text{at} \quad z = 0 \quad (4.45)$$

where

$$\begin{aligned} h &= \frac{2}{3\mu'_{tr}}, \\ A_{\text{top}} &= \frac{1 + R_2}{1 - R_1}, \quad \text{and} \\ Q(\mathbf{r}) &= 3hg'\mu'_s\pi F_0(r) \exp(-\mu'_t z/\mu_0)\mu_0(1 - r_s) \end{aligned} \quad (4.46)$$

$R_1$  and  $R_2$  are evaluated for the index of refraction ratio between the slab and the medium above the slab. The coefficient  $A_{\text{top}}$  may also be found by using the polynomial approximation (A2.51) given in Appendix A2.

The boundary condition for light at the bottom boundary (located at  $z = d$ ) is

$$\int_{2\pi} \int_{\mu \leq 0} L_d(\mathbf{r}, \hat{\mathbf{s}})(-\hat{\mathbf{s}} \cdot \hat{\mathbf{z}}) d\omega = \int_{2\pi} \int_{\mu \geq 0} r(\hat{\mathbf{z}} \cdot \hat{\mathbf{s}})L_d(\mathbf{r}, \hat{\mathbf{s}})(\hat{\mathbf{s}} \cdot \hat{\mathbf{z}}) d\omega \quad \text{at} \quad z = d \quad (4.47)$$

Since

$$\int_{2\pi} \int_{\mu \geq 0} L_d(\mathbf{r}, \hat{\mathbf{s}})r(\hat{\mathbf{s}} \cdot \hat{\mathbf{z}})(\hat{\mathbf{s}} \cdot \hat{\mathbf{z}}) d\omega = \frac{R_1}{4}\varphi_d(\mathbf{r}) + \frac{R_2}{2}(\mathbf{F}_d(\mathbf{r}) \cdot \hat{\mathbf{z}}) \quad (4.48)$$

Equation (4.29) reduces Equation (4.47) to

$$\varphi_d(\mathbf{r}) + A_{\text{bottom}}h\frac{\partial\varphi_d(\mathbf{r})}{\partial z} = A_{\text{bottom}}Q(\mathbf{r}) \quad \text{at} \quad z = d \quad (4.49)$$

The constants  $h$  and  $Q(r)$  are defined in Equation (4.46) and  $A_{\text{bottom}}$  is identical to  $A_{\text{top}}$  except that  $R_1$  and  $R_2$  are calculated using the ratio of the index of refraction of the medium beneath the slab to that above the slab. Boundary conditions (4.45) and (4.48) are appropriate for a scattering medium embedded in a non-scattering environment with a different index of refraction.

#### 4.2.4 Index mismatch, diffuse light incident

When diffuse light is incident on a slab having an index of refraction different from the medium directly above the slab, the boundary condition is given by Equation (4.36) with an extra term to account for the diffuse irradiance

$$\int_{2\pi} \int_{\mu \geq 0} L_d(\mathbf{r}, \hat{\mathbf{s}})(\hat{\mathbf{s}} \cdot \hat{\mathbf{z}}) d\omega = \int_{2\pi} \int_{\mu \leq 0} r(\hat{\mathbf{z}} \cdot \hat{\mathbf{s}}) L_d(\mathbf{r}, \hat{\mathbf{s}})(-\hat{\mathbf{s}} \cdot \hat{\mathbf{z}}) d\omega + \int_{2\pi} \int_{\mu \geq 0} t(\hat{\mathbf{z}} \cdot \hat{\mathbf{s}}) L_{di}(\mathbf{r}, \hat{\mathbf{s}})(\hat{\mathbf{s}} \cdot \hat{\mathbf{z}}) d\omega \quad \text{at} \quad z = 0 \quad (4.50)$$

where  $L_{di}(\mathbf{r}, \hat{\mathbf{s}})$  represents the isotropic radiance incident on the slab and  $t(\hat{\mathbf{s}} \cdot \hat{\mathbf{z}}) = 1 - r(\hat{\mathbf{s}} \cdot \hat{\mathbf{z}})$  is the Fresnel transmission. Since the diffuse radiance  $L_{di}(\mathbf{r}, \hat{\mathbf{s}})$  is independent of angle, Equation (4.50) reduces to the form

$$\frac{1}{4}\varphi_d(\mathbf{r}) + \frac{1}{2}(\mathbf{F}_d(\mathbf{r}) \cdot \hat{\mathbf{z}}) = \frac{R_1}{4}\varphi_d(\mathbf{r}) - \frac{R_2}{2}(\mathbf{F}_d(\mathbf{r}) \cdot \hat{\mathbf{z}}) + \pi L_{di}(\mathbf{r}, \hat{\mathbf{s}})(1 - R_1) \quad (4.51)$$

The reflection coefficient  $R_1$  is the same integral of the Fresnel reflection as defined in Equation (4.42) and is tabulated in Appendix A2. Equation (4.51) is identical to Equation (4.44) except that the included diffuse light has been reduced by the light reflected at the boundary. This relation simplifies to

$$\varphi_d(\mathbf{r}) - A_{\text{top}} h \frac{\partial \varphi_d(\mathbf{r})}{\partial z} = -A_{\text{top}} Q(\mathbf{r}) + 4\pi L_{di}(\mathbf{r}, \hat{\mathbf{s}}) \quad \text{at} \quad z = 0 \quad (4.52)$$

The boundary condition for diffuse light incident from the bottom of the slab is similar to Equation (4.52). The only difference is the hemispheres over

which the integrals are done. The boundary condition at  $z = d$ , where  $d$  is the depth of the slab is

$$\begin{aligned} \int_{2\pi} \int_{\mu \leq 0} L_d(\mathbf{r}, \hat{\mathbf{s}})(-\hat{\mathbf{s}} \cdot \hat{\mathbf{z}}) d\omega &= \int_{2\pi} \int_{\mu \geq 0} r(\hat{\mathbf{z}} \cdot \hat{\mathbf{s}}) L_d(\mathbf{r}, \hat{\mathbf{s}})(\hat{\mathbf{s}} \cdot \hat{\mathbf{z}}) d\omega \\ &+ \int_{2\pi} \int_{\mu \leq 0} t(\hat{\mathbf{z}} \cdot \hat{\mathbf{s}}) L'_{di}(\mathbf{r}, \hat{\mathbf{s}})(-\hat{\mathbf{s}} \cdot \hat{\mathbf{z}}) d\omega \quad \text{at } z = d \end{aligned} \quad (4.53)$$

where  $L'_{di}(\mathbf{r}, \hat{\mathbf{s}})$  is the diffuse light incident from the bottom. Equation (4.53) simplifies to

$$\varphi_d(\mathbf{r}) + A_{\text{bottom}} h \frac{\partial \varphi_d(\mathbf{r})}{\partial z} = A_{\text{bottom}} Q(\mathbf{r}) + 4\pi L'_{di}(\mathbf{r}, \hat{\mathbf{s}}) \quad \text{at } z = d \quad (4.54)$$

Equations (4.52) and (4.54) are the boundary conditions for diffuse light incident on a slab with an index of refraction different from its non-scattering environment. If there is no light incident from the top or bottom then set  $L_{di}(\mathbf{r}, \hat{\mathbf{s}})$  or  $L'_{di}(\mathbf{r}, \hat{\mathbf{s}})$  to zero as appropriate.

#### 4.2.5 Glass slide — no incident diffuse light

In many experiments to measure optical properties the scattering material is sandwiched between glass (or quartz) slides. The slides provide support for thin tissues and a smooth reproducible boundary. Unfortunately, the index of refraction of the slide is usually not equal to that of the tissue or that of the environment. This section shows how internal reflection from the glass slide is incorporated into the boundary conditions.

To incorporate a glass slide in the boundary conditions, Equation (A2.21) should be used to calculate the reflection coefficient  $r'(\mu)$  rather than the usual Fresnel reflection equation. Thus two new reflection coefficients  $R_1^{\text{glass}}$  and  $R_2^{\text{glass}}$  may be defined analogous to Equation (4.42)

$$\frac{R_1^{\text{glass}}}{2} = \int_0^1 r'(\mu) \mu d\mu = - \int_{-1}^0 r'(\mu) \mu d\mu$$

$$\frac{R_2^{\text{glass}}}{3} = \int_0^1 r'(\mu)\mu^2 d\mu = \int_{-1}^0 r'(\mu)\mu^2 d\mu \quad (4.55)$$

The analysis of the index mismatch section follows with  $A_{\text{top}}$  replaced by

$$A_{\text{top}}^{\text{glass}} = \frac{1 + R_2^{\text{glass}}}{1 - R_1^{\text{glass}}} \quad A_{\text{bottom}}^{\text{glass}} = \frac{1 + R_2^{\text{glass}}}{1 - R_1^{\text{glass}}} \quad (4.56)$$

Values for  $A^{\text{glass}}$  may be calculated using the polynomial approximations (A2.52)–(A2.57) in Appendix A2. The boundary conditions for the top and bottom of the slab follow from Equations (4.45) and (4.48)

$$\varphi_d(\mathbf{r}) - A_{\text{top}}^{\text{glass}} h \frac{\partial \varphi_d(\mathbf{r})}{\partial z} = -A_{\text{top}}^{\text{glass}} Q(\mathbf{r}) \quad \text{at} \quad z = 0 \quad (4.57)$$

$$\varphi_d(\mathbf{r}) + A_{\text{bottom}}^{\text{glass}} h \frac{\partial \varphi_d(\mathbf{r})}{\partial z} = A_{\text{bottom}}^{\text{glass}} Q(\mathbf{r}) \quad \text{at} \quad z = d \quad (4.58)$$

Equations (4.57) and (4.58) are appropriate for a slab of tissue sandwiched between glass slides.

#### 4.2.6 Glass slide — diffuse light incident

If diffuse light is incident on a slab bounded by glass slides then the correct boundary conditions follow from Equations (4.57) and (4.58) with the diffuse incidence incorporated as in Equations (4.52) and (4.53)

$$\varphi_d(\mathbf{r}) - A_{\text{top}}^{\text{glass}} h \frac{\partial \varphi_d(\mathbf{r})}{\partial z} = -A_{\text{top}}^{\text{glass}} Q(\mathbf{r}) + 4\pi L_{di}(\mathbf{r}, \hat{\mathbf{s}}) \quad (4.59)$$

$$\varphi_d(\mathbf{r}) + A_{\text{bottom}}^{\text{glass}} h \frac{\partial \varphi_d(\mathbf{r})}{\partial z} = A_{\text{bottom}}^{\text{glass}} Q(\mathbf{r}) + 4\pi L'_{di}(\mathbf{r}, \hat{\mathbf{s}}) \quad (4.60)$$

$L_{di}(\mathbf{r}, \hat{\mathbf{s}})$  is the isotropic diffuse radiance incident in the slab from above,  $L'_{di}(\mathbf{r}, \hat{\mathbf{s}})$  is the diffuse radiance from below. The parameters  $A_{\text{top}}^{\text{glass}}$  are calculated as in Appendix A2.



#### 4.2.7 Index matching, no incident diffuse light, both media scattering

If two slabs with the same index of refraction are juxtaposed, then the boundary conditions at the interface  $z = z_0$  are continuity of the first two moments of the radiance

$$\varphi_d^{(1)}(\mathbf{r}) = \varphi_d^{(2)}(\mathbf{r}) \quad \text{at} \quad z = z_0 \quad (4.61)$$

$$\mathbf{F}_d^{(1)}(\mathbf{r}) \cdot \hat{\mathbf{z}} = \mathbf{F}_d^{(2)}(\mathbf{r}) \cdot \hat{\mathbf{z}} \quad \text{at} \quad z = z_0 \quad (4.62)$$

This is the boundary condition required for multi-layered tissues in which there is no index of refraction difference from one medium to another. Equation (4.62) simplifies to

$$\frac{1}{\mu_{tr}^{(1)}} \frac{\partial \phi_d^{(1)}(\mathbf{r})}{\partial z} = \frac{1}{\mu_{tr}^{(2)}} \frac{\partial \phi_d^{(2)}(\mathbf{r})}{\partial z} \quad \text{at} \quad z = z_0 \quad (4.63)$$

where the superscripts 1 and 2 denote either the upper or lower medium respectively.

#### 4.2.8 Index mismatch, no incident diffuse light, both media scattering

Since the radiance over the square of the index of refraction is constant across an interface (Section A2.1) then as long as the radiance is divided by the square of the index of refraction of the medium it is in, the same methods used previously will suffice. Consequently, for light travelling upwards

$$\begin{aligned} \int_{2\pi\mu \leq 0} \frac{L^{(1)}(\mathbf{r}, \hat{\mathbf{s}})}{n_1^2} (-\hat{\mathbf{z}} \cdot \hat{\mathbf{s}}) d\omega &= \int_{2\pi\mu \geq 0} \frac{L^{(1)}(\mathbf{r}, \hat{\mathbf{s}})}{n_1^2} r^{(1)}(\hat{\mathbf{z}} \cdot \hat{\mathbf{s}})(\hat{\mathbf{z}} \cdot \hat{\mathbf{s}}) d\omega \\ &+ \int_{2\pi\mu \leq 0} \frac{L^{(2)}(\mathbf{r}, \hat{\mathbf{s}})}{n_2^2} t^{(2)}(\hat{\mathbf{z}} \cdot \hat{\mathbf{s}})(-\hat{\mathbf{z}} \cdot \hat{\mathbf{s}}) d\omega \end{aligned} \quad (4.64)$$

This means that the total amount of light travelling upwards in layer 1 from the boundary equals the light reflected back into layer 1 plus that transmitted from

the lower layer. Similarly, for light travelling downwards

$$\begin{aligned} \int_{2\pi\mu \geq 0} \frac{L^{(2)}(\mathbf{r}, \hat{\mathbf{s}})}{n_2^2} (\hat{\mathbf{z}} \cdot \hat{\mathbf{s}}) d\omega &= \int_{2\pi\mu \leq 0} \frac{L^{(2)}(\mathbf{r}, \hat{\mathbf{s}})}{n_2^2} r^{(2)} (\hat{\mathbf{z}} \cdot \hat{\mathbf{s}}) (-\hat{\mathbf{z}} \cdot \hat{\mathbf{s}}) d\omega \\ &+ \int_{2\pi\mu \geq 0} \frac{L^{(1)}(\mathbf{r}, \hat{\mathbf{s}})}{n_1^2} t^{(1)} (\hat{\mathbf{z}} \cdot \hat{\mathbf{s}}) (\hat{\mathbf{z}} \cdot \hat{\mathbf{s}}) d\omega \end{aligned} \quad (4.65)$$

The superscripts on the reflection  $r$  and the transmission  $t$  indicate the medium from which light is incident on the boundary

For upwards travelling light, Equation (4.64) can be simplified to

$$\begin{aligned} \frac{1}{n_2^2} \left[ (1 - R_1^{21}) \varphi_d^{(2)}(\mathbf{r}) - 2(1 - R_2^{21}) \mathbf{F}_d^{(2)}(\mathbf{r}) \cdot \hat{\mathbf{z}} \right] \\ = \frac{1}{n_1^2} \left[ (1 - R_1^{12}) \varphi_d^{(1)}(\mathbf{r}) - 2(1 + R_2^{12}) \mathbf{F}_d^{(1)}(\mathbf{r}) \cdot \hat{\mathbf{z}} \right] \end{aligned} \quad (4.66)$$

For downwards travelling light, Equation (4.65) becomes

$$\begin{aligned} \frac{1}{n_2^2} \left[ (1 - R_1^{21}) \varphi_d^{(2)}(\mathbf{r}) + 2(1 + R_2^{21}) \mathbf{F}_d^{(2)}(\mathbf{r}) \cdot \hat{\mathbf{z}} \right] \\ = \frac{1}{n_1^2} \left[ (1 - R_1^{12}) \varphi_d^{(1)}(\mathbf{r}) + 2(1 - R_2^{12}) \mathbf{F}_d^{(1)}(\mathbf{r}) \cdot \hat{\mathbf{z}} \right] \end{aligned} \quad (4.67)$$

Subtracting yields

$$\mathbf{F}_d^{(1)}(\mathbf{r}) \cdot \hat{\mathbf{z}} = \left( \frac{n_1}{n_2} \right)^2 \mathbf{F}_d^{(2)}(\mathbf{r}) \cdot \hat{\mathbf{z}} \quad (4.68)$$

Thus the flux across a boundary behaves the same way that the radiance does.

Equation (4.68) may be rewritten

$$\frac{1}{n_1^2 \mu_{tr}^{(1)}} \frac{d\varphi^{(1)}(\mathbf{r})}{dz} = \frac{1}{n_2^2 \mu_{tr}^{(2)}} \frac{d\varphi^{(2)}(\mathbf{r})}{dz} \quad (4.69)$$

Adding (4.67) and (4.68) yields

$$\begin{aligned} \frac{1}{n_1^2} \left[ (1 - R_1^{12}) \varphi_d^{(1)}(\mathbf{r}) - 2R_2^{12} \mathbf{F}_d^{(1)}(\mathbf{r}) \cdot \hat{\mathbf{z}} \right] \\ = -\frac{1}{n_2^2} \left[ (1 - R_1^{21}) \varphi_d^{(2)}(\mathbf{r}) + 2R_2^{21} \mathbf{F}_d^{(2)}(\mathbf{r}) \cdot \hat{\mathbf{z}} \right] \end{aligned} \quad (4.70)$$

where  $R_2^{21}$  is the second moment of the Fresnel reflection  $R_2$  for light passing from  $n_1$  to  $n_2$ . Substituting for  $F_d(r)$

$$\begin{aligned} \frac{1}{n_1^2} \left[ (1 - R_1^{12}) \varphi_d^{(1)}(\mathbf{r}) - R_2^{12} \left( \frac{1}{\mu_{tr}^{(1)}} \frac{\partial \varphi^{(1)}(\mathbf{r})}{\partial z} - Q'(\mathbf{r}) \right) \right] \\ = -\frac{1}{n_2^2} \left[ (1 - R_1^{21}) \varphi_d^{(2)}(\mathbf{r}) - R_2^{21} \left( \frac{1}{\mu_{tr}^{(2)}} \frac{\partial \varphi^{(2)}(\mathbf{r})}{\partial z} - Q'(\mathbf{r}) \right) \right] \end{aligned} \quad (4.71)$$

This equation with Equation (4.68) provides the two boundary conditions at an interface. If  $n_1 = n_2$  then  $R_2^{12} = R_2^{21} = 0$ .

### 4.3 Dimensionless form of the diffusion equation

All optical properties heretofore have been expressed in terms of dimensional parameters. This is useful for emphasizing the underlying physics of the derivation of the boundary conditions and the diffusion equation. However this notation is cumbersome and simplification is possible with the use of non-dimensional quantities. The three non-dimensional constants are the modified albedo  $a'$ , the modified optical depth  $\tau'$ , and the modified anisotropy factor  $g'$ . This section expresses  $\tau'$  and  $a'$  in terms of the absorption coefficient  $\mu_a$ , the scattering coefficient  $\mu_s$ , the delta-Eddington parameter  $f$ , and the tissue thickness  $d$ .

The usual definitions for the optical depth  $\tau$  and albedo  $a$  are independent of the phase function characterizing the medium.

$$a = \frac{\mu_s}{\mu_s + \mu_a} \quad \text{and} \quad \tau = (\mu_a + \mu_s)d \quad (4.72)$$

However, the modified optical depth  $\tau'$  and modified albedo  $a'$  are specific to the delta-Eddington approximation and depend on the delta-Eddington phase function. These modified quantities depend on reduced scattering coefficients

based on the delta-Eddington phase function:

$$P_{\text{delta-E}}(\cos \theta) = \frac{1}{4\pi} \{2f\delta(1 - \cos \theta) + (1 - f)(1 + 3g' \cos \theta)\} \quad (4.73)$$

The reduced scattering coefficient is defined as  $\mu'_s = \mu_s(1 - f)$  (Section 4.1). The modified albedo and modified optical depth are

$$a' = \frac{\mu'_s}{\mu'_s + \mu_a} = \frac{(1 - f)a}{1 - af} \quad \text{and} \quad \tau' = (\mu_a + \mu_s)d = (1 - af)\tau \quad (4.74)$$

The inverse equations are

$$a = \frac{a'}{1 - f + a'f} \quad \text{and} \quad \tau = \left(1 + \frac{a'f}{1 - f}\right) \tau'$$

The diffusion Equation is (A4.21),

$$\nabla^2 \varphi_d(\mathbf{r}) - 3\mu'_{tr}\mu_a \varphi_d(\mathbf{r}) = S(\mathbf{r}) \quad (4.75)$$

and the source function  $S(r)$  is

$$S(\mathbf{r}) = -3\mu'_s(\mu'_{tr} + \mu'_t g')(1 - r_s)\pi F_0(r) \exp(-\mu'_t z/\mu_0) \quad (4.76)$$

The boundary conditions for mismatched indices of refraction between the slab and its non-scattering environment are given by Equation (4.45) for the top surface

$$\varphi_d(\mathbf{r}) - A_{\text{top}} h \frac{\partial \varphi_d(\mathbf{r})}{\partial z} = -A_{\text{top}} Q(\mathbf{r}) \quad \text{at} \quad z = 0$$

and Equation (4.49) for the bottom surface

$$\varphi_d(\mathbf{r}) + A_{\text{bottom}} h \frac{\partial \varphi_d(\mathbf{r})}{\partial z} = A_{\text{bottom}} Q(\mathbf{r}) \quad \text{at} \quad z = d$$

The parameter  $h$  and the function  $Q(r)$  are defined by Equation (4.46).

$$h = \frac{2}{3\mu'_{tr}} \quad \text{and} \quad Q(\mathbf{r}) = 3hg'\mu'_s\pi F_0(r) \exp(-\mu'_t z/\mu_0)(1 - r_s)$$

The variables  $A_{\text{top}}$  and  $A_{\text{bottom}}$  incorporate internal reflection of light and depend only on the index of refraction of the slab (Section 4.2.3).

Converting Equation (4.75) to non-dimensional quantities, requires replacement of the cylindrical coordinates  $z$  and  $r$  by non-dimensional variables  $\zeta = z(\mu'_s + \mu_a)$  and  $\rho = r(\mu'_s + \mu_a)$ . The cylindrically symmetric form of the diffusion Equation (4.75) becomes

$$\frac{\partial^2 \varphi_d(\mathbf{r})}{\partial \zeta^2} + \frac{1}{\rho} \frac{\partial \varphi_d(\mathbf{r})}{\partial \rho} + \frac{\partial^2 \varphi_d(\mathbf{r})}{\partial \rho^2} - 3(1 - a')(1 - a'g')\varphi_d(\mathbf{r}) = S(\mathbf{r}) \quad (4.77)$$

The source term (4.76) is then

$$S(\mathbf{r}) = 3(1 - r_s)a'[1 + g'(1 - a')]\pi F_0(\rho) \exp(-\zeta/\mu_0) \quad (4.78)$$

The boundary conditions remain the same, with  $h$  replaced by  $h'$  and  $Q(r)$  by  $Q'(r)$

$$\varphi_d(\mathbf{r}) - A_{\text{top}}h' \frac{\partial \varphi_d(\mathbf{r})}{\partial \zeta} = -A_{\text{top}}Q'(\mathbf{r}) \quad \text{at} \quad \zeta = 0 \quad (4.79)$$

for the top surface and

$$\varphi_d(\mathbf{r}) + A_{\text{bottom}}h' \frac{\partial \varphi_d(\mathbf{r})}{\partial \zeta} = A_{\text{bottom}}Q'(\mathbf{r}) \quad \text{at} \quad \zeta = d(\mu_a + \mu'_s) \quad (4.80)$$

for the bottom surface. The parameters  $h'$  and  $Q'(r)$  are given by

$$h' = \frac{2}{3(1 - g'a')} \quad \text{and} \quad Q'(\mathbf{r}) = 3h'g'a'\pi F_0(\rho) \exp(-\zeta/\mu_0)\mu_0(1 - r_s) \quad (4.81)$$

Rearranging Equation (4.18) to express the diffuse radiant flux in terms of the average diffuse radiance  $d$  yields the following equation

$$\mathbf{F}_d(\mathbf{r}) = -\frac{1}{3\mu'_{tr}} \nabla \varphi_d(\mathbf{r}) + \frac{g'\mu'_s}{\mu'_{tr}} (1 - r_s)\pi F_0(\rho) \exp(-\zeta/\mu_0)\mu_0 \hat{\mathbf{z}} \quad (4.82)$$

In dimensionless parameters this is

$$\mathbf{F}_d(\mathbf{r}) = -\frac{h'}{2} \frac{\partial \varphi_d(\mathbf{r})}{\partial \rho} \hat{\mathbf{r}} - \frac{h'}{2} \left[ \frac{\partial \varphi_d(\mathbf{r})}{\partial \zeta} - 3g'a'(1 - r_s)\pi F_0(\rho)\mu_0 \exp(-\zeta/\mu_0) \right] \hat{\mathbf{z}} \quad (4.83)$$

## 4.4 Solution of the one-dimensional diffusion equation

The one-dimensional diffusion Equation (4.75), in dimensionless units, is

$$\frac{d^2\varphi_d(\zeta)}{d\zeta^2} - \kappa_d^2\varphi_d(\zeta) = S(\zeta) \quad (4.84)$$

where the source  $S(\zeta)$  and  $\kappa_d^2$  are given by

$$\begin{aligned} S(\zeta) &= -3a'[1 + g'(1 - a)](1 - r_s)\pi F_0 \exp(-\zeta/\mu_0) \\ \kappa_d^2 &= 3(1 - a')(1 - g'a') \end{aligned} \quad (4.85)$$

The solution of Equation (4.84) is the sum of a particular solution and a homogeneous solution,

$$\varphi_d(\zeta) = \varphi_d^{homo}(\zeta) + \varphi_d^{part}(\zeta) \quad (4.86)$$

The particular solution has the form

$$\begin{aligned} \varphi_d^{part}(\zeta) &= c_3 \exp(-\zeta/\mu_0) \\ c_3 &= \frac{-3\mu_0^2}{1 - \kappa_d^2\mu_0^2} a'[1 + g'(1 - a)](1 - r_s)\pi F_0 \end{aligned} \quad (4.87)$$

The homogeneous solution depends on the albedo of the slab. Solutions for various cases are given in the following subsections.

### 4.4.1 Non-conservative scattering ( $a' < 1$ ), finite slab

The homogeneous solution is (when the albedo is not equal to one)

$$\varphi_d^{homo}(\zeta) = c_1 \exp(\kappa_d\zeta) + c_2 \exp(-\kappa_d\zeta) \quad (4.88)$$

where  $c_1$  and  $c_2$  depend on the boundary conditions. The complete solution is

$$\varphi_d^{part}(\zeta) = \varphi_d^{homo}(\zeta) + \varphi_d^{part}(\zeta) = c_1 \exp(\kappa_d\zeta) + c_2 \exp(-\kappa_d\zeta) + c_3 \exp(-\zeta/\mu_0) \quad (4.89)$$

Where  $c_3$  is given by Equation (4.87). The boundary conditions at the top surface and bottom surfaces are given by Equations (4.79) and (4.80)

$$\varphi_d(\zeta) - A_{\text{top}}h' \frac{d\varphi_d(\zeta)}{d\zeta} = -A_{\text{top}}Q'(\zeta) \quad \text{at} \quad \zeta = 0 \quad (4.90)$$

$$\varphi_d(\zeta) + A_{\text{bottom}}h' \frac{d\varphi_d(\zeta)}{d\zeta} = A_{\text{bottom}}Q'(\zeta) \quad \text{at} \quad \zeta = \tau' \quad (4.91)$$

The parameter  $h'$  and  $Q'(\zeta)$  are given by Equation (4.81)

$$h' = \frac{2}{3(1-g'a')} \quad \text{and} \quad Q'(\zeta) = 3h'g'a'\pi F_0(\rho) \exp(-\zeta/\mu_0)\mu_0(1-r_s) \quad (4.92)$$

Substituting Equation (4.89) into boundary condition (4.90) yields

$$c_1(1 - A_{\text{top}}h'\kappa_d) + c_2(1 + A_{\text{top}}h'\kappa_d) = -A_{\text{top}}Q'(0) - c_3 \left[ 1 + \frac{A_{\text{top}}h'}{\mu_0} \right] \quad (4.93)$$

Substituting Equation (4.89) into boundary condition (4.91) yields

$$\begin{aligned} \exp(-\kappa_d\tau') \left[ c_1(1 + A_{\text{bottom}}h'\kappa_d) + c_2(1 - A_{\text{bottom}}h'\kappa_d) \right] = & \quad (4.94) \\ \exp(-\tau'/\mu_0) \left\{ A_{\text{bottom}}Q'(0) - c_3 \left[ 1 - \frac{A_{\text{bottom}}h'}{\mu_0} \right] \right\} & \end{aligned}$$

Equations (4.93) and (4.95) are two linear equations with constant coefficients in the two unknowns  $c_1$  and  $c_2$ . These equations are easily solved using determinants.

#### 4.4.2 Non-conservative scattering ( $a' < 1$ ), semi-infinite slab

When the thickness of the slab is infinite then to ensure the solution (4.89) is bounded at infinity,

$$c_1 = 0 \quad (4.95)$$

The other coefficient  $c_2$  may be determined using the boundary condition (4.90)

$$c_2 = -\frac{A_{\text{top}}Q'(0) + c_3(1 + A_{\text{top}}h'/\mu_0)}{1 + A_{\text{top}}h'\kappa_d} \quad (4.96)$$

Equations (4.95) and (4.98) define the homogeneous solution to the diffusion equation for a semi-infinite slab with non-conservative scattering.

#### 4.4.3 Conservative scattering $a = 1$ , finite slab

When the albedo is unity, then the differential Equation (4.84) becomes

$$\frac{d^2\varphi_d(\zeta)}{d\zeta^2} = S(\zeta) \quad (4.97)$$

The homogeneous solution is

$$\varphi_d^{hom}(\zeta) = c_1 + c_2\zeta \quad (4.98)$$

and the particular solution is given by Equation (4.87) as with  $a' = 1$ . The constants  $c_1$  and  $c_2$  are determined using the boundary conditions (4.90) and (4.91)

$$c_1 - A_{top}h'c_2 = -A_{top}Q'(0) - c_3(1 + A_{top}h'/\mu_0) \quad (4.99)$$

and

$$c_1 + c_2(\tau' + A_{bottom}h') = \{A_{bottom}Q'(0) - c_3(1 - A_{bottom}h'/\mu_0)\} \exp(-\tau'/\mu_0) \quad (4.100)$$

Equations (4.99) and (4.100) are two linear equations in the two unknowns  $c_1$  and  $c_2$ . These coefficients determine the homogeneous solution for a finite slab with conservative scattering.

#### 4.4.4 Conservative scattering ( $a = 1$ ), semi-infinite slab

If the slab is semi-infinite, the diffuse average radiance must be bounded as  $\zeta \rightarrow \infty$ . Hence

$$c_2 = 0 \quad (4.101)$$



The other constant  $c_1$  is determined using the boundary condition (4.90)

$$c_1 = -A_{\text{top}}Q'(0) - c_3(1 + A_{\text{top}}h'/\mu_0) \quad (4.102)$$

Equations (4.101) and (4.102) determine the solution for a semi-infinite slab with conservative scattering.

## 4.5 Reflection, transmission, and fluence rates in one-dimension

The diffuse radiant flux per unit area is given by Equation (4.83)

$$\mathbf{F}_d(\mathbf{r}) = -\frac{h'}{2} \frac{\partial \varphi_d(\mathbf{r})}{\partial \rho} \hat{\mathbf{r}} - \frac{h'}{2} \left[ \frac{\partial \varphi_d(\mathbf{r})}{\partial \zeta} - 3g'a'(1 - r_s)\pi F_0(\rho)\mu_0 \exp(-\zeta/\mu_0) \right] \hat{\mathbf{z}}$$

Projecting the above equation into the  $z$ -direction yields

$$\mathbf{F}_d(\zeta) \cdot \hat{\mathbf{z}} = -\frac{h'}{2} \left[ \frac{d\varphi_d(\mathbf{r})}{d\zeta} - 3g'a'(1 - r_s)\pi F_0(\rho)\mu_0 \exp(-\zeta/\mu_0)\mu_0 \right] \quad (4.103)$$

where  $h'$  is defined by Equation (4.81). This represents the net fluence at a depth  $\zeta$ . The average diffuse radiance for a non-conservative finite medium is given by Equation (4.89).

$$\varphi_d^{\text{part}}(\zeta) = c_1 \exp(\kappa_d \zeta) + c_2 \exp(-\kappa_d \zeta) + c_3 \exp(-\zeta/\mu_0) \quad (4.104)$$

The derivative of  $\varphi_d(\zeta)$  is

$$\frac{d\varphi_d^{\text{part}}(\zeta)}{d\zeta} = \kappa_d c_1 \exp(\kappa_d \zeta) - \kappa_d c_2 \exp(-\kappa_d \zeta) - c_3/\mu_0 \exp(-\zeta/\mu_0) \quad (4.105)$$

Substituting these expressions into Equation (4.103) and dividing by the total incident intensity yields the diffuse reflection and diffuse transmission. The expressions for the diffuse reflection and diffuse transmission are

$$R_d = \frac{-\mathbf{F}_d(\zeta) \cdot \hat{\mathbf{z}}}{(1 - r_s)\pi F_0 \mu_0} \Big|_{\zeta=0} \quad \text{and} \quad T_d = \frac{\mathbf{F}_d(\zeta) \cdot \hat{\mathbf{z}}}{(1 - r_s)\pi F_0 \mu_0} \Big|_{\zeta=\tau'} \quad (4.106)$$

Substituting (4.103)–(4.105) into (4.106) yields

$$R_d = - \left[ \frac{h'}{2\pi F_0 \mu_0} (\kappa_d c_2 - \kappa_d c_1 + c_3/\mu_0) + \frac{3}{2} h' g' a' (1 - r_s) \right]$$

Similarly, the transmission is

$$\begin{aligned} T_d &= \frac{h'}{2\pi F_0 \mu_0} [\kappa_d c_2 \exp(-\kappa_d \tau') + \kappa_d c_1 \exp(\kappa_d \tau') + c_3/\mu_0 \exp(-\tau'/\mu_0)] \\ &+ \frac{3}{2} h' g' a' (1 - r_s) \exp(-\tau'/\mu_0) \end{aligned}$$

The equations are the diffuse reflection and diffuse transmission for a slab illuminated uniformly by collimated light. The coefficients  $c_1$ ,  $c_2$  and  $c_3$  are given in Section 4.4. The source term for heating, or the local volumetric absorption rate is [26]

$$\Phi(\zeta) = -\frac{dF_d}{dz} - \mu_0 \frac{dF_{\text{coll}}}{dz} \quad (4.107)$$

The collimated flux is given by Equation (4.13)

$$\mathbf{F}_{\text{coll}}(\mathbf{r}) = \int_{4\pi} L_{\text{coll}}(\mathbf{r}, \hat{\mathbf{s}}') \hat{\mathbf{s}}' d\omega'$$

The collimated radiance  $L_{\text{coll}}(\mathbf{r}, \hat{\mathbf{s}})$  is defined by Equation (4.10), and the collimated flux is

$$F_{\text{coll}} = \mu_0 (1 - r_s) \pi F_0 \exp(-\zeta'/\mu_0)$$

Taking the derivative of  $F_{\text{coll}}$  above and substituting Equation (4.17) for the diffuse flux in Equation (4.107) results in

$$\Phi(\zeta) = \mu_a [\phi_c(\zeta) + \mu_0 (1 - r_s) \pi F_0 \exp(-\zeta/\mu_0)] \quad (4.108)$$

This is the one-dimensional source function for light absorbed at a depth  $\zeta$  in a slab.

## 4.6 Three-dimensional solution of the diffusion equation

The next few subsections detail a three-dimensional solution to the diffusion equation. The first part gives a formal solution in terms of a Green's function for the diffusion equation. The next section gives the Green's function for a slab bounded by non-scattering media. The last section gives explicit expressions for the solutions to the diffusion equation for various irradiation profiles.

### 4.6.1 Formal solution of $\phi_d(\mathbf{r})$ in terms of Green's functions

Define  $\phi_d(r)$  as a solution to the inhomogeneous Helmholtz equation (Equation (4.77))

$$\nabla^2 \phi_d(\mathbf{r}) - \kappa_d^2 \phi_d(\mathbf{r}) = S(\mathbf{r}) \quad (4.109)$$

where

$$S(\mathbf{r}) = S_0 \pi F_0(\rho) \exp(-\zeta) \quad S_0 = -3(1 - r_s) a' (1 + g' - a' g')$$

and

$$\kappa_d^2 = 3(1 - a')(1 - a' g')$$

subject to the following inhomogeneous mixed boundary conditions

$$\phi_d(\mathbf{r}) - A_{\text{top}} h' \frac{\partial \phi_d(\mathbf{r})}{\partial \zeta} = -A_{\text{top}} Q'(\mathbf{r}) \quad \text{at} \quad \zeta = 0 \quad (4.110)$$

and

$$\phi_d(\mathbf{r}) + A_{\text{bottom}} h' \frac{\partial \phi_d(\mathbf{r})}{\partial \zeta} = A_{\text{bottom}} Q'(\mathbf{r}) \quad \text{at} \quad \zeta = \tau' \quad (4.111)$$

with

$$Q'(\mathbf{r}) = Q_0 \pi F_0(\rho) \exp(-\zeta) \quad Q_0 = 3h' a' g' (1 - r_s)$$

Let  $G(\mathbf{r}; \mathbf{r}')$  be a Green's function solution to the *homogeneous* Helmholtz equation

$$\nabla^2 G(\mathbf{r}; \mathbf{r}') - \kappa_d^2 G(\mathbf{r}; \mathbf{r}') = -\delta(\mathbf{r} - \mathbf{r}') \quad (4.112)$$

subject to the following *homogeneous* mixed boundary conditions

$$G(\mathbf{r}; \mathbf{r}') - A_{\text{top}} h' \frac{\partial G(\mathbf{r}; \mathbf{r}')}{\partial \zeta} = 0 \quad \text{at} \quad \zeta = 0 \quad (4.113)$$

$$G(\mathbf{r}; \mathbf{r}') + A_{\text{bottom}} h' \frac{\partial G(\mathbf{r}; \mathbf{r}')}{\partial \zeta} = 0 \quad \text{at} \quad \zeta = \tau' \quad (4.114)$$

The solution to Equations (4.109)–(4.111) can be found using Green's second identity [51],

$$\int_{\text{volume}} (u \nabla^2 v - v \nabla^2 u) dV = \int_{\text{surface}} \left( u \frac{\partial v}{\partial n} - v \frac{\partial u}{\partial n} \right) dS \quad (4.115)$$

Where  $\mathbf{n}$  is the outward normal to the surface enclosing the volume of integration on the left hand side of the equation. If  $u = G(\mathbf{r}; \mathbf{r}')$  and  $v = \phi_d(\mathbf{r})$ , then Equation (4.115) becomes

$$\begin{aligned} \int_{\text{volume}} \left( G(\mathbf{r}; \mathbf{r}') \nabla^2 \phi_d(\mathbf{r}') - \phi_d(\mathbf{r}') \nabla^2 G(\mathbf{r}; \mathbf{r}') \right) dV' = \\ \int_{\text{surface}} \left( G(\mathbf{r}; \mathbf{r}') \frac{\partial \phi_d(\mathbf{r}')}{\partial n} - \phi_d(\mathbf{r}') \frac{\partial G(\mathbf{r}; \mathbf{r}')}{\partial n} \right) dS' \end{aligned} \quad (4.116)$$

Adding and subtracting  $G(\mathbf{r}; \mathbf{r}') \kappa_d^2 \phi_d(\mathbf{r})$  to the left hand side of Equation (4.116) yields

$$\begin{aligned} \text{L.H.S.} &= \int_{\text{volume}} \left( G(\mathbf{r}; \mathbf{r}') [\nabla^2 \phi_d(\mathbf{r}') - \kappa_d^2 \phi_d(\mathbf{r}')] \right. \\ &\quad \left. - \phi_d(\mathbf{r}') [\nabla^2 G(\mathbf{r}; \mathbf{r}') - \kappa_d^2 G(\mathbf{r}; \mathbf{r}')] \right) dV' \end{aligned} \quad (4.117)$$

Using Equations (4.109) and (4.112) to simplify the bracketed quantities reduces the LHS to

$$\text{L.H.S.} = \int_{\text{volume}} G(\mathbf{r}; \mathbf{r}') S(\mathbf{r}') dV' - \phi_d(\mathbf{r}) \quad (4.118)$$

The surface integral on the right hand side of Equation (4.115) can be rewritten with the stipulation that on the top surface of the slab

$$\frac{\partial}{\partial n} = -\frac{\partial}{\partial \zeta'} \quad (4.119)$$

and on the bottom surface

$$\frac{\partial}{\partial n} = \frac{\partial}{\partial \zeta'} \quad (4.120)$$

because  $\zeta$  increases with depth in the slab and  $\mathbf{n}$  is an outward normal to the slab. Upon substitution of Equations (4.119) and (4.120) into the R.H.S. of Equation (4.116),

$$\begin{aligned} \text{R.H.S.} = & - \int_{\zeta'=0} \left( G(\mathbf{r}; \mathbf{r}') \frac{\partial \varphi_d(\mathbf{r}')}{\partial \zeta'} - \varphi_d(\mathbf{r}') \frac{\partial G(\mathbf{r}; \mathbf{r}')}{\partial \zeta'} \right) dS' \\ & + \int_{\zeta'=\tau'} \left( G(\mathbf{r}; \mathbf{r}') \frac{\partial \varphi_d(\mathbf{r}')}{\partial \zeta'} - \varphi_d(\mathbf{r}') \frac{\partial G(\mathbf{r}; \mathbf{r}')}{\partial \zeta'} \right) dS' \end{aligned} \quad (4.121)$$

This equation simplifies using the boundary conditions (4.110),(4.111),(4.113) and (4.114)

$$\text{R.H.S.} = \frac{1}{h'} \int_{\zeta'=\tau'} G(\mathbf{r}; \mathbf{r}') Q'(\mathbf{r}') dS' - \frac{1}{h'} \int_{\zeta'=0} G(\mathbf{r}; \mathbf{r}') Q'(\mathbf{r}') dS' \quad (4.122)$$

Equating Equations (4.118) and (4.122) results in an expression for  $\phi_d(\mathbf{r})$  in terms of the Green's function  $G(\mathbf{r}; \mathbf{r}')$

$$\begin{aligned} \varphi_d(\mathbf{r}) = & - \int_{\text{volume}} G(\mathbf{r}; \mathbf{r}') S(\mathbf{r}') dV' + \frac{1}{h'} \int_{\zeta'=\tau'} G(\mathbf{r}; \mathbf{r}') Q'(\mathbf{r}') dS' \\ & - \frac{1}{h'} \int_{\zeta'=0} G(\mathbf{r}; \mathbf{r}') Q'(\mathbf{r}') dS' \end{aligned} \quad (4.123)$$

The volume integral accounts for the inhomogeneous (source) term in the Helmholtz Equation (4.109), and the last two integrals arise from inhomogeneous boundary conditions at the top and bottom surfaces of the slab.

#### 4.6.2 The Green's Function for an Infinite Slab

The Green's function in the cylindrical coordinate system with  $\mathbf{r}$  and  $\mathbf{r}'$  expressed in  $(\rho, \phi, \zeta)$  coordinates [50] is

$$G(\mathbf{r}; \mathbf{r}') = \sum_{n=1}^{\infty} \frac{Z_n(\zeta)Z_n(\zeta')}{2\pi N_n^2} \begin{cases} K_0(\lambda_n \rho)I_0(\lambda_n \rho') & \text{if } \rho \geq \rho'; \\ K_0(\lambda_n \rho')I_0(\lambda_n \rho) & \text{if } \rho \leq \rho'. \end{cases} \quad (4.124)$$

where  $K_0$  and  $I_0$  are modified Bessel functions and  $Z_n(\zeta)$  is an eigenfunction satisfying the differential Equation (4.112)

$$Z_n(\zeta) = \sin(k_n \zeta + \gamma_n) \quad (4.125)$$

The eigenvalue  $\gamma_n$  is obtained by substituting the Green's function into the boundary condition at  $\zeta = 0$

$$\tan \gamma_n = A_{\text{top}} h' k_n \quad (4.126)$$

The eigenvalue  $k_n$  is obtained imposing the boundary condition (4.114) at  $\zeta = \tau'$

$$\tan(k_n \tau' + \gamma_n) = A_{\text{bottom}} h' k_n \quad (4.127)$$

Using (4.126) and the sum of angles expansion for the tangent simplifies Equation (4.127)

$$\tan k_n \tau' = \frac{(A_{\text{top}} + A_{\text{bottom}})h' k_n}{A_{\text{top}} A_{\text{bottom}} (h'^2 k_n)^2 - 1} \quad (4.128)$$

Evaluation of the roots  $k_n$  of this equation are discussed in Appendix A4. The normalization factor  $N_n^2$  is given by

$$N_n^2 = \int_0^{\tau'} [z_n(\zeta)]^2 d\zeta \quad (4.129)$$

Substituting (4.125) and simplifying,

$$N_n^2 = \frac{\sin 2\gamma_n - \sin 2(k_n \tau' + \gamma_n) + 2k_n \tau'}{4k_n} \quad (4.130)$$

Finally, substituting the Green's function (4.124) into the diffusion Equation (4.112) results in a relation between  $\lambda_n$  and  $\kappa_n$

$$\lambda_n^2 = k_n^2 + \kappa_d^2 \quad (4.131)$$

### 4.6.3 Explicit Expressions for $\phi_d(\mathbf{r})$

The solution to the diffusion equation is given by Equation (4.123). Substituting the Green's function (4.124) from the previous subsection into the volume integral on the R.H.S. of Equation (4.123) yields

$$\int_{\text{volume}} G(\mathbf{r}; \mathbf{r}') S(\mathbf{r}') dV' = \sum_{n=1}^{\infty} \frac{S_0 \sin(k_n \zeta + \gamma_n)}{N_n^2} \frac{z_n}{k_n^2 + 1} \frac{B_n(\rho)}{\lambda_n^2} \quad (4.132)$$

where  $z_n$  is given by

$$\begin{aligned} z_n &= \sin \gamma_n [1 + \exp(-\tau') (k_n \sin k_n \tau' - \cos k_n \tau')] \\ &\quad \cos \gamma_n [k_n + \exp(-\tau') (\sin k_n \tau' + k_n \cos k_n \tau')] \end{aligned} \quad (4.133)$$

and the radial term  $B_n(\rho)$  is defined as

$$\begin{aligned} B_n(\rho) &= K_0(\lambda_n \rho) \int_0^\rho \pi \phi F_0(\rho') I_0(\lambda_n \rho') (\lambda_n \rho') d(\lambda_n \rho') \\ &\quad + I_0(\lambda_n \rho) \int_\rho^\infty \pi F_0(\rho') K_0(\lambda_n \rho') (\lambda_n \rho') d(\lambda_n \rho') \end{aligned} \quad (4.134)$$

The radial term depends on the source irradiance. If the source represents a beam of finite width ( $\rho_0$ ) with constant irradiance then [50]

$$B_n(\rho) = \begin{cases} \pi F_0 [1 - \lambda_n \rho_0 I_0(\lambda_n \rho) K_1(\lambda_n \rho_0)] & \text{if } \rho \leq \rho_0; \\ \pi F_0 [\lambda_n \rho_0 K_0(\lambda_n \rho) I_1(\lambda_n \rho_0)] & \text{if } \rho \geq \rho_0. \end{cases} \quad (4.135)$$

The special case of constant uniform irradiance is achieved by letting  $\rho_0 \rightarrow \infty$ .

Since  $K_1(\lambda_n \rho_0) \rightarrow 0$  as  $\rho_0 \rightarrow \infty$ , Equation (4.135) becomes

$$B_n(\rho) = \pi F_0 \quad (4.136)$$

The radial term for an impulse (delta function) located at the origin is

$$B_n(\rho) = \pi F_0 K_0(\lambda_n \rho) \quad (4.137)$$

A beam with a Gaussian irradiance profile having a  $e^{-2}$  radius of  $\rho_0$  requires that the radial term  $B_n(\rho)$  be calculated numerically using Equation (4.135) with

$$\pi F_0(\rho) = \pi F_0 \sqrt{\frac{8}{\pi}} \frac{\exp(-2\rho^2/\rho_0^2)}{\rho_0} \quad (4.138)$$

The surface integrals in Equation (4.123) describe the contribution from the top surface due to reflected light,

$$\int_{\zeta'=0} G(\mathbf{r}; \mathbf{r}') Q'(\mathbf{r}') dS' = \sum_{n=1}^{\infty} \frac{Q_0 \sin(k_n \zeta + \gamma_n) \sin \gamma_n B_n(\rho)}{N_n^2 \lambda_n^2} \quad (4.139)$$

the contribution from the bottom integral is

$$\int_{\zeta'=\tau'} G(\mathbf{r}; \mathbf{r}') Q'(\mathbf{r}') dS' = \sum_{n=1}^{\infty} \frac{Q_0 \sin(k_n \zeta + \gamma_n) \sin(k_n \tau' + \gamma_n) B_n(\rho) \exp(-\tau')}{N_n^2 \lambda_n^2} \quad (4.140)$$

Collecting Equations (4.132), (4.139), and (4.140) yields

$$\varphi_d(\mathbf{r}) = \sum_{n=1}^{\infty} \frac{\sin(k_n \zeta + \gamma_n) B_n(\rho)}{N_n^2 \lambda_n^2} \left[ -\frac{S_0 z_n}{k_n^2 + 1} - \frac{Q_0 \sin \gamma_n}{h'} + \frac{Q_0 \sin(k_n \tau' + \gamma_n) \exp(-\tau')}{h'} \right] \quad (4.141)$$

The derivative of  $\phi_d(\mathbf{r})$  with respect to  $\zeta$  is

$$\frac{\partial \varphi_d(\mathbf{r})}{\partial \zeta} = \sum_{n=1}^{\infty} \frac{k_n \cos(k_n \zeta + \gamma_n) B_n(\rho)}{N_n^2 \lambda_n^2} \left[ -\frac{S_0 z_n}{k_n^2 + 1} - \frac{Q_0 \sin \gamma_n}{h'} + \frac{Q_0 \sin(k_n \tau' + \gamma_n) \exp(-\tau')}{h'} \right] \quad (4.142)$$

The derivative of  $\phi_d(\mathbf{r})$  with respect to  $\rho$  is

$$\frac{\partial \varphi_d(\mathbf{r})}{\partial \rho} = \sum_{n=1}^{\infty} \frac{\sin(k_n \zeta + \gamma_n)}{N_n^2 \lambda_n^2} \frac{\partial B_n(\rho)}{\partial \rho} \left[ -\frac{S_0 z_n}{k_n^2 + 1} - \frac{Q_0 \sin \gamma_n}{h'} + \frac{Q_0 \sin(k_n \tau' + \gamma_n) \exp(-\tau')}{h'} \right] \quad (4.143)$$

Numerical summations of these series are detailed in Appendix A4.



#### 4.6.4 Flux, Reflection, and Transmission in Three Dimensions

The flux at a point  $\mathbf{r}$  is given by Equation (4.83)

$$\mathbf{F}_d(\mathbf{r}) = -\frac{h'}{2} \frac{\partial \phi_d(\mathbf{r})}{\partial \rho} \hat{\mathbf{r}} - \frac{h'}{2} \left[ \frac{\partial \phi_d(\mathbf{r})}{\partial \zeta} - 3g'a'(1-r_s)\pi F_0(\rho)\mu_0 \exp(-\zeta/\mu_0) \right] \hat{\mathbf{z}}$$

Equations (4.142) and (4.143) provide representations for the partial derivatives of  $\phi_d(\mathbf{r})$  needed to calculate the flux. If  $\pi F_0$  is the total power density incident on the slab then the diffuse reflectance and transmission are given by Equation (4.106) with the understanding that these are a function of radius.

### 4.7 Evaluation of the Delta-Eddington Approximation

This section compares solutions of the delta-Eddington approximation with accurate adding-doubling and Monte Carlo solutions. Heretofore comparisons have been for the index matched case, where the delta-Eddington approximation was found to agree with exact solutions for all optical depths, albedos and anisotropies [34]. This section makes comparisons for mismatched boundary conditions because of the large differences possible between fluence rates for identical tissues with different boundary conditions (cf., Figure 4.1). The following sections emphasize comparisons with an air-glass-tissue-glass-air medium. Total reflection and transmission are compared in the first subsection. This is followed by a comparison of the fluence rates for a one-dimensional slab.

#### 4.7.1 Comparison of total reflection and transmission

Tables (4.1) and (4.2) compare delta-Eddington values of total reflection and total transmission with the exact values from Tables 3.3–3.6. The first table assumes index matching and the second assumes that the medium is bounded by

glass slides to form a air-glass-tissue-glass-air medium. For this case the indices of refraction vary as 1.0/1.5/1.4/1.5/1.0 according to the layer in the air-glass-tissue-glass-air medium. The errors for the index mismatched case are roughly twice those of the index matched case. Both absolute differences and relative errors are tabulated. This is because often when the reflection or transmission is small, there is a relatively large difference between the delta-Eddington and the exact values. However, the difference is so small that for all practical purposes the difference cannot be measured.

#### 4.7.2 Comparison of Fluence Rates

This section compares the delta-Eddington fluence rates with exact values obtained from the adding-doubling method. The radiances were calculated using Equations (3.17) and (3.18) and the fluence rates were obtained by integrating the radiances over all  $4\pi$  solid angles. The delta-Eddington approximation consistently underestimates the fluence rate found with the adding-doubling method.

In Figure 4.1 the boundary conditions are varied to determine how the index of the refraction of the medium affects fluence calculations. The delta-Eddington approximation works best for index matched conditions, because no approximation must be made to account for total internal reflection of light at the boundary.

The total fluence is the sum of collimated and diffuse fluences. The collimated fluence dominates when the albedo is small. This explains Figure 4.2 in which the delta-Eddington approximation is better for low than for high albedos. Figure 4.3 illustrates that the delta-Eddington approximation is better for isotropic scattering than anisotropic scattering. In this graph, the Henyey-

$g$	$a$	$\tau$	$\Delta R$	$100\frac{\Delta R}{R}$	$\Delta T$	$100\frac{\Delta T}{T}$
0	0.6	1	0.010	7.5	0.011	2.3
0	0.6	2	0.011	7.0	0.007	3.3
0	0.6	4	0.010	6.5	-0.000	-0.7
0	0.6	8	0.010	6.5	-0.000	-18.1
0	0.9	1	0.005	1.9	0.010	1.6
0	0.9	2	0.009	2.5	0.011	3.2
0	0.9	4	0.011	2.7	0.004	3.4
0	0.9	8	0.011	2.7	-0.000	-2.5
0	0.99	1	-0.002	-0.6	0.004	0.6
0	0.99	2	-0.002	-0.4	0.006	1.2
0	0.99	4	0.001	0.2	0.004	1.4
0	0.99	8	0.003	0.5	0.001	1.0
0.5	0.6	1	0.007	13.3	0.006	1.0
0.5	0.6	2	0.007	11.2	0.004	1.5
0.5	0.6	4	0.007	9.6	-0.001	-0.8
0.5	0.6	8	0.007	9.5	-0.001	-14.8
0.5	0.9	1	0.006	4.7	0.005	0.7
0.5	0.9	2	0.008	4.1	0.011	2.0
0.5	0.9	4	0.011	4.0	0.008	3.4
0.5	0.9	8	0.011	3.9	0.000	0.0
0.5	0.99	1	0.001	0.9	0.000	0.0
0.5	0.99	2	-0.001	-0.2	0.004	0.7
0.5	0.99	4	-0.000	-0.0	0.006	1.4
0.5	0.99	8	0.004	0.6	0.003	1.4
0.875	0.6	1	0.002	20.6	-0.001	-0.1
0.875	0.6	2	0.001	12.2	-0.002	-0.5
0.875	0.6	4	0.001	6.1	-0.002	-1.4
0.875	0.6	8	0.001	5.5	-0.000	-2.3
0.875	0.9	1	0.004	17.1	-0.002	-0.2
0.875	0.9	2	0.006	15.1	-0.001	-0.2
0.875	0.9	4	0.008	11.5	0.002	0.3
0.875	0.9	8	0.007	8.6	0.003	1.4
0.875	0.99	1	0.004	12.6	-0.004	-0.4
0.875	0.99	2	0.006	8.9	-0.005	-0.5
0.875	0.99	4	0.007	4.9	-0.003	-0.3
0.875	0.99	8	0.005	2.0	0.006	0.9

Table 4.1: Delta-Eddington errors for an index matched medium. The  $\Delta R$  and  $\Delta T$  values are the differences between the delta-Eddington and the exact values.

$g$	$a$	$\tau$	$\Delta R$	$100\frac{\Delta R}{R}$	$\Delta T$	$100\frac{\Delta T}{T}$
0	0.6	1	0.022	20.4	0.018	4.5
0	0.6	2	0.017	15.7	0.005	3.0
0	0.6	4	0.016	14.6	-0.002	-5.2
0	0.6	8	0.016	14.6	-0	-27.8
0	0.9	1	0.028	12	0.022	4.3
0	0.9	2	0.029	10.8	0.012	4.1
0	0.9	4	0.027	9.5	0	0.2
0	0.9	8	0.026	9.2	-0.001	-8.7
0	0.99	1	0.004	1.3	-0.002	-0.3
0	0.99	2	0.012	2.7	-0.004	-0.8
0	0.99	4	0.016	3	-0.005	-1.6
0	0.99	8	0.015	2.4	-0.003	-1.8
0.5	0.6	1	0.017	21.6	0.013	2.8
0.5	0.6	2	0.012	16.5	0.004	1.8
0.5	0.6	4	0.011	15.4	-0.002	-3.6
0.5	0.6	8	0.011	15.4	-0.001	-21.0
0.5	0.9	1	0.025	15.3	0.021	3.5
0.5	0.9	2	0.025	13.6	0.017	4.2
0.5	0.9	4	0.023	12.3	0.003	1.7
0.5	0.9	8	0.022	11.7	-0.002	-6.0
0.5	0.99	1	0.003	1.3	-0.001	-0.1
0.5	0.99	2	0.008	2.4	0	0.0
0.5	0.99	4	0.016	3.8	-0.003	-0.7
0.5	0.99	8	0.017	3.5	-0.003	-1.4
0.875	0.6	1	0.006	10.2	-0.003	-0.5
0.875	0.6	2	0.003	6.7	-0.005	-1.4
0.875	0.6	4	0.002	4.5	-0.003	-2.3
0.875	0.6	8	0.002	4.9	-0.0	-1.9
0.875	0.9	1	0.019	21.1	0.002	0.3
0.875	0.9	2	0.020	21.1	0.003	0.5
0.875	0.9	4	0.014	15.6	0.006	1.5
0.875	0.9	8	0.011	13.2	0.003	1.9
0.875	0.99	1	0.012	9.1	-0.009	-1.0
0.875	0.99	2	0.014	8.2	-0.006	-0.8
0.875	0.99	4	0.012	5.2	0.005	0.8
0.875	0.99	8	0.015	5.2	0.012	2.5

Table 4.2: Delta-Eddington errors for an air-glass-tissue-glass-air medium. The  $\Delta R$  and  $\Delta T$  values are the differences between the delta-Eddington and exact values.

Greenstein phase function is used with  $g_{\text{HG}} = 0.875$ . The equivalent delta-Eddington parameters ( $g' = 0.47$ ,  $f = 0.77$ ) can be calculated using Equations (1.4) and (1.5). The effective thickness  $\tau'$  of the sample is 0.97. Consequently, the diffusion region is not reached in the strongly forward scattering media in four mean free paths ( $\tau = 4$ )

## 4.8 Conclusions

This chapter solved the diffusion equation for mismatched boundary conditions. Comparison of the approximate delta-Eddington solutions with adding-doubling calculations indicates that delta-Eddington approximation works well for calculations of reflection and transmission. It works moderately well for many fluence rate calculations, but should not be used to calculate fluence rates in tissues with high albedos and mismatched boundary conditions.

Depth	Matched			Unmatched		
	Exact	Diffusion	Error	Exact	Diffusion	Error
0.000	1.307	1.297	-0.7	2.866	2.191	-23.6
0.125	1.364	1.314	-3.7	2.872	2.210	-23.0
0.250	1.401	1.329	-5.1	2.878	2.228	-22.6
0.375	1.429	1.343	-6.0	2.883	2.244	-22.2
0.500	1.453	1.355	-6.7	2.889	2.259	-21.8
0.625	1.473	1.366	-7.3	2.894	2.273	-21.5
0.750	1.490	1.375	-7.7	2.899	2.284	-21.2
0.875	1.504	1.382	-8.1	2.904	2.295	-21.0
1.000	1.516	1.388	-8.4	2.908	2.304	-20.8
1.125	1.526	1.393	-8.7	2.912	2.312	-20.6
1.250	1.533	1.397	-8.9	2.916	2.319	-20.5
1.375	1.538	1.399	-9.1	2.920	2.325	-20.4
1.500	1.542	1.400	-9.2	2.924	2.329	-20.3
1.625	1.543	1.400	-9.3	2.927	2.333	-20.3
1.750	1.543	1.398	-9.4	2.930	2.335	-20.3
1.875	1.541	1.396	-9.4	2.933	2.337	-20.3
2.000	1.537	1.392	-9.4	2.936	2.337	-20.4
2.125	1.532	1.388	-9.4	2.938	2.337	-20.5
2.250	1.524	1.382	-9.3	2.941	2.335	-20.6
2.375	1.515	1.376	-9.2	2.943	2.333	-20.7
2.500	1.505	1.368	-9.1	2.945	2.330	-20.9
2.625	1.492	1.360	-8.9	2.947	2.326	-21.1
2.750	1.478	1.351	-8.6	2.950	2.321	-21.3
2.875	1.462	1.341	-8.3	2.952	2.315	-21.6
3.000	1.444	1.330	-7.9	2.955	2.309	-21.9
3.125	1.424	1.318	-7.4	2.957	2.302	-22.2
3.250	1.402	1.305	-6.9	2.960	2.294	-22.5
3.375	1.377	1.292	-6.2	2.963	2.286	-22.9
3.500	1.349	1.278	-5.3	2.967	2.277	-23.3
3.625	1.318	1.263	-4.2	2.971	2.267	-23.7
3.750	1.281	1.248	-2.6	2.975	2.257	-24.1
3.875	1.236	1.232	-0.3	2.980	2.246	-24.6
4.000	1.162	1.215	4.6	2.985	2.234	-25.2

Table 4.3: Percent errors in the delta-Eddington fluence rates. Both sets of data assume that  $g_{\text{HG}} = 0.875$ ,  $a = 0.99$ , and an optical depth of 4.0. The unmatched data corresponds to an air-glass-tissue-glass-air medium which has indices of refraction 1.0/1.5/1.4/1.5/1.0. Delta-Eddington is more accurate for matched boundaries.

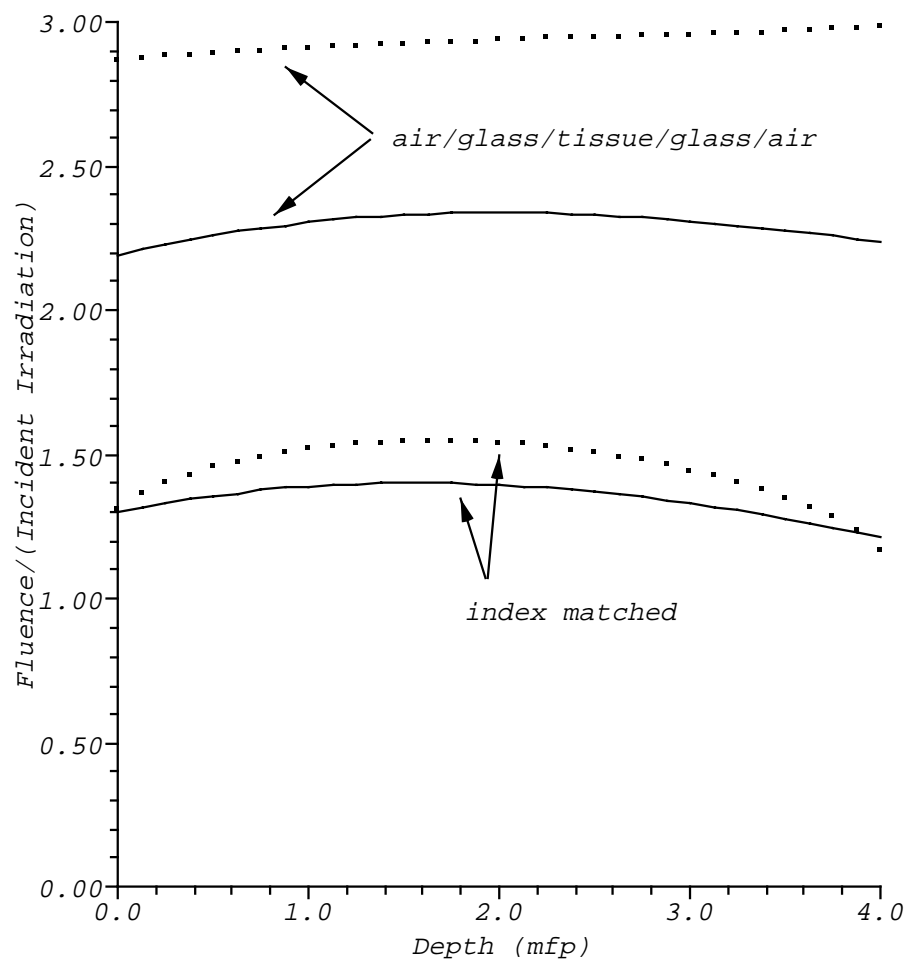


Figure 4.1: Comparison of delta-Eddington (solid lines) and adding-doubling (squares) fluence rates. The optical properties are  $g_{\text{HG}} = 0.875$ ,  $a = 0.99$ , and an optical depth of 4.0. The upper curves for an air-glass-tissue-glass-air medium have indices of refraction 1.0/1.5/1.4/1.5/1.0.

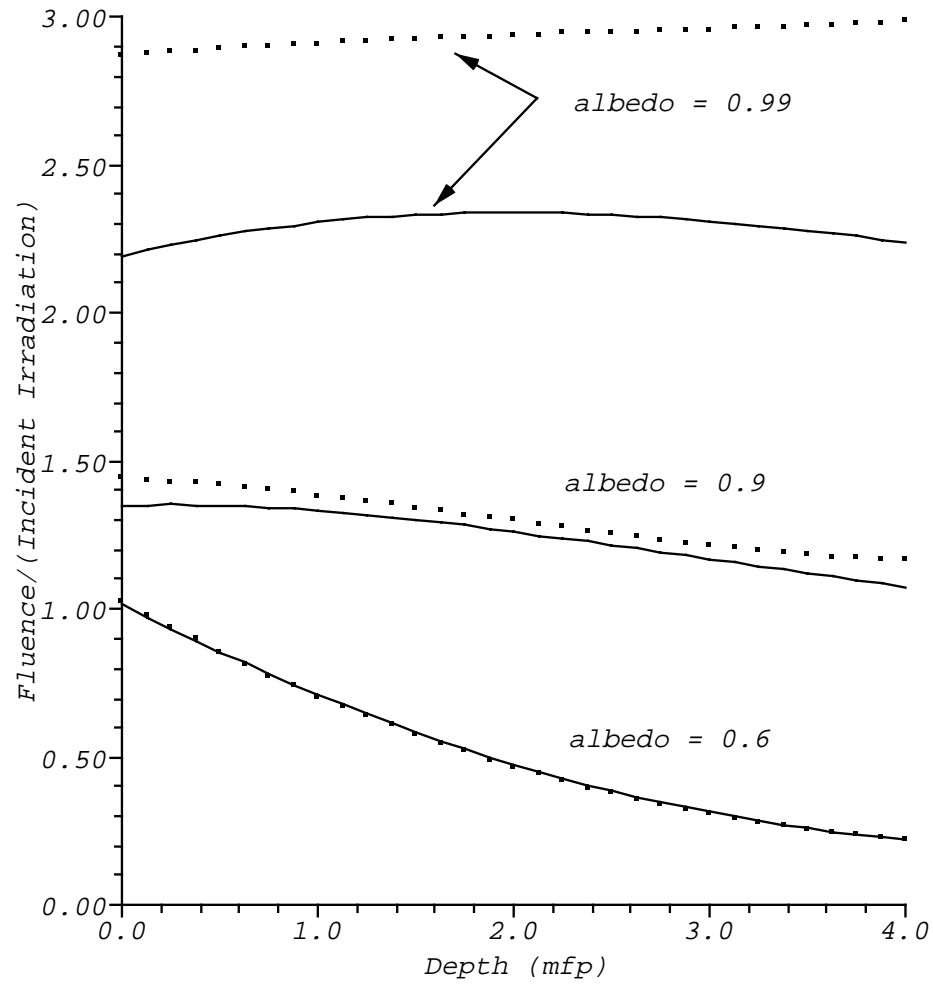


Figure 4.2: Comparison of delta-Eddington (solid lines) and adding-doubling (squares) fluence rates. The optical properties are  $g_{\text{HG}} = 0.875$ ,  $\tau = 4$ , and an air-glass-tissue-glass-air medium with indices of refractions 1.0/1.5/1.4/1.5/1.0. Differences between the two methods decrease with decreasing albedo.



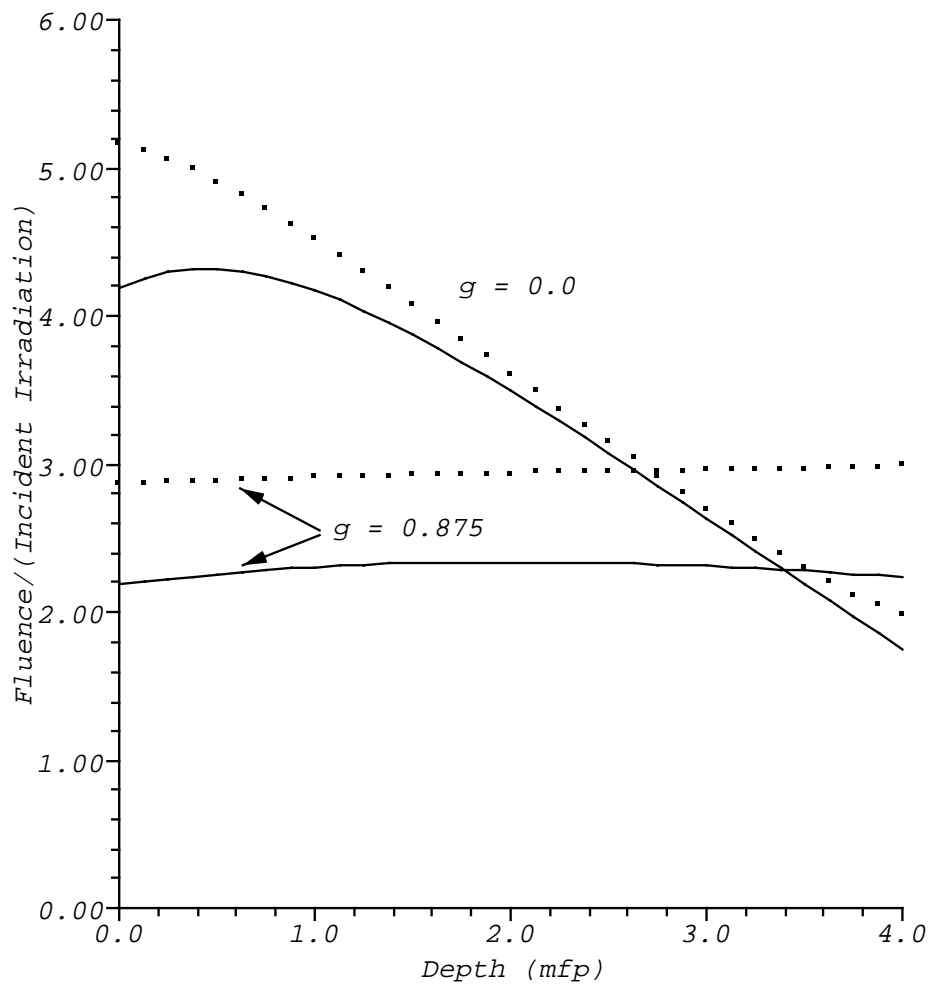


Figure 4.3: Comparison of delta-Eddington (solid lines) and adding-doubling (squares) fluence rates. Both sets of lines assume  $a = 0.99$ ,  $\tau = 4$ , and an air-glass-tissue-glass-air medium with indices of refraction 1.0/1.5/1.4/1.5/1.0.

# Chapter 5

## Goniophotometry

### Introduction

Goniophotometry is the measurement of light intensity as a function of angle. Only a few goniophotometer measurements on tissue have been published [5, 12, 32]. None of these presents a theoretical framework in which goniophotometer measurements may be analyzed. In this chapter, a method for measuring the phase function characterizing light scattering in tissue is presented. The method requires optically thin ( $\tau \ll 1$ ) tissue samples to ensure the validity of the single scattering approximation. Because multiple scattering is avoided, there is a simple functional relationship between the phase function and measurements of reflection and transmission as a function of angle.

In Section 5.1, the functional dependence of reflected and transmitted light on the phase function is developed. In Section 5.2, a description of a device to measure reflected and transmitted light as a function of angle (a goniophotometer) is presented. In Section 5.3 the experimental method used to measure reflected and transmitted light is outlined. Section 5.4 introduces the necessary corrections to convert measured data into reflection and transmission values for use with the theory in Section 5.1. Section 5.5 shows how the experimental measurements of the phase function may be fitted to a modified Henyey-Greenstein

phase function using a least squares algorithm. Section 5.6 presents experimental results for normal human dermis.

## 5.1 Single scattering approximation

From Chapter 3, the first order scattering and transmission functions for uniform normal incidence on a slab of thickness  $\tau$  are given by Equations (3.30)–(3.34)

$$\begin{aligned} R(1, -\mu) &= \frac{a\mu p(1, -\mu)}{1 + \mu} [1 - \exp(-\tau/\mu - \tau)] \\ T(1, \mu) &= \frac{a\mu p(1, \mu)}{1 - \mu} [\exp(-\tau) - \exp(-\tau/\mu)] \\ T(1, 1) &= (a\tau p(1, 1) + 1) \exp(-\tau) \end{aligned} \quad (5.1)$$

where  $a$  is the albedo,  $\tau$  is the optical thickness of the sample,  $\mu$  is the cosine of the angle that light exiting with the normal to the sample, and  $p(1, \mu)$  is the phase function. Equations (5.1) have been multiplied by  $2\pi$  to remove the integration over azimuthal angles and divided by  $2\mu$  to remove the factor of  $2\mu$  that was included to satisfy the star multiplication algebra. The redistribution function  $h(\mu_0, \mu)$  can be replaced by the phase function because the cosine of the angle of incidence is unity (see Equation (3.24)).

Henceforth the phase function  $p(1, \mu)$  will be written  $p(\mu)$ . It is assumed that the phase function is independent of azimuthal angle (implicit in the multiplication by  $2\pi$  above) and that  $p(\mu)$  is a complete description of the phase function. No azimuthal dependence was observed in any experiments. Equations (5.1) are exact for uniform normal illumination and are a good approximation only when the width of the incident beam is much larger than the thickness of the slab. Since typical beam diameters are about 1.0 mm and the tissue samples used are approximately 0.020–0.100 mm in thickness this assumption is reasonable.

If the exponentials in Equations (5.1) are expanded in a Taylor series then

$$\begin{aligned}
 R(1, -\mu) &= a\tau p(-\mu) \left[ 1 - \frac{\tau(1+\mu)}{2\mu} + \dots \right] \\
 T(1, \mu) &= a\tau p(\mu) \left[ 1 - \frac{\tau(1+\mu)}{2\mu} + \dots \right] \\
 T(1, 1) &= (a\tau p(1, 1) + 1) \left[ 1 - \tau + \frac{\tau^2}{2} - \dots \right]
 \end{aligned} \tag{5.2}$$

The factor of  $a\tau$  indicates that the amount of scattered light is directly proportional to the product of the optical thickness and the albedo (the fraction of light scattered to the total amount of light scattered and absorbed). Alternatively,  $a\tau = \mu_s d$  ( $d$  is the sample thickness) indicates that the reflected and transmitted light is directly proportional to the amount of light scattered. If the phase function is isotropic,  $p(\mu, \mu') = 1/4\pi$ , then reflection and transmission are equal and independent of the angle of exitance. These equations show the direct correspondence between the phase function and the reflected and transmitted light for very thin slabs ( $t \ll 1$ ).

Unfortunately, there are always angles  $\mu$  such that  $\tau/\mu$  is not small and the above approximation is invalid. These angles correspond to reflection or transmission at angles nearly parallel to the slab. If the multiplicative factor required to convert reflection and transmission into a phase function value are denoted by  $c_R$  and  $c_T$  respectively then

$$p(-\mu) = c_R R(1, -\mu) \quad \text{and} \quad p(\mu) = c_T T(1, \mu) \tag{5.3}$$

where

$$c_R = \frac{1+\mu}{a\mu} [1 - \exp(-\tau/\mu - \tau)]^{-1} \tag{5.4}$$

$$c_T = \frac{1 - \mu}{a\mu} [\exp(-\tau) - \exp(-\tau/\mu)]^{-1}$$

Equations (5.4) are plotted in Figure 5.1 for an optical thickness and albedo of unity. The correction factor is largest for light exiting at grazing angles and the measurement error at these angles will be magnified accordingly. Consequently, the phase function data at these angles will be least reliable. However, the correction factor is nearly constant for angles up to  $30^\circ$  from the normal and at these angles the light exiting the slab is nearly proportional to the phase function.

## 5.2 Experimental apparatus

The goniophotometer used at Wellman Laboratory is shown in Figure 5.2. The interior of the tank was painted flat black and filled with saline to minimize internal reflections from the box and within the sample. A helium-neon laser delivered a 1 mW beam normal to the sample which was sandwiched between glass microscope slides. The beam diameter was 1 mm. The 3 mm diameter detecting fiber located at the end of an 8.5 cm long arm was attached to a computer-controlled stepping motor. The stepping motor made  $1.8^\circ$  steps throughout a full  $360^\circ$  circle. A 1.17 mm aperture was placed over the end of the detecting fiber to increase the resolution of the goniophotometer. Light collected by the fiber was measured with a photomultiplier tube whose output was connected to the computer.

The angular resolution ( $\alpha_{\text{resolution}}$ ) of the goniophotometer depends on several different factors: the width of the detector ( $W_{\text{detector}}$ ), the acceptance angle of the detector ( $\alpha_{\text{acceptance}}$ ), the width of the beam on the sample ( $W_{\text{beam}}$ ),

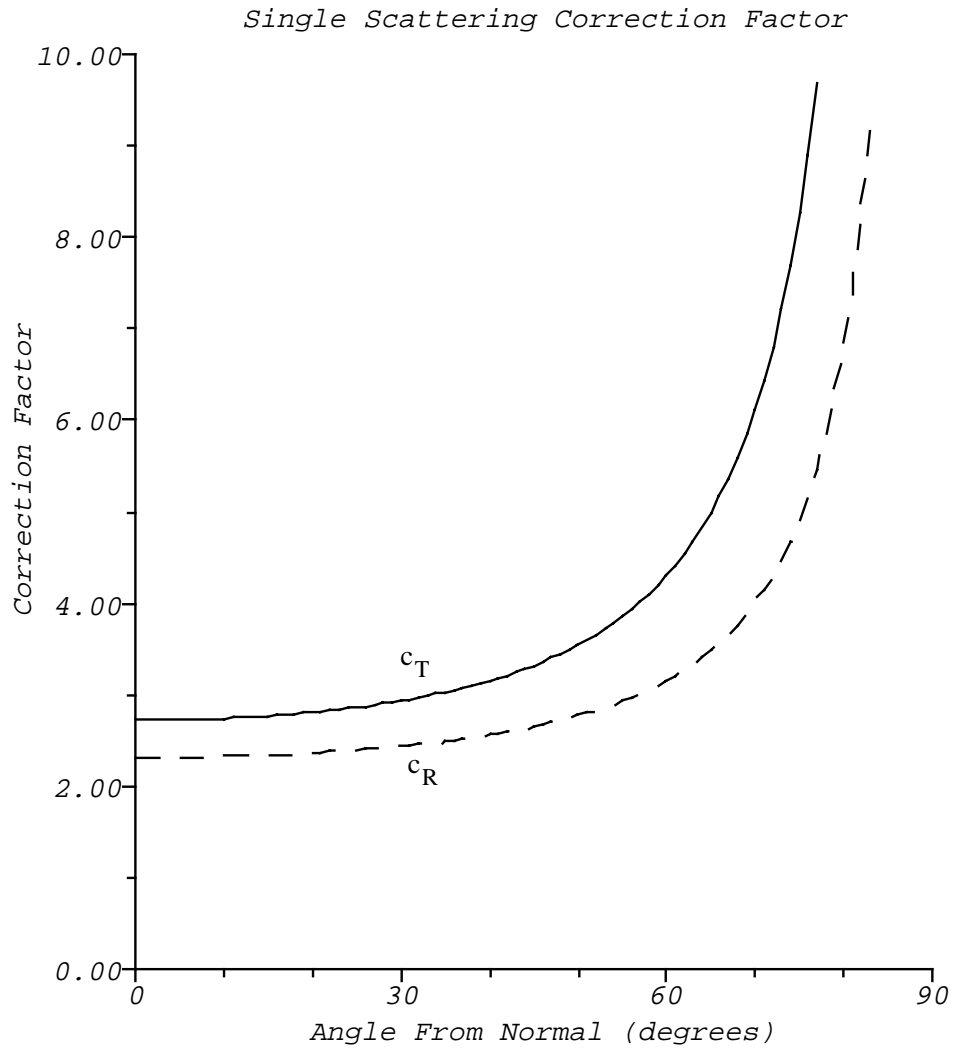


Figure 5.1: Correction factor as a function of angle required to convert measurements of reflection and transmission into phase function measurements. These correction factors are for an optical depth of unity and an albedo of one-half. The solid line is the correction factor required for transmitted light and the dashed line is that needed for reflected light.

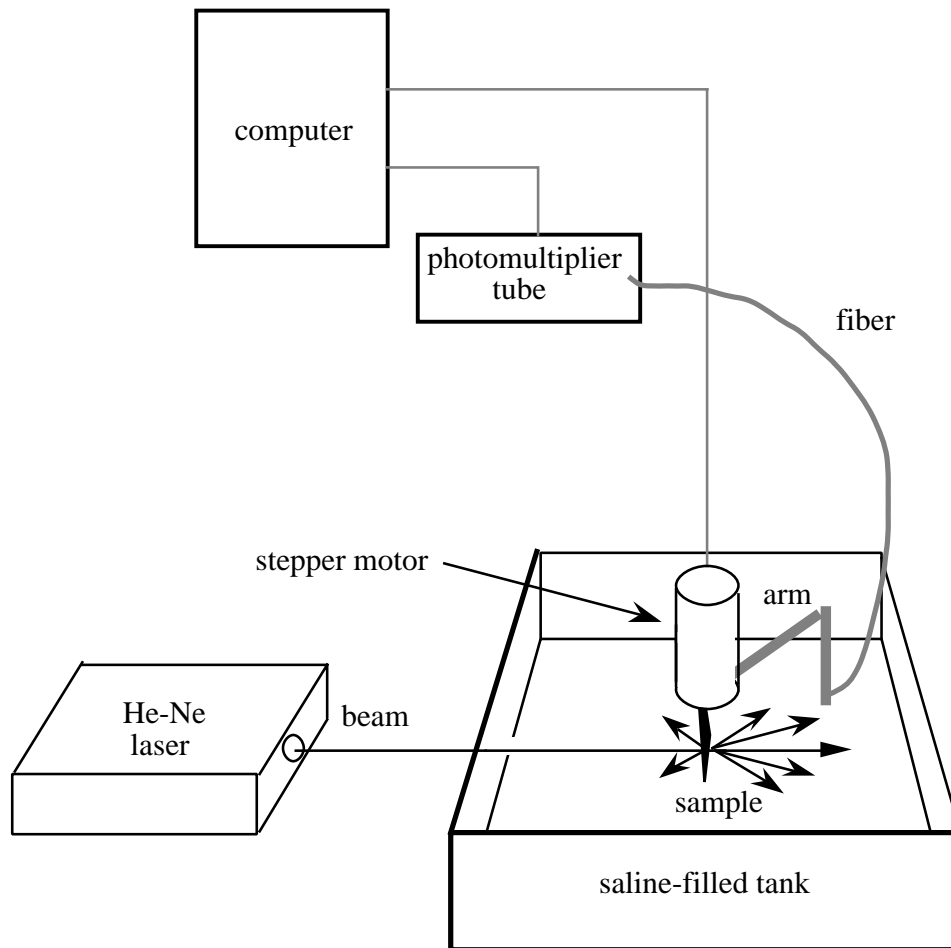


Figure 5.2: The goniophotometer apparatus. Helium-neon laser light enters the saline filled tank through a glass port on the side. The light strikes the sample and is scattered. The light is detected by a fiber attached to an arm driven by a computer controlled stepper motor. The fiber is connected to a photomultiplier tube which is monitored by a computer.

and the distance from the sample to the detector ( $D$ ). The angle subtended by the beam is approximately (Figure 5.3A)

$$\alpha_{\text{spot}} = \frac{W_{\text{beam}}}{D} \quad (5.5)$$

Any light leaving the sample at angles larger than this will not reach the detector. The angle subtended by the detector is approximately (Figure 5.3B)

$$\alpha_{\text{detector}} = \frac{W_{\text{detector}}}{D} \quad (5.6)$$

Again any light leaving the sample at angles larger than this will not reach the detector. The angular resolution of the goniophotometer is usually determined by the larger of  $\alpha_{\text{beam}}$  and  $\alpha_{\text{detector}}$  since the acceptance angle of the detector is usually much larger than the other angles. Thus, the larger of diameters of the beam and the detector determine the resolution of the goniophotometer. The angular resolution of the goniophotometer used for these experiments was about  $0.8^\circ$ .

### 5.3 Tissue preparation

Skin was obtained from the abdomen at autopsy. The epidermis was manually separated following mild thermal treatment (two minute exposure in a  $55^\circ\text{C}$  water bath) which avoids thermal denaturation of dermal collagen. The dermal sample was frozen. The dermis was cut two different ways: (1) with a cold dermatome to yield dermal sections 200–400 microns in thickness and (2) with a freezing microtome to obtain 20 micron thick samples from 6 millimeter diameter punch biopsies. Both the dermatome and the freezing microtome made cuts parallel to the surface of the dermis. Dermatome specimens from five subjects



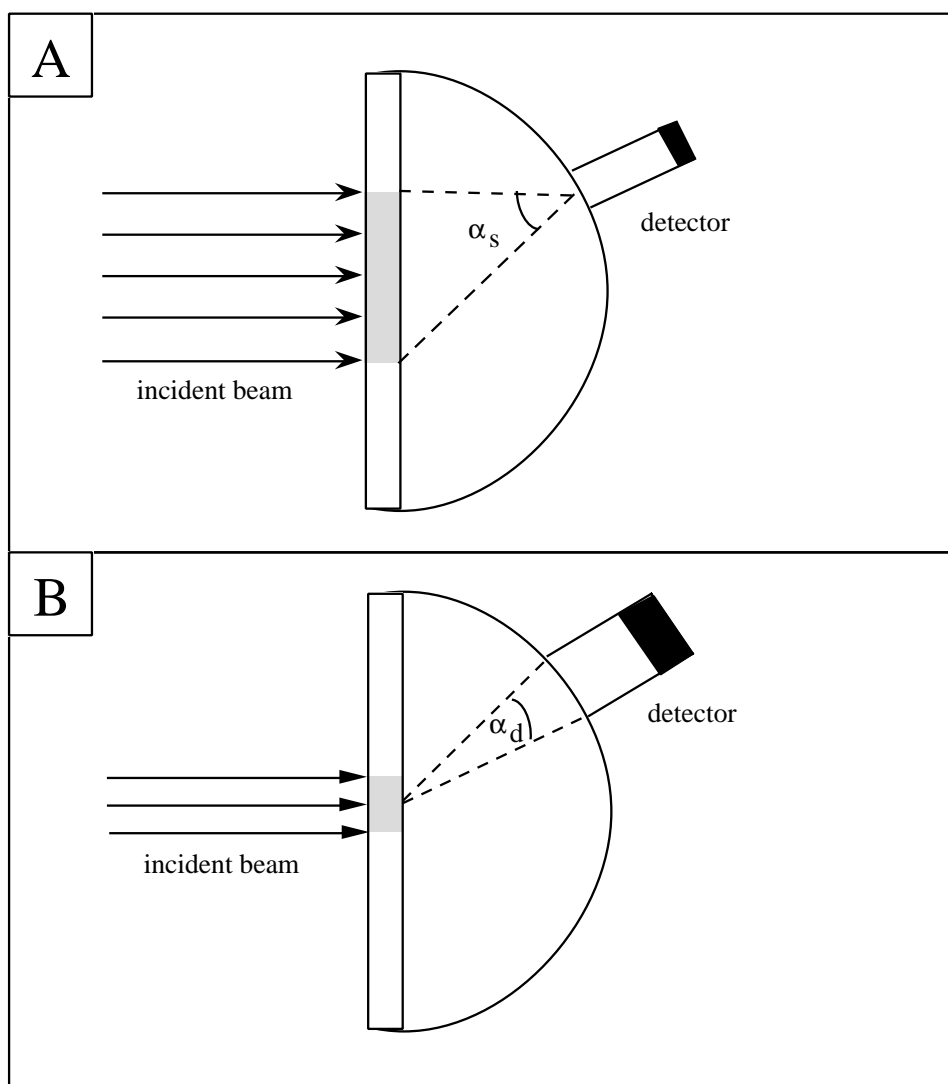


Figure 5.3: Angular resolution of the goniophotometer is determined by the relative size of the detector and the spot size when the detector is sufficiently far from the sample. This figure defines the angles subtended by the spot and the detector.

were studied with nine measurements at different sites on each specimen. To obtain different very thin sample thicknesses, several 20 micron sections were stacked to obtain 40, 60, 80, and 100 micron samples. Freezing microtome specimens from four subjects were studied: twenty-six 20 micron samples, nine 40 micron samples, four 60 micron samples, four 80 micron samples, and ten 100 micron samples. All samples were soaked in saline prior to measurements to ensure standardized 85% hydrated dermis. All samples were sandwiched between glass microscope slides.

Tissue samples were placed in the center of the tank with the front surface oriented perpendicular to the incident beam. Before each experiment the total beam power was measured. The detector was aligned so that  $0^\circ$  corresponded to an on-axis measurement. An initial on-axis measurement was made. The detector was moved in  $1.8^\circ$  steps clockwise around the sample until it reached the on-axis (co-linear) position again. It was found that for all samples the reproducibility of an entire scan was excellent if the sample was not moved between scans. When the beam was moved to a different location on the sample there was often a substantial change in the measured distribution. This was especially true of thin tissue sections or thick sections that were not uniform in thickness. Nine scans were made on each sample to assess this variability.

## 5.4 Data reduction

The first subsection (5.4.1) describes corrections needed to convert measured quantities to phase function parameters. The second subsection (5.4.2) describes a data transformation that allows the data to be fitted to a modified Henyey-Greenstein equation using a weighted least squares fit.

#### 5.4.1 Corrections for internal reflection and refraction

The tissue samples were held between two glass slides and submerged in saline. Because of the differing indices of refraction, corrections for the reflectance and refraction at the saline-glass-tissue interface were made. The index of refraction of glass ( $n_{\text{glass}}$ ) was measured to be 1.54. The assumed value for index of refraction of 0.9% saline solution ( $n_{\text{saline}}$ ) was 1.33. The index of refraction for tissue ( $n_{\text{tissue}}$ ) was based on the generalization that the index of refraction of a tissue varies linearly between 1.33 to 1.5 for water contents between 100 percent and 0 percent [2]. The index of refraction would vary from 1.38 to 1.36 as water content varies from 70 to 85 percent, and so  $n_{\text{tissue}}$  was chosen to be 1.37.

The specular reflection of the incident beam is given by Equation (A2.21)

$$r(\theta) = \frac{r_1 + r_2 - 2r_1r_2}{1 - r_1r_2} \quad (5.7)$$

with  $\theta = 0^\circ$  and where  $r_1$  is the Fresnel reflection for light passing normal to saline-glass interface and  $r_2$  is the coefficient for light passing from glass to tissue. Using Equation (A2.29) to find  $r_1$  and  $r_2$  yields  $r_1 = 0.0054$ ,  $r_2 = 0.0034$ , and  $r_s = r(0^\circ) = 0.0088$  or a specular reflectance of about 0.9%.

The raw data was subjected to a series of calculation steps to achieve a description of the light that exited the tissue at a given angle  $\theta_{\text{exit}}$  as opposed to the light that was observed at a given angle  $\theta_{\text{obs}}$ .

1. The raw data, recorded as Volts (V) but representing collected power in Watts, was normalized by the direct beam measurement ( $V_{\text{direct}}$ ) to obtain the collected power relative to a one Watt incident beam. Division by  $(1 - r_s)$  corrected for the specular reflectance from the front glass slide as

the incident beam entered the tissue

$$P(\theta_{\text{obs}}) = \frac{V(\theta_{\text{obs}})}{V_{\text{direct}}(1 - r_s)} \quad \text{in Watts} \quad (5.8)$$

2. The collected power was divided by the solid angle of collection of the optical fiber bundle ( $\omega$ ). The solid angle is  $\omega = 4\pi(A_d/4\pi R_g^2)$  steradians where  $A_d$  was the collection area of the fiber bundle and  $R_g$  was the radius of the goniophotometer arm. This calculation yielded the observed radiant intensity  $A(\theta_{\text{obs}})$

$$A(\theta_{\text{obs}}) = \frac{P(\theta_{\text{obs}})}{\omega} \quad \text{in Watts/steradian} \quad (5.9)$$

3. The observed radiant intensity was corrected for the refraction at the tissue-glass-saline interfaces which caused the solid angle to expand as light exited the tissue (the  $n^2$ -Law see Appendix A2).

$$B(\theta_{\text{obs}}) = A(\theta_{\text{obs}}) \frac{\cos(\theta_{\text{exit}})n_{\text{saline}}^2}{\cos(\theta_{\text{obs}})n_{\text{tissue}}^2} \quad \text{in Watts/steradian} \quad (5.10)$$

where  $\theta_{\text{exit}}$  is the angle at which light exits the tissue before refraction

$$n_{\text{tissue}} \sin(\theta_{\text{exit}}) = n_{\text{saline}} \sin(\theta_{\text{obs}}) \quad (5.11)$$

4. The value  $B(\theta_{\text{obs}})$  was corrected for Fresnel reflection at the tissue-glass and glass-saline interfaces, which allowed only a fraction,  $1 - r(\theta)$ , of the light to escape and reach the detector

$$I(\theta_{\text{obs}}) = \frac{B(\theta_{\text{obs}})}{1 - r(\theta_{\text{exit}})} \quad (5.12)$$

where  $r(\theta_{\text{exit}})$  is determined using Equation (5.7) with  $r_1$  equal to the Fresnel reflection for light passing from the tissue to the glass slide and  $r_2$

equal to the reflection for light passing from the glass slide to the saline solution. The value  $I(\theta_{\text{obs}})$  was then attributed to the true angle of exitance from the tissue,  $\theta_{\text{exit}}$  as opposed to the observed angle,  $\theta_{\text{obs}}$ , in consideration of the refraction at the tissue-glass and glass-saline interfaces.

5. Finally, modified correction factors  $c'_R = ac_R$  and  $c'_T = ac_T$  were applied to the reflected and transmitted light respectively. The modified correction factors permitted analysis of the data without knowledge of the albedo characterizing the tissue by allowing the albedo to be lumped with other unknown calibration factors in a multiplicative constant  $g$  described Section 5.4.2. Combining the corrections into one equation yields

$$ap(\theta_{\text{exit}}) = \frac{c'_T V(\theta_{\text{obs}}) \cos(\theta_{\text{exit}}) n_{\text{saline}}^2}{(1\text{Watt}) V_{\text{direct}} (1 - r_s) \omega \cos(\theta_{\text{obs}}) n_{\text{tissue}}^2 (1 - r(\theta_{\text{exit}}))} \quad \text{in } 1/\text{sr} \quad (5.13)$$

where  $c'_T$  should be replaced with  $c'_R$  for reflected angles.

The most significant correction factors are  $c'_R$  and  $c'_T$ . The other corrections are relatively small and only become significant at oblique angles. Figure 5.4 shows the raw goniometric data as a function of the angle measured with the goniophotometer and Figure 5.5 shows the corrected data as a function of the angle that light leaves the tissue before being refracted.

The goniophotometer resolution is 0.005 V which corresponds to an intensity of 0.01 W/sr. This is determined by the A/D conversion unit in the computer. The background noise was comparable to the resolution of the goniophotometer. The error bars in Figure 5.4 have a constant magnitude. In Figure 5.5 the errors in the phase function  $p_{\text{meas}}(\theta_{\text{exit}})$  differ because the correction factor depends on the angle. Data in the ranges  $90 \pm 15^\circ$  and  $-90 \pm 15^\circ$  in Figure

5.5 are absent because light exiting the tissue at these angles is totally internally reflected ( $\theta_{\text{critical}}$  is about  $75^\circ$ ).

#### 5.4.2 Least squares fit

Once the experimental data has been converted into an equivalent phase function measurement  $p_{\text{meas}}$  using Equation (5.13), it must be fit to a phase function. It was found that a modified Henyey-Greenstein phase function

$$p_{\text{m-HG}}(\cos \theta) = \frac{1}{4\pi} \left\{ \beta + (1 - \beta) \frac{1 - g_{\text{HG}}^2}{(1 + g_{\text{HG}}^2 - 2g_{\text{HG}} \cos \theta)^{3/2}} \right\} \quad (5.14)$$

accurately represented the phase function for human dermis. If the albedo for a tissue is unknown, or a correction factor in Equation (5.13) is not known precisely, then it is convenient to include an arbitrary multiplicative factor in the expression for the phase function. If this is done then

$$p_{\text{meas}}(\cos \theta) = \gamma p_{\text{m-HG}}(\cos \theta) \quad \gamma = \frac{1}{4\pi a}$$

The second equality ( $\gamma = 1/4\pi a$ ) is useful only when all factors in Equation (5.13) are known. This is a poor way to measure the albedo of a material because it requires excellent absolute accuracy in the goniometric measurement rather than good relative accuracy. To fit the modified Henyey-Greenstein phase function to the measured phase function three parameters must be determined: the multiplicative factor  $g$ , the amount of light scattered isotropically  $\beta$ , and the anisotropy factor  $g_{\text{HG}}$ .

One of the assumptions in the modified Henyey-Greenstein phase function is that light scattered in the backwards direction (reflected light) is scattered isotropically. Figure 5.5 shows a plot of the corrected data. The light reflected

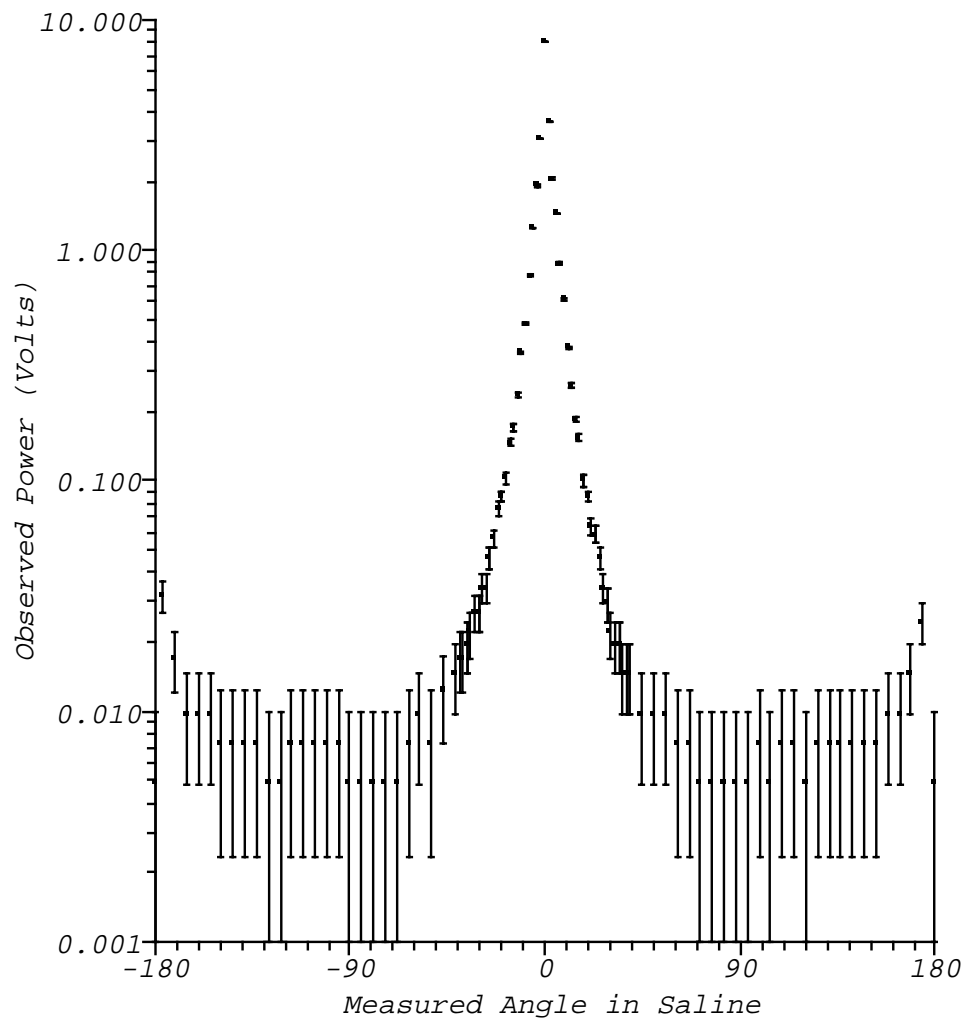


Figure 5.4: Raw goniophotometer data from  $100\ \mu\text{m}$  sample of human dermis. Error bars are constant in magnitude and equal to the resolution of the A/D converter in the computer (0.005 V).

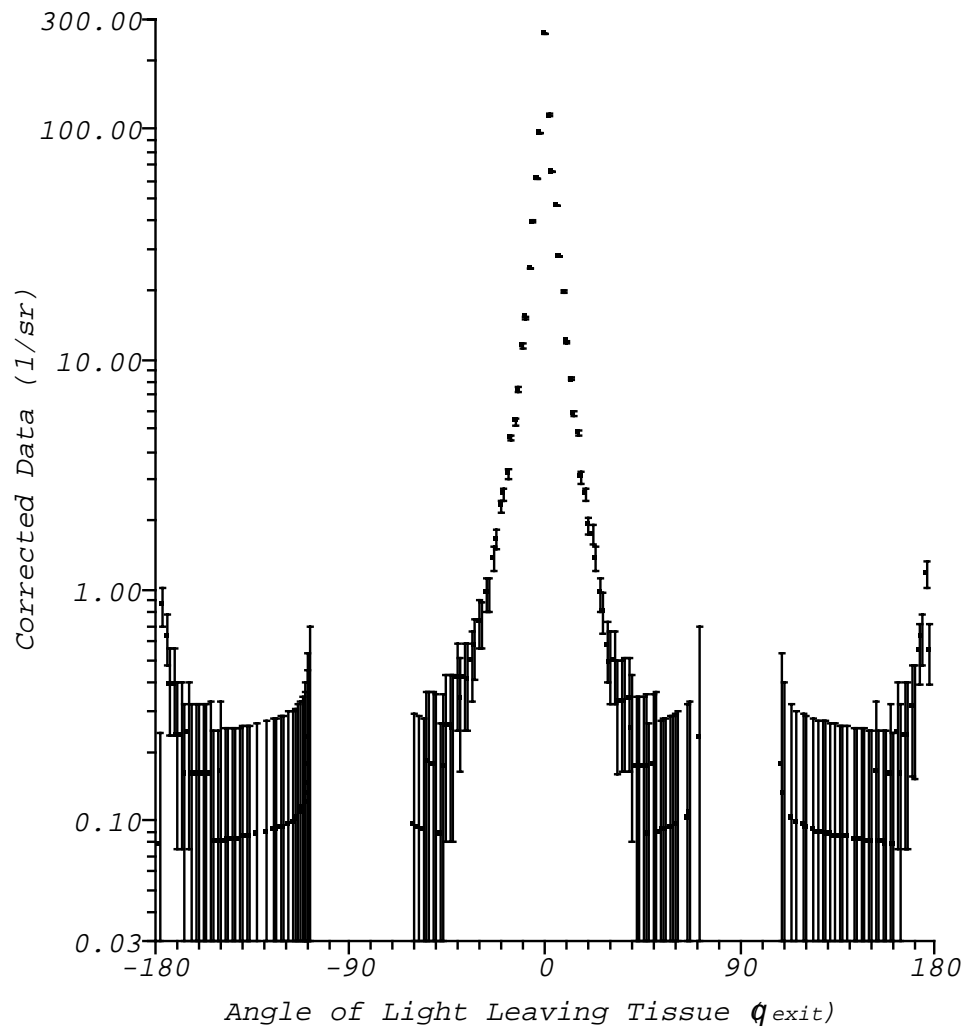


Figure 5.5: Corrected goniophotometer data from a  $100\ \mu\text{m}$  sample of human dermis. Error bars have also been corrected and no longer have a constant magnitude.



is not absolutely isotropic (a flat response) but increases slightly around  $\pm 180^\circ$  due to internal reflectance of the forward peak. Subtraction of this reflected light yields a nearly constant value in the backwards direction. The fraction of light scattered isotropically ( $\gamma\beta$ ) is determined by averaging values for  $p_{\text{meas}}(\theta_{\text{exit}})$  in the backwards direction.

The reflected data provides information for  $\gamma\beta$  and the transmitted data is used to find two more parameters  $g_{\text{HG}}$  and  $\gamma$ . The transformation

$$x = \cos \theta \quad \text{and} \quad y = (p(\theta) - \gamma\beta)^{-2/3} \quad (5.15)$$

reduces the modified Henyey-Greenstein equation into a linear equation of the form  $y = mx + b$ . The slope and intercept are given by

$$m = -\frac{2g_{\text{HG}}}{[\gamma(1-\beta)(1-g_{\text{HG}}^2)]^{2/3}} \quad \text{and} \quad b = \frac{1+g_{\text{HG}}^2}{[\gamma(1-\beta)(1-g_{\text{HG}}^2)]^{2/3}} \quad (5.16)$$

If Equation (5.15) is used to transform the data then a graph similar to Figure 5.4 is obtained. The error values were calculated with a fixed photometric error of 0.005 V in the goniophotometer. The errors in  $p_{\text{meas}}(\theta)$  are roughly proportional to the correction factor shown in Figure 5.2. A weighted least squares fit must be used to find the slope and intercept of the best-fit line because of the widely varying errors between data points. The error in the slope ( $\Delta m$ ) and intercept ( $\Delta b$ ) may also be calculated [4].

The phase function parameters  $\beta$  and  $g_{\text{HG}}$  may be recovered from the slope and intercept by solving Equations (5.16). This results in the following physical expressions for  $g_{\text{HG}}$  and  $\beta$  in terms of the calculated intercept  $b$ , slope  $m$ , and product  $\gamma\beta$

$$g_{\text{HG}} = -\frac{b}{m} - \sqrt{\frac{b^2}{m^2} - 1} \quad (5.17)$$

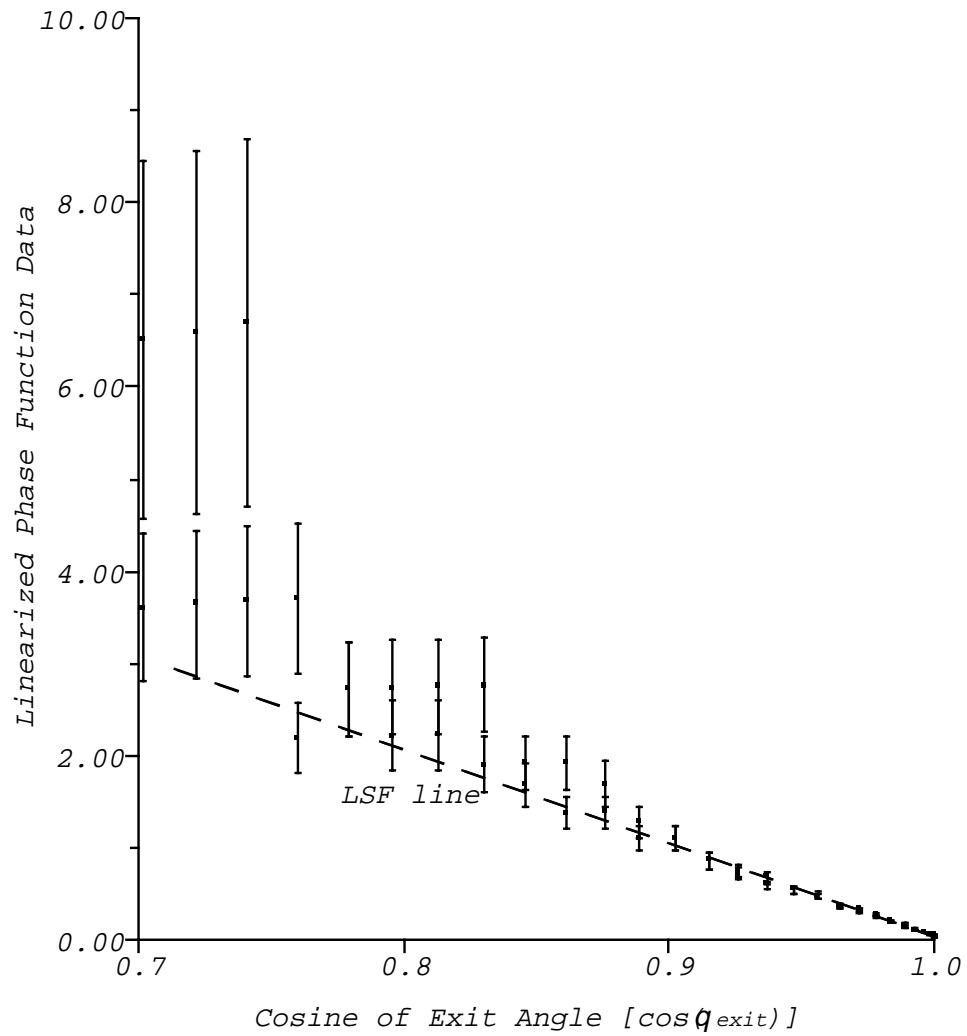


Figure 5.6: Linearized phase function data from 100  $\mu\text{m}$  sample of human dermis showing increasing error for grazing angles (small  $\cos \theta_{\text{exit}}$ ).

$$\gamma = -\frac{2(g_{\text{HG}}/m)^{3/2}}{1 - g_{\text{HG}}^2} + \gamma\beta \quad \text{and} \quad \beta = \frac{\gamma\beta}{\gamma}$$

The errors in the values calculated for  $g_{\text{HG}}$  and  $\beta$  are found using the standard error propagation formula,

$$(\Delta g_{\text{HG}})^2 = \left( \frac{\partial g_{\text{HG}}}{\partial m} \Delta m \right)^2 + \left( \frac{\partial g_{\text{HG}}}{\partial b} \Delta b \right)^2 \quad (5.18)$$

Inserting Equations (5.17) leads to the following equation for the error in the anisotropic value of  $g_{\text{HG}}$

$$\Delta g_{\text{HG}} = \frac{1}{m} \left( 1 + \frac{b}{\sqrt{b^2 - m^2}} \right) \left( (\Delta b)^2 + \frac{b^2 (\Delta m)^2}{m^2} \right)^{1/2} \quad (5.19)$$

The error in  $\gamma$  is

$$\Delta \gamma = \gamma \left[ \frac{(9\Delta m)^2}{4m^2} + \left( \frac{3}{2}\gamma + \frac{g_{\text{HG}}^2 \gamma}{1 - g_{\text{HG}}^2} \right)^2 \frac{(\Delta g_{\text{HG}})^2}{g_{\text{HG}}^2} \right]^{1/2} \quad (5.20)$$

The error in  $\beta$  is

$$\Delta \beta = \beta \sqrt{\left( \frac{\Delta(\gamma\beta)}{\gamma\beta} \right)^2 + \left( \frac{\Delta(\gamma)}{\gamma} \right)^2} \quad (5.21)$$

where  $\Delta(\gamma\beta)$  is the standard deviation of the average of the backwards scattered light used to find  $\gamma\beta$ . Intra-sample variation of  $g_{\text{HG}}$  and  $\beta$  was much greater than the errors arising from the fitting process.

## 5.5 Evaluation of the method

The method for measuring phase functions was evaluated using theoretical values for reflected and transmitted light from slabs of varying thicknesses. The light exiting a uniformly illuminated slab as a function of angle was calculated using the adding-doubling method. All calculations assumed an albedo of 0.98 (the measured albedo of the dermis at 632 nm) and an isotropy factor of  $g_{\text{HG}}=0.9$

(again, close to that of dermis at 632 nm). Four sets of data were calculated: matched and mismatched boundaries with  $\beta = 0.1$  and  $\beta = 0$ . Each of the four cases was calculated for a series of optical depths ranging from  $\tau = 0.1$  to  $\tau = 5$ . The mismatched boundary case was equal to that for tissue-glass-saline and the indices of refraction were 1.37/1.54/1.33.

The reflected and transmitted light as a function of angle for  $\beta = 0$  and  $\tau = 0.1$ , with matched and mismatched boundaries is shown in Figure 5.7. Both boundary conditions manifest a strong forward peak at  $0^\circ$ . However, when the indices of refraction are mismatched, a backward peak at  $180^\circ$  results from internal reflection ( $\sim 1\%$ ) of the forward peak. The method for obtaining the phase function from measured quantities was tested using the four sets of calculated data. The known values of  $\beta = 0.1$  and  $g_{\text{HG}}=0.9$  are compared with the fitted values using the procedure outlined in Section 5.4. The fitted parameters  $\beta$  and  $g_{\text{HG}}$  are presented in Figures 5.8 and 5.9 as a function of the optical thickness of the theoretical sample.

The values of  $g_{\text{HG}}$  for all four sets of data were identical. Figure 5.8 shows  $g_{\text{HG}}$  for only one set of data is shown ( $\beta=0$ , mismatched conditions). This suggests that  $g_{\text{HG}}$  is insensitive to changes in the isotropy factor  $\beta$  and boundary condition. For sample thicknesses less than one optical depth the error in the fitted phase function is less than five percent. Thicknesses greater than one optical depth multiply scatter and cause large errors in the fitted phase function.

Figure 5.9 shows the dependence of the fitted isotropy parameter  $\beta$  as a function of optical thickness. The isotropy factor  $\beta$  is more sensitive to thickness than  $g_{\text{HG}}$  and errors do not become small until optical thicknesses approach 0.1.

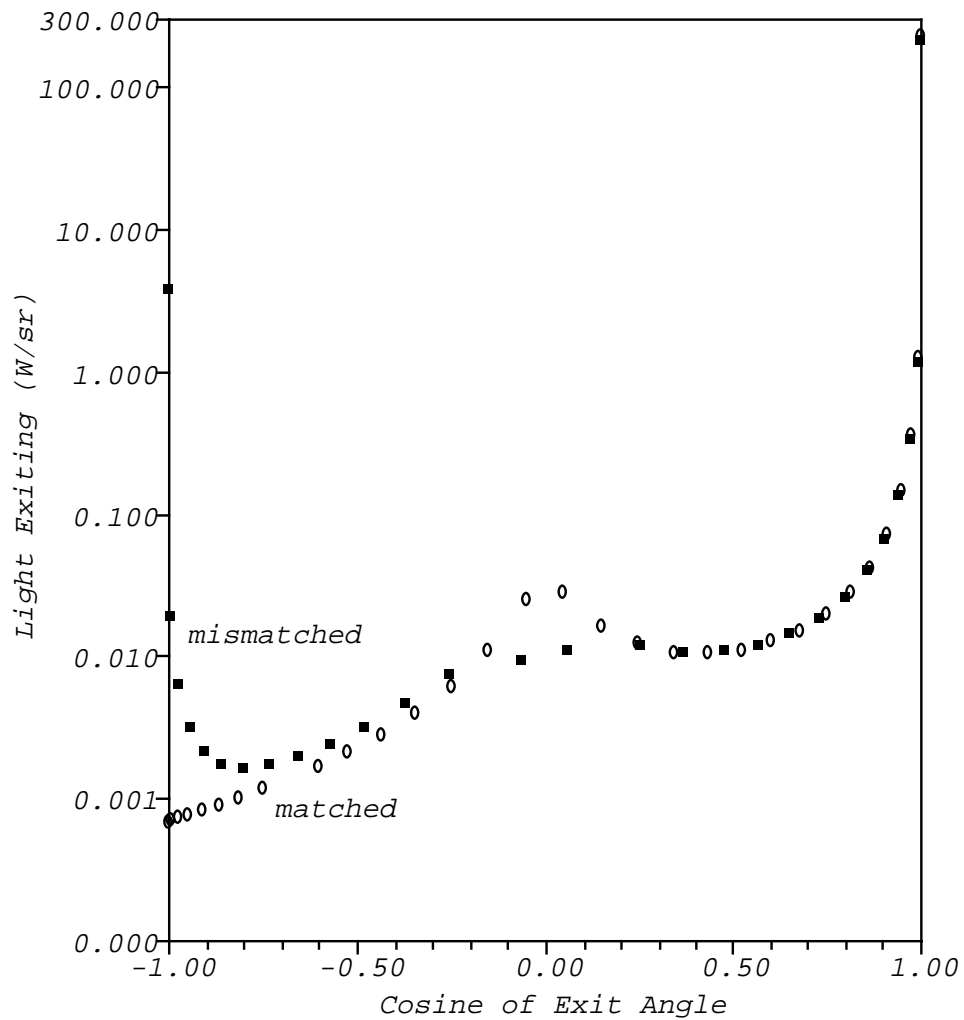


Figure 5.7: Light leaving a uniformly illuminated slab as calculated by the adding-doubling method with  $a = 0.98$ ,  $g_{\text{HG}}=0.9$ ,  $\tau = 0.1$ . Matched (empty circles) and mismatched (1.37/1.54/1.3) conditions are shown. The peak at  $\cos \theta_{\text{exit}} = -1$  in the mismatched case arises from internal reflection of the forward peak ( $\cos \theta_{\text{exit}} = 1$ ).

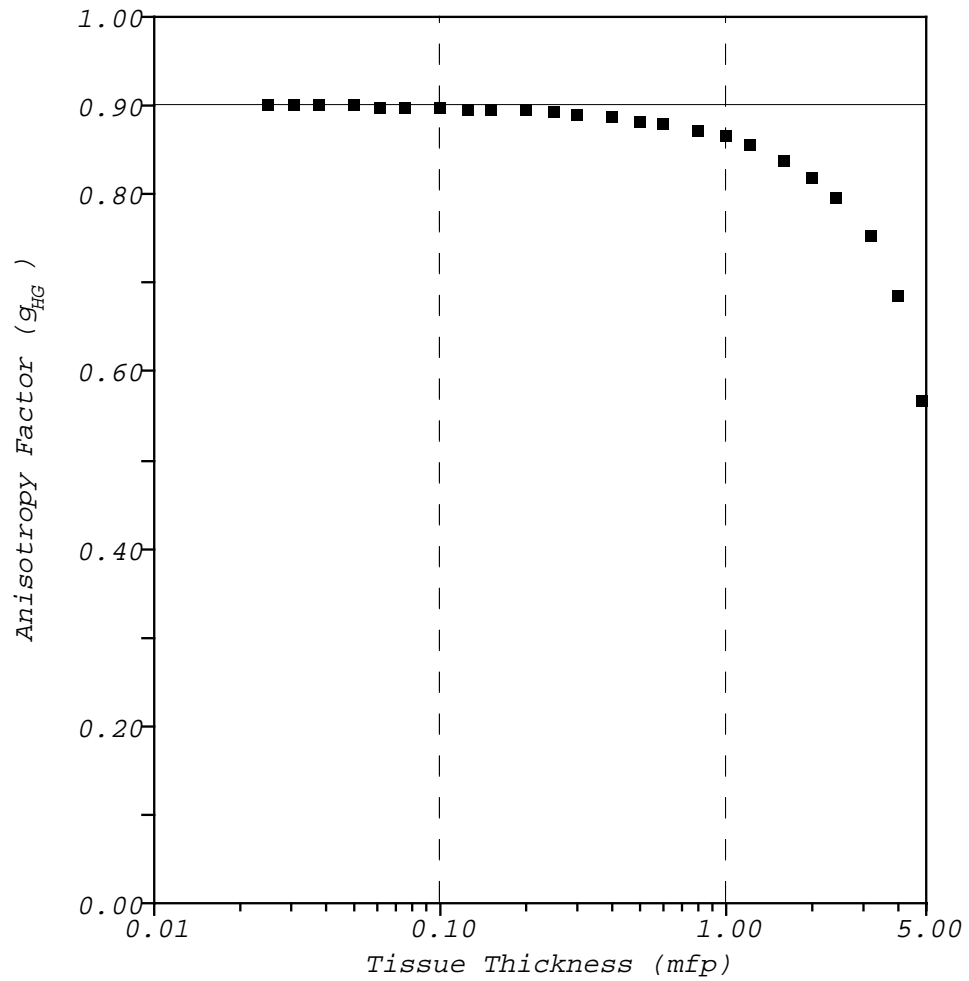


Figure 5.8: Dependence of fitted anisotropy factor  $g_{HG}$  on sample thickness. The true value of  $g_{HG}$  for all optical depths is 0.9. The deviation of the fitted values from the true value is caused by multiple scattering.

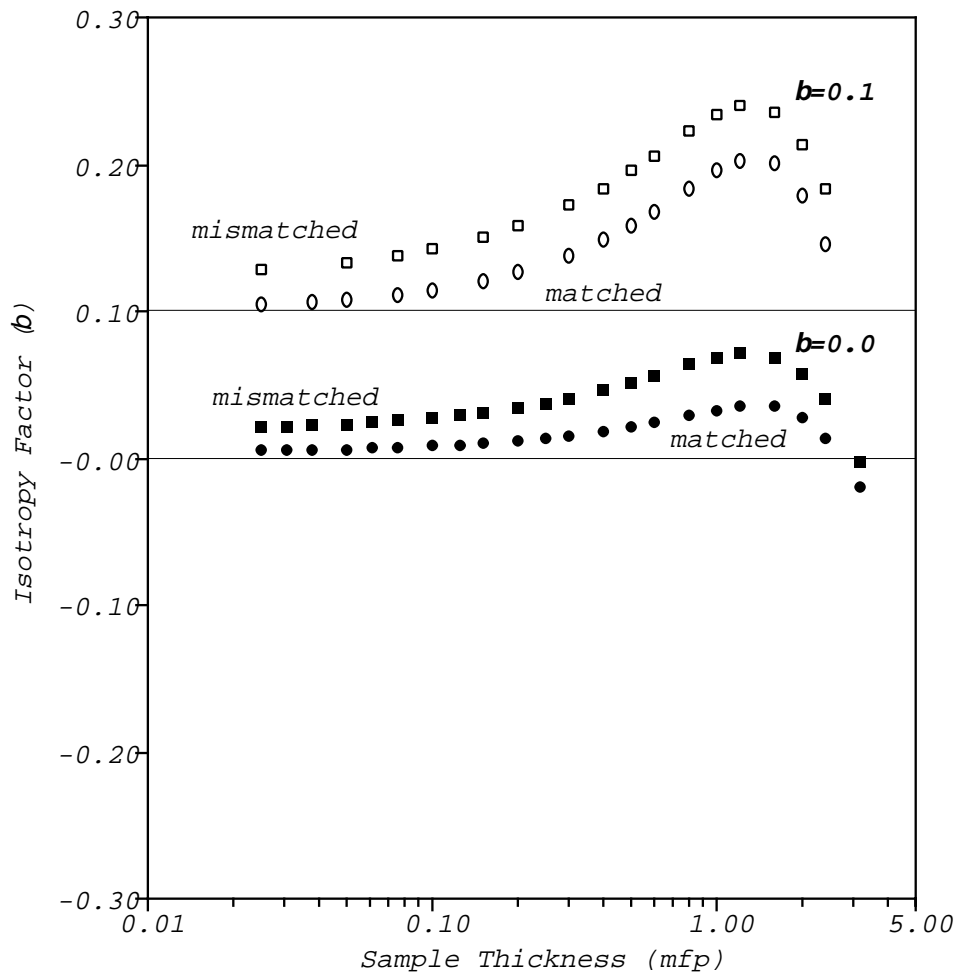


Figure 5.9: Sensitivity of  $\beta$  to sample thickness and boundary conditions. The empty points correspond to fitted values with  $\beta=0.1$  and the filled correspond to  $\beta=0$ . The squares indicate mismatched conditions and the circles correspond to matched conditions.

Moreover,  $\beta$  is very sensitive to boundary conditions and significant errors exist for even very thin tissues with mismatched boundaries. The discrepancy occurs because internal reflection increases the path length of light in the tissue for which the single scattering model cannot account. The data presented in Figure 5.9 suggests that  $\beta$  cannot be measured reliably because any real experiment will have mismatched boundaries and subsequent analysis will overestimate the isotropy factor. Therefore, Figure 5.9 should be used to correct any measured value of  $\beta$  to obtain the true value of  $\beta$  for light scattered isotropically.

## 5.6 Experimental results

Experiments were done on different thicknesses of human dermis. The first set consists of nine measurements on five different samples ranging 200–400  $\mu\text{m}$  thick. The second set used 24 samples (including twelve 20  $\mu\text{m}$  samples) on thin microtomed sections varying from 20–100  $\mu\text{m}$  thick. The attenuation coefficient  $\mu_t = \mu_a + \mu_s$  was obtained by making total attenuation measurements on all samples and averaging the results. The total attenuation measurement so obtained is  $190 \text{ cm}^{-1}$  and was used to convert all sample thicknesses into optical depths. These optical depths were used to calculate the correction factors. A typical fit is shown in Figure 5.10.

The Henyey-Greenstein phase function parameter  $g_{\text{HG}}$  as a function of thickness is shown in Figure 5.11. The limiting value for the anisotropy factor was  $g_{\text{HG}}=0.92$ . The error bars are the standard deviation of the fitted values of  $g_{\text{HG}}$  for each sample thickness. The increased error for the thinnest samples ( $\tau = 0.38$ ) is caused by tearing occurring during the tissue preparation process. The solid curve is identical to that in Figure 5.7 and is included to indicate the



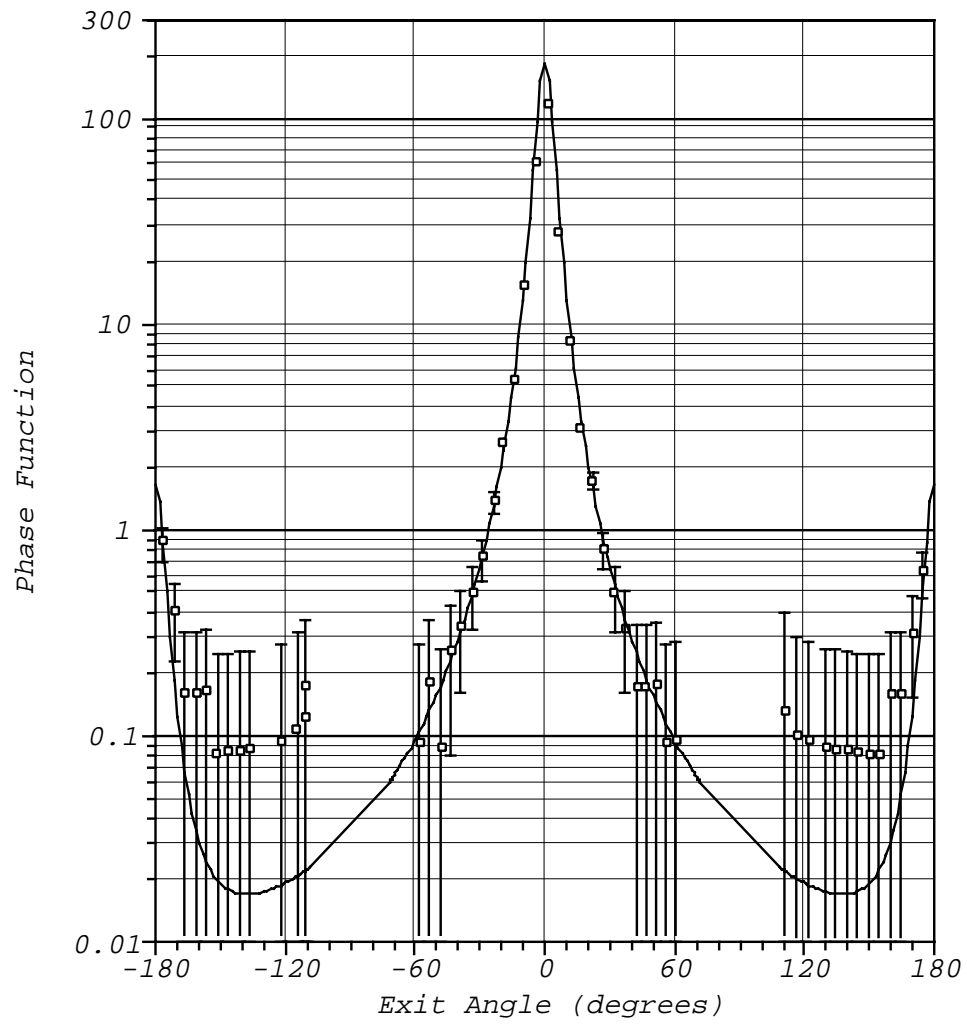


Figure 5.10: Experimental data and fitted phase function for 100  $\mu\text{m}$  thick human dermis. Solid line is the fitted phase function. Squares and error bars indicate measured values and uncertainty in measurements.

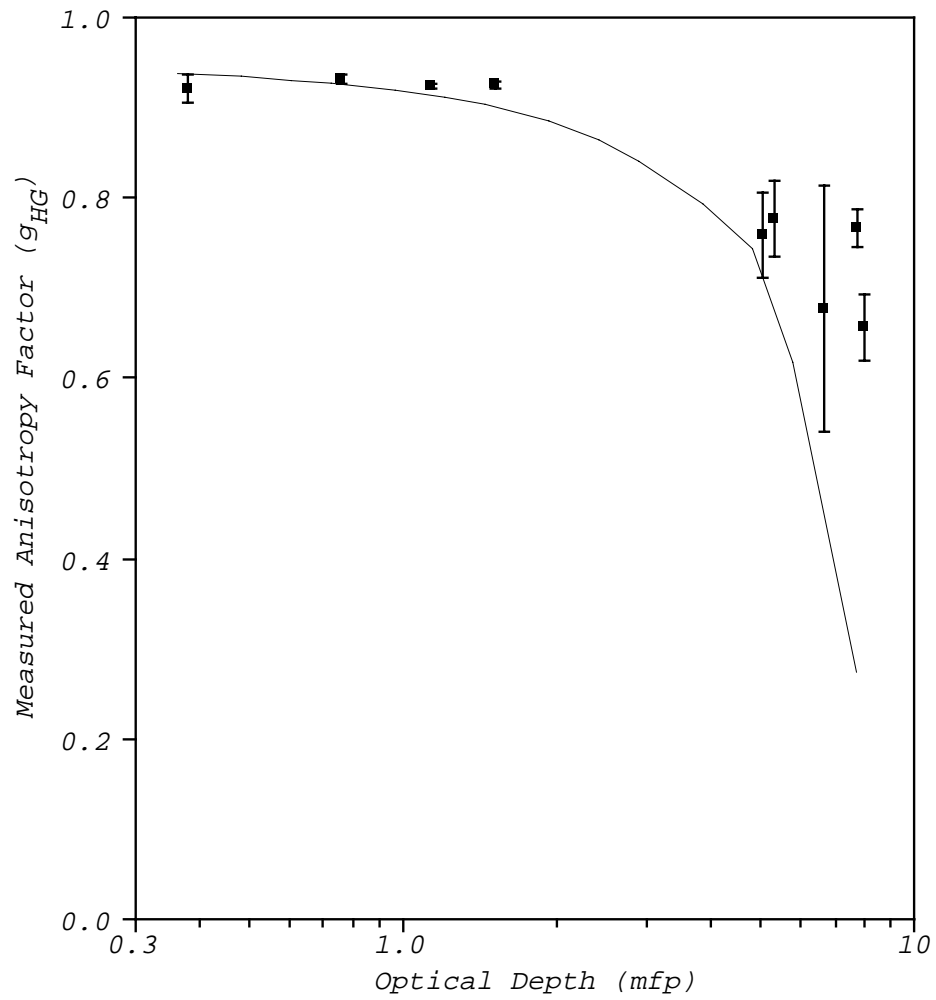


Figure 5.11: The measured anisotropy factor  $g_{HG}$  for human dermis as a function of sample thickness. The solid line indicates the dependence of the measurement technique on sample thickness. The limiting value of  $g_{HG}$  is 0.92. Error bars indicate the standard deviation of the data.

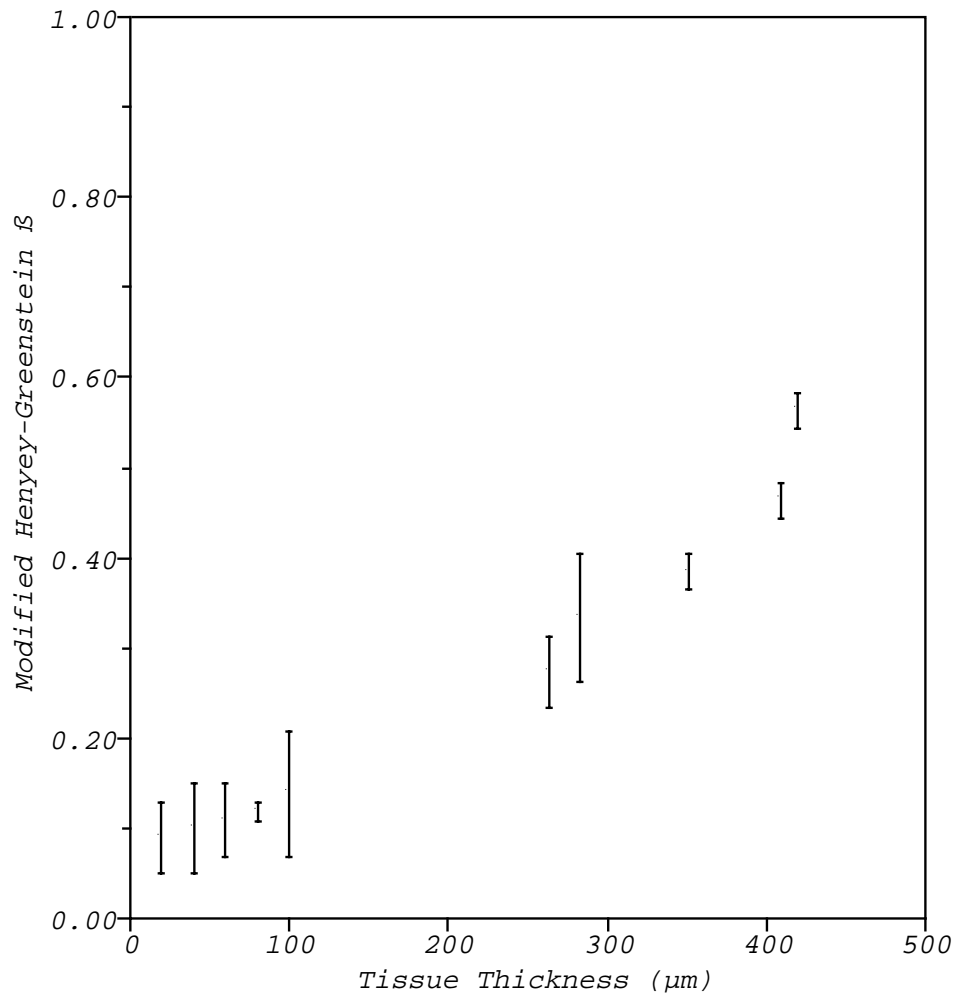


Figure 5.12: The measured isotropy factor  $\beta$  for human dermis as a function of sample thickness. The limiting value of  $\beta$  is 0.05. Error bars indicate the standard deviation of the data.

dependence of the fitted value of  $g_{\text{HG}}$  on the thickness of the sample. Figure 5.12 shows corrected values for the isotropy  $\beta$  as a function of thickness.

## 5.7 Conclusions

Measurements of the reflection and transmission of light as a function of angle allow direct measurement of the single-scattering phase function. It has been shown that these measurements are directly proportional to the phase function for very thin samples. Correction factors for reflection and refraction at boundaries have been presented. The method for measuring the phase function has been evaluated using reflection and transmission values computed with the adding-doubling method. Calculation of the anisotropy factor  $g_{\text{HG}}$  is insensitive to boundary conditions and values of the isotropy factor  $\beta$ . In contradistinction, the values for the isotropy factor  $\beta$  were very sensitive to thickness and boundary conditions—leading to a systematic overestimation of the isotropy factor which could be corrected using Figure 5.9. Experimental measurements on human dermis indicate that the Henyey-Greenstein phase function accurately models the phase function with anisotropy coefficient  $g_{\text{HG}}=0.92$ ,  $\beta=0.05$  and an average cosine of the phase function  $g = g_{\text{HG}}(1 - \beta) = 0.87$ .

# Chapter 6

## Spectrophotometry

### Introduction

This chapter presents a method for measuring the optical properties of tissue using a spectrophotometer. The spectrophotometer measures direct transmission of light through a sample as a function of wavelength. When equipped with an integrating sphere attachment, the spectrophotometer can also measure the diffuse reflection and total transmission of a sample. Three different measurements are therefore available as a function of wavelength. This chapter presents a method for determining the three optical properties characterizing a tissue based on these three measurements or on two integrating sphere measurements and one goniophotometric measurement.

Knowledge of the optical properties of tissue as a function of wavelength allows identification of optimal irradiation wavelengths for a particular application. A particular medical treatment requires that a certain amount of light reach a given tissue location. For example, in the treatment of port wine stains, anomalous subsurface blood vessels must be damaged with minimal injury to the epidermis and dermis above the blood vessel. Determining wavelengths which deposit more light in the blood vessel relative to the amount of light absorbed in the intervening layers increases the success rate for this application.

The optical properties characterizing a tissue are the albedo  $a$ , the optical thickness  $\tau$ , and the average cosine of the phase function  $g_{\text{HG}}$ —or equivalently the scattering coefficient  $\mu_s$ , the absorption coefficient  $\mu_a$ , and the average cosine of the phase function  $g_{\text{HG}}$ . Two types of methods exist for measuring optical properties: direct and indirect. Direct methods require very thin samples in which multiple scattering may be ignored [12] and do not need a light transport model to interpret measurements. The primary disadvantage of direct methods is the very thin tissues required are susceptible to preparation artifact and the methods are not suitable for use with a spectrophotometer (which facilitates measurement of optical properties as a function of wavelength).

Indirect methods permit optical properties to be inferred from measurements of reflection and transmission using a light transport model. The delta-Eddington model used in this chapter provides fast, accurate calculations of reflection and transmission for any optical properties of a sample (see Chapter 4). One advantage of indirect methods is that samples of any optical thickness that transmit measurable quantities of light may be used. This eliminates some potential problems in the tissue preparation process. Unfortunately, the method is considerably more complicated than direct methods and requires extensive computation to derive optical properties from measurements. Finally, the use of an approximate model may introduce errors.

In Section 6.1 the uniqueness of solutions obtained with the inversion method of this chapter is discussed in addition to presenting details of the inversion method. The errors arising from using an approximate model are addressed in Section 6.2. In Section 6.3 results for mouse dermis and human aorta during moderate power argon laser irradiation are presented. Finally, Section 6.4

contains concluding remarks.

## 6.1 Inverse method

The concept behind the inverse method described in this chapter is straightforward (Figure 6.1): (a) guess a set of optical properties; (b) calculate the reflection and transmission; (c) compare the calculated values with the measured reflection and transmission; (d) if the calculated and measured values are not equal then repeat the process with a new guess.

Three measurements are required to determine three unknowns. Two possible sets of measurements are the diffuse reflection  $R_{\text{diffuse}}^{\text{meas}}$ , the total transmission  $T_{\text{total}}^{\text{meas}}$ , and the collimated transmission  $T_{\text{coll}}^{\text{meas}}$ , or alternatively,  $R_{\text{diffuse}}^{\text{meas}}$ ,  $T_{\text{total}}^{\text{meas}}$ , and the anisotropy of the phase function  $g_{\text{HG}}$ . The first set requires removal of the integrating sphere assembly in the spectrophotometer and the second set requires an independent measurement of the anisotropy of the tissue with a goniophotometer. In Section 6.1.1 below the uniqueness of the optical properties obtained from such measurements is discussed. Section 6.1.2 contains details of the inversion process.

### *Uniqueness of inverse procedure*

The iteration method implicitly assumes that a unique combination of the albedo  $a$ , the optical depth  $\tau$ , and the anisotropy  $g_{\text{HG}}$  will be determined by a specified set of reflection and transmission measurements. Consider the case when the optical thickness is held constant. Increasing the albedo increases reflection and decreases transmission. Decreasing the anisotropy also increases the reflection and decreases the transmission, and so the anisotropy and the albedo are not

obviously independent functions of the reflection and transmission.

In Figure 6.2 the dependence of the total transmission and the diffuse reflection on the anisotropy and albedo is shown. The grid was computed with the collimated transmission fixed at ten percent ( $T_{\text{coll}}^{\text{meas}}=0.1$ ) and the boundaries of the sample are matched with the outside. The intersection of the appropriate measured diffuse reflection and measured total transmission grid lines determines a unique albedo and anisotropy. Diffuse reflectances above about 0.5 are physically impossible for the assumed boundary conditions and assumed collimated transmission. The albedo and anisotropy are most sensitive to errors in the magnitudes of the diffuse reflection and total transmission measurements when the magnitudes of both these measurements are small (e.g.,  $R = 0.1$ ,  $T = 0.2$ ).

Now let  $g_{\text{HG}}$  be held constant: in this case the two parameters which may be varied are the albedo  $a$  and the optical depth  $\tau$ . Increasing the albedo increases the reflection and decreases transmission. Since increasing the optical depth also increases reflection and decreases transmission, the optical depth is again not clearly independent of the albedo. Figure 6.3 shows how  $T$  (total transmission) and  $R + T$  (diffuse reflection plus total transmission) depend on the albedo and optical thickness for the case when  $g_{\text{HG}} = 0$  and the sample boundaries are matched with the environment. This graph is typical of other anisotropies and boundary conditions. Measured values for  $R$  and  $T$  (or equivalently,  $T$  and  $R + T$ ) determine a unique intersection point whose ordinate is a simple function of the albedo  $a$  and whose abscissa is the optical depth  $\tau$ . The axes in Figure 6.3 were chosen to linearize the  $T$  and the  $R + T$  contour curves.



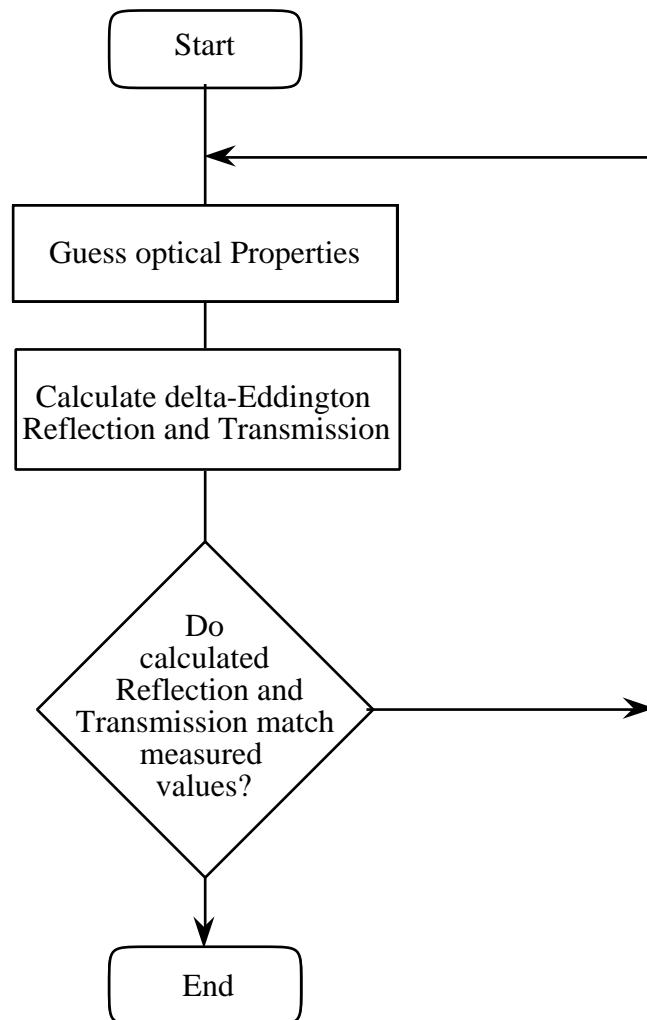


Figure 6.1: Flowchart for inversion process. The method involves guessing the optical properties of a tissue, calculating the reflection and transmission for these properties, comparing the calculated with the measured reflection and transmission, and repeating this process until the calculated and measured transmission match.

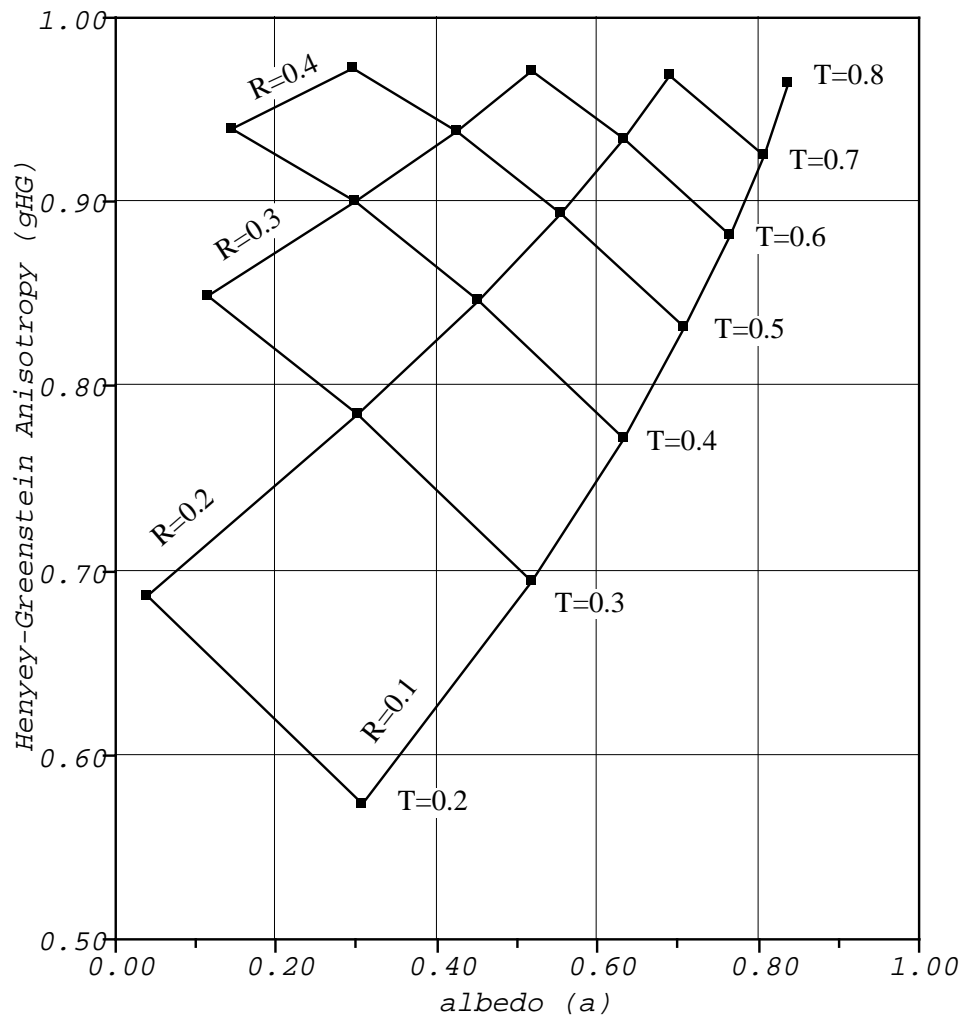


Figure 6.2: Typical diffuse reflectance ( $R$ ) and total transmission ( $T$ ) grid for a fixed collimated transmission ( $T_c = 0.1$ ). For every pair of measurements  $R$  and  $T$ , the  $R - T$  grid intersection defines a unique pair of optical properties for the albedo  $a$  and the anisotropy  $g_{HG}$  for that tissue.

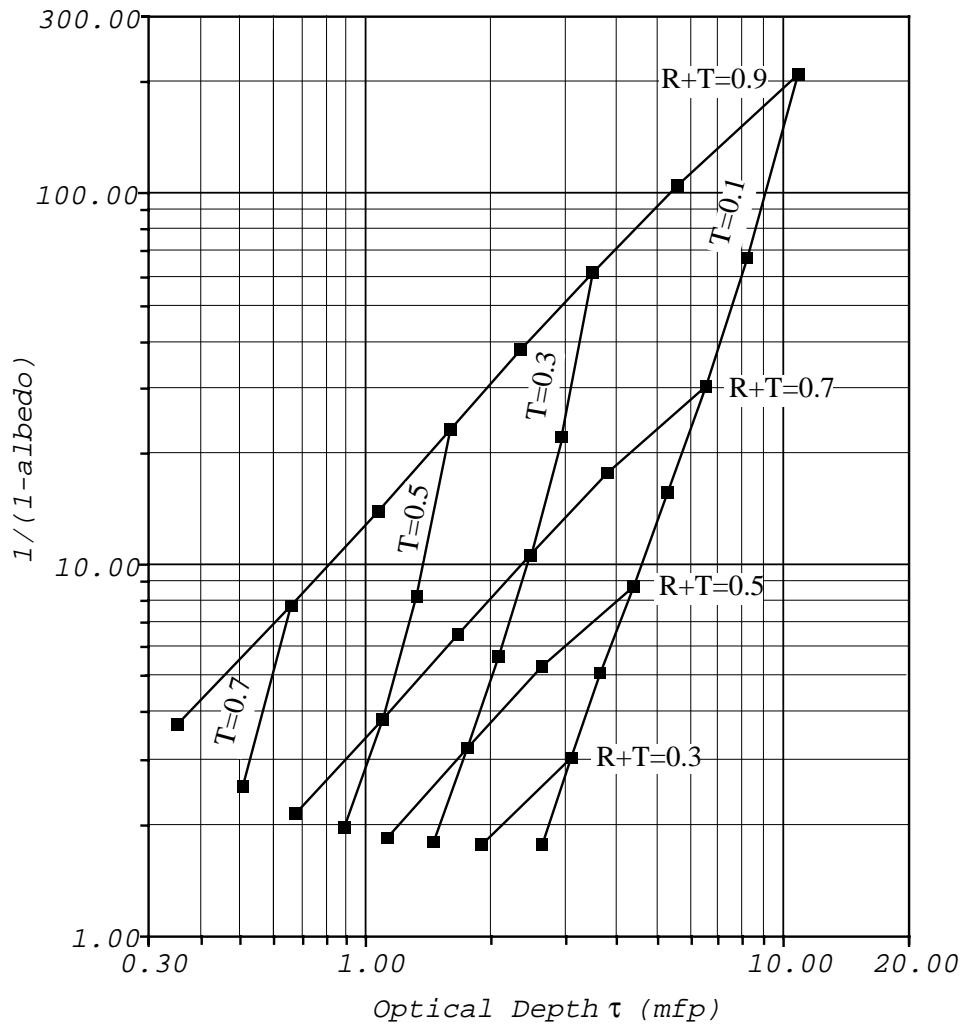


Figure 6.3: Typical diffuse reflectance ( $R$ ) and total transmission plus diffuse reflectance ( $R + T$ ) grid for a fixed anisotropy ( $g_{\text{HG}} = 0$ ). For every pair of measurements  $R$  and  $T$ , the  $T/R + T$  grid intersection defines a unique pair of optical properties for the albedo  $a$  and the optical depth  $\tau$  for that tissue.

*Details of the iteration procedure*

The inverse method uses an  $N$ -dimensional minimization algorithm called AMOEBA [49]. This algorithm is based on the downhill simplex method of [45]. The function to be minimized is

$$F(a', \tau', g') = |R_{\text{diffuse}}^{\delta-E} - R_{\text{diffuse}}^{\text{meas}}| + |T_{\text{coll}}^{\delta-E} - T_{\text{diffuse}}^{\text{meas}}| \quad (6.1)$$

where  $R_{\text{diffuse}}^{\delta-E}$  and  $T_{\text{coll}}^{\delta-E}$  are the diffuse reflection and total transmission as calculated with the delta-Eddington model. Only two measurements are used because either the collimated transmission  $T_{\text{coll}}^{\text{meas}}$  is known and consequently the delta-Eddington optical depth  $\tau'$  is known

$$\tau = -\ln\left(\frac{T_{\text{coll}}^{\text{meas}}}{(1-r_s)^2}\right) \quad \text{and} \quad \tau' = (1-af)\tau \quad (6.2)$$

or  $g_{\text{HG}}$  is known (from which  $g'$  can be derived). Thus the function  $F(a', \tau', g')$  in Equation (6.1) is really a function of only two variables.

The total light transmitted in the delta-Eddington model is

$$T_{\text{coll}}^{\delta-E} = T_{\text{diffuse}}^{\delta-E} + (1-r_s)^2 \exp(-\tau') \quad (6.3)$$

where is the diffuse transmission given by Equation (4.106). It should be emphasized that the delta-Eddington collimated transmission is not equal to the measured collimated transmission (except in the special case when  $f = 0$  and  $\tau' = \tau$ ). In particular

$$T_{\text{coll}}^{\delta-E} = (1-r_s)^2 \exp(-\tau') \quad \text{and} \quad T_{\text{diffuse}}^{\text{meas}} = (1-r_s)^2 \exp(-\tau') \quad (6.4)$$

The delta-Eddington collimated transmission is not physically observable, but merely a mathematical finesse to improve the accuracy of the approximation by treating some fraction of highly forward scattered light as ‘collimated’ light.

A Henyey-Greenstein shape may be imposed on the phase function (to second order in Legendre polynomials—see Section 1.3.3) by varying  $g_{\text{HG}}$  instead of  $g'$ . This places a restriction on the relation between  $g'$  and  $f$ . This has the added advantage of removing  $f$  as an unknown parameter. Currently no evidence for the shape of a phase function at wavelengths other than 633 nm exists, and this restriction should be made with caution. If the Henyey-Greenstein phase function is assumed then  $g'$  and  $f$  are calculated according to Equations (1.4) and (1.5).

$$f = (1 - \beta)g_{\text{HG}}^2 \quad \text{and} \quad g' = \frac{g_{\text{HG}}(1 - g_{\text{HG}})}{\frac{1}{1-\beta} - g_{\text{HG}}^2} \quad (6.5)$$

Finally, it is possible to vary  $g'$  independently of  $f$ , and omit calculating  $a$  and  $\tau$  from the final values  $a'$  and  $\tau'$  (which requires knowledge of  $f$ ), but such model dependent parameters have not been found useful.

The minimization routine `amoeba` assumes the range over which parameters may be varied is  $-\infty$  to  $\infty$ . Unfortunately, the anisotropy and albedo have fixed ranges. This is remedied by transforming the albedo and anisotropy into a “calculation space.” As  $a_{\text{calc}}$  varies from  $-\infty$  to  $\infty$  in the calculation space, the actual albedo  $a$  varies from 0 to 1. The same transformation is made on the anisotropy, since all tissues measured heretofore have had positive anisotropies. The transformation function is

$$x_{\text{calc}} = \frac{2x - 1}{x(1 - x)} \quad (6.6)$$

where  $x$  represents either  $g_{\text{HG}}$  or  $a$  depending on the need. If negative anisotropies are included, then the transformation function for  $g_{\text{HG}}$  must be altered to vary from  $-1$  to  $1$  as the calculation parameter varies from  $-\infty$  to  $\infty$ .

Flowcharts for algorithms based on either known  $g_{\text{HG}}$  or known  $\tau'$  are shown in Figures 6.4 and 6.5. These illustrate the changes of variables which take place during each iteration of the method.

Starting values for an initial guess of  $a'$ ,  $\tau'$ , and  $g'$  maybe obtained in a few different ways. First, Kubelka-Munk optical properties may be calculated from the reflection and transmission and these may be converted to transport optical properties. This turns out to be not any better than just starting at fixed intermediate values of the optical properties ( $a' = 0.5$ ,  $\tau' = 1$ , and  $g' = 0.2$ ). However, when calculating optical properties for a series of different wavelengths, excellent starting values to use for the next wavelength are the optical properties of the previous wavelength.

### 6.1.1 Evaluation of the inverse method

To evaluate the accuracy of the iteration method, diffuse reflection and total transmission were calculated using the adding-doubling technique for a variety of optical properties (Table 3.4 and 3.5). These calculated values were used in place of measured reflection and transmission, and consequently, the true optical properties characterizing each set of reflection and transmission are known. Two separate evaluations were performed: one for a known anisotropy  $g_{\text{HG}}$  and one for known collimated transmission. Either the anisotropy or the collimated transmission was known accurately and any errors presented in Tables 6.1 and 6.2 do not include possible errors in determining these known values.

Tables 6.1 and 6.2 indicate how the approximate delta-Eddington model used in the iteration procedure affects the optical properties calculated. For both cases (fixed collimated transmission and fixed anisotropy) the errors are least

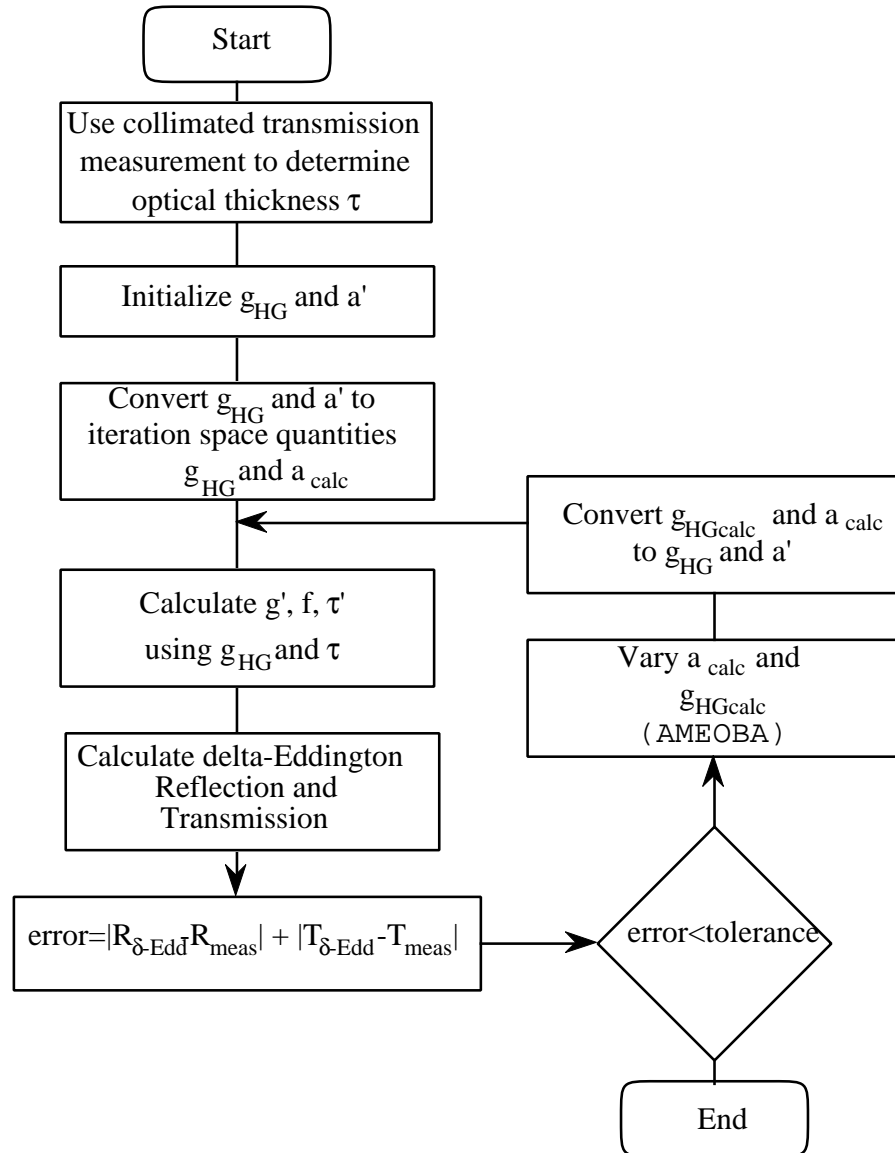


Figure 6.4: Detailed flowchart for the inversion algorithm when the collimated transmission is known. This flowchart illustrates the changes in variables necessary to vary all the parameters during each iteration.

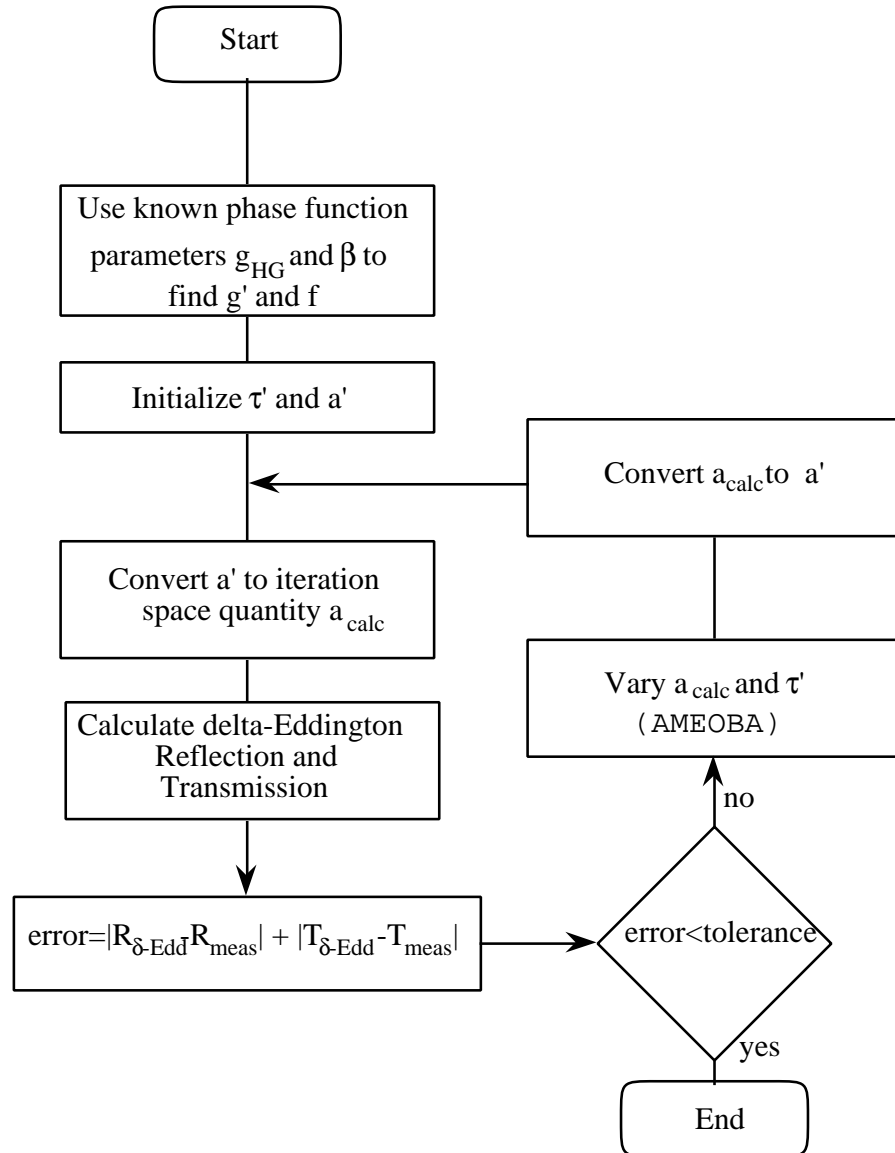


Figure 6.5: Detailed flowchart for the inversion algorithm when the anisotropy is known. This flowchart illustrates the changes in variables necessary to vary all the parameters properly during the iteration process.



$n$	$g = 0.0$			$g = 0.5$			$g = 0.875$		
	$a = .6$	$a = .9$	$a = .99$	$a = .6$	$a = .9$	$a = .99$	$a = .6$	$a = .9$	$a = .99$
	$a_{calc} - a$								
-2	0.04	-0.00	0.01	0.13	0.02	0.01	0.31	0.08	0.01
-1	-0.01	-0.02	0.01	0.05	-0.01	0.01	0.25	0.05	0.01
0	-0.03	-0.02	-0.00	0.01	-0.02	0.00	0.20	0.02	0.01
1	-0.02	-0.02	-0.00	0.01	-0.01	-0.00	0.17	0.00	0.00
2	-0.02	-0.01	-0.00	0.01	-0.01	-0.00	0.17	0.00	-0.00
3	-0.02	-0.01	-0.00	0.01	-0.01	-0.00	0.17	0.00	-0.00
4	-0.02	-0.01	-0.00	0.01	-0.01	-0.00	0.17	0.00	-0.00
	Percent Errors								
-2	7	-0	1	21	3	1	52	9	1
-1	-2	-3	1	8	-1	1	42	6	1
0	-4	-3	-0	2	-2	0	33	2	1
1	-4	-2	-0	1	-2	-0	28	0	0
2	-3	-1	-0	1	-1	-0	28	0	-0
3	-3	-1	-0	1	-1	-0	29	0	-0
4	-3	-1	-0	1	-1	-0	29	0	-0
	$\tau_{calc} - \tau$								
-2	0.07	0.07	0.09	0.12	0.11	0.14	0.54	0.45	0.52
-1	0.07	0.07	0.07	0.10	0.09	0.11	0.56	0.38	0.43
0	0.06	0.05	0.05	0.08	0.07	0.09	0.63	0.27	0.29
1	0.03	0.00	-0.01	0.07	0.04	0.06	0.90	0.16	0.20
2	-0.08	-0.15	-0.12	0.00	-0.10	-0.07	1.71	0.18	0.25
3	-0.39	-0.52	-0.25	-0.22	-0.46	-0.25	3.28	0.25	0.29
4	-2.18	-1.42	-0.52	0.36	-1.21	-0.48	6.21	-0.13	-0.30
	Percent Errors								
-2	29	29	36	46	44	57	217	181	208
-1	14	14	13	20	19	22	112	76	87
0	6	5	5	8	7	9	63	27	29
1	2	0	-0	3	2	3	45	8	10
2	-2	-4	-3	0	-2	-2	43	5	6
3	-5	-7	-3	-3	-6	-3	41	3	4
4	-14	-9	-3	2	-8	-3	39	-1	-2

Table 6.1: Differences and percent errors between calculated and true optical thickness ( $\tau = 2^n$ ) and albedo  $a$ . The Henyey-Greenstein anisotropy  $g_{HG}$  is assumed known. The reflection and transmission used as truth were taken from Tables 3.4 and 3.5.

$n$	$g = 0.0$			$g = 0.5$			$g = 0.875$		
	$a = .6$	$a = .9$	$a = .99$	$a = .6$	$a = .9$	$a = .99$	$a = .6$	$a = .9$	$a = 0.99$
	$a_{calc} - a$								
-2	0.12	0.10	0.01	0.01	-0.01	0.01	0.11	0.06	0.01
-1	0.01	0.01	0.01	-0.04	-0.03	0.01	0.08	0.02	0.01
0	-0.02	-0.02	0.01	-0.03	-0.03	0.00	0.06	0.00	0.01
1	-0.02	-0.02	-0.00	-0.01	-0.02	-0.00	0.06	-0.00	0.00
2	-0.00	-0.01	-0.00	0.01	-0.01	-0.00	0.06	-0.00	-0.00
3	0.00	-0.00	-0.00	0.02	-0.00	-0.00	0.07	-0.00	-0.00
4	0.00	-0.00	-0.00	0.04	-0.00	-0.00	0.07	0.00	-0.08
	Percent Errors								
-2	20	11	1	2	-1	1	19	6	1
-1	1	1	1	-6	-4	1	13	2	1
0	-4	-2	1	-5	-3	0	10	0	1
1	-4	-2	-0	-2	-2	-0	10	-1	0
2	-0	-1	-0	1	-1	-0	11	-0	-0
3	0	-0	-0	4	-0	-0	11	-0	-0
4	0	-0	-0	7	-0	-0	12	0	-8
	$g_{calc} - g$								
-2	0.00	0.00	0.00	-0.50	-0.36	-0.44	-0.46	-0.27	-0.30
-1	0.00	0.00	0.00	-0.23	-0.14	-0.14	-0.23	-0.11	-0.12
0	0.00	0.00	0.00	-0.09	-0.05	-0.06	-0.12	-0.04	-0.04
1	0.00	0.00	0.00	-0.03	-0.01	-0.02	-0.09	-0.01	-0.01
2	0.05	0.05	0.03	-0.00	0.01	0.01	-0.08	-0.01	-0.01
3	0.05	0.07	0.03	0.02	0.03	0.02	-0.07	-0.00	-0.00
4	0.05	0.09	0.03	0.05	0.04	0.02	-0.07	0.00	-0.84
	Percent Errors								
-2	—	—	—	-100	-73	-87	-53	-31	-35
-1	—	—	—	-45	-27	-28	-26	-13	-14
0	—	—	—	-17	-10	-11	-14	-4	-4
1	—	—	—	-6	-3	-4	-10	-1	-2
2	—	—	—	-0	3	2	-9	-1	-1
3	—	—	—	5	6	3	-8	-0	-1
4	—	—	—	11	8	3	-8	0	-96

Table 6.2: Differences and percent errors between calculated and true Henyey-Greenstein anisotropies ( $g_{HG}$ ) and albedos ( $a$ ). The collimated transmission is assumed known for various optical depths ( $\tau = 2^n$ ). The reflection and transmission used as truth were taken from Tables 3.4 and 3.5.

when the albedos are large. Changes in the anisotropy have little affect upon the accuracy of the calculated optical properties. Increasing optical thickness tends to decrease percent error. The method should not be used with thin samples ( $\tau < 1$ ) because of the large errors in the calculated values. However for any albedo, any anisotropy, and optical thicknesses larger than one, the inverse method has intrinsic errors less than ten percent when the collimated transmission is known (Table 6.2).

### 6.1.2 Experimental measurements

Two sets of experiments are presented in this section: measurements on bloodless human dermis as a function of wavelength and measurements on bloodless human aorta during moderate power laser irradiation.

#### *Bloodless human dermis as a function of wavelength*

A sample of human dermis was obtained from the abdomen at autopsy. The epidermis was manually separated following mild thermal treatment (two minute exposure in a 55°C water bath). The dermal sample was soaked in saline prior to measurement to remove residual blood. One 2 × 2 centimeter sample was cut with a dermatome. The sample was sandwiched between glass microscope slides and the tissue thickness (360 μm) was determined with micrometer.

A spectrophotometer (Beckman UV 5270) was used for measurements of reflection and transmission. The sample was placed at the entry port of the integrating sphere for measurements of total transmission. Collimated light directly struck the sample, and all light passing through the sample was collected by the integrating sphere. Diffuse reflection was measured by placing the sample

in the exit port of the sphere. Specularly reflected light from the sample travelled back along the incident beam path and was not collected by the integrating sphere. For calibration purposes, zero and 98% reflection were obtained by measuring the reflectance with the sample removed and with a BaSO<sub>4</sub> plate respectively. Collimated transmission measurements were made by removing the integrating sphere assembly and placing the sample in the path of the beam. Collimated light struck the sample, but only light propagating co-linear with the incident beam was detected. The measurements of reflection and transmission as a function of wavelength are presented in Figure 6.6.

The iteration algorithm was used to convert these measurements to optical properties. These properties are shown in Figures 6.7. Both absorption and scattering coefficients decrease with increasing wavelength. This indicates that longer wavelengths of light penetrate deeper into a tissue. The anisotropy increases with wavelength indicating that light scattering increases in the forward direction.

#### *Aorta during moderate power argon irradiation*

The thermal response of tissue during laser irradiation is highly dependent upon the optical properties of the tissue. Many laser treatments produce temperatures substantially above normal tissue temperatures (50°–300°C). At such temperatures, dehydration, protein denaturation, coagulation, charring, pyrolysis or ablation may occur. Any of these processes changes the appearance of the tissue and hence the optical properties of the tissue. Heretofore, there has been no attempt to measure the optical properties of tissue during irradiation.

The experimental apparatus in Figure 6.8 was used to measure the scat-

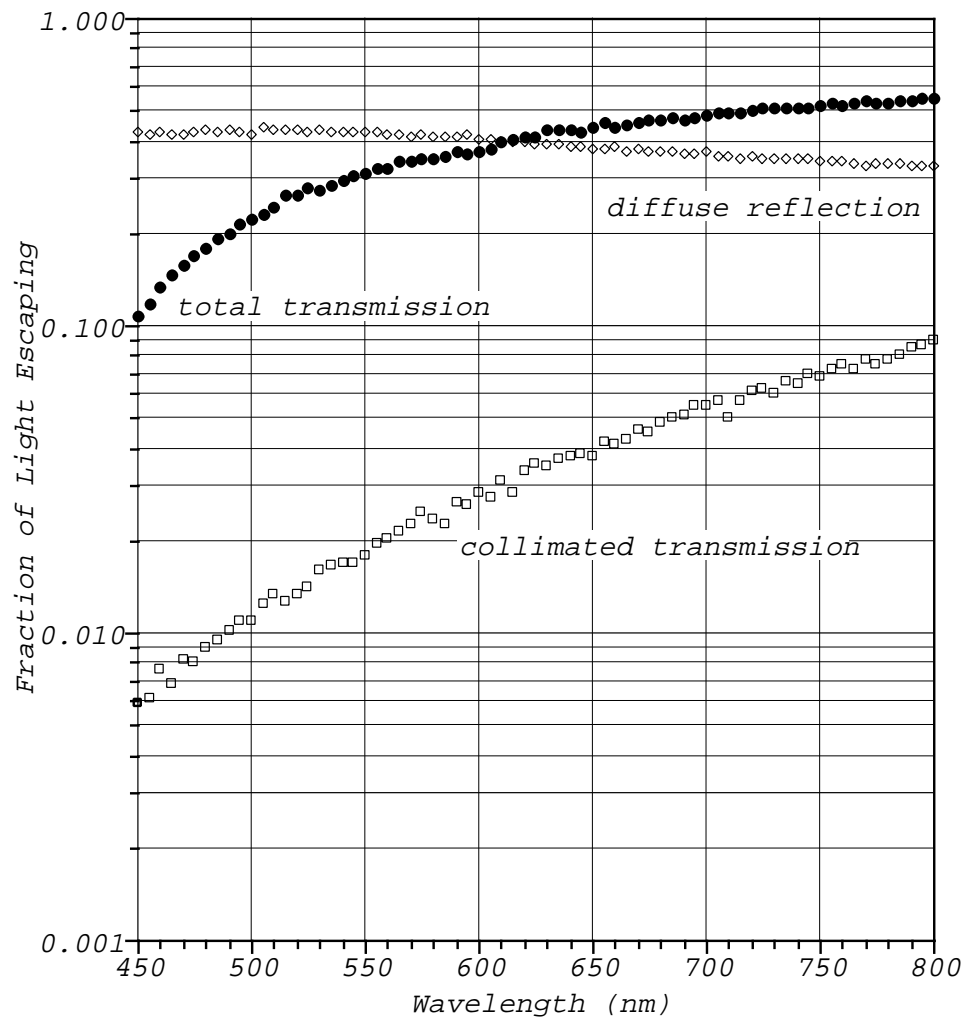


Figure 6.6: Total transmission, collimated transmission, and diffuse reflection from a  $360\ \mu\text{m}$  sample of bloodless human dermis. Transmission increase with wavelength and reflection decreases with wavelength.

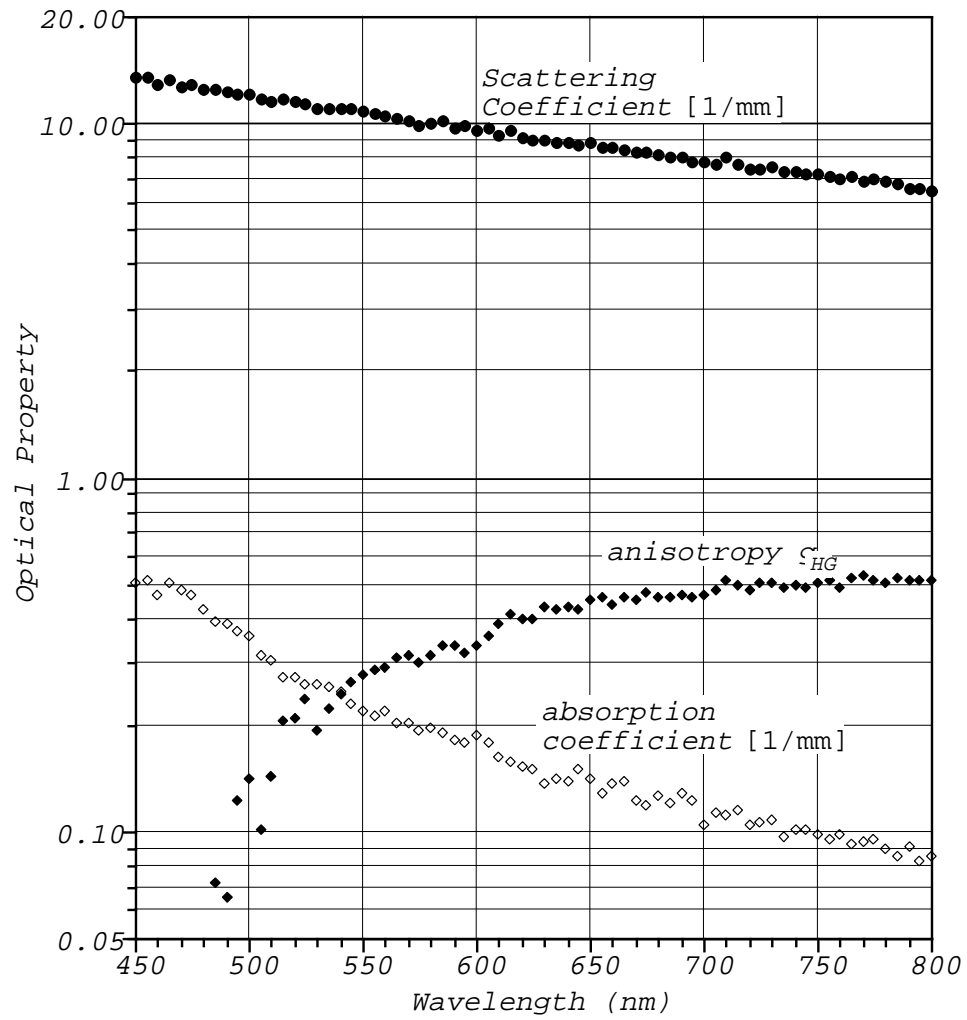


Figure 6.7: Optical properties of bloodless human dermis as a function of wavelength.

tered transmission, the scattered reflectance, and the collimated transmission during irradiation of human aorta by an argon laser. Reflectance and transmission were measured during irradiation, digitized and saved on a computer for later analysis. The laser used was a 20 W argon laser (Coherent CR-18) operating in the multi-line mode. Two integrating spheres (Labsphere) were used to measure scattered light. The larger sphere (24 cm in diameter) was used to measure scattered transmission and the smaller (12 cm) was used to measure scattered reflectance. Collimated transmission was measured with a 4 mm diameter photodiode located 170 cm from the exit port of the larger integrating sphere. The detectors used to measure light in the integrating sphere were also photodiodes (RCA SK2031). To ensure uniform heating of the sample, the central flat portion of the beam was used. This was obtained by expanding the laser beam with a 5× microscope objective (f26.4 mm) and collimating it with an f126 mm convex lens, resulting in a net magnification of 4.8. The edges of the beam were blocked with a circular aperture 8 mm in diameter, thereby allowing only the central ‘flat’ portion of the Gaussian beam profile to reach the sample. The spot size was 8 mm in diameter.

Aorta was obtained from the morgue the morning the experiments were done. The aorta was kept in chilled saline until used. The adventitia was removed leaving samples with full thickness media and the intima intact. Typical sample thicknesses were about 1.5 mm. The aorta was not sandwiched between glass slides which allowed the tissue to change shape during irradiation. Typically the samples became thinner during irradiation due to dehydration. Both experiments described here use aorta samples from the same subject.

During irradiation the tissue passed through a series of phases. The first

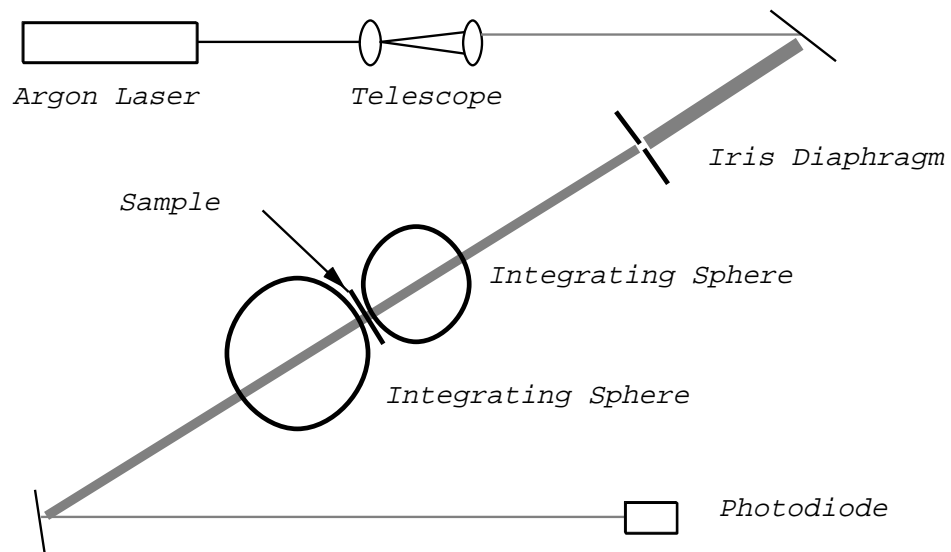


Figure 6.8: Experimental apparatus to measure optical properties of tissue during heating with an argon laser. The laser beam was expanded and passed through a diaphragm to obtain a flat beam profile. The sample was located between two integrating spheres to detect diffuse reflection and transmission. The photodiode was located about one meter from the sample to ensure that most of the light collected was collimated transmitted light.



phase, coagulation, was marked by whitening of the tissue. This was followed by dehydration, by boiling, and finally by charring. Before each experiment, measurements of 0% and 100% scattered transmission, primary transmission and scattered reflectance were made to allow scaling of detector voltages into fractions of the total possible reflectance or transmission. These values are plotted in Figure 6.9 for two experiments with differing irradiances: 130 and 90 W/mm<sup>2</sup>. As expected, reflectance and transmission change more quickly for the higher irradiance. The tissue response for irradiances between 130 and 90 mW/mm<sup>2</sup> was similar and, for clarity, is not shown.

The difference in magnitude illustrated by the scattered and primary transmission plots at the right is caused by differing sample thicknesses. (1.65 mm for the higher irradiance and 1.70 mm for the other.) Since one mean free path (mfp) is about 0.1 mm, this is a significant thickness change. This difference is not as evident in the reflectance graph because the samples are so thick ( $\sim 15$  mfp) that thickness variations do not substantially affect the net reflectance.

Both the primary and the scattered transmission drop significantly in the first 50–75 seconds. Presumably this is due to surface coagulation and dehydration. The initial drop in transmission is followed by an increase in transmission caused by subsurface vapor production. Once the vapor pressure exceeds the yielding point of the tissue the bubble of vapor explodes, announced by an audible “pop.” This time is indicated by the dashed lines in Figures 6.9 and 6.10. In Figure 6.10 the lower irradiance also has an anomalous early “pop” indicated. This may have been due to a small plaque deposit. The onset of charring is marked by a sudden decrease in the reflectance. This is also indicated by a labelled dashed line. Not surprisingly, as the tissue blackens during charring, the

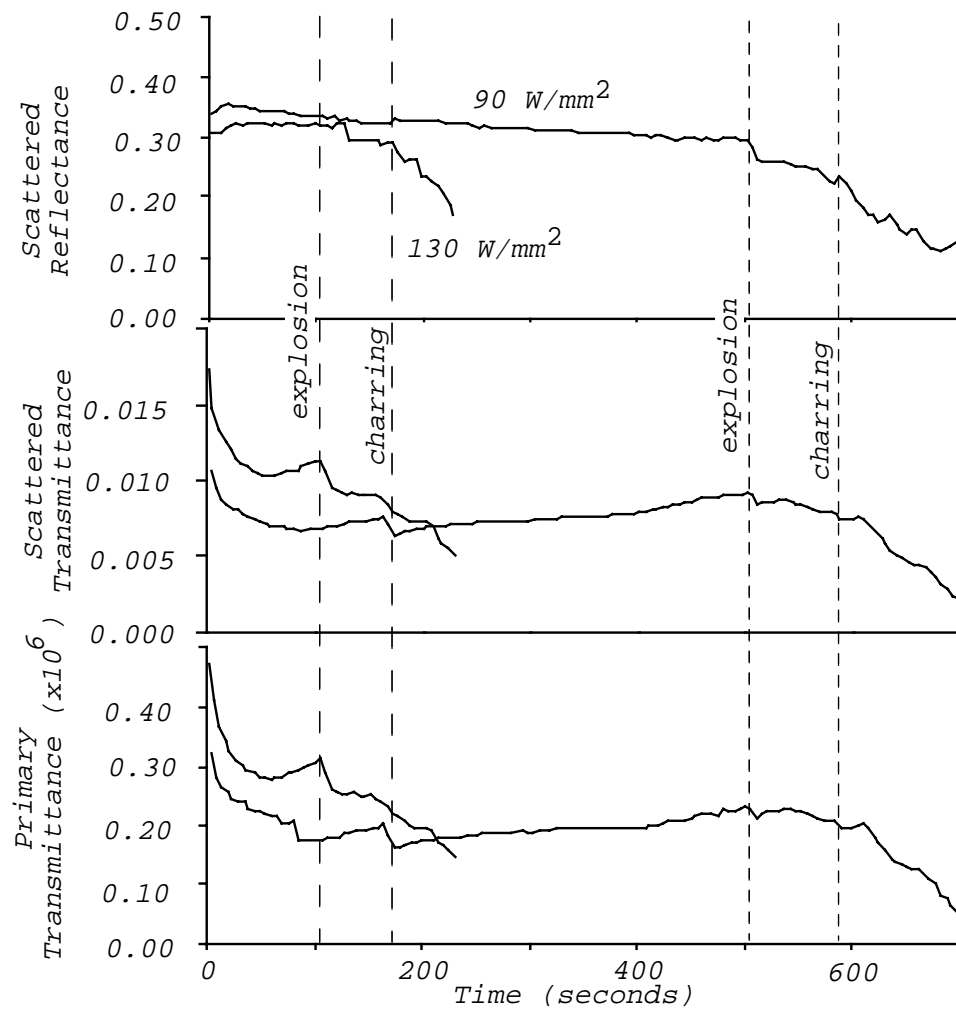


Figure 6.9: Reflection and transmission during argon laser irradiation of normal human aorta. Irradiances of 90 and 130 W/mm<sup>2</sup> are shown. Dashed lines indicate explosions and onset of charring (see text) and correspond to the same lines in Figure 6.10.

transmission also drops.

Halldórsson et al. have made similar types of measurements using a Nd-YAG laser on canine stomach wall [23]. They used much higher power densities, smaller spot sizes and shorter irradiation times. They found that the reflectance initially increased and the transmission decreased, followed by a rapid increase in reflectance and continued decrease in transmission during the evaporation or dehydration phase. Finally, during the carbonization phase they reported that the reflectance decreased and the transmission increased. Clearly, these results differ from those reported here. This discrepancy is most likely caused by the greater penetration depth of Nd-YAG (1060 nm) light in tissue. This difference causes changes in the light distribution, and consequently, in the thermal profile and the damage pattern for the tissue.

Dimensionless optical properties were calculated for the measured reflections and transmissions. The use of dimensionless optical properties allowed optical properties to be obtained without knowing the thickness of the sample during irradiation. The thickness was not monitored during the experiment and so it was not possible to extract values for the absorption and scattering coefficients from the dimensionless optical parameters. The dimensionless parameters shown in Figure 6.10 are the transport albedo ( $a'$ ), the optical depth ( $\tau'$ ), and the delta-Eddington anisotropy ( $g'$ ). The index of refraction was assumed to be constant, despite some evidence that the index of refraction of tissue varies with water content [2]. This assumption was not too extreme since the estimated variation in the index of refraction (1.38 to 1.45) only changed the measured optical properties by 10%.

The most surprising finding is that there is very little change in the trans-

port albedo until after the tissue explodes. At this time there is a slight decrease in the albedo corresponding to the onset of tissue boiling. After the onset of carbonization, the transport albedo drops sharply, indicating an increase in tissue absorption.

The initial drop in the anisotropy corresponds to tissue coagulation or blanching. This decrease indicates that the tissue scatters light more isotropically. Subsequent to the initial fall, the anisotropy increases linearly, corresponding to tissue dehydration and thinning. Thinning reduces the distance between scattering centers thereby increasing the effective size of the scatterers and, as in Mie scattering, the anisotropy as well.

The optical depth depends on the physical thickness of the sample. This thickness changes during irradiation due to tissue dehydration: if the absorption and scattering were constant, the optical depth would still change. The optical depth is quite sensitive to tissue coagulation and substantial changes occur in the first 50–75 seconds.

As expected the most drastic changes in optical properties are associated with charring: the albedo decreased and the delta-Eddington anisotropy  $g'$  increased. Unexpectedly, the effective albedo  $a'$  was relatively constant during coagulation and dehydration. These preliminary experiments illustrate a combined experimental and theoretical technique for measuring the optical properties of tissue during laser irradiation. Although the parameters presented are independent of tissue thickness, evaluation of absorption and scattering coefficients will require measurement of tissue thickness during irradiation.

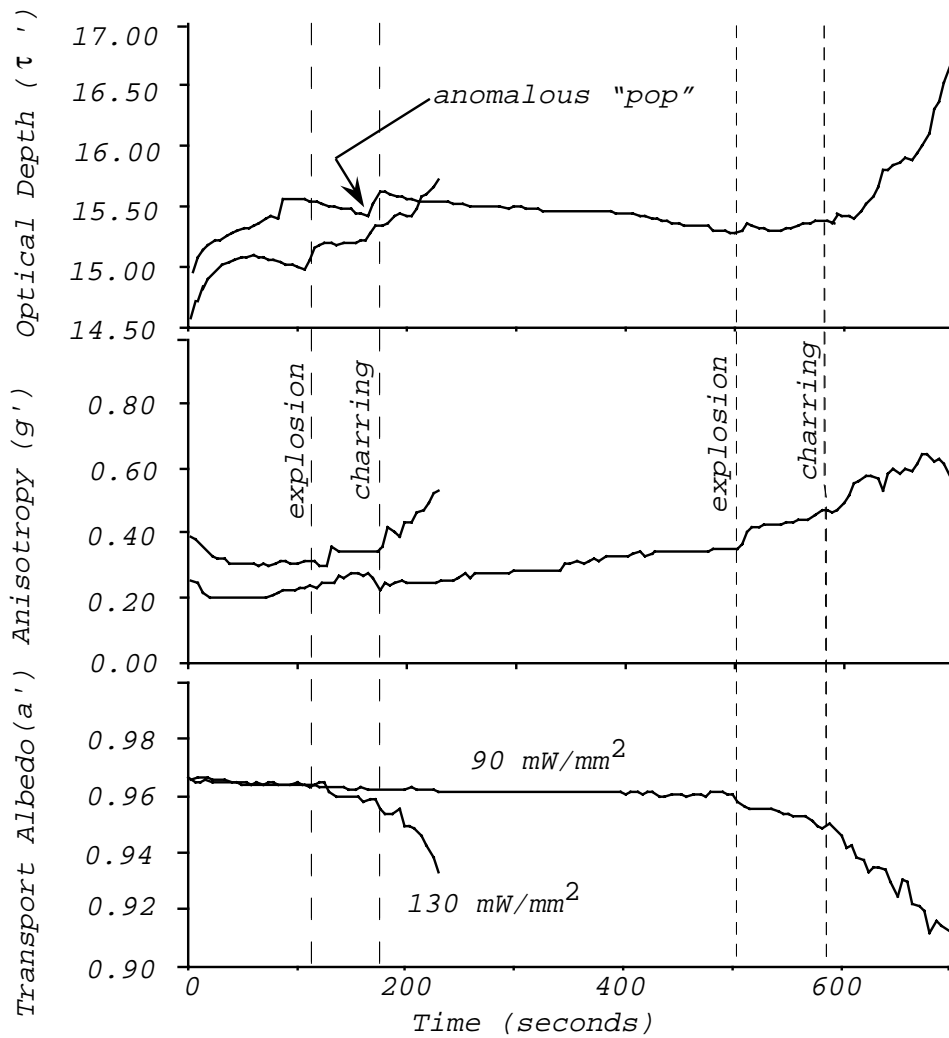


Figure 6.10: Optical properties during argon laser irradiation of normal human aorta. Irradiances of 90 and 130 W/mm<sup>2</sup> are shown. Dashed lines indicate explosions and onset of charring. The anomalous “pop” was probably caused by the presence of plaque in the tissue.

### 6.1.3 Conclusions

This chapter presented a method for measuring the optical properties of a tissue using an iteration technique. This technique is shown to calculate optical properties within ten percent of the “true” optical properties for all sample thicknesses greater than one optical depth. Measurements of the optical properties of human dermis as a function of wavelength and human aorta during moderate power argon irradiation have also been presented.

## Chapter 7

### Conclusions

#### Review

A variable-stepsize, weighted Monte Carlo model was implemented in Chapter 2. This method was validated by comparison with published tables. This model may be used to calculate fluence rates for finite beams by convolving the impulse response with either flat or Gaussian beam irradiation profiles. Analytic expressions that facilitate these calculations have been presented.

An adding-doubling model was implemented with mismatched boundary conditions and anisotropic scattering functions. The adding-doubling method is one-dimensional and a modest number of quadrature angles ( $N = 16$ ) will yield very accurate results (0.01%). The adding-doubling method is not as flexible as the Monte Carlo method, but provides a standard against which other models may be compared. Reflection and transmission Tables 3.1 through 3.6 serve as references for testing and evaluating other models.

A delta-Eddington model was implemented with mismatched boundary conditions and anisotropic scattering in Chapter 4. Comparison of the approximate delta-Eddington solutions with adding-doubling calculations indicates that delta-Eddington approximation works well for calculation of reflection and transmission for all possible optical properties. The delta-Eddington approximation

works moderately well for many fluence rate calculations, but should not be used to calculate fluence rates in tissues with high albedos and mismatched boundary conditions.

A method for measuring the single-scattering phase function of a tissue was presented in Chapter 5. Measurements of reflection and transmission are directly proportional to the phase function for very thin samples. Correction factors for reflection and refraction at boundaries have been presented. The method for measuring the phase function was evaluated using reflection and transmission values computed with the adding-doubling method. Calculation of the anisotropy factor  $g_{\text{HG}}$  was found insensitive to boundary conditions and values of the isotropy factor  $\beta$ . In contradistinction, the values for the isotropy factor  $\beta$  were very sensitive to thickness and boundary conditions—leading to a systematic overestimation of the isotropy factor which could be corrected using Figure 5.9. Experimental measurements on human dermis indicate that the Henyey-Greenstein phase function accurately modeled the phase function with anisotropy coefficient  $g_{\text{HG}} = 0.92$ ,  $\beta = 0.05$  and an average cosine of the phase function  $g = g_{\text{HG}}(1 - \beta) = 0.87$ .

A method for measuring the optical properties of a tissue using an iteration technique was presented in Chapter 6. This technique was shown to calculate optical properties within ten percent of the “true” optical properties for all sample thicknesses greater than one optical depth. Measurements of the optical properties of human dermis as a function of wavelength and human aorta during moderate power argon irradiation were also presented.



## 7.1 Discussion

The novel aspect of this dissertation is that both anisotropic scattering and mismatched boundary conditions are included in light transport models. These phenomena significantly affect light transport and have not been included in tissue models previously. Three different light transport models (the Monte Carlo, the adding-doubling, and the delta-Eddington) have been presented. A method for measuring the phase function of a tissue has been introduced, as well as an indirect method for measuring the optical properties of tissue. The measurement methods and the calculation models are complementary: light transport cannot be modeled without knowing the optical properties of the tissue and the optical properties cannot be determined without an optical model for converting reflection and transmission measurements into optical properties.

Mismatched boundary conditions have a strong influence on fluence rates. For example, in Figure 4.1 the fluence rate at a mismatched surface is twice that for a matched surface. Careful implementation of the boundary conditions in the delta-Eddington model, indicates that this approximation is not particularly good for calculating fluences near mismatched boundaries. This results from using only the first two moments of the radiance distribution to model internal reflection. At the boundaries, highly anisotropic radiance distributions make higher order radiance moments comparable to the lower order moments and the accuracy of the delta-Eddington model suffers accordingly. Consequently, fluence rates for tissues with mismatched boundaries and high anisotropies should not be estimated with the delta-Eddington approximation

Anisotropic scattering also affects the fluence rate in tissue (Figure 4.2). Both the adding-doubling and the Monte Carlo methods are capable of accommo-

dating an arbitrary scattering phase function. Unfortunately, the phase function has not been measured at wavelengths besides 633 nm. The phase function needs to be measured at other wavelengths before accurate light transport calculations may be made.

The adding-doubling method should be used when one-dimensional calculations are needed. Approximate methods like the delta-Eddington approximation should be avoided whenever possible. In particular, it would be desirable to replace the delta-Eddington method with the adding-doubling in the iteration technique of Chapter 6. Preliminary work indicates that the adding-doubling method yields accurate values for reflection and transmission with as few as four quadrature points. Calculations with such a model are only 10–100 times slower than delta-Eddington calculations, and do not suffer from the approximations of the delta-Eddington model.

Finally, the Monte Carlo method cannot be recommended highly enough. This method allows modelling of complex structures without approximation. Perhaps most importantly, the Monte Carlo method is the only reliable method for calculating fluence rates in tissue for finite beam irradiances. In particular, the convolution formulas derived in Chapter 2 allow fluence rate calculation for finite beams to be made quickly, once an impulse response has been calculated. These fluence rates may then be used in a thermal model to calculate tissue damage or ablation.

## Appendices

## Appendix A1

### Random Variables with Non-Uniform Density Functions

#### Introduction

Routines to generate pseudo-random numbers uniformly distributed between zero and one are readily available [15, 49]. In the Monte Carlo method it is often necessary to generate numbers  $\xi$  with specified probability density functions  $p(\xi)$ .

This appendix describes three different methods for generating such random numbers. The first method requires some mathematical analysis, which may be difficult if the probability density function is complicated. The second method is slightly slower than the first, but can be applied to any distribution. The third method is a fast, discrete form of the first method.

#### A1.1 Analytic Method

One method of generating a random number  $\xi$  with a specified distribution  $p(\xi)$  is to create a random event for the variable  $\xi$  such that the random event falls with frequency  $p(x)dx$  in the interval  $(\xi, \xi + d\xi)$ . This method requires the normalization of the probability density function over the interval  $(a, b)$

$$\int_a^b p(\xi) d\xi = 1 \tag{A1.1}$$

This is done by choosing a random number  $R$  uniformly distributed in the interval  $[0, 1]$  and requiring

$$R = \int_a^\xi p(\xi') d\xi' \quad (\text{A1.2})$$

[6, 56]. Note that  $R(\xi)$  represents the cumulative probability distribution function for  $p(\xi')$ .

In the variable stepsize Monte Carlo method, the stepsize is randomly generated based on the probability that the photon will interact in a given distance. If the unnormalized probability density function for the distance  $\Delta s$  is

$$p(\Delta s) = \exp(-\Delta s) \quad (\text{A1.3})$$

then the normalized probability density function over the interval  $(0, \tau)$

$$p(\Delta s) = \frac{\exp(-\Delta s)}{1 - \exp(-\tau)} \quad (\text{A1.4})$$

When the probability density function  $p(\Delta s)$  is substituted into (A1.2), a generating function for  $\Delta s$  is obtained

$$\Delta s = -\ln [1 - R(1 - \exp(-\tau))] \quad (\text{A1.5})$$

If the random variable  $\xi$  is distributed over the interval  $(0, \infty)$  then the appropriate generating function is

$$\Delta s = -\ln(1 - R) \quad (\text{A1.6})$$

Since  $R$  is a random number uniformly distributed between zero and one, so is  $(1 - R)$ . If  $R'$  is a random number uniformly distributed between zero and one, then it may be substituted for  $(1 - R)$  and Equation (A1.6) may be simplified to

$$\Delta s = -\ln R' \quad (\text{A1.7})$$

A normalized phase function describes the probability density function for the azimuthal and longitudinal angles for a photon when it is scattered. If the phase function has no azimuthal dependence, then the azimuthal angle  $\phi$  is uniformly distributed between 0 and  $2\pi$ , and may be generated by multiplying a pseudo-random number  $R$  uniformly distributed over the interval  $[0,1]$  by  $2\pi$

$$\phi = 2\pi R \quad (\text{A1.8})$$

The probability density function for the longitudinal angle  $\theta$  between the current photon direction and the scattered photon direction is found by integrating the phase function over all azimuthal angles  $p(\cos \theta)$ . For example, the probability density function for an isotropic distribution is

$$p(\cos \theta) = \frac{1}{2} \quad (\text{A1.9})$$

Substituting Equation (A1.9) into Equation (A1.2) yields the following generating function for cosine of the longitudinal angle  $\theta$

$$\cos \theta = 2R - 1 \quad (\text{A1.10})$$

The probability density function corresponding to the Henyey-Greenstein phase function is

$$p(\cos \theta) = \frac{1}{2} \frac{1 - g_{\text{HG}}^2}{(1 + g_{\text{HG}}^2 - 2g_{\text{HG}} \cos \theta)^{3/2}} \quad (\text{A1.11})$$

The generating function for this distribution obtained using Equation (A1.2) [68] is

$$\cos \theta = \frac{1}{2g_{\text{HG}}} \left\{ 1 + g_{\text{HG}}^2 - \left[ \frac{1 - g_{\text{HG}}^2}{1 - g_{\text{HG}} + 2g_{\text{HG}}R} \right] \right\} \quad (\text{A1.12})$$

This equation should not be used for isotropic scattering—Equation (A1.10) should be used in that case. The probability density function for the modified Henyey-Greenstein phase function is

$$\cos \theta = \frac{1}{2} \left\{ \beta + \frac{(1 - \beta)(1 - g_{\text{HG}}^2)}{(1 + g_{\text{HG}}^2 - 2g_{\text{HG}} \cos \theta)^{3/2}} \right\} \quad (\text{A1.13})$$

To generate a longitudinal angle with this distribution, two random numbers ( $R_0$  and  $R$ ) uniformly distributed between zero and one are needed. In this distribution, light is either scattered isotropically or anisotropically. The first random number is used to determine which type of scattering occurs. The fraction of light scattered isotropically ( $\beta$ ) is compared with the first random number, if  $\beta < R_0$  then the photon is scattered isotropically according to Equation (A1.10), otherwise the photon is scattered using the generating function given by Equation (A1.12).

## A1.2 Monte Carlo Method

The drawback to using Equation (A1.2) to determine generating function for a particular distribution is that solving for the random variable  $x$  in terms of  $R$  is difficult. A second method, similar to the way integration is done stochastically, is to generate pairs of random numbers. A point  $R_1$  is generated such that  $R_1$  is uniformly distributed over the interval  $(a, b)$  and  $R_2$  over the interval from 0 to the maximum value that the function  $p$  takes on in  $(a, b)$ . If

$$p(R_1) > R_2 \quad (\text{A1.14})$$

then  $R_1$  is the new random variable. Otherwise new points  $R_1$  and  $R_2$  are generated until the condition (A1.14) is satisfied. The speed of this technique

depends on how many unsatisfactory points  $R_1$  and  $R_2$  must be discarded until a good pair is obtained [6].

### **A1.3 Discrete form of the Analytic Method**

A third technique is to divide the interval  $(a, b)$  into a number of pieces. Next create an array such that the number of entries with a particular value  $\xi_1$  is proportional to the value  $p(\xi_1)$ . A random integer uniformly distributed between one and the last entry in this array will serve as the index which selects the new scattering angle.



## Appendix A2

### Internal Reflection

#### Introduction

When light strikes a boundary, the fraction of light reflected depends on the polarization and angle of incidence of the light as well as the ratio of refraction indices between the two media. The first section of this appendix reviews the basic reflection formulas needed for later calculations in this appendix. The second section discusses multiple internal reflection of radiance in a glass slide. The third section calculates the first three moments of Fresnel reflection. The next few sections give details and tables for various approximations for these moments made by other authors. Finally, the last sections calculate a boundary condition parameter used in the boundary conditions of the diffusion (delta-Eddington) approximation.

#### A2.1 Basic Reflection Formulas

The relationship between the angle of incidence and angle of transmission is given by Snell's law

$$n_i \sin \theta_i = n_t \sin \theta_t \tag{A2.1}$$

The angle at which total internal reflection occurs is called the critical angle is obtained by setting  $\theta_t = \pi/2$

$$\theta_c = \sin^{-1} \frac{n_t}{n_i} = \sin^{-1} \frac{1}{n} \quad \text{where} \quad n = \frac{n_i}{n_t} \quad (\text{A2.2})$$

The cosine of the critical angle  $\mu_c$  is then

$$\mu_c = \cos(\sin^{-1} \frac{1}{n}) = \sqrt{1 - \frac{1}{n^2}} \quad (\text{A2.3})$$

Reflection of light at the boundary separating two media of different indices of refraction is dependent on the angle of incidence (Figure A2.3). The reflection is given by the Fresnel equations which depend on the incidence angle ( $\theta_i$ ), the transmission angle ( $\theta_t$ ) and the electric field polarization [30]

$$R_{\parallel} = \frac{\tan(\theta_i - \theta_t)}{\tan(\theta_i + \theta_t)} \quad R_{\perp} = -\frac{\sin(\theta_i - \theta_t)}{\sin(\theta_i + \theta_t)} \quad (\text{A2.4})$$

$$T_{\parallel} = \frac{2 \sin \theta_t \cos \theta_i}{\sin(\theta_i + \theta_t) \cos(\theta_i - \theta_t)} \quad T_{\perp} = \frac{2 \sin \theta_t \cos \theta_i}{\sin(\theta_i + \theta_t)} \quad (\text{A2.5})$$

where  $\parallel$  indicates that the electric field is parallel to the plane of incidence and  $\perp$  indicates that the electric field is perpendicular. The reflected radiance is

$$L_{\text{reflected}} = |R_{*}|^2 L_{\text{incident}} \quad (\text{A2.6})$$

where  $R_{*}$  equals either  $R_{\parallel}$  or  $R_{\perp}$  depending on the polarization. For unpolarized light the net reflection is

$$R(\theta) = \frac{1}{2}(R_{\perp}^2 + R_{\parallel}^2) \quad (\text{A2.7})$$

$$R(\theta_i) = \frac{1}{2} \left[ \frac{\sin^2(\theta_i - \theta_t)}{\sin^2(\theta_i + \theta_t)} + \frac{\tan^2(\theta_i - \theta_t)}{\tan^2(\theta_i + \theta_t)} \right] \quad (\text{A2.8})$$

This formula is not useful for two cases. First, for normal incidence  $\theta_i = \theta_t = 0$  and evaluation of Equation (A2.8) results in division by zero. For normally incident light the correct expression (the limit of Equation (A2.8) as  $\theta \rightarrow 0$ ) is

$$R(\theta = 0) = \frac{(n_i - n_t)^2}{(n_i + n_t)^2} \quad (\text{A2.9})$$

When the incidence angle is larger than the critical angle ( $\theta_i > \theta_c$ ), no transmitted angle exists. This is the case for total internal reflection of light and  $R(\theta) = 1$  when  $\theta > \theta_c$ .

To implement Fresnel reflection at the boundaries in the diffusion approximation, the first few moments of the Fresnel reflection over a hemisphere are required. Defining the zeroth moment  $R_0$  as the integral of the Fresnel reflection over a hemisphere without weighting leads to

$$R_0 = \frac{\int_{2\pi} R(\theta) d\omega}{\int_{2\pi} d\omega} = \int_0^{\pi/2} R(\theta) \sin \theta d\theta \quad (\text{A2.10})$$

The first moment of the Fresnel reflection is obtained by including a  $\cos \theta$  factor

$$R_1 = \frac{\int_{2\pi} R(\theta) \cos \theta d\omega}{\int_{2\pi} \cos \theta d\omega} = 2 \int_0^{\pi/2} R(\theta) \cos \theta \sin \theta d\theta \quad (\text{A2.11})$$

The second moment is found by including a factor of  $\cos^2 \theta$

$$R_2 = \frac{\int_{2\pi} R(\theta) \cos^2 \theta d\omega}{\int_{2\pi} \cos^2 \theta d\omega} = 3 \int_0^{\pi/2} R(\theta) \cos^2 \theta \sin \theta d\theta \quad (\text{A2.12})$$

The reflection moments are normalized such that each is unity when  $R(\theta) \equiv 1$ .

A useful property governing radiance as it travels through media with differing indices of refraction is the  $n^2$ -law of radiance. This law states that the ratio of the radiance over the square of the index of refraction is invariant along a light path

$$\frac{L_1}{n_1^2} = \frac{L_2}{n_2^2}. \quad (\text{A2.13})$$

Figure A2.1 shows the physical basis for this law. As a cone of light passes from  $n_i$  into  $n_t$  the angle of the cone changes due to refraction of light at the interface. Since the same total amount of light passes across the boundary (ignoring reflection) the energy per steradian must change [48].

Finally, a result which relates  $R_1$  for light passing from one medium to another to that for light travelling in the reverse direction is [11]

$$\frac{1 - R_1(n_i/n_t)}{n_t^2} = \frac{1 - R_2(n_t/n_i)}{n_i^2} \quad (\text{A2.14})$$

## A2.2 Fresnel Reflection in a Glass Slide

Consider a radiance ( $L_i/n_i^2$ ) incident from a medium with an index of refraction  $n_i$  on a glass slide ( $n_g$ ) atop a medium into which light is transmitted ( $n_t$ ). The  $n^2$ -law states that, ignoring reflection at boundaries, the ratio of the radiance over the square of the index of refraction is invariant from medium to medium.

$$\frac{L_i}{n_i^2} = \frac{L_g}{n_g^2} = \frac{L_t}{n_t^2}. \quad (\text{A2.15})$$

The problem of multiple internal reflection of radiances in the glass slide is equivalent to the usual multiple internal reflection of light rays (Figure A2.2). The first reflection coefficient ( $r_1$ ) is equal to the Fresnel reflection for light passing from an index of refraction  $n_i$  into  $n_g$  at an angle  $\theta_i$ . The second coefficient ( $r_2$ ) is that for light passing from an index of refraction  $n_g$  into  $n_t$  at an angle  $\theta_g$ . Summing all the transmitted radiances The infinite series can be summed to yield or

$$\begin{aligned} L_{\text{transmitted}} &= L_t(1 - r_1)(1 - r_2) + L_t(1 - r_1)(1 - r_2)r_1r_2 + \\ &+ L_t(1 - r_1)(1 - r_2)(r_1r_2)^2 + \dots \end{aligned} \quad (\text{A2.16})$$

The infinite series can be summed to yield

$$L_{\text{transmitted}} = L_t \left[ 1 - \frac{r_1 + r_2 - 2r_1r_2}{1 - r_1r_2} \right] \quad (\text{A2.17})$$

or

$$L_{\text{transmitted}} = L_t \frac{n_t^2}{n_i^2} \left[ 1 - \frac{r_1 + r_2 - 2r_1r_2}{1 - r_1r_2} \right] \quad (\text{A2.18})$$

The reflected radiance is

$$\begin{aligned} L_{\text{reflected}} &= L_i r_1 + L_i (1 - r_1)^2 r_2 + L_i (1 - r_1)^2 r_2 (r_1 r_2) + \dots \\ &= L_i \left[ \frac{r_1 + r_2 - 2r_1 r_2}{1 - r_1 r_2} \right] \end{aligned} \quad (\text{A2.19})$$

When  $n_i$  exceeds the critical angle at the  $n_i/n_t$  interface, light is totally internally reflected and

$$L_{\text{reflected}} = L_i \quad (\text{A2.20})$$

This suggests that the reflection coefficient at a glass slide boundary may be defined as

$$r'(\hat{\mathbf{s}} \cdot \hat{\mathbf{z}}) = \frac{r_1 + r_2 - 2r_1 r_2}{1 - r_1 r_2} \quad \text{if} \quad \theta_i < \theta_c \quad (\text{A2.21})$$

$$r'(\hat{\mathbf{s}} \cdot \hat{\mathbf{z}}) = 1 \quad \text{if} \quad \theta_i > \theta_c \quad (\text{A2.22})$$

where it is understood that  $r_1 = r(\theta_i)$  is the Fresnel reflection coefficient for light passing from tissue to glass and  $r_2 = r(\theta_g)$  is that for light passing from glass to air. The angle of light passing through the glass  $\theta_g$  is determined using Snell's Law

$$n_{\text{glass}} \sin \theta_g = n_{\text{tissue}} \sin \theta_i \quad (\text{A2.23})$$

### A2.3 Reflection Moments $R_0$ , $R_1$ , and $R_2$

For light incident on a medium with a greater index of refraction, no critical angle exists. Consequently, the Equations (A2.10)–(A2.12) are straightforward numerical integrals in which theta varies from 0 to  $\pi/2$ . When light travels into

a less dense medium, a critical angle exists and the equation for calculating  $R_0$ ,  $R_1$ , and  $R_2$  must be modified. Since  $R(\theta) = 1$  when  $\theta > \theta_c$ ,  $R_0$  becomes

$$R_0 = \int_0^{\theta_c} R(\theta) \sin \theta d\theta + \int_{\theta_c}^{\pi/2} \sin \theta d\theta \quad (\text{A2.24})$$

so

$$R_0 = \mu_c + \int_{\mu_c}^1 R(\mu) d\mu \quad (\text{A2.25})$$

where  $\mu = \cos \theta$  and  $\mu_c = \cos \theta_c$ . Similarly, the other two moments become

$$R_1 = \mu_c^2 + 2 \int_{\mu_c}^1 R(\mu) \mu d\mu \quad (\text{A2.26})$$

and

$$R_2 = \mu_c^3 + 3 \int_{\mu_c}^1 R(\mu) \mu^2 d\mu \quad (\text{A2.27})$$

Depending on the index of refraction ratio, either Equations (A2.10)–(A2.12) or (A2.25)–(A2.27) were used to numerically evaluate the reflection moments. An adaptive eighth-order quadrature algorithm which yields numerical results accurate to any specified tolerance [15] was implemented. In the table below the accuracy is  $\pm 0.001$ . Values for  $R_0$  and  $R_2$  do not exist in the literature, however  $R_1$  values were identical to those of Orchard [46] and Ryde [53, 54].

## A2.4 Star's Approximation

Star [58] has suggested that the Fresnel reflection  $R(\theta)$  be replaced by

$$R(\theta) \begin{cases} 0, & \text{if } \theta < \theta_c; \\ 1, & \text{otherwise.} \end{cases} \quad (\text{A2.28})$$

This is suggested by the step-function behavior of the Fresnel reflection about  $\theta = \theta_c$  as shown in Figure A2.3. This approximation leads to the following

$\frac{n_i}{n_t}$	$R_0$	$R_1$	$R_2$
0.50	0.260	0.161	0.134
0.55	0.241	0.137	0.108
0.60	0.224	0.116	0.087
0.65	0.207	0.097	0.068
0.70	0.190	0.081	0.053
0.75	0.173	0.066	0.040
0.80	0.156	0.053	0.029
0.85	0.136	0.040	0.019
0.90	0.113	0.027	0.011
0.95	0.081	0.015	0.004
1.00	0.001	0.000	0.000
1.05	0.324	0.107	0.036
1.10	0.440	0.195	0.089
1.15	0.518	0.271	0.144
1.20	0.578	0.337	0.199
1.25	0.626	0.395	0.252
1.30	0.665	0.445	0.301
1.35	0.698	0.490	0.347
1.40	0.726	0.530	0.390
1.45	0.750	0.565	0.429
1.50	0.771	0.597	0.465
1.55	0.789	0.626	0.499
1.60	0.805	0.651	0.529
1.65	0.820	0.675	0.558
1.70	0.833	0.696	0.584
1.75	0.845	0.716	0.608
1.80	0.855	0.733	0.631
1.85	0.864	0.749	0.652
1.90	0.873	0.764	0.671
1.95	0.881	0.778	0.689
2.00	0.888	0.791	0.705

Table A2.1: The Fresnel reflection moments  $R_0$ ,  $R_1$ , and  $R_2$ . Light is incident from a medium with an index of refraction of  $n_i$  and transmitted into a medium with index  $n_t$ . The moments in this table are accurate to 0.001.

closed-form equations for calculating  $R_0$ ,  $R_1$ , and  $R_2$ ,

$$R_0^{\text{Star}} = \left[ 1 - \left( \frac{n_t}{n_i} \right)^2 \right]^{1/2} \quad (\text{A2.29})$$

$$R_1^{\text{Star}} = \left[ 1 - \left( \frac{n_t}{n_i} \right)^2 \right] \quad (\text{A2.30})$$

$$R_2^{\text{Star}} = \left[ 1 - \left( \frac{n_t}{n_i} \right)^2 \right]^{3/2} \quad (\text{A2.31})$$

These equations are evaluated in Table A2.2 and compared with the exact values calculated in Section (A2.3) for various ratios of indices of refraction. The differences are nearly constant for all ratios tabulated.

## A2.5 Keijzer's Approximation

Keijzer [39] makes a simple modification of Star's approximation . When  $n_i > n_t$ , Keijzer recommends

$$R(\theta) \begin{cases} R(0), & \text{if } \theta < \theta_c; \\ 1, & \text{otherwise.} \end{cases} \quad (\text{A2.32})$$

Here Keijzer assumed that the reflection coefficient for all angles less than the critical angle equals that for light incident normal to the boundary. The Keijzer approximation results in the following equations for the reflection moments

$$R_0^{\text{Keijzer}} = \mu_c + (1 - \mu_c)R(0) \quad (\text{A2.33})$$

$$R_1^{\text{Keijzer}} = \mu_c^2 + (1 - \mu_c^2)R(0) \quad (\text{A2.34})$$

$$R_2^{\text{Keijzer}} = \mu_c^3 + (1 - \mu_c^3)R(0) \quad (\text{A2.35})$$

Keijzer has suggested the following approximation when  $n_i < n_t$  (Figure A2.4)

$$R^{\text{Keijzer}}(\theta) = \exp(b \cos \theta) \quad (\text{A2.36})$$



$$b = 2 \ln R(\pi/3) \quad (\text{A2.37})$$

where  $R(\pi/3)$  is the Fresnel reflection for an incident angle of  $60^\circ$ . This approximation leads to the following expressions for  $R_0$ ,  $R_1$ , and  $R_2$

$$R_0^{\text{Keijzer}} = \frac{R^2(\pi/3) - 1}{b} \quad (\text{A2.38})$$

$$R_1^{\text{Keijzer}} = 2 \left[ \frac{R^2(\pi/3)(b-1)}{b^2} + \frac{1}{b^2} \right] \quad (\text{A2.39})$$

$$R_2^{\text{Keijzer}} = 3 \left[ \frac{R^2(\pi/3)(b^2 - 2b + 2)}{b^3} - \frac{2}{b^3} \right] \quad (\text{A2.40})$$

The Keijzer approximations for  $R_0$ ,  $R_1$ , and  $R_2$  are shown in Table A2.3. The Keijzer approximation is better than the Star approximation for all cases.

## A2.6 Walsh's Analytic Solution for $R_1$

The integral of the first moment of the Fresnel reflection  $R_1$  has been found analytically by Walsh, (see [53, 54])

$$\begin{aligned} R_1^{\text{Walsh}} &= \frac{1}{2} + \frac{(m-1)(3m+1)}{6(m+1)^2} + \left[ \frac{m^2(m^2-1)^2}{(m^2+1)^3} \right] \ln \frac{m-1}{m+1} \\ &\quad - \frac{2m^3(m^2+2m-1)}{(m^2+1)(m^4-1)} + \left[ \frac{8m^4(m^4+1)}{(m^2+1)(m^4-1)^2} \right] \ln m \end{aligned} \quad (\text{A2.41})$$

where Walsh's parameter  $m$  is the reciprocal of the index of refraction ratio in Equation (A2.2) that is,  $m = 1/n = n_t/n_i$ . Equation (A2.41) was used as a check on the numerical integration of  $R_1$ . Equation (A2.41) is only valid when  $n_i < n_t$  then Equation (A2.14) should be used.

## A2.7 Egan Polynomial Approximation for $R_1$

Another approximation for  $R_1$  is Egan and Hilgeman's [11] polynomial fit of the data of Orchard [46]. Orchard's data was generated using Walsh's formula

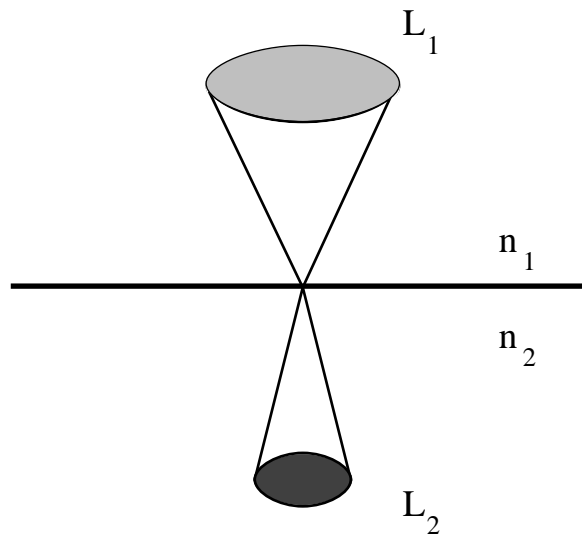


Figure A2.1: The change in radiance passing through media of different indices of refraction. As light passes into a medium with a smaller index of refraction ( $n_1$  to  $n_2$ ) the angle of a cone will increase. The net change in radiance is equal to the square of the indices of refraction.

$\frac{n_i}{n_t}$	$R_0^{\text{Star}}$	$R_1^{\text{Star}}$	$R_2^{\text{Star}}$	$\Delta R_0$	$\Delta R_1$	$\Delta R_2$
1.00	0.000	0.000	0.000	0.000	0.000	0.000
1.10	0.417	0.174	0.072	0.023	0.022	0.016
1.20	0.553	0.306	0.169	0.025	0.032	0.030
1.30	0.639	0.408	0.261	0.026	0.037	0.040
1.40	0.700	0.490	0.343	0.026	0.040	0.047
1.50	0.745	0.556	0.414	0.025	0.041	0.051
1.60	0.781	0.609	0.476	0.025	0.042	0.054
1.70	0.809	0.654	0.529	0.024	0.042	0.055
1.80	0.831	0.691	0.575	0.024	0.042	0.056
1.90	0.850	0.723	0.615	0.023	0.041	0.056

Table A2.2: Comparison of Star's approximation for  $R_0$ ,  $R_1$ , and  $R_2$  with the exact values. The  $\Delta$ 's indicate the difference between the Star approximation and the exact values.

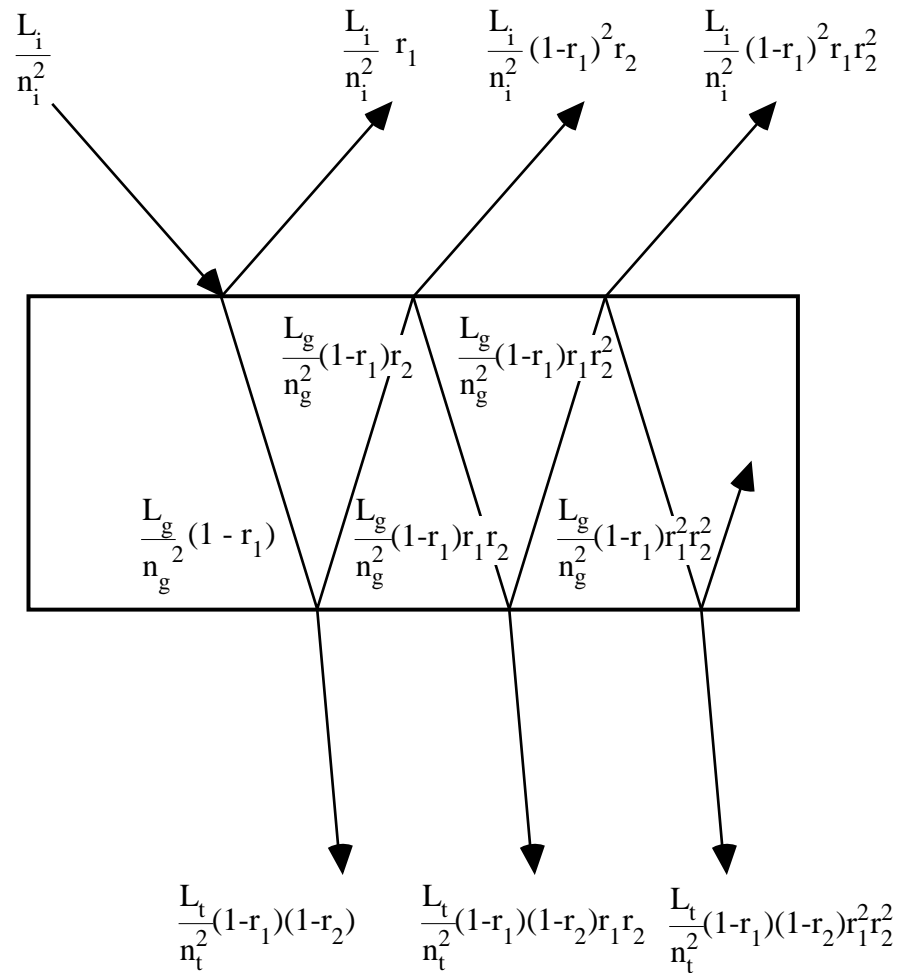


Figure A2.2: Multiple reflections in a glass slide. Light is incident from a medium with an index of refraction  $n_i$ , on a glass slide with index of refraction  $n_g$  and transmitted into a medium with index of refraction  $n_t$ .

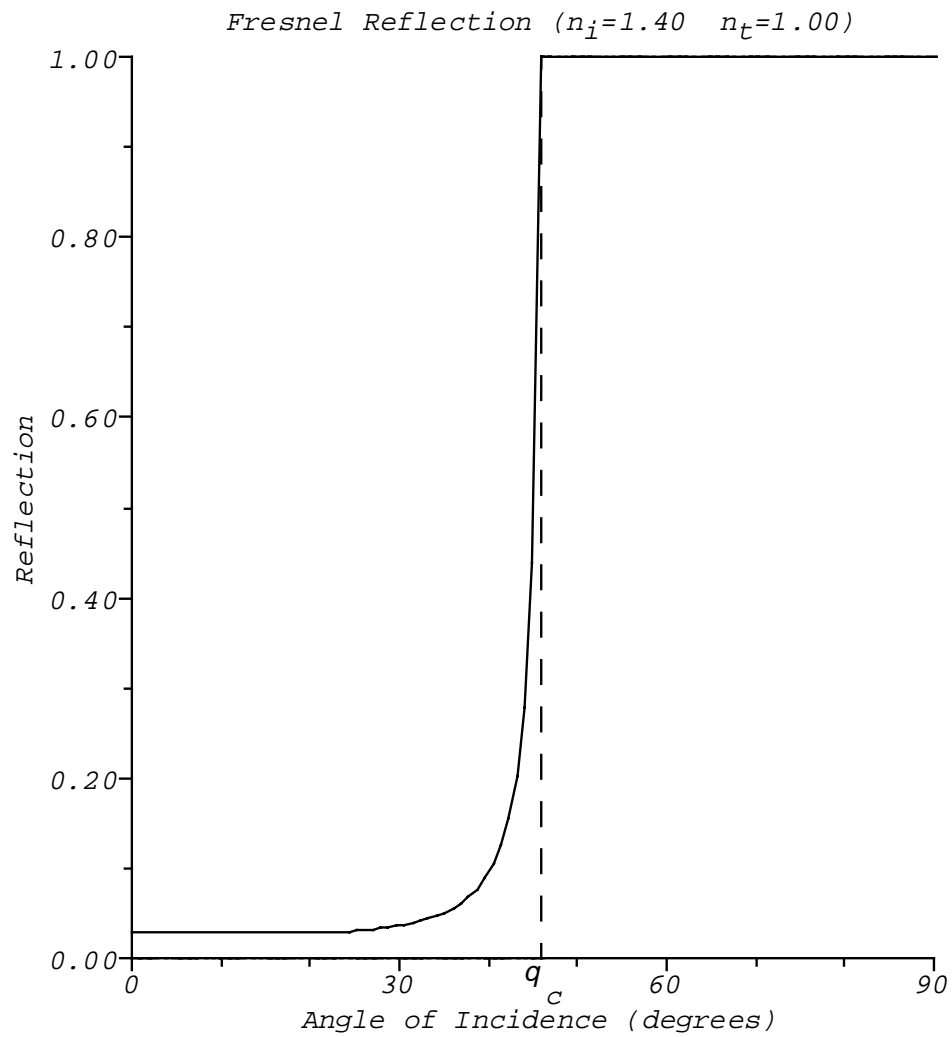


Figure A2.3: The Fresnel Reflection is the solid line. The Star approximation is the dashed line. The Keijzer approximation assumes that when  $\theta \leq \theta_c$ , that the reflection is constant at the normal incidence value  $R(0)$ .

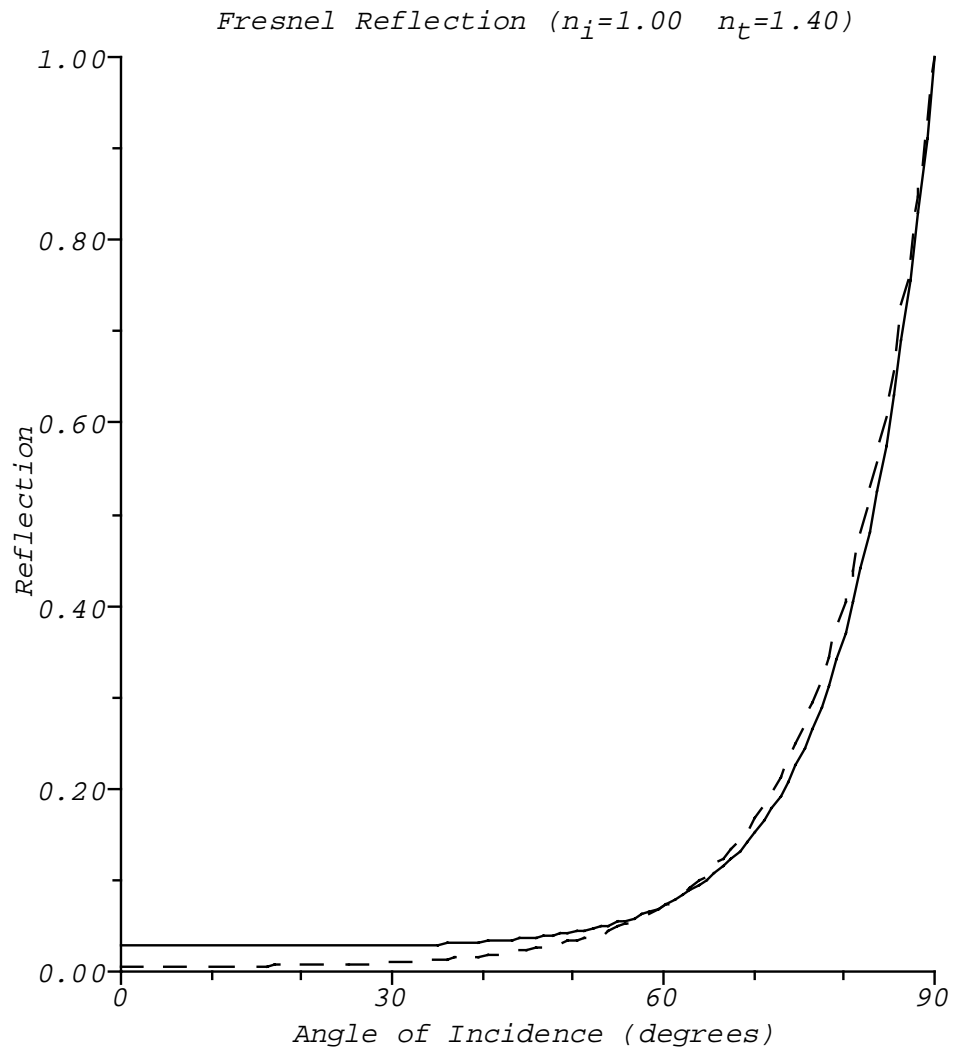


Figure A2.4: Keijzer's approximation (dashed line) compared with the exact value (solid line) of the Fresnel reflection. Notice that the approximation is poor when the angle of incidence is less than sixty degrees.

$n_i/n_t$	$R_0^{\text{Keijzer}}$	$R_1^{\text{Keijzer}}$	$R_2^{\text{Keijzer}}$	$\Delta R_0$	$\Delta R_1$	$\Delta R_2$
0.50	0.267	0.132	0.087	-0.007	0.029	0.047
0.60	0.228	0.100	0.060	-0.005	0.016	0.027
0.70	0.194	0.073	0.039	-0.004	0.008	0.014
0.80	0.159	0.050	0.023	-0.004	0.003	0.006
0.90	0.119	0.029	0.010	-0.007	-0.001	0.001
1.00	0.000	0.000	0.000	0.000	0.000	0.000
1.10	0.418	0.175	0.074	0.022	0.020	0.014
1.20	0.556	0.311	0.176	0.022	0.026	0.024
1.30	0.645	0.418	0.273	0.020	0.027	0.028
1.40	0.708	0.504	0.361	0.017	0.026	0.029
1.50	0.756	0.573	0.438	0.015	0.024	0.028
1.60	0.792	0.630	0.504	0.013	0.021	0.026
1.70	0.822	0.677	0.561	0.011	0.019	0.024
1.80	0.845	0.717	0.610	0.010	0.017	0.021
1.90	0.865	0.750	0.652	0.008	0.015	0.019

Table A2.3: Comparison of Keijzer approximated Fresnel reflection moments with the exact values. The  $\Delta$ 's indicate the difference between the Keijzer values and the exact values. When the index of refraction ratio is larger than one, then the Keijzer approximation is an improvement on the Star approximation. The exponential approximation (A2.36) is not particularly good because it minimizes contributions from angles less than  $60^\circ$  from the normal (Figure A2.4).

(A2.41). The polynomial is

$$R_1^{\text{Egan}} = -0.4399 + 0.7099n^{-1} - 0.3319n^{-2} + 0.0636n^{-3}. \quad (\text{A2.42})$$

where  $n = n_i/n_t < 1$ . If  $n > 1$  then Equation (A2.14) should be used.

In Table A2.4 values for  $R_1$  calculated using the various approximations are presented. Walsh's or Egan's method are superior to the approximations of Star and Keizer. Since the approximate methods are not sufficiently faster, their loss in accuracy dictates that they should not be used.

## A2.8 Polynomial Approximations to $R_0$ , $R_1$ , and $R_2$

The excellent agreement between the Egan approximation for  $R_1$  and the exact values (Table A2.4) suggested making polynomial fits for  $R_0$  and  $R_2$ . For completeness an expression for  $R_1$  is presented also

$$R_0(n) = 2.20714n^3 - 11.0303n^2 + 18.44687n - 9.50765 \quad (\text{A2.43})$$

$$R_1(n) = 0.7857n^3 - 4.3259n^2 + 8.26405n - 4.71306 \quad (\text{A2.44})$$

$$R_2(n) = -0.02043n^3 - 0.38418n^2 + 2.01132n - 1.62198 \quad (\text{A2.45})$$

The accuracy of these expressions is presented in Table A2.5, where it is apparent that the cubic polynomials generate values of  $R_1$  and  $R_2$  accurate to better than 0.005.

## A2.9 Approximations for the Boundary Coefficient $A$

In Section 4.3 a constant  $A$  characterizing the boundary conditions for the diffusion approximation was defined. It depends on the Fresnel moments  $R_1$  and

$n_i/n_t$	$R_1^{\text{exact}}$	$R_1^{\text{Walsh}}$	$R_1^{\text{Egan}}$	$R_1^{\text{Keijzer}}$	$R_1^{\text{Star}}$
0.50	0.161	0.161	0.161	0.132	0.000
0.60	0.116	0.116	0.116	0.100	0.000
0.70	0.081	0.081	0.083	0.073	0.000
0.80	0.053	0.053	0.053	0.050	0.000
0.90	0.027	0.027	0.026	0.029	0.000
1.00	0.000	0.000	0.002	0.000	0.000
1.10	0.195	0.194	0.193	0.175	0.174
1.20	0.337	0.336	0.336	0.311	0.306
1.30	0.445	0.444	0.445	0.418	0.408
1.40	0.530	0.529	0.530	0.504	0.490
1.50	0.597	0.596	0.597	0.573	0.556
1.60	0.651	0.651	0.651	0.630	0.609
1.70	0.696	0.696	0.696	0.677	0.654
1.80	0.733	0.733	0.732	0.717	0.691
1.90	0.764	0.764	0.764	0.750	0.723

Table A2.4: The first moment of the Fresnel reflection calculated using various approximations. The values for  $R_1$  when  $n_i/n_t < 1$  are obtained using Equation (A2.14), except for the Keizer approximation which uses Equation (A2.39). The analytic Walsh values are identical to the numerical (exact) values. The Egan polynomial approximation is much better than either the Keijzer or Star approximations.



$R_2$ ,

$$A = \frac{1 + R_2}{1 - R_1} \quad (\text{A2.46})$$

Values for  $A$  may be calculated three different ways:

1. numerical integration of Equations (A2.10)-(A2.12),
2. Keijzer's approximation, or
3. Star's approximation.

Substituting Equations (A2.34) and (A2.35) into Equation (A2.46) gives,

$$A^{\text{Keijzer}} = \frac{1 + R_2^{\text{Keijzer}}}{1 - R_1^{\text{Keijzer}}} = \frac{1 + \mu_c^3 + (1 - \mu_c^3)R_F(0)}{1 - \mu_c^2 - (1 - \mu_c^2)R_F(0)} \quad (\text{A2.47})$$

which reduces to

$$A^{\text{Keijzer}} = \frac{n(n^2 + 1)}{2} + \left(n - \frac{1}{n}\right) \sqrt{n^2 - 1} \quad (\text{A2.48})$$

Similarly using Equations (A2.30) and (A2.31) yields

$$A^{\text{Star}} = \frac{1 + R_2^{\text{Star}}}{1 - R_1^{\text{Star}}} = \frac{1 + \mu_c^3}{1 - \mu_c^2} = \frac{1 - \mu_c + \mu_c^2}{1 - \mu_c} \quad (\text{A2.49})$$

$$A^{\text{Star}} = n^2 + \frac{(n^2 - 1)^{3/2}}{n} \quad (\text{A2.50})$$

Exact values for  $A$  obtained by calculating  $R_1$  and  $R_2$  numerically are presented in Table A2.6. These values were fitted to a cubic polynomial to find

$$A^{\text{cubic}}(n) = -0.13755n^3 + 4.3390n^2 - 4.90466n + 1.68960 \quad (\text{A2.51})$$

Table A2.6 shows a comparison of the various approximations for  $A$ . The errors resulting from the cubic approximation are an order of magnitude smaller than those from the Star and Keijzer approximations.

$n_i/n_t$	$\Delta R_0$	$\Delta R_1$	$\Delta R_2$
1.000	-0.115	-0.011	0.015
1.100	0.065	0.006	-0.009
1.200	0.019	0.005	-0.004
1.300	-0.016	-0.001	0.002
1.400	-0.029	-0.004	0.005
1.500	-0.023	-0.005	0.003
1.600	-0.005	-0.002	0.000
1.700	0.015	0.002	-0.003
1.800	0.024	0.004	-0.004
1.900	0.012	0.003	-0.002

Table A2.5: Difference between polynomial approximations (A2.43) to (A2.45) of the moments of the Fresnel reflection and the exact values. The approximations for  $R_1$  and  $R_2$  are much better than the approximation for  $R_0$ .

$n_i/n_t$	$A^{\text{exact}}$	$\Delta A^{\text{cubic}}$	$\Delta A^{\text{Keijzer}}$	$\Delta A^{\text{Star}}$
1.00	1.000	0.010	0.000	0.000
1.10	1.353	0.015	-0.050	-0.056
1.20	1.810	0.011	-0.103	-0.683
1.30	2.346	0.004	-0.157	-0.131
1.40	2.955	0.000	-0.211	-0.632
1.50	3.636	-0.001	-0.237	-0.454
1.60	4.388	0.003	-0.322	-0.778
1.70	5.213	0.008	-0.378	-0.610
1.80	6.113	0.016	-0.434	-1.010
1.90	7.089	0.023	-0.490	-1.260

Table A2.6: The boundary condition  $A$  and errors in the cubic polynomial, the Keijzer and the Star approximations. The cubic approximation is much better for nearly all cases.

## A2.10 The Boundary Condition Parameter in the Presence of a Glass Slide

When a glass slide is present at the boundary then the reflection moments  $R_1$  and  $R_2$  must be calculated using the method outlined in Section A2.3. This means that the parameter  $A$  is a function of two variables—the ratio of the index of refraction of the medium to that of the environment and the ratio of the index of refraction of the glass slide to the environment. Since the index of refraction of glass and quartz varies between 1.40 and 1.60, values in this limited range are presented in Table A2.7.

Polynomial approximations for the tabulated values of  $A$  in Table A2.7 are

$$A^{1.00}(n) = -0.13755n^3 + 4.33904n^2 - 4.90466n + 1.68960 \quad (\text{A2.52})$$

$$A^{1.40}(n) = -0.40853n^3 + 5.17127n^2 - 6.33960n + 2.80840 \quad (\text{A2.53})$$

$$A^{1.45}(n) = -0.41535n^3 + 5.16138n^2 - 6.27852n + 2.79732 \quad (\text{A2.54})$$

$$A^{1.50}(n) = -0.42592n^3 + 5.17218n^2 - 6.24603n + 2.79862 \quad (\text{A2.55})$$

$$A^{1.55}(n) = -0.43239n^3 + 5.16867n^2 - 6.19220n + 2.78879 \quad (\text{A2.56})$$

$$A^{1.60}(n) = -0.44400n^3 + 5.19174n^2 - 6.17761n + 2.79812 \quad (\text{A2.57})$$

These values are compared with the exact values in Table A2.8. If indices of refraction of glass are required then it is necessary to interpolate between values given by Equations (A2.53)-(A2.57).

$n_i/n_t$	$A^{1.00}$	$A^{1.40}$	$A^{1.45}$	$A^{1.50}$	$A^{1.55}$	$A^{1.60}$
1.00	1.000	1.253	1.286	1.320	1.354	1.389
1.10	1.353	1.535	1.570	1.606	1.643	1.681
1.20	1.810	1.935	1.971	2.009	2.047	2.087
1.30	2.346	2.411	2.448	2.486	2.526	2.568
1.40	2.955	2.955	2.991	3.030	3.071	3.114
1.50	3.636	3.562	3.597	3.636	3.677	3.721
1.60	4.388	4.232	4.266	4.303	4.344	4.388
1.70	5.213	4.966	4.996	5.032	5.072	5.116
1.80	6.113	5.763	5.790	5.823	5.861	5.904
1.90	7.089	6.626	6.648	6.678	6.713	6.754

Table A2.7: Values of  $A$  for various indices of refraction. Light is incident from a medium ( $n_i$ ), passes through glass ( $n_g$ ), and transmitted into another medium ( $n_t$ ). The superscripts indicate  $n_g/n_t$ .

$n_i/n_t$	$\Delta A^{1.00}$	$\Delta A^{1.40}$	$\Delta A^{1.45}$	$\Delta A^{1.50}$	$\Delta A^{1.55}$	$\Delta A^{1.60}$
1.00	0.014	0.021	0.021	0.021	0.021	0.021
1.10	-0.009	-0.013	-0.013	-0.013	-0.013	-0.013
1.20	-0.005	-0.007	-0.007	-0.006	-0.007	-0.007
1.30	0.002	0.002	0.003	0.002	0.002	0.002
1.40	0.005	0.007	0.007	0.007	0.007	0.007
1.50	0.005	0.006	0.006	0.007	0.006	0.006
1.60	0.001	0.002	0.002	0.002	0.002	0.002
1.70	-0.003	-0.003	-0.004	-0.003	-0.003	-0.003
1.80	-0.005	-0.007	-0.007	-0.007	-0.007	-0.006
1.90	-0.002	-0.003	-0.004	-0.003	-0.004	-0.003

Table A2.8: Differences between of polynomial approximations for  $A$  and the exact values. See caption for Table A2.7 for details.

## Appendix A3

### Solid Angle Integrals and Dirac-Delta Functions

#### Introduction

This appendix explicitly evaluates a number of solid angle vector integrals over entire spheres and hemispheres. It also includes a discussion of the properties of the three-dimensional delta function and various differences in notation between authors.

#### A3.1 Integrals over entire spheres

There are several common integrals over solid angles. The simplest is the integral of a constant over all  $4\pi$  steradians

$$\int_{4\pi} d\omega = \int_{-\pi}^{\pi} d\phi \int_0^{\pi} \sin \theta d\theta = 2\pi \int_{-1}^1 d(\cos \theta) = 2\pi \int_{-1}^1 d\mu = 4\pi \quad (\text{A3.1})$$

Here the  $4\pi$  beneath the integral is used to indicate that the integral is done over all  $4\pi$  steradians. The angles  $\phi$  and  $\theta$  refer to the usual azimuthal and longitudinal angles in a spherical geometry. The differential  $d\omega = \sin \theta d\theta d\phi$  is a differential solid angle with  $\hat{\mathbf{s}}$  as an outward normal unit vector. The substitution  $\mu = \cos \theta$  has been made.

The integral of  $\hat{\mathbf{s}}$  over all angles is zero, by symmetry

$$\int_{4\pi} \hat{\mathbf{s}} d\omega = 0 \quad (\text{A3.2})$$

The integral is zero because for each  $\hat{\mathbf{s}}$  in the upper hemisphere there is a unit vector  $\hat{\mathbf{s}}'$  in the lower hemisphere pointed in the opposite direction (Figure A3.1a). When  $\hat{\mathbf{s}}$  is integrated over all angles then the contribution from the upper hemisphere is exactly cancelled by that from the lower hemisphere.

The next integral is slightly more complicated

$$\int_{4\pi} \hat{\mathbf{s}}(\hat{\mathbf{s}} \cdot \mathbf{A}) d\omega = \frac{4\pi}{3} \mathbf{A} \quad (\text{A3.3})$$

The vertical axis is chosen parallel to the arbitrary vector  $\mathbf{A}$  (Figure A3.1b). The vector  $\hat{\mathbf{s}}(\hat{\mathbf{s}} \cdot \mathbf{A})$  has a magnitude of  $|\mathbf{A}| \cos \theta$ . Now choose a vector  $\hat{\mathbf{s}}'$ , such that  $\hat{\mathbf{s}}' \cdot \mathbf{A} = \hat{\mathbf{s}} \cdot \mathbf{A}$  and such that  $\hat{\mathbf{s}}'$ ,  $\hat{\mathbf{s}}$  and  $\mathbf{A}$  are co-planar. From Figure A3.1b it is evident that adding  $\hat{\mathbf{s}}'(\hat{\mathbf{s}}' \cdot \mathbf{A})$  to  $\hat{\mathbf{s}}(\hat{\mathbf{s}} \cdot \mathbf{A})$  results in a vector in the  $\mathbf{A}$  direction. The magnitude of the vector sum is the projection of each of these vectors onto  $\mathbf{A}$ . Since the magnitude of  $\hat{\mathbf{s}}'(\hat{\mathbf{s}}' \cdot \mathbf{A})$  is equal to that of  $\hat{\mathbf{s}}(\hat{\mathbf{s}} \cdot \mathbf{A})$ , we have

$$\hat{\mathbf{s}}(\hat{\mathbf{s}} \cdot \mathbf{A}) + \hat{\mathbf{s}}'(\hat{\mathbf{s}}' \cdot \mathbf{A}) = 2(|\mathbf{A}| \cos \theta) \cos \theta \frac{\mathbf{A}}{|\mathbf{A}|} = 2 \cos^2 \theta \mathbf{A} \quad (\text{A3.4})$$

The integral (A3.3) is then

$$\int_{4\pi} \hat{\mathbf{s}}(\hat{\mathbf{s}} \cdot \mathbf{A}) d\omega = \int_0^\pi d\phi \int_0^\pi 2\mathbf{A} \cos^2 \theta \sin \theta d\theta = 2\pi \mathbf{A} \int_{-1}^1 \mu^2 d\mu = \frac{4\pi}{3} \mathbf{A} \quad (\text{A3.5})$$

The azimuthal integral in  $\phi$  is done only from 0 to  $\pi$  to account for adding  $\hat{\mathbf{s}}'$  and  $\hat{\mathbf{s}}$  in Equation (A3.4).

The next integral is

$$\int_{4\pi} \hat{\mathbf{s}}(\hat{\mathbf{s}} \cdot \mathbf{A})(\hat{\mathbf{s}} \cdot \mathbf{B}) d\omega = 0 \quad (\text{A3.6})$$

This integral is evaluated by decomposing  $\mathbf{B}$  into components parallel and perpendicular to  $\mathbf{A}$

$$\mathbf{B} = \mathbf{B}_\perp + \mathbf{B}_\parallel \quad (\text{A3.7})$$

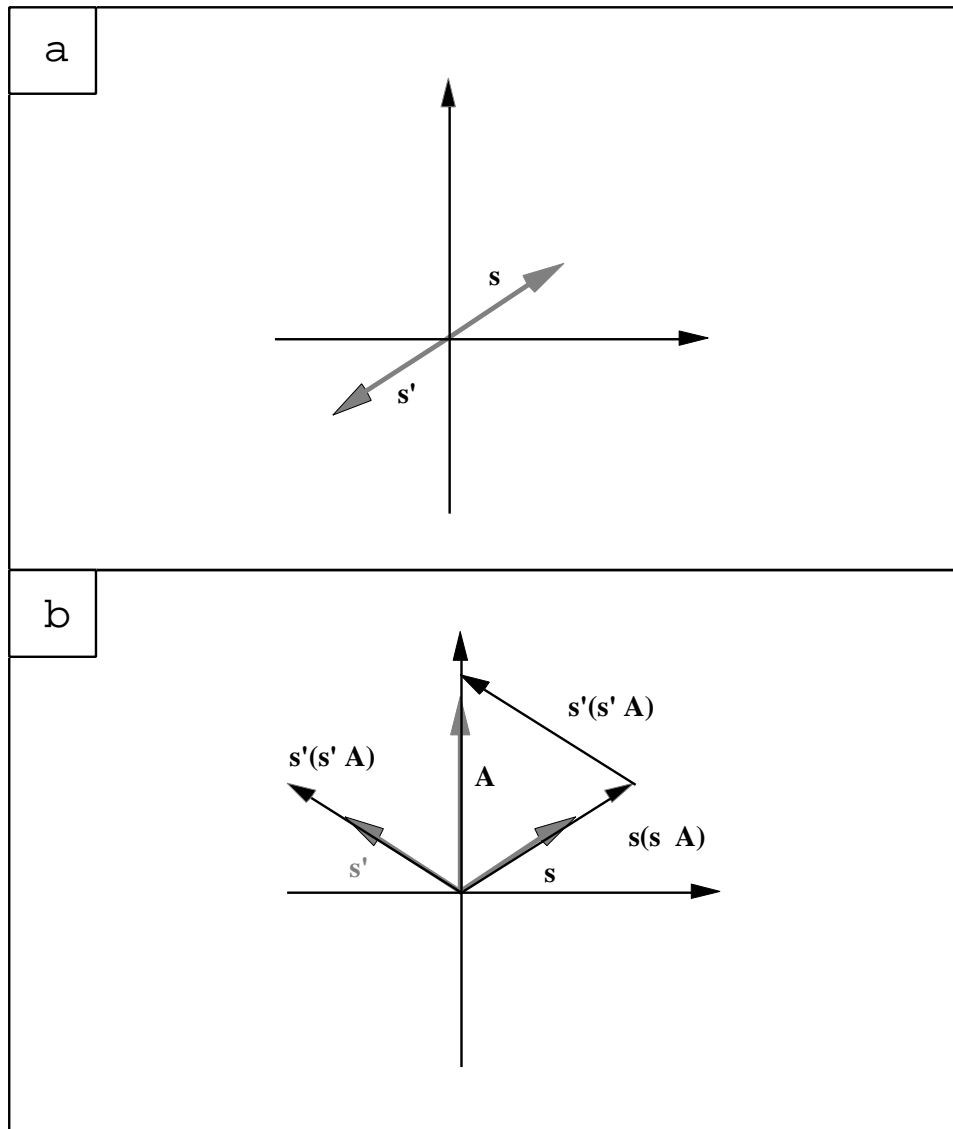


Figure A3.1: Geometry used to evaluate integrals (A3.2) and (A3.3).

The integral in Equation (A3.6) becomes

$$\int_{4\pi} \hat{\mathbf{s}}(\hat{\mathbf{s}} \cdot \mathbf{A})(\hat{\mathbf{s}} \cdot \mathbf{B}_{\parallel}) d\omega + \int_{4\pi} \hat{\mathbf{s}}(\hat{\mathbf{s}} \cdot \mathbf{A})(\hat{\mathbf{s}} \cdot \mathbf{B}_{\perp}) d\omega = 0 \quad (\text{A3.8})$$

The first integral is very similar to Equation (A3.3). The difference is an additional factor of  $\mathbf{B} \cos \theta$ , i.e.,

$$\begin{aligned} \int_{4\pi} \hat{\mathbf{s}}(\hat{\mathbf{s}} \cdot \mathbf{A})(\hat{\mathbf{s}} \cdot \mathbf{B}_{\parallel}) d\omega &= \int_0^{\pi} d\phi \int_0^{\pi} 2\mathbf{A} \cos^2 \theta (|\mathbf{B}_{\parallel}| \cos \theta) \sin \theta d\theta \\ &= 2\pi \mathbf{A} |\mathbf{B}_{\parallel}| \int_{-1}^1 \mu^3 d\mu = 0 \end{aligned} \quad (\text{A3.9})$$

The second integral is evaluated by referring to Figure A3.2a. If  $\hat{\mathbf{s}}'$  is chosen as in Figure A3.2a, then

$$\begin{aligned} \hat{\mathbf{s}} \cdot \mathbf{A} &= |\mathbf{A}| \cos \theta & \hat{\mathbf{s}} \cdot \mathbf{B}_{\perp} &= |\mathbf{B}_{\perp}| \sin \theta \\ \hat{\mathbf{s}}' \cdot \mathbf{A} &= -|\mathbf{A}| \cos \theta & \hat{\mathbf{s}}' \cdot \mathbf{B}_{\perp} &= -|\mathbf{B}_{\perp}| \sin \theta \end{aligned}$$

It is clear that  $\hat{\mathbf{s}}(\hat{\mathbf{s}} \cdot \mathbf{A})(\hat{\mathbf{s}} \cdot \mathbf{B}_{\perp}) + \hat{\mathbf{s}}'(\hat{\mathbf{s}}' \cdot \mathbf{A})(\hat{\mathbf{s}}' \cdot \mathbf{B}_{\perp}) = 0$  since both vectors have the same magnitude and are pointed in opposite directions.

Using the previously computed vector integrals two common scalar integrals may be found. For example, using Equation (A3.2)

$$\int_{4\pi} (\hat{\mathbf{s}} \cdot \mathbf{A}) d\omega = \mathbf{A} \cdot \int_{4\pi} \hat{\mathbf{s}} d\omega \quad (\text{A3.10})$$

and using Equation (A3.3)

$$\int_{4\pi} (\hat{\mathbf{s}} \cdot \mathbf{A})(\hat{\mathbf{s}} \cdot \mathbf{B}) d\omega = \mathbf{B} \cdot \int_{4\pi} \hat{\mathbf{s}}(\hat{\mathbf{s}} \cdot \mathbf{A}) d\omega = \frac{4\pi}{3} (\mathbf{A} \cdot \mathbf{B}) \quad (\text{A3.11})$$

## A3.2 Integrals over hemispheres

The integral of a unit vector  $\hat{\mathbf{s}}$  over a hemisphere with the  $z$ -axis as its pole is obtained by summing vectors as in Figure A3.2, but omitting the extra factor



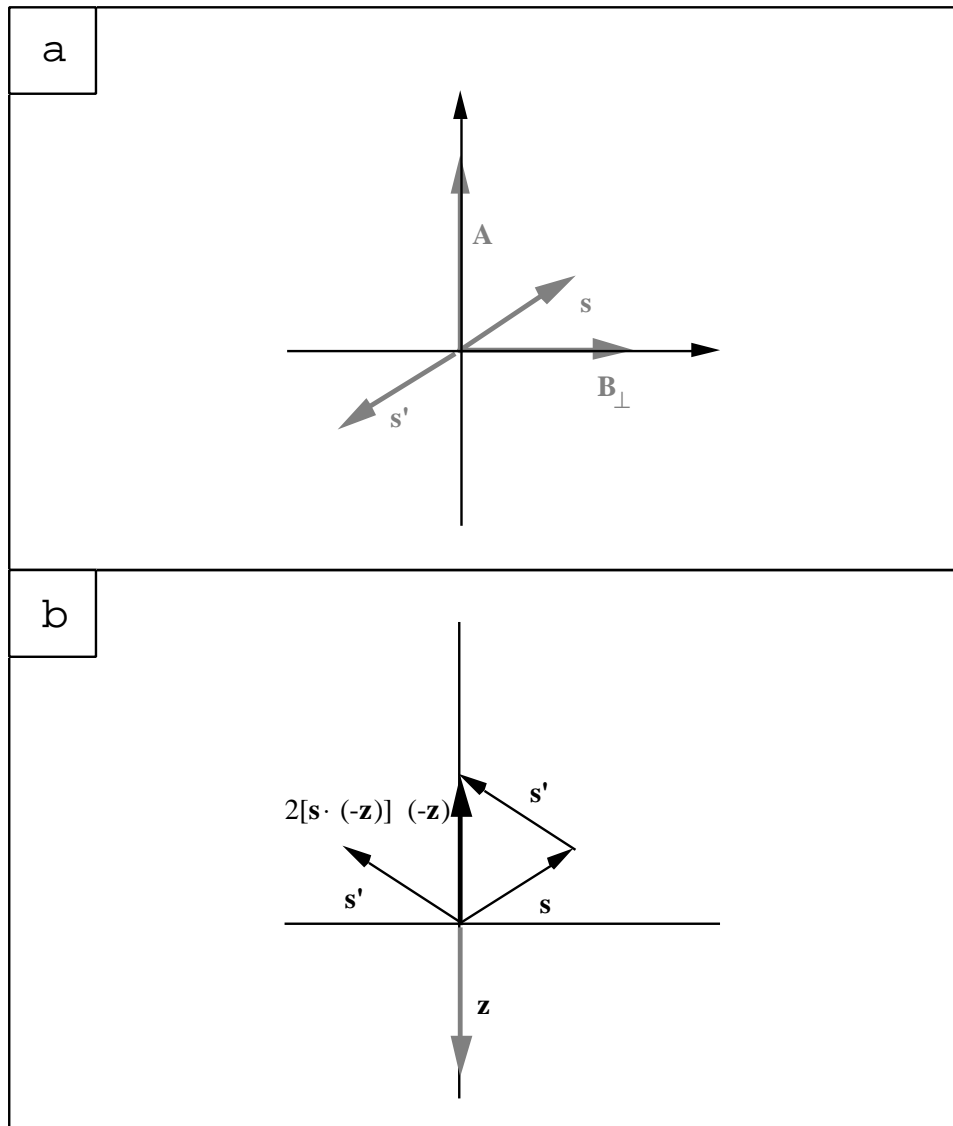


Figure A3.2: Figures for integrals (A3.6) and (A3.12).

of  $\cos \theta$

$$\int_{2\pi} \int_{\mu \geq 0} \hat{\mathbf{s}} \, d\omega = \hat{\mathbf{z}} \int_0^\pi d\phi \int_0^{\pi/2} 2 \cos \theta \sin \theta \, d\theta = 2\pi \hat{\mathbf{z}} \int_0^1 \mu \, d\mu = \pi \hat{\mathbf{z}} \quad (\text{A3.12})$$

Because the integral over the  $\mu \leq 0$  hemisphere is oriented in the opposite direction from the above integral, care must be taken to ensure that signs remain consistent. In Figure A3.3 the vectors in the  $\mu \leq 0$  hemisphere add to a vector in the  $-z$  direction.

$$\int_{2\pi} \int_{\mu \leq 0} \hat{\mathbf{s}} \, d\omega = -\hat{\mathbf{z}} \int_0^\pi d\phi \int_{\pi/2}^\pi (-2 \cos \theta) \sin \theta \, d\theta = 2\pi(-\hat{\mathbf{z}}) \int_{-1}^0 (-\mu) \, d\mu = -\pi \hat{\mathbf{z}} \quad (\text{A3.13})$$

Clearly, the sum of the integrals over each hemisphere equals zero—the result for the integral over the whole sphere (Equation A3.2). The following integrals follow immediately from (A3.12) and (A3.13)

$$\frac{1}{4\pi} \int_{2\pi} \int_{\mu \geq 0} (\hat{\mathbf{z}} \cdot \hat{\mathbf{s}}) \, d\omega = \frac{1}{4} \quad (\text{A3.14})$$

and

$$\frac{1}{4\pi} \int_{2\pi} \int_{\mu \leq 0} (-\hat{\mathbf{z}} \cdot \hat{\mathbf{s}}) \, d\omega = \frac{1}{4} \quad (\text{A3.15})$$

Figure A3.3 shows how the vectors may be combined in a similar fashion to evaluate the following integral

$$\int_{2\pi} \int_{\mu \geq 0} \hat{\mathbf{s}} (\hat{\mathbf{z}} \cdot \hat{\mathbf{s}}) \, d\omega = \hat{\mathbf{z}} \int_0^\pi d\phi \int_0^{\pi/2} 2 \cos^2 \theta \sin \theta \, d\theta = 2\pi \hat{\mathbf{z}} \int_0^1 \mu^2 \, d\mu = \frac{2\pi}{3} \hat{\mathbf{z}} \quad (\text{A3.16})$$

The integral over the other hemisphere is

$$\begin{aligned} \int_{2\pi} \int_{\mu \leq 0} \hat{\mathbf{s}} (-\hat{\mathbf{z}} \cdot \hat{\mathbf{s}}) \, d\omega &= -\hat{\mathbf{z}} \int_0^\pi d\phi \int_{\pi/2}^\pi 2 \cos^2 \theta \sin \theta \, d\theta \\ &= -2\pi \hat{\mathbf{z}} \int_{-1}^0 \mu^2 \, d\mu = -\frac{2\pi}{3} \hat{\mathbf{z}} \end{aligned} \quad (\text{A3.17})$$

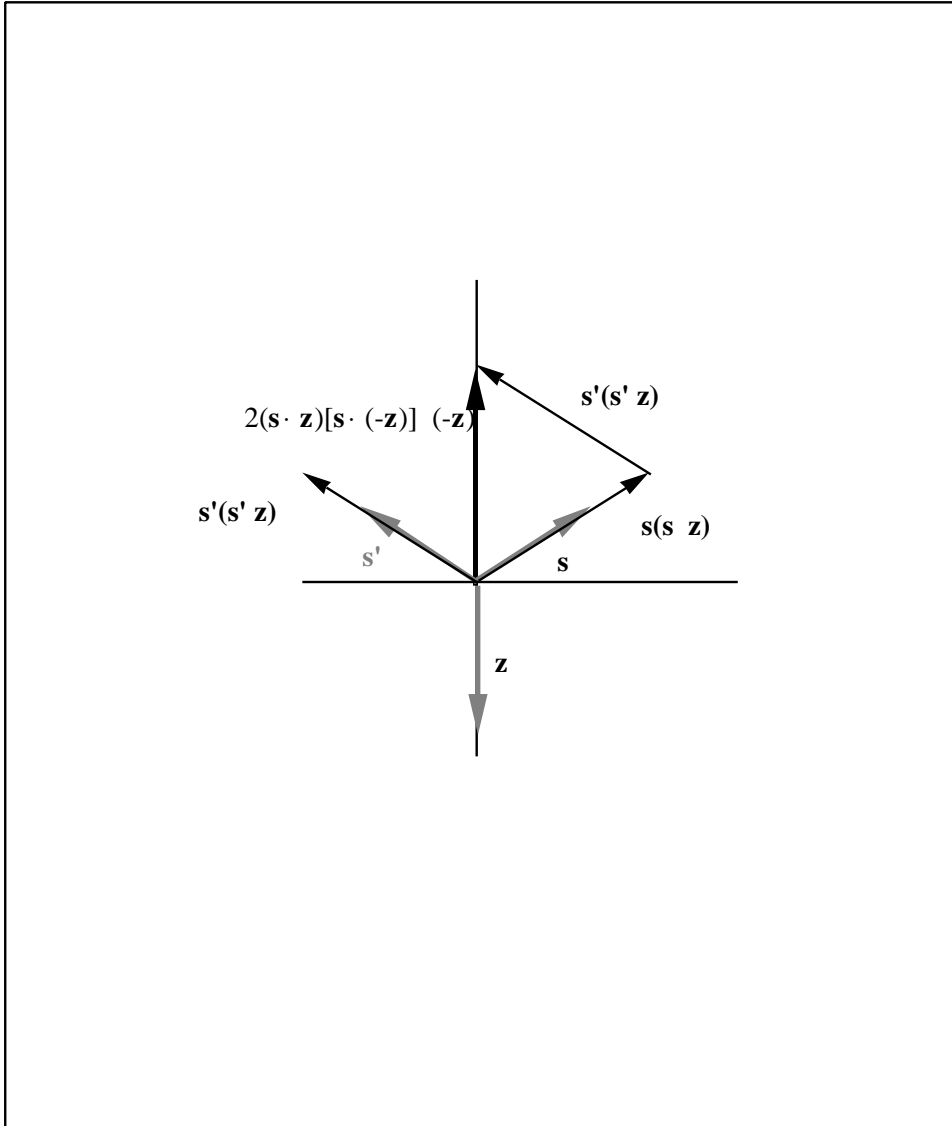


Figure A3.3: Geometry for integral (A3.16).

### A3.3 Delta functions

The delta function used in radiative transport calculations differs slightly from the usual form of a delta function. It has the usual properties: it is zero if  $\hat{\mathbf{s}} \neq \hat{\mathbf{s}}'$

$$\delta(\hat{\mathbf{s}} - \hat{\mathbf{s}}') = 0, \quad \text{if} \quad \hat{\mathbf{s}} \neq \hat{\mathbf{s}}' \quad (\text{A3.18})$$

and the integral of the delta function with another function equals that function evaluated at  $\hat{\mathbf{s}}' = \hat{\mathbf{s}}$

$$\int_{4\pi} f(\hat{\mathbf{s}}') \delta(\hat{\mathbf{s}} - \hat{\mathbf{s}}') d\omega' = f(\hat{\mathbf{s}}) \quad (\text{A3.19})$$

The delta function  $\delta(\hat{\mathbf{s}} - \hat{\mathbf{s}}')$  is two-dimensional and is written as the product of two ordinary Dirac delta functions [7]

$$\delta(\hat{\mathbf{s}} - \hat{\mathbf{s}}') = \delta(\mu - \mu') \delta(\phi - \phi') \quad (\text{A3.20})$$

where  $\hat{\mathbf{s}}$  and  $\hat{\mathbf{s}}'$  are described by the angle pairs  $(\theta, \phi)$  and  $(\theta', \phi')$  on the unit circle and  $\mu = \cos \theta$  and  $\mu' = \cos \theta'$ . To write Equation (A3.20) in terms of  $\theta$  instead of  $\mu$  then using the property [51] of delta functions that

$$\delta(f(x)) = \frac{\delta(x - x_0)}{|f'(x_0)|} \quad (\text{A3.21})$$

where  $f(x)$  is a function which vanishes only at  $x_0$ . This property may be used because the integrals are done over the sphere and consequently,  $(\cos \theta' - \cos \theta)$  will vanish at one point. The following relation may be obtained

$$\delta(\hat{\mathbf{s}} - \hat{\mathbf{s}}') = \frac{\delta(\theta - \theta') \delta(\phi - \phi')}{|\sin \theta|} \quad (\text{A3.22})$$

Equation (A3.20) is valid as long as neither  $\hat{\mathbf{s}}$  nor  $\hat{\mathbf{s}}'$  coincide with the  $z$ -axis. In this case, the azimuthal coordinate is an ignorable coordinate [51] and the expression for the delta function becomes

$$\delta(\hat{\mathbf{s}} - \hat{\mathbf{z}}) = \frac{1}{2\pi} \delta(1 - \mu) \quad (\text{A3.23})$$

This ensures that the integral over all angles remains unity. Equations (A3.23) and (A3.21) relate a solid angle delta function depending only on one parameter with the usual two parameter definition [34]

$$\delta(1 - \cos \theta) = 2\pi\delta(\mu - \mu')\delta(\phi - \phi') \quad (\text{A3.24})$$

where  $\cos \theta$  is the angle between the direction specified by  $(\mu, \phi)$  and  $(\mu', \phi')$

$$\cos \theta = \mu\mu' + \sqrt{1 - \mu^2}\sqrt{1 - \mu'^2} \cos(\phi - \phi') \quad (\text{A3.25})$$

### A3.4 Examples of Delta Functions

Collimated light is often modelled with a Dirac delta function, In particular, if light is incident from the direction  $\hat{\mathbf{s}}'$  then the radiant intensity is written

$$I(\mathbf{r}, \hat{\mathbf{s}}) = E_0(\mathbf{r})\delta(1 - \hat{\mathbf{s}} \cdot \hat{\mathbf{s}}') \quad (\text{A3.26})$$

where  $I$  is the radiant intensity [W/cm<sup>2</sup>/sr],  $E_0$  is the irradiance [W/cm<sup>2</sup>], and the Dirac delta function has units of 1/sr. The integral of the radiance over all angles is the irradiance  $E_0$  since

$$\int_{4\pi} \delta(1 - \hat{\mathbf{s}} \cdot \hat{\mathbf{z}}) d\omega = \int_{-\pi}^{\pi} d\phi \int_{-1}^1 \frac{1}{2\pi} \delta(\mu - 1) d\mu = 1 \quad (\text{A3.27})$$

The integral of the delta-Eddington phase function

$$P_{\text{delta-E}}(\cos \theta) = \frac{1}{4\pi} \{2f\delta(1 - \cos \theta) + (1 - f)(1 + 3g' \cos \theta)\} \quad (\text{A3.28})$$

over all angles is unity since

$$\int_{4\pi} 2f\delta(1 - \cos \theta) d\omega = 2f \int_{-\pi}^{\pi} \delta(\phi - \phi') d\phi \int_{-1}^1 2\pi\delta(\mu - \mu') d\mu = 4\pi f \quad (\text{A3.29})$$

and

$$\int_{4\pi} (1 - f)(1 + 3g' \cos \theta) d\omega = 4\pi(1 - f) \quad (\text{A3.30})$$

## Appendix A4

### Numerical Details of the 3D Diffusion Solution

#### Introduction

This appendix bounds the  $k_n$ th eigenvalue of the diffusion equation. Formulas for evaluating the infinite sums necessary to find the diffuse radiance are discussed.

#### A4.1 Eigenvalues

The eigenvalues  $k_n$  of the diffusion Equation (4.109) are solutions to the following transcendental equation.

$$\tan k_n \tau' = \frac{(A_{\text{top}} + A_{\text{bottom}})h'k_n}{A_{\text{top}}A_{\text{bottom}}(h'k_n)^2 - 1} \quad (\text{A4.1})$$

This equation must be solved numerically. A number of numerical methods (e.g., Newton's method, interval bisection) exist that will solve

$$\tan k_n \tau' - \frac{(A_{\text{top}} + A_{\text{bottom}})h'k_n}{A_{\text{top}}A_{\text{bottom}}(h'k_n)^2 - 1} = 0 \quad (\text{A4.2})$$

but all require that local root  $k_n$  be bounded above and below. This section gives bounds for each eigenvalues. The function  $\tan(k_n \tau')$  has singularities whenever

$$k_n = \frac{(2n + 1)\pi}{2\tau'} \quad (\text{A4.3})$$

and the R.H.S. of Equation (A4.10) has a double pole when

$$k_{\text{pole}} = \frac{1}{h' \sqrt{A_{\text{top}} A_{\text{bottom}}}} \quad (\text{A4.4})$$

The two cases which arise are discussed in the next two sections.

#### A4.1.1 One eigenvalue less than $\pi/2\tau'$

If

$$\frac{1}{h'\sqrt{A_{\text{top}}A_{\text{bottom}}}} < \frac{\pi}{2\tau'} \quad (\text{A4.5})$$

then there is exactly one eigenvalue between zero and  $\pi/2\tau'$ . This case is shown in Figure A4.1. The ordinates of the intersections of the two curves are the eigenvalues  $k_n$ . There are an infinite number of eigenvalues. The first eigenvalue is bounded by

$$\frac{1}{h'\sqrt{A_{\text{top}}A_{\text{bottom}}}} < k_1 < \frac{\pi}{2\tau'} \quad (\text{A4.6})$$

Furthermore, due to the periodicity of the tangent there is always one eigenvalue in the interval

$$(n-1)\frac{\pi}{\tau'} < k_n < \left(n - \frac{1}{2}\right)\frac{\pi}{\tau'} \quad \text{if} \quad n > 1 \quad (\text{A4.7})$$

Moreover, since the R.H.S. of Equation (A4.1) monotonically decreases for  $k_n > k_{\text{pole}}$ , each successive eigenvalue is closer to a zero value of the tangent  $n\pi/\tau'$  than the preceding one,

$$k_n - (n-1)\frac{\pi}{\tau'} > k_{n+1} - \frac{n\pi}{\tau'} \quad \text{if} \quad n > 1 \quad (\text{A4.8})$$

The  $n$ th eigenvalue is therefore bounded by

$$(n-1)\frac{\pi}{\tau'} < k_n < k_{n-1} + \frac{\pi}{\tau'} \quad \text{if} \quad n > 1 \quad (\text{A4.9})$$

Finally, as  $n$  increases the eigenvalues approach the zeros of  $\tan(n\pi/\tau')$

$$k_n \rightarrow \frac{(n-1)\pi}{\tau'} \quad \text{as} \quad n \rightarrow \infty \quad (\text{A4.10})$$

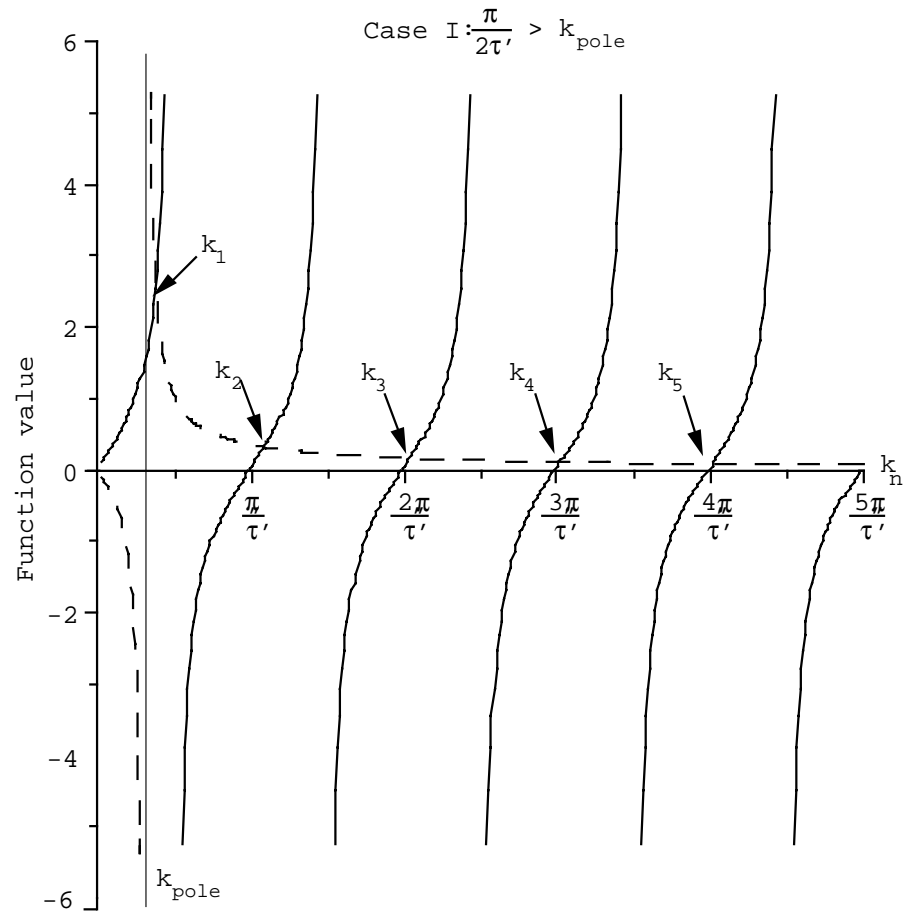


Figure A4.1: Eigenvalues of the diffusion equation. The dotted line represents the RHS of Equation (A4.1) and the solid lines correspond to the LHS. The functions are plotted as a function of  $k_n$ . The ordinate of an intersection of the dashed line with a solid line represents an eigenvalue  $k_n$ . Notice that the intersections approach  $(n - 1)\pi/\tau'$  for large  $n$ .



#### A4.1.2 More than one eigenvalue less than $\pi/2\tau'$

If

$$\frac{1}{h' \sqrt{A_{\text{top}} A_{\text{bottom}}}} > \frac{\pi}{2\tau'} \quad (\text{A4.11})$$

at least two eigenvalues less than  $\pi/2\tau'$  exist (Figure A4.2). For all eigenvalues less than  $k_{\text{pole}}$  (Equation (A4.4), the following criteria holds

$$(2n-1)\frac{\pi}{2\tau'} < k_n < k_{n-1} + \frac{\pi}{\tau'} \quad \text{if} \quad n > 1 \quad \text{and} \quad k_n < k_{\text{pole}} \quad (\text{A4.12})$$

with the first eigenvalue bounded by

$$\frac{\pi}{2\tau'} < k_1 < \frac{\pi}{\tau'} \quad (\text{A4.13})$$

For eigenvalues  $k_n$  larger than  $k_{\text{pole}}$  the first such eigenvalue is bounded by

$$k_{\text{pole}} < k_n < \frac{n\pi}{n} \quad (\text{A4.14})$$

and subsequent eigenvalues are bounded by

$$(n-1)\frac{\pi}{\tau'} < k_n < k_{n-1} + \frac{\pi}{\tau'} \quad (\text{A4.15})$$

Finally, the asymptotic behavior of the eigenvalues is the same as shown in the previous section

$$k_n \rightarrow \frac{(n-1)\pi}{\tau'} \quad \text{as} \quad n \rightarrow \infty \quad (\text{A4.16})$$

## A4.2 Summation of series

In the previous section it was shown that for large  $N$ , that is, when  $k_N \gg k_{\text{pole}}$  the eigenvalue approaches

$$k_N \rightarrow \frac{(N-1)\pi}{\tau'} \quad \text{as} \quad N \rightarrow \infty \quad (\text{A4.17})$$

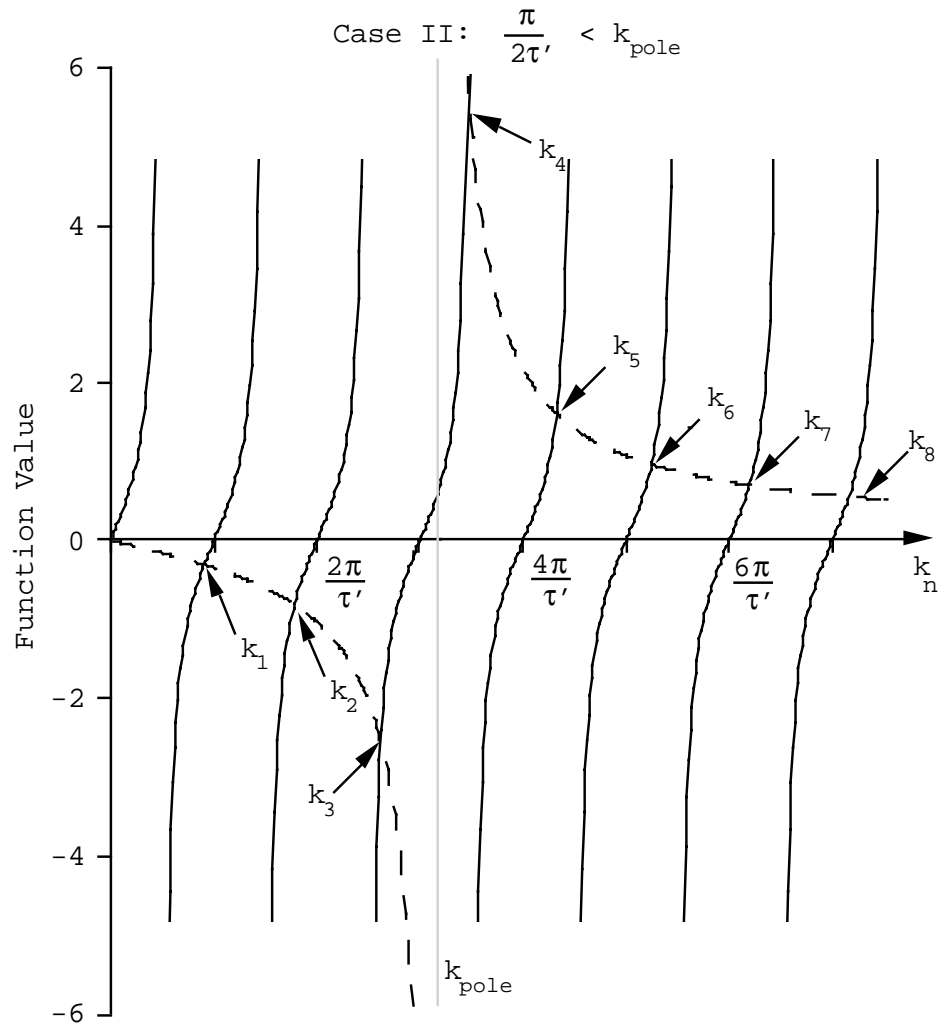


Figure A4.2: Eigenvalues of the diffusion equation. The dashed line represents the function on the R.H.S. of Equation (A4.10) and the solid lines correspond to the L.H.S. The functions are plotted as a function of  $k_n$ . This graph shows that if the singularity of the R.H.S. of Equation (A4.10) is greater than the first singularity of the L.H.S., then a number of eigenvalues exist less than the singularity given in Equation (A4.3).

in both cases. The total diffuse radiance in the three-dimensional solution to the delta-Eddington approximation is expressed as an infinite sum, Equation (4.141)

$$\varphi_d(\mathbf{r}) = \sum_{n=1}^{\infty} \frac{\sin(k_n \zeta + \gamma_n) B_n(\rho)}{N_n^2 \lambda_n^2} \left[ -\frac{S_0 z_n}{k_n^2 + 1} - \frac{Q_0 \sin \gamma_n}{h'} + \frac{Q_0 \sin(k_n \tau' + \gamma_n) \exp(-\tau')}{h'} \right]$$

As  $k_N \rightarrow (N - 1)\pi/\tau'$  the following limits are valid

$$\begin{aligned} \lambda_N^2 &\rightarrow k_N^2 & N_N^2 &\rightarrow \frac{\tau'}{2} \\ \sin k_N \tau' &\rightarrow 0 & \cos k_N \tau' &\rightarrow (-1)^{N-1} \\ \sin \gamma_N &\rightarrow 1 & \cos \gamma_N &\rightarrow 0 \end{aligned} \quad (\text{A4.18})$$

Furthermore, as  $(N - 1)\pi/\tau' \rightarrow \infty$ , then the limit of  $z_N$  may also be found

$$\lambda_N^2 \rightarrow k_N^2 \quad z_N \rightarrow 1 \quad (\text{A4.19})$$

Substituting the limiting forms of Equations (A4.18) and (A4.19) into Equation (4.141), yields the following expression for the total diffuse radiance in three dimensions.

$$\begin{aligned} \phi_d(\mathbf{r}) &= \sum_{n=1}^N \phi_d^n(\mathbf{r}) - \frac{S_0 \tau'^3 B_N(\rho)}{45 h'} \frac{90}{\pi^4} \sum_{n=N-1}^{\infty} \frac{\cos(n\pi\zeta/\tau')}{n^4} \\ &- \frac{Q_0 \tau' B_N(\rho)}{h'} \left[ 1 + (-1)^N \exp(-\tau') \right] \frac{6}{\pi^2} \sum_{n=N-1}^{\infty} \frac{\cos(n\pi\zeta/\tau')}{n^2} \end{aligned} \quad (\text{A4.20})$$

The lower index is correct because  $k_N \rightarrow (N - 1)\pi/\tau'$ .

The anisotropic surface term in the equation above converges as  $1/n^2$ . This is very slow. A better method for evaluating these sums numerically is to use

$$\sum_{n=N-1}^{\infty} \frac{\cos(n\pi\zeta/\tau')}{n^2} = \sum_{n=1}^{\infty} \frac{\cos(n\pi\zeta/\tau')}{n^2} - \sum_{n=1}^{N-2} \frac{\cos(n\pi\zeta/\tau')}{n^2} \quad (\text{A4.21})$$

$$\sum_{n=N-1}^{\infty} \frac{\cos(n\pi\zeta/\tau')}{n^4} = \sum_{n=1}^{\infty} \frac{\cos(n\pi\zeta/\tau')}{n^4} - \sum_{n=1}^{N-2} \frac{\cos(n\pi\zeta/\tau')}{n^4} \quad (\text{A4.22})$$

The infinite sums are [17, Equation 1.443]

$$\sum_{n=1}^{\infty} \frac{\cos(n\pi\zeta/\tau')}{n^2} = \frac{\pi^2}{6} \left[ 1 - 3\frac{\zeta}{\tau'} + \frac{3}{2}\frac{\zeta^2}{\tau'^2} \right] \quad \text{if} \quad 0 \leq \frac{\zeta}{\tau'} \leq 2 \quad (\text{A4.23})$$

$$\sum_{n=1}^{\infty} \frac{\cos(n\pi\zeta/\tau')}{n^4} = \frac{\pi^4}{90} \left[ 1 - \frac{15}{2}\frac{\zeta^2}{\tau'^2} + \frac{15}{2}\frac{\zeta^3}{\tau'^3} - \frac{15}{8}\frac{\zeta^4}{\tau'^4} \right] \quad \text{if} \quad 0 \leq \frac{\zeta}{\tau'} \leq 2 \quad (\text{A4.24})$$

A similar correction exists for the derivative of the diffuse radiance with respect to  $z$ . This derivative is needed to calculate flux densities and may be used to calculate fluence rates. In the expression below, the isotropic term converges as  $1/n^3$  and the anisotropic term converges as  $1/n$ . Consequently, the numerical finesse used above is even more useful for calculating the derivative

$$\begin{aligned} \frac{\partial\varphi_d(\mathbf{r})}{\partial\zeta} &= \sum_{n=1}^N \phi_d^n(\mathbf{r}) - \frac{S_0\tau'^2 B_N(\rho)}{3h'} \frac{6}{\pi^3} \sum_{n=N-1}^{\infty} \frac{\sin(n\pi\zeta/\tau')}{n^3} \\ &+ \frac{Q_0 B_N(\rho)}{h'} \left[ 1 + (-1)^N \exp(-\tau') \right] \frac{2}{\pi} \sum_{n=N-1}^{\infty} \frac{\sin(n\pi\zeta/\tau')}{n} \end{aligned} \quad (\text{A4.25})$$

The correction terms may be evaluated using the following infinite sum formulas

$$\sum_{n=1}^{\infty} \frac{\sin(n\pi\zeta/\tau')}{n^3} = \frac{\pi^3}{6} \left[ \frac{\zeta}{\tau'} - \frac{3}{2}\frac{\zeta^2}{\tau'^2} + \frac{1}{2}\frac{\zeta^3}{\tau'^3} \right] \quad \text{if} \quad 0 \leq \frac{\zeta}{\tau'} \leq 2 \quad (\text{A4.26})$$

$$\sum_{n=1}^{\infty} \frac{\sin(n\pi\zeta/\tau')}{n^4} = \frac{\pi}{2} \left[ 1 - \frac{\zeta}{\tau'} \right] \quad \text{if} \quad 0 \leq \frac{\zeta}{\tau'} \leq 2 \quad (\text{A4.27})$$

Equation (A4.28) cannot be used when  $\zeta = 0$ . Physically, this corresponds to the top boundary. The easiest method for finding the derivative at this point is to use the boundary condition (4.79). In this case, the derivative of the diffuse radiance is given by

$$\frac{\partial\varphi_d(\mathbf{r})}{\partial\zeta} = \frac{A_{\text{top}} Q_0 \pi F_0(\rho) + \varphi_d(\mathbf{r})}{A_{\text{top}} h'} \quad (\text{A4.28})$$

## Bibliography

- [1] V. A. Ambartsumian. Diffuse reflection of light by a foggy medium. *Compt. Rend. (Doklady) Akad. U. R. S. S.*, 38:257, 1943.
- [2] Bausch and Lomb: Analytic Systems Division. *Refractive index and percent dissolved solids scale*.
- [3] R. E. Bellman, R. Kalaba, and M. C. Prestud. *Invariant Imbedding and Radiative Transfer in Slabs of Finite Thickness*. Am. Elsevier, New York, 1963.
- [4] P. R. Bevington. *Data Reduction and Error Analysis for the Physical Sciences*. McGraw-Hill Book Co., New York, 1969.
- [5] W. A. G. Bruls and J. C. van der Leun. Forward scattering properties of human epidermal layers. *Photochem. Photobiol.*, 40:231–242, 1984.
- [6] L. L. Carter and E. D. Cashwell. *Particle-Transport Simulation with the Monte Carlo Method*. USERDA Technical Information Center, Oak Ridge, 1975.
- [7] K. M. Case and P. F. Zweifel. *Linear Transport Theory*. Addison-Wesley Publishing Co., Reading, 1967.
- [8] S. Chandrasekhar. *Radiative Transfer*. Dover, New York, 1960.

- [9] W. F. Cheong, M. Motamedi, and A. J. Welch. Optical modeling of laser photocoagulation of bladder tissue. *Lasers Surg. Med.*, 7:72, 1987.
- [10] A. L. Crosbie and R. G. Schrenker. Multiple scattering in a two-dimensional rectangular medium exposed to collimated radiation. *J. Quant. Spectrosc. Radiat. Transfer*, 33:101–125, 1985.
- [11] W. G. Egan, T. W. Hilgeman, and J. Reichman. Determination of absorption and scattering coefficients for nonhomogeneous media. 2: Experiment. *Appl. Opt.*, 12:1816–1823, 1973.
- [12] S. T. Flock, B. C. Wilson, and M. S. Patterson. Total attenuation coefficients and scattering phase functions of tissues and phantom materials at 633 nm. *Med. Phys.*, 14:835–841, 1987.
- [13] S. T. Flock, B. C. Wilson, and M. S. Patterson. Hybrid Monte Carlo-diffusion theory modelling of light distributions in tissue. In M. W. Berns, editor, *SPIE Proceedings of Laser Interaction with Tissue*, volume 908, pages 20–28, 1988.
- [14] R. A. Forester and T. N. K. Godfrey. MCNP—A general Monte Carlo code for neutron and photon transport. In R. Alcouffe, R. Dautray, A. Forster, G. Ledanois, and B. Mercier, editors, *Methods and Applications in Neutronics, Photonics and Statistical Physics*, pages 33–47. Springer-Verlag, New York, 1983.
- [15] G. E. Forsythe, M. A. Malcolm, and C. B. Moler. *Computer Methods for Mathematical Computations*. Prentice-Hall Inc., Englewood, 1977.

- [16] R. G. Giovanelli. Reflection by semi-infinite diffusers. *Optica Acta*, 2:153–162, 1955.
- [17] I. S. Gradshteyn and I. M. Ryzhik. *Table of Integrals, Series, and Products*. Academic Press, New York, 1980.
- [18] I. P. Grant and G. E. Hunt. Radiative transfer in a Rayleigh scattering atmosphere. *J. Quant. Spectrosc. Radiat. Transfer*, 8:1817–1832, 1968.
- [19] I. P. Grant and G. E. Hunt. Solution of radiative transfer problems in planetary atmospheres. *Icarus*, 9:526–534, 1968.
- [20] I. P. Grant and G. E. Hunt. Solution of radiative transfer problems using the invariant  $S_n$  method. *Monthly Notices of the Royal Astronomical Society*, 141:27–41, 1968.
- [21] I. P. Grant and G. E. Hunt. Discrete space theory of radiative transfer I. Fundamentals. *Proceedings of the Royal Society of London A*, A313:183–197, 1969.
- [22] I. P. Grant and G. E. Hunt. Discrete space theory of radiative transfer II. Stability and non-negativity. *Proceedings of the Royal Society of London A*, A313:199–216, 1969.
- [23] T. Halldórsson, W. Rother, J. Langerholc, and F. Frank. Theoretical and experimental investigations prove Nd:YAG laser treatment to be safe. *Lasers Surg. Med.*, 1:253–262, 1981.
- [24] J. E. Hansen and L. D. Travis. Light scattering in planetary atmospheres. *Space Science Reviews*, 16:525–610, 1974.

- [25] J. S. Hendricks and T. E. Booth. MCVP variance reduction overview. In R. Alcouffe, R. Dautray, A. Forster, G. Ledanois, and B. Mercier, editors, *Methods and Applications in Neutronics, Photonics and Statistical Physics*, pages 83–92. Springer-Verlag, New York, 1983.
- [26] W. G. Houf and F. P. Incropera. An assessment of techniques for predicting radiation transfer in aqueous media. *J. Quant. Spectrosc. Radiat. Transfer*, 23:101–115, 1980.
- [27] G. E. Hunt. A review of computational techniques for analysing the transfer of radiation through a model cloudy atmosphere. *J. Quant. Spectrosc. Radiat. Transfer*, 11:655–690, 1971.
- [28] W. M. Irvine. Multiple scattering by large particles. *Astrophys. J.*, 142:1463–1475, 1965.
- [29] W. M. Irvine. Multiple scattering in planetary atmospheres. *Icarus*, 25:175–204, 1975.
- [30] A. Ishimaru. Limitation on image resolution imposed by a random medium. *Appl. Opt.*, 17:348–, 1978.
- [31] A. Ishimaru. *Wave Propagation and Scattering in Random Media*, volume 1. Academic Press, New York, 1978.
- [32] S. L. Jacques, C. A. Alter, and S. A. Prahl. Angular dependence of HeNe laser light scattering by human dermis. *Lasers Life Sci.*, 1:309–333, 1987.
- [33] E. Jahnke and F. Emde. *Tables of Functions*. Dover, New York, 1945.



- [34] J. H. Joseph, W. J. Wiscombe, and J. A. Weinman. The delta-Eddington approximation for radiative flux transfer. *J. Atmos. Sci.*, 33:2452–2459, 1976.
- [35] H. Kahn. Random sampling Monte Carlo techniques in neutron attenuation problems I. *Nucleonics*, 6:27–37, 1950.
- [36] H. Kahn. Random sampling Monte Carlo techniques in neutron attenuation problems II. *Nucleonics*, 6:61–65, 1950.
- [37] H. Kahn. Use of different Monte Carlo sampling techniques. In H. A. Meyer, editor, *Symposium on Monte Carlo Methods*, pages 146–190, New York, 1956. John Wiley and Sons Inc.
- [38] H. Kahn and T. E. Harris. Estimation of particle transmission by random sampling. In *Monte Carlo Method*, volume 12 of *National Bureau of Standards Applied Mathematics Series*. U. S. Government Printing Office, 1951.
- [39] M. Keijzer, W. M. Star, and P. R. M. Storchi. Optical diffusion in layered media. *Appl. Opt.*, 2:1820–1824, 1988.
- [40] K. N. Liou. A numerical experiment on Chandrasekhar’s discrete ordinate method for radiative transfer: Applications to cloudy and hazy atmospheres. *J. Atmos. Sci.*, 30:1303–1326, 1973.
- [41] K. N. Liou. *An Introduction to Atmospheric Radiation*. Academic Press, New York, 1980.

- [42] N. Metropolis and S. Ulam. The Monte Carlo method. *J. Am. Statistical Association*, 44:335–341, 1949.
- [43] H. H. Michels. Abscissas and weight coefficients for Lobatto quadrature. *Mathematical Computation*, 17:237–244, 1963.
- [44] P. M. Morse and H. Feshbach. *Methods of Theoretical Physics*. McGraw-Hill Book Co. Inc., New York, 1953.
- [45] J. A. Nelder and R. Mead. *Computer J.*, 7:380, 1965.
- [46] S. E. Orchard. Reflection and transmission of light by diffusing suspensions. *J. Opt. Soc. Am.*, 59:1584–1597, 1969.
- [47] G. N. Plass, G. W. Kattawar, and F. E. Catchings. Matrix operator theory of radiative transfer. 1: Rayleigh scattering. *Appl. Opt.*, 12:314–329, 1973.
- [48] R. W. Preisendorfer. *Hydrologic Optics*. U. S. Department of Commerce, 1976.
- [49] W. H. Press, B. P. Flannery, S. A. Teukolsky, and W. T. Vetterling. *Numerical Recipes: The Art of Scientific Computing*. Cambridge University Press, New York, 1986.
- [50] L. Reynolds, C. C. Johnson, and A. Ishimaru. Diffuse reflectance from a finite blood medium: Applications to the modeling of fiber optic catheters. *Appl. Opt.*, 15:2059–2067, 1976.
- [51] G. F. Roach. *Green's Functions*. Cambridge University Press, Cambridge, 1982.

- [52] G. B. Rybicki. The searchlight problem with isotropic scattering. *J. Quant. Spectrosc. Radiat. Transfer*, 11:827–849, 1971.
- [53] J. W. Ryde. The scattering of light by turbid media—Part I. *Proc. Roy. Soc. (London)*, A131:451–464, 1931.
- [54] J. W. Ryde and B. S. Cooper. The scattering of light by turbid media—Part II. *Proc. Roy. Soc. (London)*, A131:464–475, 1931.
- [55] E. P. Shettle and J. A. Weinman. The transfer of solar irradiance through inhomogeneous turbid atmospheres evaluated by Eddington’s approximation. *J. Atmos. Sci.*, 27:1048–1055, 1970.
- [56] Y. A. Shreider. *The Monte Carlo Method*. Pergamon Press Inc., New York, 1966.
- [57] I. M. Sobol’. *The Monte Carlo Method*. The University of Chicago Press, Chicago, 1974.
- [58] W. M. Star, J. P. A. Marijnissen, and M. J. C. van Gemert. Light dosimetry in optical phantoms and in tissues: I. Multiple flux and transport theory. *Phys. Med. Biol.*, 33:437–454, 1988.
- [59] H. C. van de Hulst. A new look at multiple scattering. Technical report, NASA Institute for Space Studies, New York, 1962.
- [60] H. C. van de Hulst. *Multiple Light Scattering*, volume 1. Academic Press, New York, 1980.
- [61] H. C. van de Hulst. *Multiple Light Scattering*, volume 2. Academic Press, New York, 1980.

- [62] H. C. van de Hulst and M. M. Davis. *Proc. Koninkl. Nederl. Akad. Wet.*, B64:220, 1961.
- [63] H. C. van de Hulst and W. M. Irvine. General report on radiation transfer in planets: Scattering in model planetary atmospheres. *Mem. Soc. Roy. Sci. Liège*, 15th Ser 7:78, 1963.
- [64] M. J. C. van Gemert and W. M. Star. Relations between the Kubelka-Munk and the transport equation models for anisotropic scattering. *Lasers Life Sci.*, 1:287–298, 1987.
- [65] B. C. Wilson and G. Adam. A Monte Carlo model for the absorption and flux distributions of light in tissue. *Med. Phys.*, 10:824–830, 1983.
- [66] W. J. Wiscombe. On initialization, error and flux conservation in the doubling method. *J. Quant. Spectrosc. Radiat. Transfer*, 16:637–658, 1976.
- [67] W. J. Wiscombe. Doubling initialization revisited. *J. Quant. Spectrosc. Radiat. Transfer*, 18:245–248, 1977.
- [68] A. N. Witt. Multiple scattering in reflection nebulae I. A Monte Carlo approach. *Astrophys. J.*, S35:1–6, 1977.
- [69] G. Yoon. *Absorption and Scattering of Laser Light in Biological Media — Mathematical Modeling and Methods for Determining Optical Properties*. PhD thesis, University of Texas at Austin, 1988.
- [70] G. Yoon, A. J. Welch, M. Motamedi, and M. C. J. Van Gemert. Development and application of three-dimensional light distribution model for laser irradiated tissue. *IEEE J. Quantum Electron.*, QE-23:1721–1733, 1987.

## Vita

Scott Alan Prah1 was born in Laramie, Wyoming, on July 10, 1960, the son of Susan Gay Prah1 and Robert Dennis Prah1. After completing his work at Enterprise High School, Redding, California, in 1978, he entered The California Institute of Technology in Pasadena, California. He received the degree of Bachelor of Science in applied physics from The California Institute of Technology in June 1982. In September 1982, he entered The Graduate School of The University of Texas at Austin.

Permanent address: OMLC  
St. Vincent Hospital  
9205 SW Barnes Rd  
Portland, OR 97225

This dissertation was typeset by the author.